

**The design and characterisation of miniature robotics for astronomical  
instruments**

**William Andrew Cochrane**

Submitted for the degree of Doctor of Engineering

Heriot-Watt University

School of Engineering and Physical Sciences

September 2015

The copyright in this thesis is owned by the author. Any quotation from the thesis or use of any of the information contained in it must acknowledge this thesis as the source of the quotation or information.

## ABSTRACT

Micro robotics has the potential to improve the efficiency and reduce cost of future multi-object instruments for astronomy. This thesis reports on the development and evolution of a micro autonomous pick-off mirror called the Micro Autonomous Positioning System (MAPS) that can be used in a multi-object spectrograph. The design of these micro-autonomous pick-off mirrors is novel as they are capable of high precision positioning using electromagnetic propulsion through utilising non-conventional components and techniques. These devices are self-driven robotic units, which with the help of an external control system are capable of positioning themselves on an instruments focal plane to within 24  $\mu\text{m}$ . This is different from other high precision micro robotics as they normally use piezoelectric actuators for propulsion. Micro robots have been developed that use electromagnetic motors, however they are not used for high precision applications.

Although there is a plethora of literature covering design, functionality and capability of precision micro autonomous systems, there is limited research on characterisation methods for their use in astronomical applications. This work contributes not only to the science supporting the design of a micro-autonomous pick-off mirror but also presents a framework for characterising such miniature mechanisms.

The majority of instruments are presented with a curved focal plane. Therefore, to ensure that the pick-off mirrors are aligned properly with the receiving optics, either the pick-off mirror needs to be tipped or the receiving optics repositioned. Currently this function is implemented in the beam steering mirror (i.e. the receiving optics). The travel range required by the beam steering mirror is relatively large, and as such, it is more difficult to achieve the positional accuracy and stability. By incorporating this functionality in the pick-off mirror, the instrument can be optimised in terms of size, accuracy and stability. A unique self-adjusting mirror (SAM) is thus proposed as a solution and detailed.

As a proof-of-concepts both MAPS and SAM usability in multi-object spectrographs was evaluated and validated. The results indicate their potential to meet the requirements of astronomical instruments and reduce both the size and cost.

## ACKNOWLEDGEMENTS

I would like to thank my supervisors Dr. Theodore Lim and Dr. Hermine Schnetler for their guidance and patience especially with reviewing my thesis. I would also like to take this moment to thank Ian for reviewing my thesis. I want to thank my examiners, Dr. Xianwen Kong and Dr. Jean-Marc Breguet, for taking their time to go over my thesis and provide me with valuable input.

I must thank all of my colleagues at the UK Astronomy Technology Centre. I find myself learning more everyday by working alongside each of you. The guys in the workshops deserve a special mention because no matter how much of a nuisance I must have been, they have always provided me with their best efforts and a few laughs. There are far too many people at the UK ATC that I want to thank for me to name. However, that being said special thanks must be given to Dr. William Taylor. Since starting there we have worked closely together on MAPS. There has been many frustrating days in the lab and just as many good days. It has been a pleasure.

I would like to thank the support provided by the staff within the Engineering Doctorate Centre at Heriot Watt University. Alison and Linda do an excellent job helping me.

Finally, to my family and friends, thank you. The patience and support is greatly appreciated. My parents and brother have always been a great source of encouragement, understanding and inspiration.

Thank you.

# ACADEMIC REGISTRY

## Research Thesis Submission



Name:	William Andrew Cochrane		
School/PGI:	School of Engineering and Physical Sciences		
Version: <i>(i.e. First, Resubmission, Final)</i>	Final	Degree Sought (Award <b>and</b> Subject area)	Doctor of Engineering in Optic and Photonic Technologies

### Declaration

In accordance with the appropriate regulations I hereby submit my thesis and I declare that:

- 1) the thesis embodies the results of my own work and has been composed by myself
- 2) where appropriate, I have made acknowledgement of the work of others and have made reference to work carried out in collaboration with other persons
- 3) the thesis is the correct version of the thesis for submission and is the same version as any electronic versions submitted\*.
- 4) my thesis for the award referred to, deposited in the Heriot-Watt University Library, should be made available for loan or photocopying and be available via the Institutional Repository, subject to such conditions as the Librarian may require
- 5) I understand that as a student of the University I am required to abide by the Regulations of the University and to conform to its discipline.

\* *Please note that it is the responsibility of the candidate to ensure that the correct version of the thesis is submitted.*

Signature of Candidate:		Date:	2015-09-17
-------------------------	--	-------	------------

### Submission

Submitted By <i>(name in capitals)</i> :	William Andrew Cochrane
Signature of Individual Submitting:	
Date Submitted:	2015-09-17

### For Completion in the Student Service Centre (SSC)

Received in the SSC by <i>(name in capitals)</i> :			
<b>Chapter 1</b> Method of Submission <i>(Handed in to SSC; posted through internal/external mail):</i>			
<b>Chapter 2E</b> -thesis Submitted <i>(mandatory for final theses)</i>			
Signature:		Date:	



## Table of Contents

<b>LIST OF TABLES</b> .....	vi
<b>LIST OF FIGURES</b> .....	vii
<b>LIST OF PUBLICATIONS</b> .....	x
Chapter 1 – Introduction.....	1
1.1 Large Ground Based Telescopes.....	1
1.2 Multi Object Spectrographs .....	2
Chapter 2 - Miniature Mechatronics for Astronomy Observations .....	9
2.1 Astronomers’ Requirements.....	9
2.1.1 Miniature Autonomous Robot Candidates for Astronomy .....	11
2.1.2 MAPS Overall System Design.....	15
2.2 MAPS Robot (MA-BOT) Requirements.....	17
2.3 Concept Designs .....	18
2.3.1 Command and Control Module .....	21
Chapter 3 – The MAPS Robot (MA-BOT1) .....	24
3.1 The Design .....	24
3.2 Initial Design Assessment .....	30
3.3 Theoretical Performance .....	33
3.4 Actual Performance.....	35
3.5 MA-BOT1.1 .....	40
3.5.1 MA-BOT 1.1 PowerFloor Test .....	43
Chapter 4 – The MAPS Robot (MA-BOT2) .....	47
4.1 MA-BOT2 On-Board Electronics .....	47
4.2 Modifications to the robot.....	48
4.3 Expected Performance .....	52
4.4 Actual Performance – Open-Loop Straight Line.....	52
4.5 Actual Performance – Open-Loop Rotational Tests .....	57
4.6 Actual Performance – Open-Loop Turret Tests .....	61
4.7 Closed Loop System Tests.....	63
4.7.1 Dual Camera Configuration.....	63
4.7.2 Faro Laser Tracker Setup.....	68
4.8 Conclusions .....	71
Chapter 5 - Self Adjusting Mirror .....	73
5.1 The Reason for SAM .....	73
5.2 Current Miniature Self Adjustable Mirrors .....	75
5.3 System Design.....	77
5.4 Potential Concepts.....	82
5.5 SAM Computer Aided Design Evaluation .....	85
5.6 Description of evaluation model .....	89
5.7 The Expected Performance .....	99
5.7.1 Tip Module .....	100
5.7.2 Rotation Module .....	100
5.8 Actual Performance.....	101
5.8.1 Tip Module .....	101
5.8.2 Rotation Module Tests.....	114
5.9 Conclusions .....	119
Chapter 6 – Conclusion and Future Work .....	120
6.1 MAPS & SAM Compared .....	123
6.2 Precision Autonomous Mirror.....	124
6.2.1 Going One Step Further .....	126
6.2.2 Closing Remarks.....	127
Appendix A – MAPS Assembly and BOM .....	128
Appendix B - SAM BOM.....	129

## LIST OF TABLES

Table I-1-1: Nomenclature .....	ix
Table 1-1: Positioner Summary .....	6
Table 2-1: Pick-Off System Performance Characteristics [42].....	10
Table 2-2: Summary of Autonomous Robots (Electromagnetic) .....	11
Table 2-3: Summary of Autonomous Robots (Piezoelectric) .....	12
Table 2-4: Driving Requirements for MAPS [57] .....	17
Table 2-5: Summary of investigated designs .....	19
Table 2-6: Command and Control Module Summary .....	21
Table 3-1: Symbols used in (3-1) .....	27
Table 4-1: Straight Line Test Results .....	55
Table 4-2: 274300 Motor Step Straight Line Test Results .....	55
Table 4-3: Linear Repetition from different clock rates .....	57
Table 4-4: Rotation Test Results .....	58
Table 4-5: Turret Results .....	61
Table 4-6: Angular Robot Misalignment .....	68
Table 4-7: Measured Tip Angles .....	68
Table 4-8: MAPS Robot Closed Loop Repeatability .....	71
Table 4-9: Summary of MABOT2 .....	71
Table 4-10: Cost Comparison .....	72
Table 5-1: Summary of Adjustable Mirrors.....	76
Table 5-2: SAM Requirements .....	81
Table 5-3: Summary of Classical Mechanical Methods .....	83
Table 5-4: Scoring Determination .....	84
Table 5-5: Numerical Analysis Template .....	84
Table 5-6: Results of Numerical Analysis .....	85
Table 5-7: Summary of SAM designs part 1 .....	86
Table 5-8: Summary of SAM designs, part 2 .....	87
Table 5-9: Results from Varying Breadth.....	98
Table 5-10: Torsion Equation Variables.....	113
Table 5-11: SAM Capabilities .....	119
Table 6-1: EAGLE/MAPS Requirement/Capabilities Comparison.....	121
Table 6-2: SAM Capabilities .....	122
Table 6-3: Miniature Astronomical Pick-Off Technologies .....	123

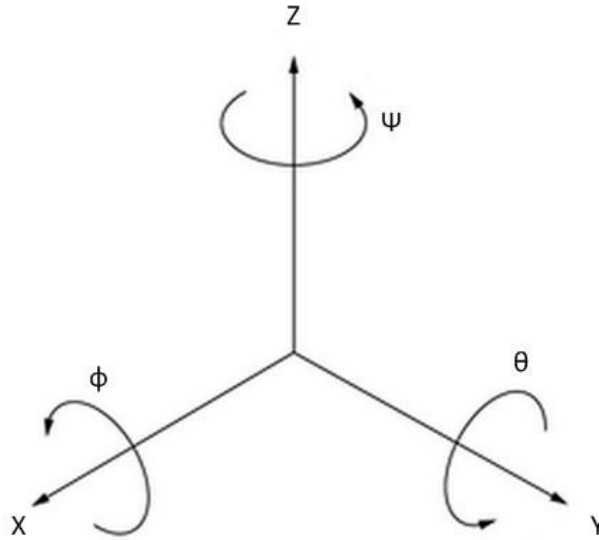
# LIST OF FIGURES

Figure I-1-1: Coordinate System .....	ix
Figure 1-1: ELT Optical Design [7] .....	2
Figure 1-2: Trend Analysis of MOS Instruments [32] .....	3
Figure 1-3: Star-Picker [35] .....	4
Figure 1-4: KMOS [31] .....	5
Figure 1-5: Miniature Autonomous Robot Concept .....	7
Figure 2-1: Critique diagrams of current micro autonomous electromagnetic robots .....	13
Figure 2-2: Critique diagrams of current micro autonomous piezoelectric robots .....	14
Figure 2-3: MAPS System Architecture [55] .....	16
Figure 3-1: MA-BOT1 CAD Model .....	24
Figure 3-2: Smoovy 0308B Motor .....	25
Figure 3-3: MAPS Chassis .....	26
Figure 3-4: Sectional View of Chassis Illustrating Grub Screw Interface .....	26
Figure 3-5: Axles .....	27
Figure 3-6: Wheels .....	28
Figure 3-7: Stabiliser Heights .....	28
Figure 3-8: MA-BOT1 .....	29
Figure 3-9: Stabilisers .....	29
Figure 3-10: Four Assembled Iteration 1 Robots .....	30
Figure 3-11: Spring Holes .....	31
Figure 3-12: Illustration of wheel misalignment with motor pinion .....	31
Figure 3-13: Pinions Crowned and Non-Crowned .....	32
Figure 3-14: Gear head Assembly [61] .....	33
Figure 3-15: Schematic of wheel and pinion combination .....	34
Figure 3-16: Rotational Step Theory .....	34
Figure 3-17: MA-BOT1 Straight Line Repeatability Test Setup .....	35
Figure 3-18: Features measured using the Nikon microscope .....	36
Figure 3-19: Sample of Repeatability Test Results .....	37
Figure 3-20: Deviation of Measured Results from Theoretical Prediction .....	38
Figure 3-21: Deviation plot of robot from starting position .....	39
Figure 3-22: Distance Travelled for X Steps .....	40
Figure 3-23: PowerFloor .....	42
Figure 3-24: Power Brush PCB .....	42
Figure 3-25: MA-BOT1.1 .....	43
Figure 3-26: MA-BOT1.1 PowerFloor Test – A Single Run .....	44
Figure 3-27: Bar Plot of Power Loss Durations .....	44
Figure 3-28: 90 mm Travel Power Loss Duration .....	45
Figure 4-1: MAPS Robot Evolution .....	47
Figure 4-2: MA-BOT2 Electronics .....	48
Figure 4-3: Wire routing between power boards .....	49
Figure 4-4: Stabiliser Locations for PowerFloor Robot (a) First Location, (b) New Location .....	49
Figure 4-5: Second Iteration Robot with Copper Weight .....	51
Figure 4-6: FRS with Electronics Cube Sub-Assembly .....	51
Figure 4-7: MA-BOT2 .....	52
Figure 4-8: Faro Precision Measurements .....	53
Figure 4-9: Target Mirror used to replace the POM .....	53
Figure 4-10: 21100 Step Results for 274300 Step overall travel .....	54
Figure 4-11: 274300 Step Motion .....	56
Figure 4-12: Robot's Motion along the PowerFloor at 10,000 Hz Clock Rate .....	57
Figure 4-13: Angle to Step Relationship based on tested results .....	58
Figure 4-14: Rotational Slippage 60° Rotations .....	59
Figure 4-15: Chassis Backlash Test Procedure .....	60
Figure 4-16: Rotational Backlash .....	60
Figure 4-17: Turret Motor Steps to Delta Angle Relationship .....	61
Figure 4-18: Turret x-y Position for changes in angle .....	62
Figure 4-19: Closed Loop Test Setup .....	64
Figure 4-20: Beam Spot Description .....	66

Figure 4-21: Normalised Image of Centroid Measurements on PowerFloor Surface .....	67
Figure 4-22: Faro Tracker Alignment.....	69
Figure 4-23: Robot Offset from Commanded Position for red & green laser positions .....	70
Figure 5-1: Optical Misalignment Description [32] .....	74
Figure 5-2: (a) BSM arrangement around the focal plane, (b) BSM Design [57] .....	75
Figure 5-3: Simplified BSM .....	75
Figure 5-4: Top-Level Function Diagram .....	77
Figure 5-5: POM/BSM Configuration Functional Flow Diagram.....	79
Figure 5-6: SAM System Design Overview .....	80
Figure 5-7: SAM Rivet Geometry .....	90
Figure 5-8: Power Module Underside .....	91
Figure 5-9: Rotation Module .....	92
Figure 5-10: Rotation Module Lid.....	93
Figure 5-11: Tip Module .....	94
Figure 5-12: Linear Guide Assembly .....	95
Figure 5-13: Tip Module Cover.....	96
Figure 5-14: Mirror Holder.....	96
Figure 5-15: Breakdown of Forces .....	97
Figure 5-16: Mirror Flexure.....	98
Figure 5-17: SAM.....	99
Figure 5-18: Tip Module Theoretical Results.....	100
Figure 5-19: Optical Method Output .....	102
Figure 5-20: Zemax model .....	103
Figure 5-21: Comparison of Zemax and Measured Output .....	103
Figure 5-22: Zemax and Experimental Results Comparison .....	104
Figure 5-23: CMM Test Setup.....	105
Figure 5-24: Comparison of CMM Measurements and Expected Results.....	105
Figure 5-25: Comparison of Optical & CMM Results .....	106
Figure 5-26: Combined Tip Module Graph.....	107
Figure 5-27: Single Squiggle Motor Step Motions.....	108
Figure 5-28: Individual Stepping Results .....	109
Figure 5-29: Zemax Ray-trace of SAM in EAGLE .....	110
Figure 5-30: Mirror Module Re-Design .....	111
Figure 5-31: Illustration of SAM Torsion Rotation .....	112
Figure 5-32: Optical Measuring System .....	115
Figure 5-33: RM Smoovy Motor Step to Angle Relationship .....	116
Figure 5-34: Repeatability of 10,000 Step Command .....	117
Figure 5-35: Mirror's X-Y Shift during rotation .....	117
Figure 5-36: Resolution Test Results.....	118
Figure 6-1: Belt Driven Robot Concept.....	125
Figure 6-2: Mini Robot Spectrograph Concept .....	126

## COORDINATE SYSTEM

The following is the coordinate system used for this thesis work:



**Figure I-1-1: Coordinate System**

**Table I-1-1: Nomenclature**

Symbol	Definition	Name
X, Y, Z	Reference Coordinates	N/A
$\Phi$	Rotation around X-axis	Tilt
$\theta$	Rotation around Y-axis	Tip
$\psi$	Rotation around Z-axis	Rotation

## ACRONYMS AND DEFINITIONS

Acronym	Definition
ATC	Astronomy Technology Centre
BSM	Beam Steering Mirror
CAD	Computer Aided Design
CFi	Centre for Instrumentation
E-ELT	European Extremely Large Telescope
ESO	European Southern Observatory
GMT	Giant Magellan Telescope
GUI	Graphical User Interface
KMOS	K-band Multi Object Spectrograph
MAPS	Micro Autonomous Positioning System
MOS	Multi-Object Spectrograph
POM	Pick-Off Mirror
PWM	Pulse Width Modulation
SAM	Self-Adjusting Mirror
SCARA	Selective Compliance Assembly Robot
TMT	Thirty Metre Telescope
VLT	Very Large Telescope

## LIST OF PUBLICATIONS

W. A. Cochrane, “Conceptual Design of an Autonomous Micro-Robot for Astronomical Instrumentation,” Heriot Watt University, Edinburgh, (2009)

D. Atkinson, W. Cochrane, D. Montgomery et al, “A Micro Autonomous Positioning System for Mirror Deployment,” Institute for Integrated Systems, (2010)

W. Taylor, D. Atkinson, W. Cochrane et al, “A prototype micro-autonomous positioning system for mirror deployment within multi-object instruments,” Proc. SPIE **7739**, 9780819482297 (2010)

W. Cochrane, X. Luo, T. Lim, and H. Schnetler, “New Pick-Off Systems for Multi-Object Observations within Astronomical Instrumentation,” IDC Optics and Photonics, (2011)

W. Cochrane, X. Luo, T. Lim et al, “Design of a Micro-Autonomous Robot for use in Astronomical Instruments,” Int. J. Optomechatronics **5**, 1559-9620 (2011)

W. Cochrane, X. Luo, T. Lim et al, “Recent testing of a micro autonomous positioning system for multi-object instrumentation,” Proc. SPIE **8450**, Modern Tech. in Space- and Ground-based Telescopes and Instrumentation II, 845019, (2012)

W. Taylor, H. Schnetler, W. Cochrane et al, “MAPS: where have the robots got to?” Proc. SPIE **8450**, Modern Tech. in Space- and Ground-based Telescopes and Instrumentation II, 845057 (2012)

# Chapter 1 – Introduction

The purpose of this thesis is to describe the design, development and verification of the use of micro-autonomous pick-off mirrors (POMs) in the next generation of ground-based telescopes multi-object spectrographs. These mirrors will be used to pick-off astronomical targets of interest and transfer the image to the Beam Steering Mirror (BSM) which passes the image through path correction and adaptive optics before delivering the image to the spectrograph for analysis. This thesis describes two developments: a micro autonomous robot<sup>1</sup> called the Micro-Autonomous Positioning Sub-System (MAPS) project and the development of a Self-Adjusting Mirror (SAM)<sup>2</sup>. For both developments, the designs were manufactured and characterised for their suitability in astronomical instrumentation.

It was intended to use this research to determine if miniature robotics can be used as an alternative to current pick-off systems. If successful this new technology could improve the overall design of multi-object spectrographs as they will no longer need to accommodate large, heavy pick-off systems.

This chapter provides a short overview of the application area.

## 1.1 Large Ground Based Telescopes

Astronomers study the origins and evolution of the universe. By using telescopes both in space and on the ground, the spectrum of light from stars is studied to help us understand what these objects are made of as well as to develop models to describe the dynamic behaviour of these most distant objects. Advancements in technology, allowing for larger telescopes to be produced with beam splitters and/or fold mirrors and CCD detectors, have made it possible for astronomers to observe multiple objects simultaneously, thus lowering costs and increasing the efficiency of observations. As the understanding of the universe increases and current technology is pushed to its limit, the need for more sensitive instruments to gain greater insight is required [1 - 3]. The collecting area and angular resolution are the key factors that determine a telescope's capability; with the angular resolution dominating the design of telescopes until the primary mirror diameter reaches the atmospheric seeing limit [4]. At that point, the collecting area becomes the dominant factor requiring the primary mirror to be larger, which

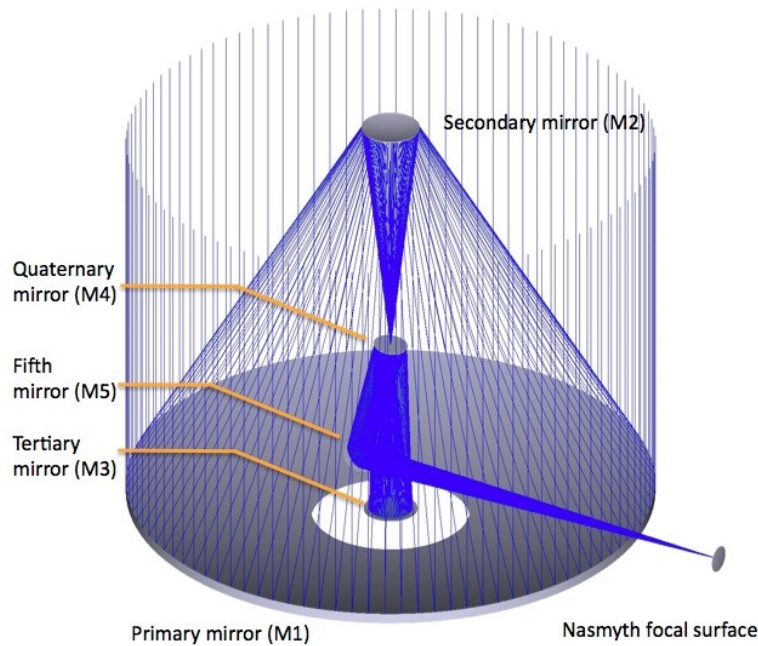
---

<sup>1</sup> Funded by the Centre for Instrumentation (Cfi)

<sup>2</sup> Funded by Opticon FP-7 Work Package 5

allows the collection of more photons thus making the observation of fainter distant objects possible. This has led to the development of concepts for extremely large telescopes such as the Thirty Metre Telescope (TMT), the Giant Magellan Telescope (GMT) and the European Extremely Large Telescope (E-ELT). One of the most interesting of these future telescopes is the E-ELT as when completed it will be the largest optical and infrared ground-based telescope in the world [5, 6]. The E-ELT is being developed by the European Southern Observatory (ESO), which the UK ATC is a member of.

Expected to be ready by 2024, the E-ELT will have a primary collecting mirror with a diameter of 38.5 m, built from 798 hexagonal segments. The Multi-Object Spectrograph (MOS) instrument will be located at the Nasmyth Platform focal station (Figure 1-1) where the photons from the selected objects will be spectrally analysed.



**Figure 1-1: ELT Optical Design [7]**

## 1.2 Multi Object Spectrographs

Spectroscopy is the separation of light into its constituent wavelengths for spectral analysis [8, 9], to study the chemical compositions of astronomical objects and to determine types of stars, galaxies and other astronomical objects. By multiplexing the collected light on an instrument's focal plane, multiple similar objects can be analysed simultaneously. This is a more efficient method compared to studying each object sequentially. Various types of multi-object spectrographs (MOS) have been developed over the last couple of decades. There are at

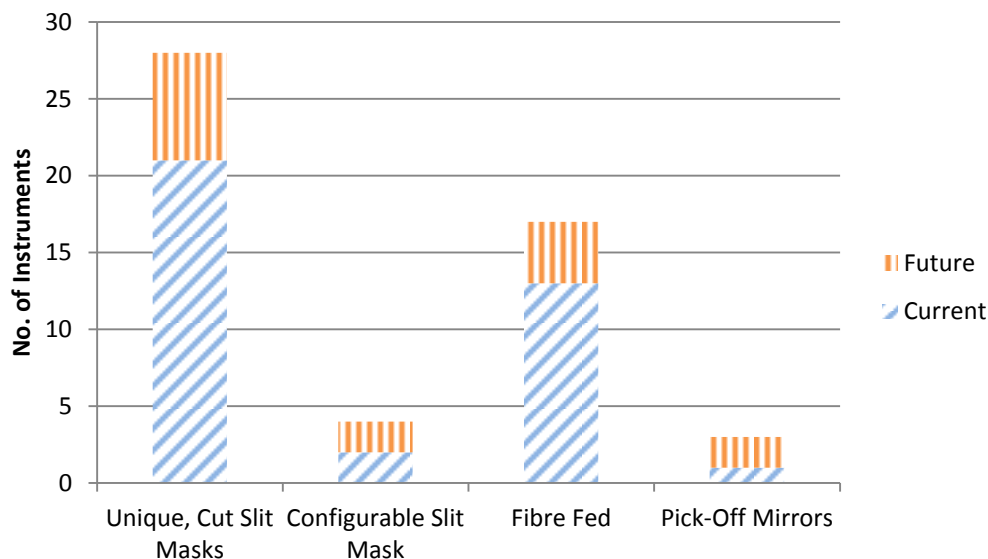


least three mainstream MOS instrument types currently deployed on various ground-based and space telescopes, namely:

- Slit Masks (ensures maximum throughput) [8, 10 - 20]
- Fibre Fed (highest number of astronomical objects can be observed simultaneously) [17, 21- 30]
- Pick-Off Mirrors (POMs) (no loss of spatial information) [31]

Figure 1-2 shows the current and planned deployment of MOS instruments. Slit masks are commonly used due to their simplicity. However, they suffer a major drawback, as plates must be pre-made for every observation. This limits the re-configurability and versatility of the instrument. To address this there are configurable slit masks that utilise sliders or micro-shutters but these are large mechanisms that need to cover the entire focal plane.

Due to the increased number of objects that can be observed simultaneously compared to slit masks, fibre-fed instruments are now the de facto standard. There are two broad categories for the robotic positioning of fibres, one is sequential and the other parallel. As the name suggests sequential positioners placed the fibres in position one at a time while the parallel method positions multiple fibres simultaneously. Fibre-fed instruments suffer more photon loss than other types of multi-object instruments due to absorption within the fibres' glass resulting in a lower throughput compared to that of slit masks.



**Figure 1-2: Trend Analysis of MOS Instruments [32]**

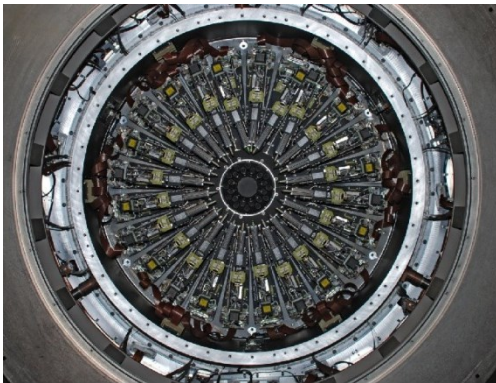
For some science cases [33, 34], the spatial information is as important as the spectral information. For these instruments, pick-off mirrors (POMs) are being developed, as slit masks do not provide spatial information quickly, and have a higher throughput compared to a fibre. For a slit mask, the spatial resolution is determined from the dimension along the slit and by stepping the position of the slit providing multiple spectrum points. This is slow compared to a fibre integral field unit as a bundle of fibres can each obtain a spectrum simultaneously and be combined to provide the spatial information. The POMs are positioned in the same manner as fibres, namely ‘Pick and Place systems’ and ‘Robotic Arms’.

Pick and place systems are typically through Cartesian or SCARA (Selective Compliance Assembly Robot Arm) robots. These types of positioning systems are capable of high repeatability. An excellent example of a SCARA type robot is StarPicker (Figure 1-3), which is capable of positioning buttons to within 10  $\mu\text{m}$  repeatedly. StarPicker has an overall reach of 450 mm and can work at cryogenic temperatures. It places magnetic buttons on the focal plate very precisely. There are two focal plates so that during an observation the second plate can be configured for the next observation. Typically the plates are mounted back-to-back such that at the completion of an observation the plates are flipped over maximising the observation time. This robot weighs over 500 kg and is relatively heavy compared to the mirrors it is moving that only weight a few grams.



**Figure 1-3: Star-Picker [35]**

Robotic arm positioners refer to arms where the end effector is a fixed mirror. Geometrically the arm is composed of a single revolute joint and one prismatic joint, and could be categorised as a cylindrical arm. This type of geometry is used in the K-band Multi Object Spectrograph (KMOS) (Figure 1-4), which is installed at the Very Large Telescope (VLT) in Chile. These arms when fully retracted occupy a volume of  $445 \times 70 \times 180 \text{ mm}^3$  while each pick-off mirror is only 3 mm in diameter, showing that a large amount of real estate is being used to position a relatively small object.



(a) 24 KMOS arms around the focal plane



(b) Single KMOS Arm

**Figure 1-4: KMOS [31]**

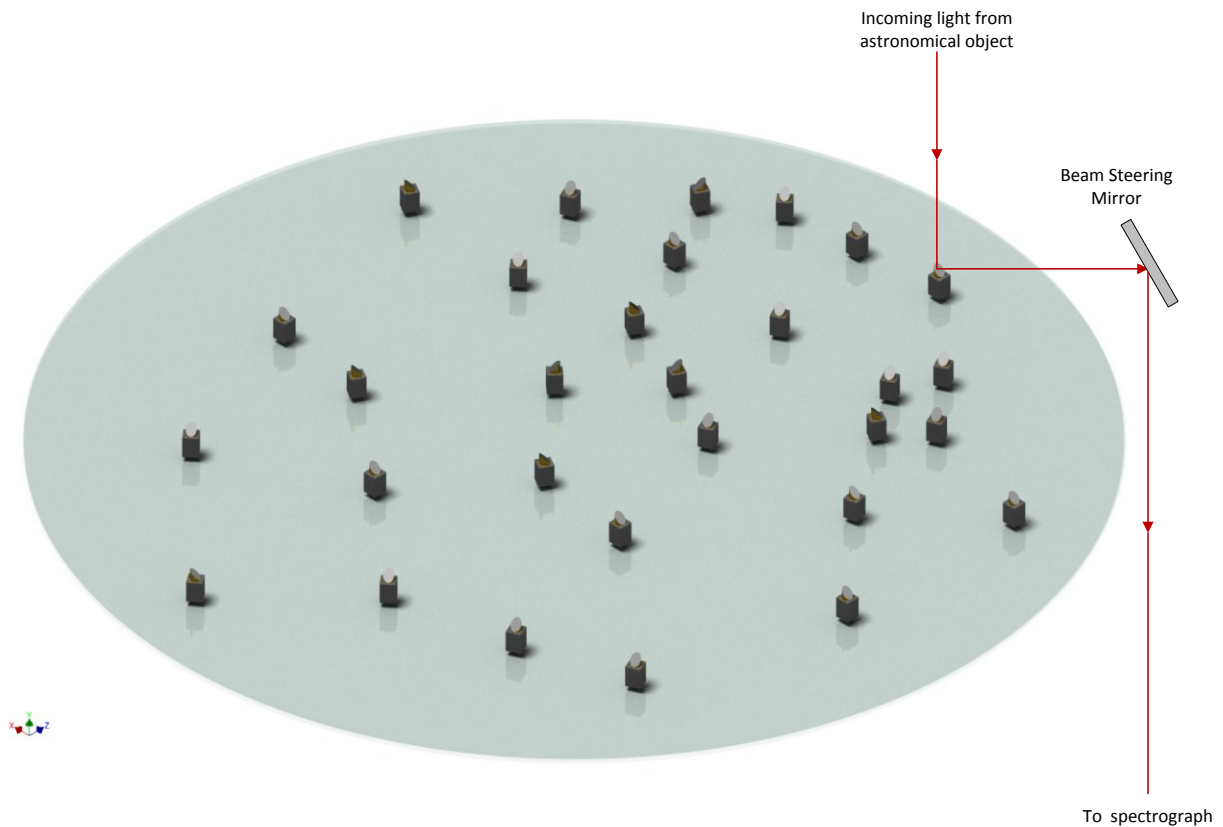
Due to the positioning of the arms around the circumference of the focal plane, the maximum number of POMs within the instrument is constrained by how many arms can fit around the focal plane. Regardless of this limiting factor, the arms are advantageous compared to the pick and place method as they can position all POMs concurrently allowing quick reconfigurations without the need of preparing focal plates beforehand.

Table 1-1 summarises the advantages and disadvantages of both methods. Unfortunately, for the MOS instrument currently under development for the E-ELT, robotic arms can no longer be considered due to the focal planes size and available volume. Pick and place is still a viable option however it has long configuration times due to the sequential placement of POMs. These mechanisms need to be large and sturdy enough to reach the entire focal plate. This means a relatively large mechanism in comparison to the POM.

**Table 1-1: Positioner Summary**

<b>Placement Technique</b>	<b>Advantages</b>	<b>Disadvantages</b>
<b>Pick and Place</b>	Place POMs anywhere on the focal plane	Long configuration times
	Clustering of POMs	Sequential placement of POMs
	Not a limiting factor for the number of POMs	As the focal plane increases in size so does the pick and place mechanism, requiring sturdier supports
<b>Robotic Arms</b>	Parallel Configuration of POMs	Limited number of POMs
	Short configuration times	Cannot cluster POMs Flexural issues as reach increases
<b>Micro Autonomous Robot</b>	Place POMs anywhere on the focal plane	Never been used for this application
	Clustering of POMs	
	Parallel Configuration of POMs	

Given the constraints and the disadvantages of the aforementioned positioning methods, the idea of a micro-autonomous pick-off mirror was conceptualised (Figure 1-5). Micro autonomous robots have not been used within MOS instruments and it was unknown if one could be developed that can precisely position pick-off components. The concept consists of a pick-off mirror mounted on a small (20 mm x 20 mm) self-propelled base that communicates via a radio frequency link and does not need a tether to obtain power. The robots will need to be capable of positioning and orientating themselves with high precision to ensure that they gather all the photons from the objects that are being studied. Long exposure times are needed for the objects being studied because they are very faint. This requires multiple frames to be stacked together to get a meaningful signal at the detector. It is therefore essential that the photons from the source object are directed to the same part of the detector so that the signal being studied is not lost to noise.



**Figure 1-5: Miniature Autonomous Robot Concept**

The research objectives were to determine if miniature mechatronics could be used to position pick-off optics with a high accuracy within Multi-Object Spectrographs (MOS), thus potentially lowering the costs of MOS instruments as they are currently positioned by relatively large bulky systems that are relatively expensive in comparison. The goals for this work were:

- Characterise the MAPS robot, critically analysing the design to determine whether miniature robots are suitable for high precision positioning within multi-object instruments for astronomy
- Design a Self-Adjusting Mirror by adding functionality to the POM to correct for optical misalignments within MOS instruments
- Characterise SAM to determine whether a miniature self-adjusting mirror can replace some of the BSM functionality resulting in a smaller and more cost effective solution
- Prove that micro robotics can be used in astronomy instrumentation

This chapter has described the background and reason behind this research work. It has also summarised the research objectives that were investigated. Chapter 2 carries this concept idea forward by listing the requirements and describing the MAPS system design that lays down the foundation to determine if micro autonomous robots can be used to position pick-off elements for astronomy. In Chapter 3, the design of the micro autonomous robot is described, also highlighting the initial problems experienced and the methodology followed to achieve an operational robot. Chapter 4 summarises the performance of the robot in terms of its required characteristics. Chapter 5 describes the design and capabilities of a self-adjusting mirror, developed to determine if a miniature mechanism can be used to correct for the optical misalignment at the focal plane of a MOS instrument.

## Chapter 2- Miniature Mechatronics for Astronomy Observations

This chapter outlines the requirements for the micro autonomous positioning system (MAPS). These requirements act as the foundation that determines if micro autonomous robots can be used for the positioning of pick-off optics. A review of the current-state-of-the-art technologies is presented showing that there are currently no micro robots available for this astronomy application. The overall system design is then presented and the chapter concludes with some initial concept ideas for the MAPS robot.

Miniature mechatronics is a field of engineering that has been expanding, mainly enabled by the availability of microelectronic components. A limiting factor is the supply of power to the robots. Current day batteries that can physically fit within the footprint do not have sufficient energy storage capacity to power the robots. This is due to the laws of scaling, as the energy density of batteries is related to the physical volume of the battery, which scales by  $\sim L^3$  where  $L$  is considered to be a reference dimension of the battery [36]. The effects of scaling are not just limited to power, but to all aspects of the robot including the motor efficiency.

Generally, miniature robots are ideal candidates for tasks that are in hard to reach places, repetitive, precise and potentially dangerous [37]. The inspiration for the development of small autonomous robots for these types of tasks comes from the potential applications they bring at a low cost [38] applications that include searching for survivors in burning buildings or rubble [39]; identifying defects within pipes [40, 41]; reporting on the conditions of locations that are hard to reach by a person and more. Since miniature robots are showing promise for use in a wide range of applications including high precision work within scanning electron microscopes (SEM) they may be adaptable to meet the needs of astronomical instrumentation.

### 2.1 Astronomers' Requirements

The primary functions required of the pick-off system for a MOS instrument are [42]:

- Positioning POMs precisely for picking off science objects and reference stars to aid the adaptive optics system.
- Ensuring that the POM and next optical element in the light path are aligned such that the astronomical objects imaged are centred on the surface of the next optical element.

Table 2-1 summarises the pick-off system's performance requirements based on the EAGLE concept design being proposed for the E-ELT. Although, these requirements can be met by current positioning systems they have their limitations (see section 1.2). Therefore, miniature robots are being examined to determine their feasibility of meeting the same requirements without the disadvantages inherent to the current positioning systems.

**Table 2-1: Pick-Off System Performance Characteristics [42]**

Parameter	Requirement
Total Patrol Field Area	$\geq 2000 \text{ mm} \times 1500 \text{ mm}$
Number of Pick-Off-Mirrors	$\geq 30$
Physical Pick-Off Mirror Diameter	$\sim 20 \text{ mm}$ base with a $45^\circ$ cut
POM Positioning	Within a science object's patrol field with a resolution of $\leq 30 \pm 5 \mu\text{m}$
POM Orientation	$1 \pm 0.1 \text{ mrad}$ to align the centre of the POM to that of the receiving optics
POM Positioning Repeatability	POMs will be capable of returning to a previous set position to within $30 \pm 5 \mu\text{m}$
Configuration Time	Less than 300 seconds for every 3600 seconds observation time, including time required to align POM with receiving optics
Environment Temperature	The pick-off system must be able to operate between temperatures of $-20$ and $+10^\circ\text{C}$ .

The requirements that govern the pick-off system are derived from the science requirements that the MOS instrument is developed to study. This includes the number of pick-off mirrors that are determined from the amount of detectors available. The pick-off mirrors physical size must allow POMs to be positioned to within 20 mm edge-to-edge of each other and be able to collect all the photons from the source object. This was determined to be achievable with an  $\text{Ø}20 \text{ mm}$  base diameter. The positioning, orientation and positioning repeatability was determined based on what is needed to ensure that all the objects of interest's photons is collected and delivered from the focal plane of the MOS instrument to the detectors via the correction optics.

Miniature autonomous robots have been developed with a footprint within the physical POM diameter. Therefore, a literature survey was conducted to determine if the currently developed miniature robots would be capable of meeting the astronomy instruments requirements.






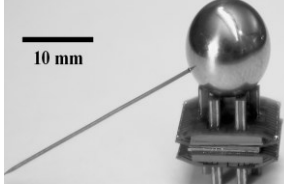
### 2.1.1 Miniature Autonomous Robot Candidates for Astronomy

Over the years, many small autonomous robots have been developed primarily for research; however there are few examples of commercially available autonomous robots for specific applications. Table 2-2 and 2-3 present a summary of a selection of these robots. Most of these robots are driven by piezoelectric or electromagnetic actuators.

**Table 2-2: Summary of Autonomous Robots (Electromagnetic)**

Robot Identification		Application & Commercial Availability	Driving Mechanism	Designed for High Precision?
Inchy, Jemmy & Smoovy [36] [43]		Feasibility research projects	Smoovy DC Motors, gears and wheels	No
Miniature Autonomous Robotic Vehicle (MARV) [44]		Feasibility research project	Smoovy DC Motor, pulleys and tracks	No
PICO [43] [45]		Hobbyist developed. Commercially available light chasing robot	DC Motor (Mobile Phone), worm gear to shafts with wheels	No
ANTS [46]		Swarm robotics research	DC Motor, gears and chain tracks	Unlikely
EMRoS Series (Monsieur, Monsieur II-P, Nino, Ricordo, Rubie) [47]		Company capabilities showcase, miniature technology research	Homemade Ultra-miniature stepper motor to wheels	No
Alice [36] [38] [48]		Research and education	Watch motor to wheels (one version with tracks)	No

**Table 2-3: Summary of Autonomous Robots (Piezoelectric)**

Robot Identification		Application	Driving Mechanism	Designed for High Precision?
NanoWalker [49]		Research into STM applications such as manipulation and probing at a Nano scale	Piezoelectric legs on a vibrating PowerFloor	Yes – 0.3 $\mu\text{m}$ resolution
miBot [50]		SEM & FIB applications such as probing and manipulation at Nano to micro level	Piezoelectric legs – Stick/slip principle	Yes – Resolutions of 40 nm Stepping Mode (AC voltage)
Starbugs [51] [52]		Research for MOS applications within Astronomy	Piezoelectric tube following the stick/slip principle	Yes – Less than 4 $\mu\text{m}$ Resolution
Miniman [53] [54]		Research for micro-assembly robotics	Piezo legs	Yes – 20 nm resolution

Greater detail of these robots has been summarised in the critique diagrams Figure 2-1 and 2-2. The critique diagrams detail the types of sensors, motors and capabilities of each robot reported in Table 2-2Table 2-3. It has been broken down into the robots attributes and issues in reference to the application of positioning optical components on a MOS instrument. Like the summary tables, the critique diagrams have been separated into electromagnetic robots and piezoelectric robots based on their drive mechanism.

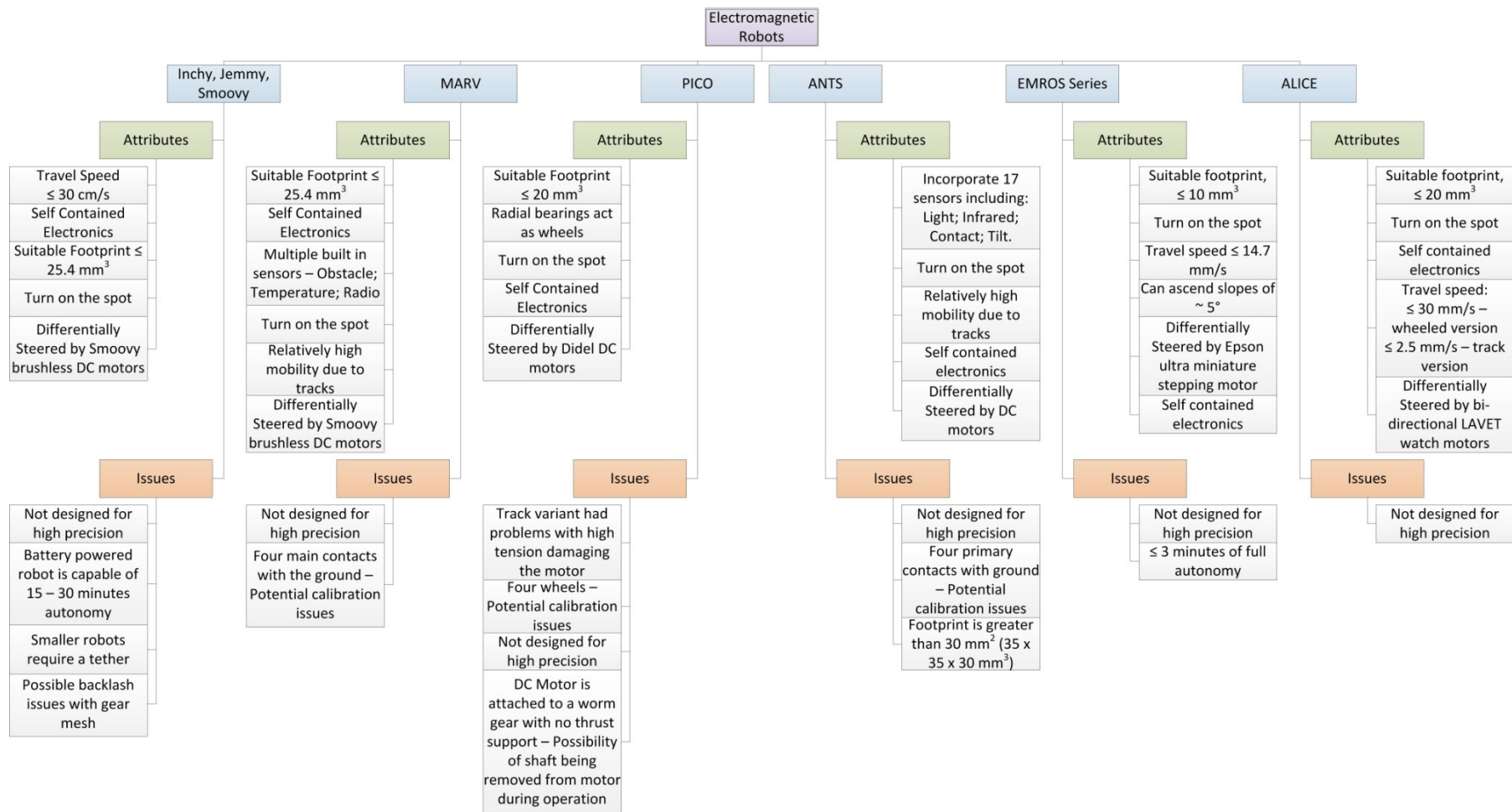


Figure 2-1: Critique diagrams of current micro autonomous electromagnetic robots

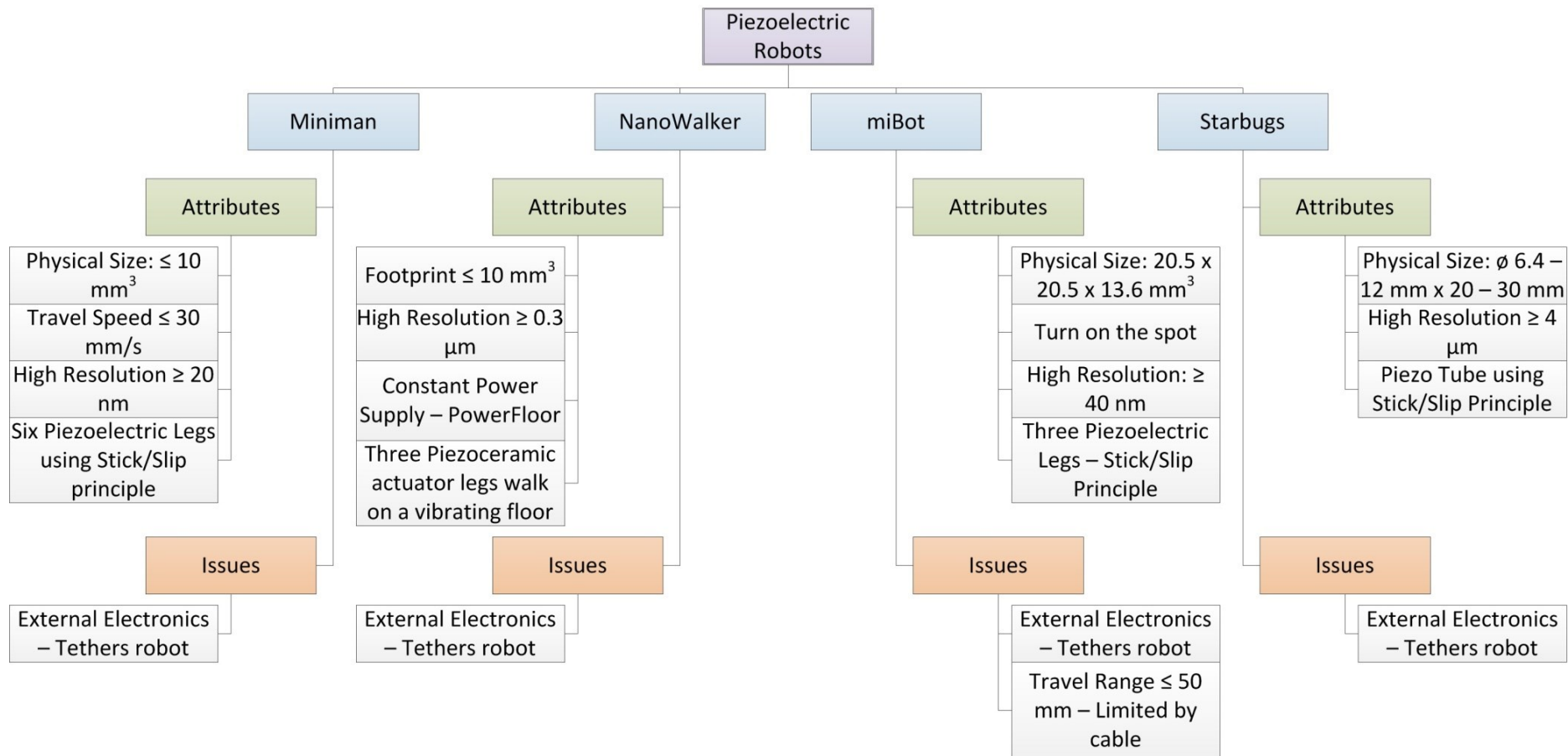


Figure 2-2: Critique diagrams of current micro autonomous piezoelectric robots

From the critique diagrams, it can be seen that the piezoelectric driven robots can achieve sub-micron resolution, generally using the SEM environment that they have been developed for, within a footprint that is less than 30 mm<sup>3</sup>. However, these robots were tethered to external control electronics and power supplies; limiting their travel range and presenting path-planning issues for multiple robots operating together. The electromagnetic robots do not require a tether as the electronics are self-contained, but they have a short continuous run time, usually less than an hour. These were also not designed for high precision tasks.

The study showed that robots within this volume can operate with high precision however it was clear that none of the existing robot developments were ideal for positioning POMs on the focal plane of a large astronomical instrument. Based on the outcome of the review it was decided to develop a robot driven by small brushless DC motors as these have the potential to be driven making use of micro-stepping thus make high precision positioning within a small form factor that does not require high-power control electronics possible.

The high precision micro autonomous robots identified in the literature generally operate in environments like scanning electron microscopes and because of this the microscope can be used to guide the robot into a required position. This means fewer bulky components are needed on the robot. For these high precision micro robots, power was supplied externally through a tether allowing a continuous supply. These high precision micro robots are not ideal for astronomy due to combination of the tethers and large operating arena. The tethers make the path planning process more complicated as they become obstacles for other robots to cross. They could also block a robot by being in its required position. However, the external metrology and power that these high precision robots used helped guide the overall system architecture of MAPS.

### ***2.1.2 MAPS Overall System Design***

The MAPS design comprises of three modules: command and control, robot(s) and power. Figure 2-3 shows how these modules interact.

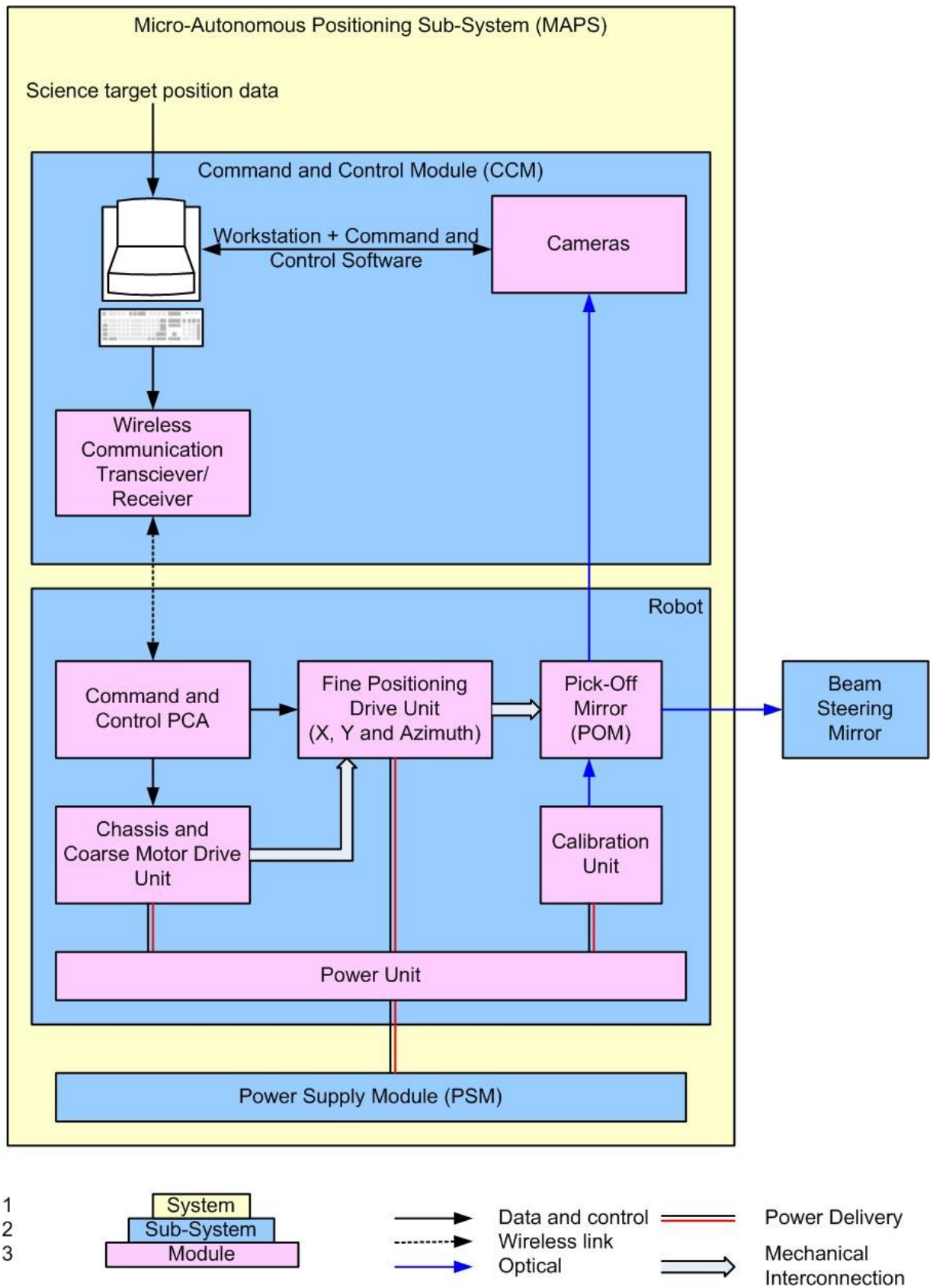


Figure 2-3: MAPS System Architecture [55]

In this thesis, focus is placed on the mechanical design, manufacturing and assembly process of the robot and the power module, which is discussed in detail in Chapter 4. The research focus is to determine if electromagnetic actuated micro robots can be developed for the high precision positioning of pick-off mirrors in astronomy. The MAPS command and control module reported by Taylor [32] is used to control the robot remotely. A summary of the command and control module's operation is provided to aid in the understanding of the overall system.

A micro robot specific requirement was created based on the astronomy requirements and overall system architecture detailed in section 2.1.

## 2.2 MAPS Robot (MA-BOT) Requirements

The MAPS robot requirements were derived from the pick-off system requirements Table 2-1. Table 2-4 summarises the key requirements for the robot [56].

**Table 2-4: Driving Requirements for MAPS [57]**

<i><b>Parameter</b></i>	<i><b>Requirement</b></i>	<i><b>Critical Parameters</b></i>
X – Y Positioning Accuracy	$\leq 10 \mu\text{m}$	High
Z – Axis Angular Resolution	$\leq 1 \text{ mrad}$	High
Speed	$\geq 10 \text{ mm/s}$	Low
Operation Time	$\geq 8 \text{ hours per night}$	Med
Footprint	$\leq 30 \text{ mm} \times 30 \text{ mm}$	Med
Height	$\leq 60 \text{ mm}$	Med
Communication Range	$\geq 4 \text{ m}$	Low
Environment Temperature	Between $-10$ and $+20^\circ\text{C}$	Low

The most important requirements are the positioning and angular resolution as these capture the photons needed by the scientists. If the pick-off mirror is not positioned on the focal plane to within the stated parameters of Table 2-4 the vital photons needed do not reach the detector.

The operation time and size of the micro robot was the next priority. The operation time was determined from how long the instrument would be surveying the sky. This requirement has a direct impact on the power module of the micro robot. A power source would either need to have a large enough capacity to last at least 8 hours or intelligent power control. This could be



achieved by putting the robot in a power saving mode once it is in position. The footprint requirement was derived from the minimum clustering requirement needed by the science case which was 20 mm edge to edge assuming a Ø20 mm POM. This translates to 40 mm centre to centre. Therefore, the POM's can at maximum be Ø40 mm. The micro robots presented in the literature review are all within a footprint of 30 mm x 30 mm. This provides an acceptable guideline for the maximum footprint of the robot.

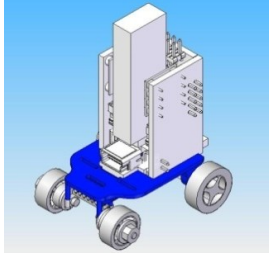
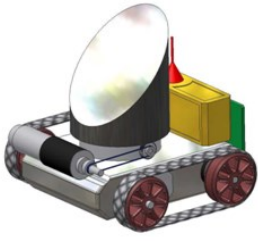
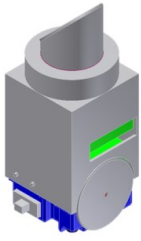
Finally, the communication and speed of the micro robot was determined from the 2 m diameter of the focal plane. It is assumed that the robots may need to travel from one end of the focal plane to the other with 3 minutes to get into position. Therefore, the robot needs to travel faster than 7 mm/s. The 10 mm/s requirement was used to also provide time for fine positioning once the robot approximately reaches its position. The communication module needs to at least be able to talk to a robot from the opposite end. However, it is conceivable that the communications module at the command and control sub-system will not be located at the perimeter of the focal plane. Therefore, a greater communication range is desirable.

### **2.3 Concept Designs**

There is evidence from the micro robotics literature review (section 2.1.1) that electromagnetic driven micro robots have lower power consumption and simpler control electronics than Piezo driven micro robots. Therefore, a Faulhaber Smoovy 0308B brushless DC motor with 03A 125:1 planetary gear head was chosen [58, 59] to drive the robot, as a result of the literature review and its small size high-torque output. By controlling the motor using pulse width modulation (PWM) control signal it is driven like a stepper motor [60]. The Smoovy motor's datasheet [61] also indicates that it can be micro-stepped. There are other motors available that meet the small size and torque requirements, however the Faulhaber Smoovy motors datasheet [61] indicates that it has the highest-torque output. Based around the chosen motor three designs were explored that led to the development of the current robot. The three designs are summarised in Table 2-5 including a list of the advantages and disadvantages of each design.



**Table 2-5: Summary of investigated designs**

	<b>C-Bot [62]</b>	<b>T-Bot</b>	<b>D-Bot</b>
			
<b>Footprint, mm<sup>2</sup></b>	23.4 x 30.5	12 x 12 (Estimated)	30 x 30
<b>Steering Mechanism</b>	Rear wheeled drive Rack & Pinion	Directly driven Differentially Steered	Directly Driven Differentially Steered
<b>Number of Drive Motors</b>	1 Drive 1 Steering	2	2
<b>Advantages</b>	<ul style="list-style-type: none"> <li>No need to synchronise drive motors due to single drive motor</li> </ul>	<ul style="list-style-type: none"> <li>Turn on the spot</li> <li>Fine turret stage</li> </ul>	<ul style="list-style-type: none"> <li>Turn on the spot</li> <li>Few components required</li> <li>Three point contact with ground</li> </ul>
<b>Disadvantages</b>	<ul style="list-style-type: none"> <li>Small complex parts</li> <li>Difficult to assemble</li> <li>Cannot turn on the spot</li> <li>Four contacts with the ground, not ideal in precision mechanics</li> </ul>	<ul style="list-style-type: none"> <li>High torque required</li> <li>Motor side-load would be high</li> <li>Concept has not allocated space for electronics</li> <li>Four contacts with the ground (at the pulleys for the tracks) affects calibration [63]</li> <li>Turning accuracy can be lower for tracks</li> </ul>	<ul style="list-style-type: none"> <li>Motor side-load too high damaging the motor</li> </ul>
<b>Reason design was not chosen</b>	<ul style="list-style-type: none"> <li>Too complex to manufacture and assemble</li> <li>Uncertain of its tip/tilt when moved to a position due to four ground contacts</li> </ul>	<ul style="list-style-type: none"> <li>Motor radial load would exceed acceptable allowance without an intermediate stage</li> <li>Uncertain of its tip/tilt when moved to a position due to four ground contacts</li> <li>Possible slipping</li> </ul>	<ul style="list-style-type: none"> <li>Motor radial load would exceed acceptable allowance without an intermediate stage</li> </ul>

To ease the assembly process and lower the cost of manufacturing it is necessary to minimise the number and complexity of components. After performing a parts count it was determined that a differentially steered robot will require less components compared to the C-Bot design. The C-Bot design requires more complex components such as the steering mechanism where small gears and layout may require linkages to the front wheels that are a few millimetres in size. Components of this size are difficult to assemble manually with precision. A differentially steered robot could use simpler components as the steering is incorporated with the drive section. It also allows the robot to turn on the spot, which simplifies the path analysis required to configure the focal plane. This difficulty in assembly highlights the problem with assembling robots within this size domain. Robots these sizes are difficult to assemble as they are too large for micro assembly techniques and too small for common macro assembly techniques.

D-Bot showed that directly driving the wheels from the selected Smoovy motors is not possible due to the high radial load; therefore an intermediate stage would be needed to protect the motors and the gear head. The tank design of T-Bot could be adopted to protect the motors by controlling the belt's tension. The T-Bot design has four points of rigid contact between the robot and ground. Compliancy would be required between the robot and the focal plane to stop the robot from rocking between two of these contacts [63]. This led to concerns that the POM could have varying physical angles between the mirrored surface and focal plane for different placements of the POM on the focal plane. This angle could vary for the same robot at the same placement due to having more than three rigid contacts with the surface. It would be uncertain which three contacts would be touching the surface each time the robot drives into position. Therefore, each time the robot gets into position calibration would be required to ensure that the alignment between the POMs and receiving optics is within specification.

Therefore, it was decided to make use of a modified D-bot design with an intermediate stage, described in chapter 3, to protect the Smoovy motors. Three rigid contacts between the robot and focal plane will be used thus the physical mirror angle to the focal plane should be the same for all positions.

### 2.3.1 Command and Control Module

The command and control module comprised of the metrology, wireless command and user interface. Table 2-6 briefly defines the function of each component.

**Table 2-6: Command and Control Module Summary**

<b>Module Sub-Systems</b>	<b>Functional Description</b>
Wireless Command	• RF Communication to transmit commands and receive status updates with the robot(s)
	• Communicate with all robots
Workstation including software components	• Receive image data from MMM
	• Identify each robot
	• Determine robot's location
	• Path planning and command sending to the robots to get them to a required position
	• GUI interface for directing the robot(s)
	• Translate communications for users and robots
Cameras	• Image focal plane
	• Relay information to user interface

The robot's metrology has to be an off-board process due to a lack of space available within the robot. Techniques such as current sensing and ultrasound triangulation were investigated but it was decided that optical imaging would provide the best measuring accuracy and requires the least volume [32].

The following is a brief summary of the command and control module's operation:

- Lumenera cameras are used to image the entire focal plane.
- A command is sent requesting a response from all active robots.
- A centroiding algorithm determines the location of each robot by identifying and processing the target pattern of spots on top of the body of each robot.
- To determine which robot is associated with a specific ID, commands are sent to each robot in turn and the centroiding process is repeated as to determine the exact position of each robot.

A monochrome Lumenera Lw11059M with a Kodak JIA-11002 10.7 megapixel sensor was chosen for its low noise and high sensitivity. The individual pixels of the sensor are 9  $\mu\text{m}$  square pixels. This combined with the centroiding software allows the cameras to measure the position of each robot to a resolution of 1  $\mu\text{m}$ , which exceeds the required MAPS positional attainment of 10  $\mu\text{m}$ . This was determined using ambient light.

The control strategy consists of the command and control module following these steps:

- Determine which available robot is closest to a desired position.
- Compute the required commands to get the robot to this position.
- Execute commands measuring the position of the robot between commands.
- If the robots position is deviating from the desired position, the required commands are recalculated and issued to the robot.

The metrology system was designed by a colleague at the UK ATC [32] and is not a part of this thesis.

With each robot identified and their position's ascertained, commands can be sent wirelessly to the robots through a graphical user interface (GUI). The GUI was developed for research purposes to characterise the robot's performance, it also included commands for fault diagnostics. When implemented as part of an instrument, a template file with each robot's position and orientation will be used. The GUI allows commands to be sent to the robot(s) in either open or closed loop. In open loop, the number of steps the robot should traverse in forwards, backwards or angular directions is used to direct the robot into position. For the closed-loop control, desired locations are input as x-y and theta coordinates. The control software determines the path which the robot should follow and also sends the required commands to the robot. During the robot's journey the metrology continually updates the control software with the robot's actual positions such that corrective commands can be calculated and sent to the robot to ensure that the robot will reach its final position to within the specified accuracy.

Chapter 2 showed that miniature autonomous robots can potentially be developed to meet the demanding requirements imposed by astronomical instrumentation. The research shows that this is an application area that is currently not being addressed by miniature robots. Although there are high precision miniature autonomous robots they do not currently meet the astronomy requirements. The high precision robots were piezo driven requiring large electronics that are external to the robot. This is because they require power greater than 100 volts to achieve actuation. Thus requiring a wire 'tether' that would complicate path planning and positioning of the POM's. The electromagnetic driven robots have the electronics on-board due to their need for only a few volts to achieve actuation (~3 volts) and therefore do not require a tether. However, these robots have not been shown to be capable of high precision positioning. From the literature survey it was decided to develop an electromagnetically propelled robot and this

survey indicated that the Smoovy DC motor was a suitable choice of motor for its high torque output and small size. Various concept designs were detailed and indicated that a differentially steered robot design should be taken forward primarily due to it being easier to assemble. The D-bot design was determined to be easier to assemble as the C-bot design was going to require small complex components that would be difficult to hold align and attach. However, it may have been possible to design C-bot components to be less complex and is perhaps worth reviewing in the future.

In chapter 3 the final concept design solution based around the D-Bot is described in more detail together with the manufacturing process that was developed to build these robots. This design shows if it is possible to use a micro autonomous robot that is propelled by small DC motors for the high precision positioning of pick-off mirrors on astronomical instrumentation.

## Chapter 3 – The MAPS Robot (MA-BOT1)

This chapter details the design and characterisation of the first iteration of the robot which was battery powered. This design is based on the D-Bot, however it has been altered to protect the motor as directly driving wheels was not possible due to the high radial load damaging the motors. Also, due to the limited run time, a PowerFloor concept was trialled using an adapted robot, MA-BOT1.1. This chapter concludes with a summary of the robots capabilities and limitations.

### 3.1 The Design

Figure 3-1 shows the CAD assembly model of the robot without the battery and electronics.

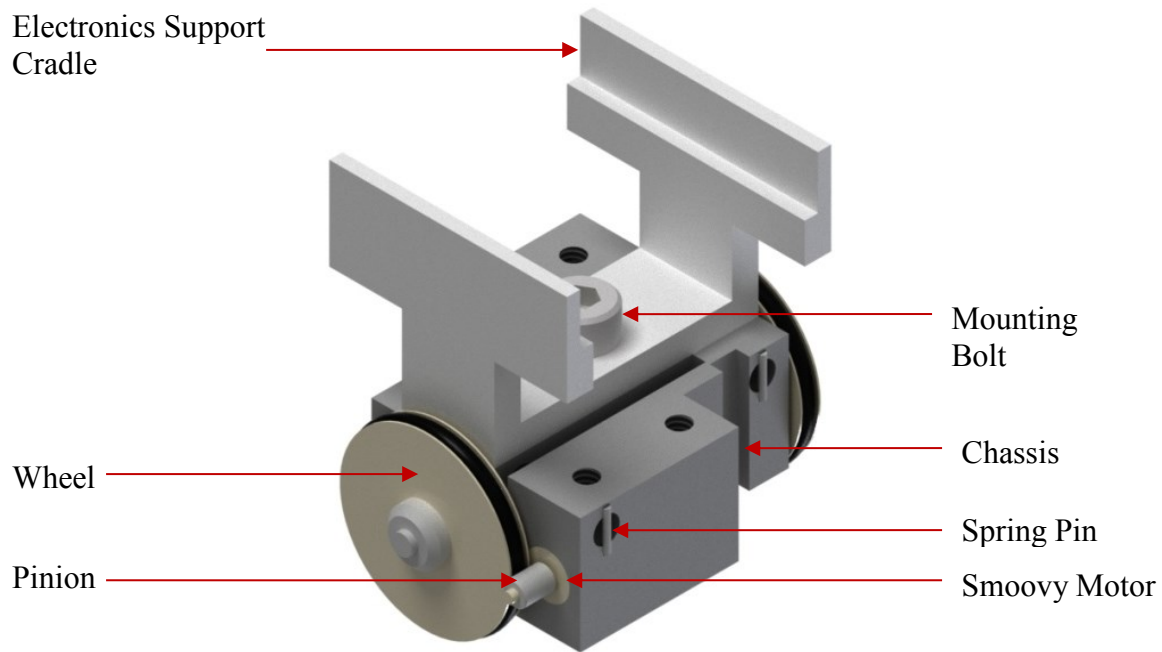
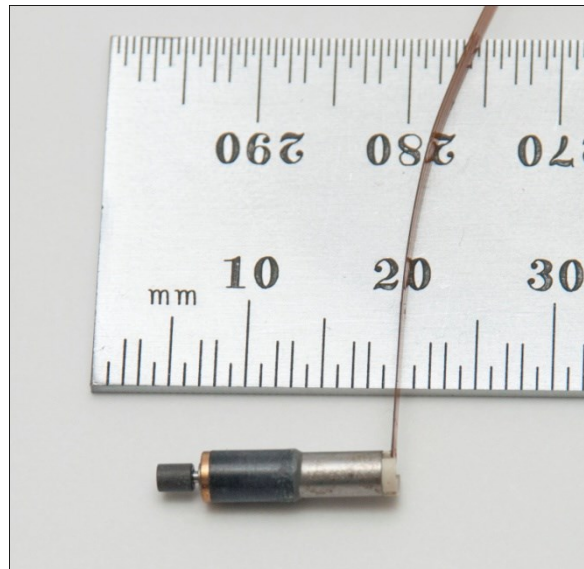


Figure 3-1: MA-BOT1 CAD Model

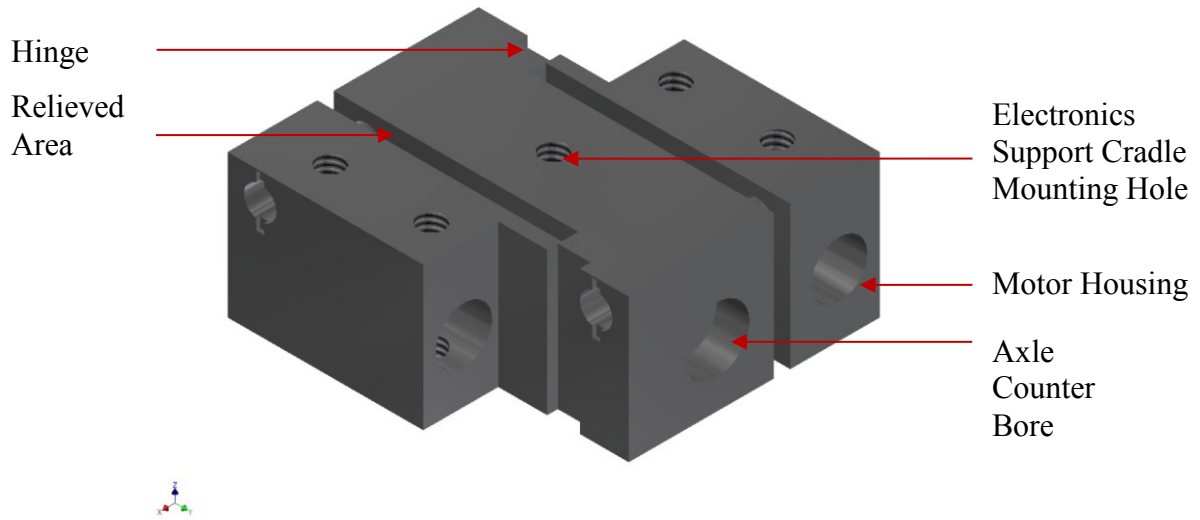
The two Smoovy motors (Figure 3-2) are arranged to independently drive the wheels that are aligned on a common axis. This is achieved through a friction drive arrangement. The friction drive arrangement was chosen over geared methods to overcome problems of backlash associated with gear systems. Although, there will still be backlash of  $4^\circ$  inherent to the gearheads being used by the motor. This translates to  $0.5^\circ$  at the robots wheel. Although this design layout overcomes backlash after the motor's gearhead it could be susceptible to slippage and increased wear. Slippage normally occurs in friction drive mechanisms due to environmental factors such as water. This should effect the robot as it will operate in a

controlled environment on the MOS instrument. Each motor has a pinion attached to the output shaft of the gear head and is held in place with Loctite retainer. The motors are slotted into the chassis as depicted in Figure 3-1 and typically held in place by a set screw which is a common macro assembly procedure. However early assemblies showed that the set screw could damage the motor, hence an interference fit was used.

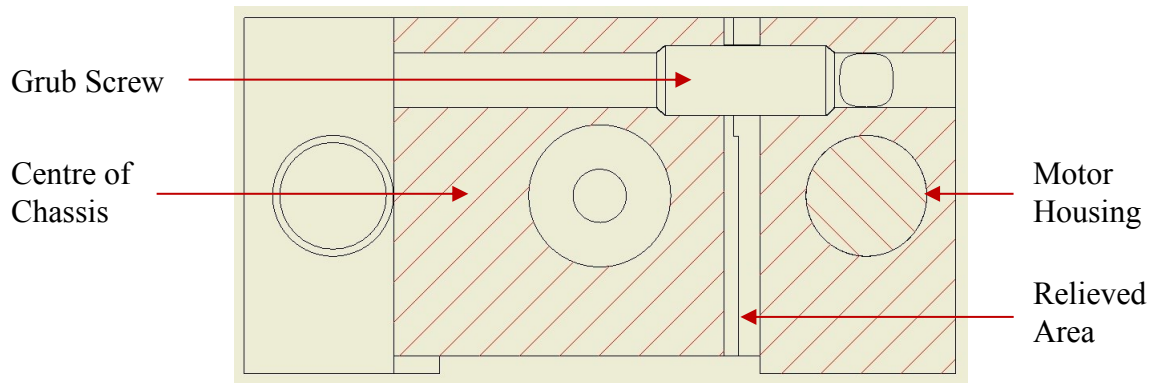


**Figure 3-2: Smoovy 0308B Motor**

The chassis is a single piece of Delrin (Figure 3-3) with two relief slots cut at either end to form flexures or ‘hinges’ for the motor housings. Delrin is an Acetal thermoplastic with low friction and low moisture absorption suited for creating precision parts for use in cryogenic applications. It also has excellent strength and density compared to Nylon and ABS. MOS instruments generally operate at cryogenic temperatures and, although the EAGLE instrument that is guiding this concept research is operating at room temperature, it was decided to use a material that could potentially be taken forward as a foundation for developing the robots to operate at cryogenic temperatures because many MOS instruments do operate at cryogenic temperatures. A hinge (Figure 3-3) is used to provide control over the force between the motor and wheel, keeping it below 0.1 N to protect the motor shaft as dictated by the datasheet [64]. A motor slides into each end of the chassis. The relieved area allows movement of the motor in relation to the wheel. To control the force between the motor pinion and the wheel, a grub screw is used (Figure 3-4). The grub screw is tightened forcing the motor housing towards the wheel taking up the space of the relieved area.



**Figure 3-3: MAPS Chassis**



**Figure 3-4: Sectional View of Chassis Illustrating Grub Screw Interface**

Two steel dowels (Figure 3-5), used as axles, are press fit into counter-bores on opposite sides of the chassis. The axles support the wheels, which are machined from Vespel, a self-lubricating polyimide plastic chosen as it is a bearing material. The wheel and dowel interact in the same fashion as a bushing on a rotating shaft. The pressure-velocity (PV) value was calculated using equation (3-1) and compared to the Vespel PV value provided in the datasheets [65]. The symbols are defined in Table 3-1.

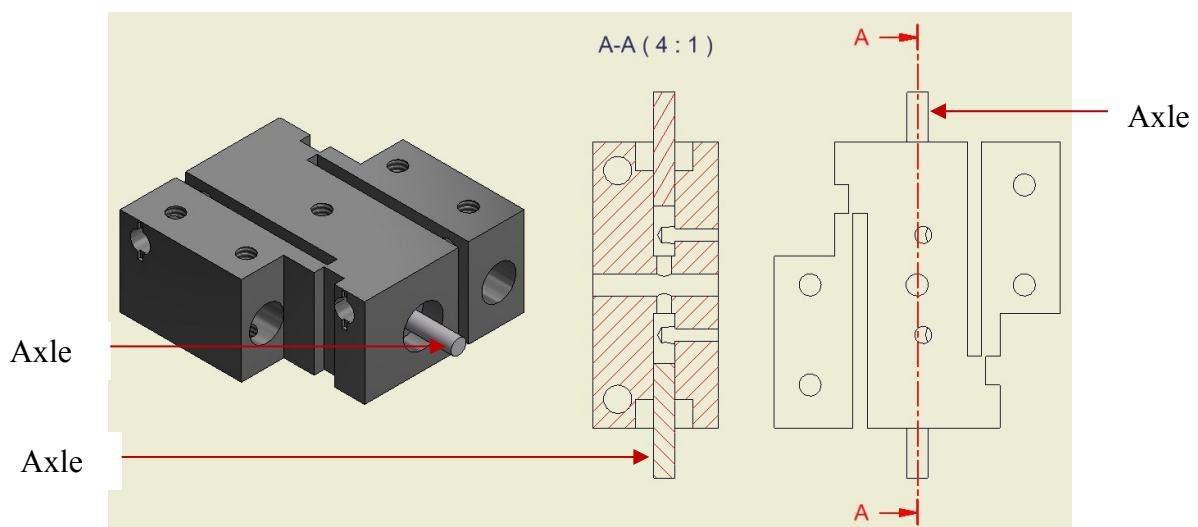
$$PV = \text{Pressure} * \text{Velocity} = \frac{W}{Ld} * \frac{\pi Dn}{12} \quad (3-1)$$



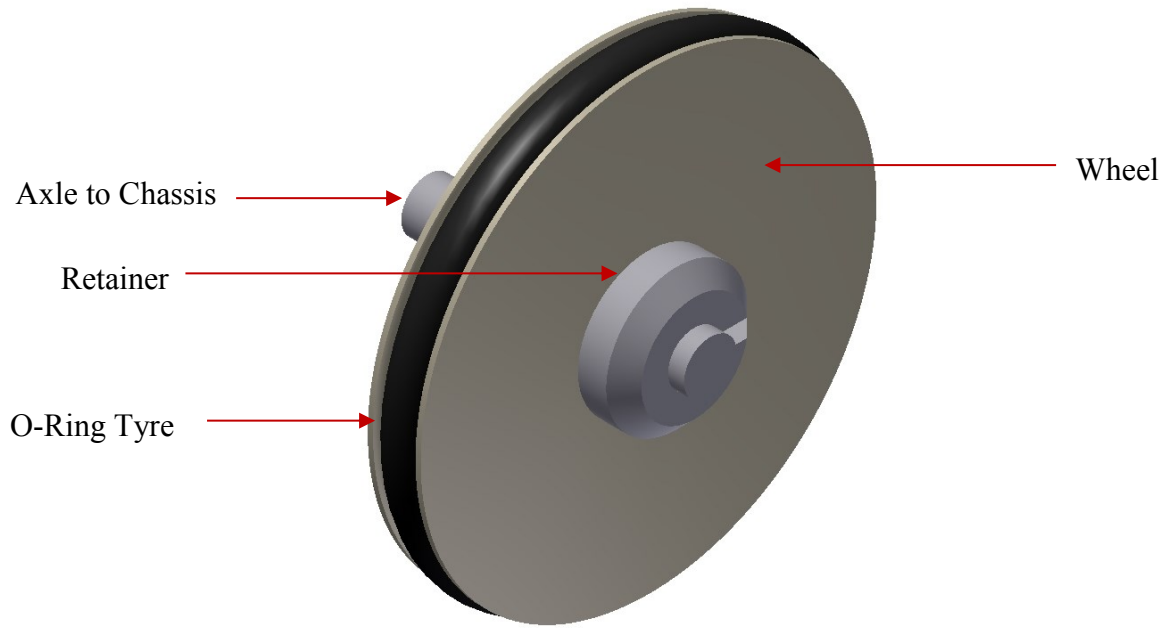
**Table 3-1: Symbols used in (3-1)**

Symbol	Definition	Units
PV	Pressure-Velocity value used as a failure indicator	MPa*m/s
P	Pressure based on the radial load (applied load from the motor) and projected area of contact with the shaft	MPa
V	Sliding velocity is the velocity of the shaft surface in contact with the wheel	m/s
W	Radial load applied to the wheel	N
L	Contact length of the wheel bore on the shaft	m
d	Diameter of hole on the wheel to accommodate the shaft	m
D	Shaft diameter	m
n	Rotational velocity of the wheel	RPS (rotations per second)

The PV value was calculated to be  $0.1547 \times 10^{-3}$  MPa\*m/s, this is well within PV value of 0.875 MPa\*m/s provided by the material datasheet [65]. This suggests that the wheel should not wear at a significant rate. Each wheel locates onto the axle and is retained with c-clips. O-rings act as tyres and are stretched onto annular grooves on the wheels (Figure 3-6). The O-ring is the point of contact with the motor's pinion.

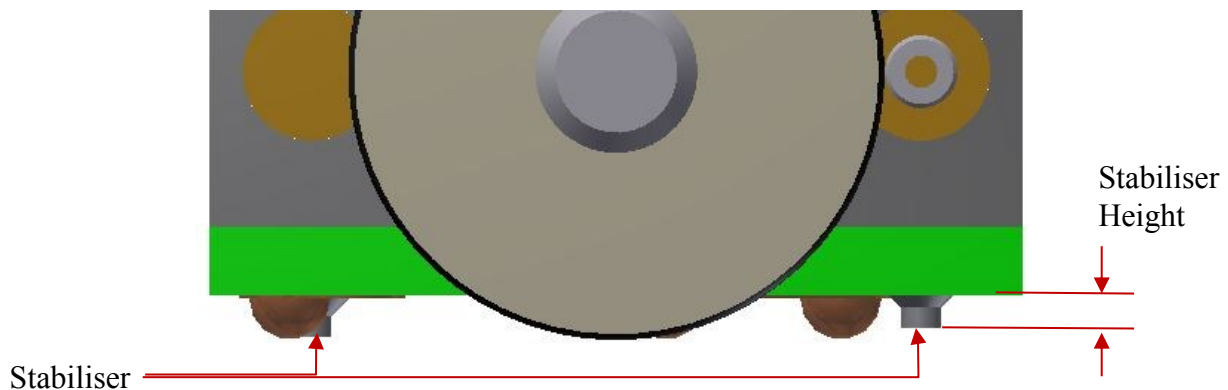


**Figure 3-5: Axles**

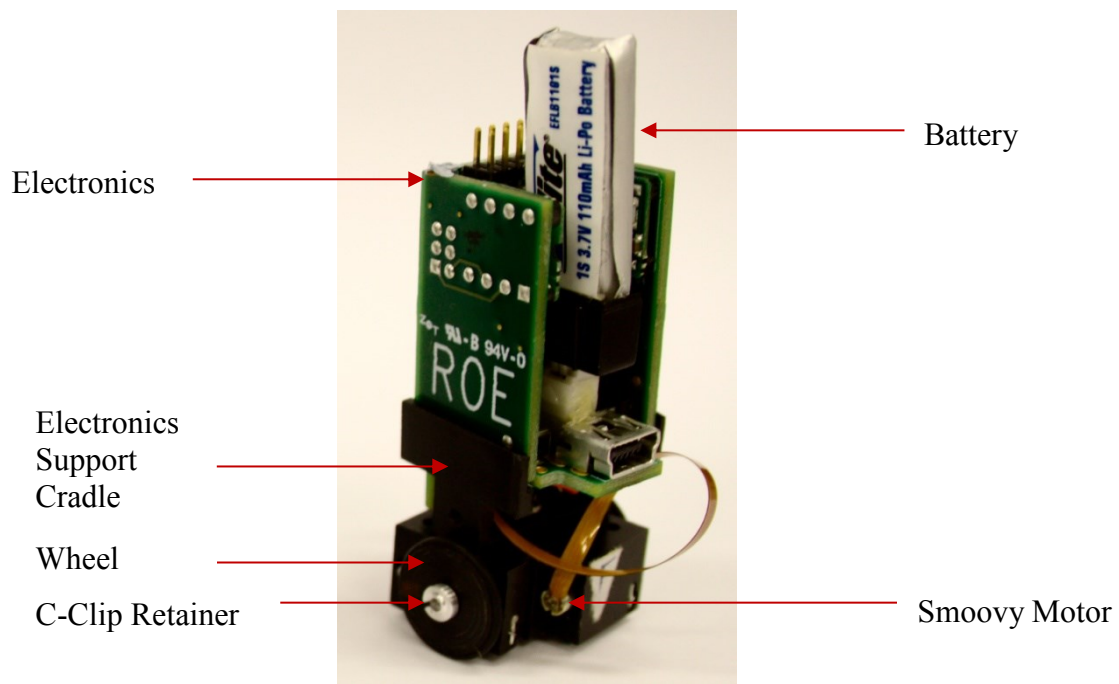


**Figure 3-6: Wheels**

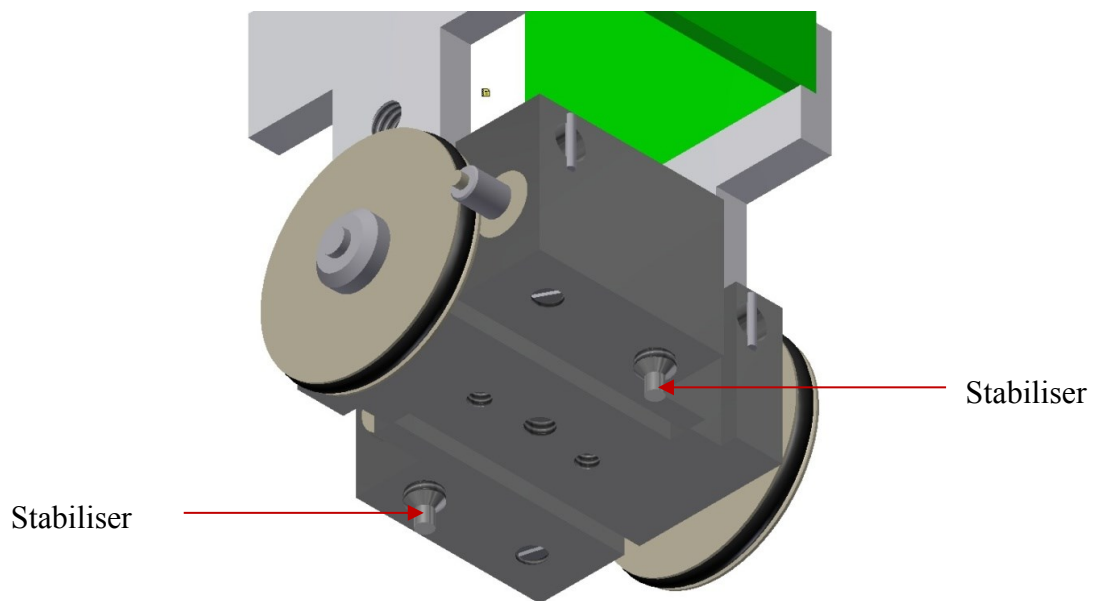
A threaded hole on top of the chassis (Figure 3-3) serves as a mounting hole for the clamp (Electronics support cradle) that is bolted to the chassis (Figure 3-1). The electronics are slotted into the cradle as shown in Figure 3-8. The MAPS electronics modules were designed and built by Dreampact [66]. A 3.7 V, 110 mAh lithium-ion single cell battery powered the electronics. It was capable of running two motors and was packaged into a  $25 \times 18.5 \times 38 \text{ mm}^3$  cube. Two threaded holes at each end of the chassis provide locations for the stabilisers, which were made from nylon tipped grub screws (Figure 3-9). These are screwed into the chassis from the top to the bottom. These are adjustable to ensure that three-points are always in contact with the ground, namely one of the stabilisers and the two wheels. The maximum distance that a stabiliser can be set to is 1 mm. For every 0.01 mm difference between the two stabiliser heights (Figure 3-7) the POM angle will alter in reference to the ground by 0.076 degrees.



**Figure 3-7: Stabiliser Heights**

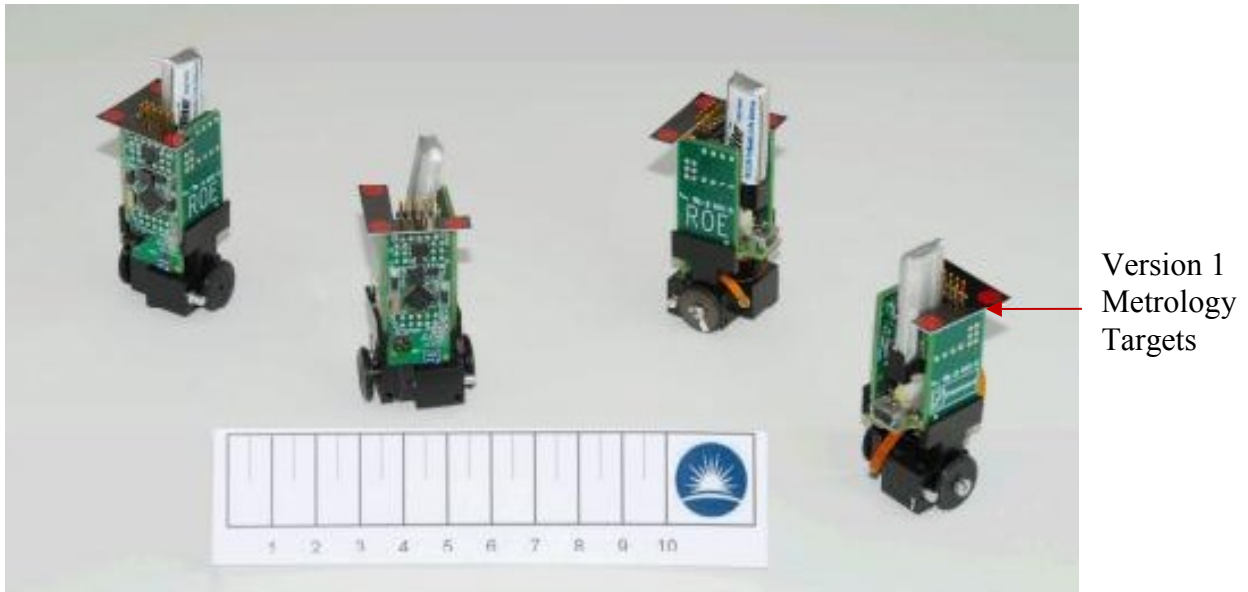


**Figure 3-8: MA-BOT1**



**Figure 3-9: Stabilisers**

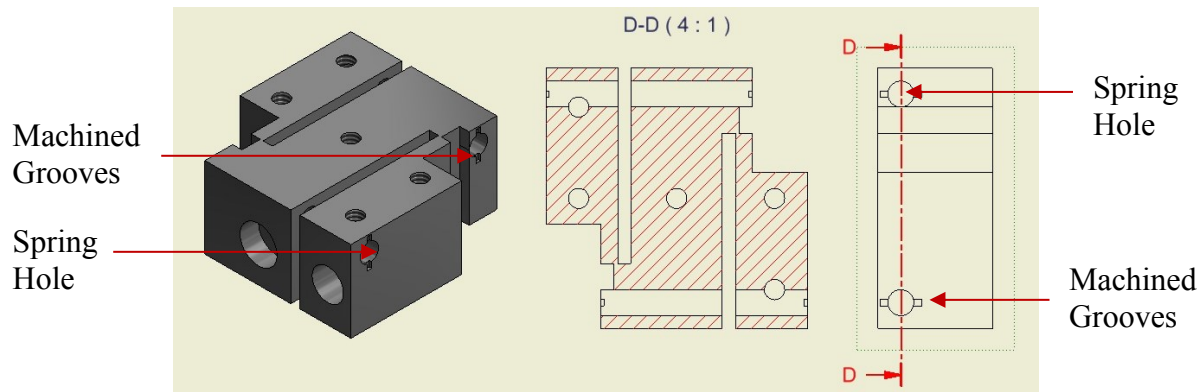
Figure 3-10 shows four fully assembled robots. The footprint of each robot is 20 mm x 20 mm. Mounted on the top of the electronics is the metrology targets.



**Figure 3-10: Four Assembled Iteration 1 Robots**

### **3.2 Initial Design Assessment**

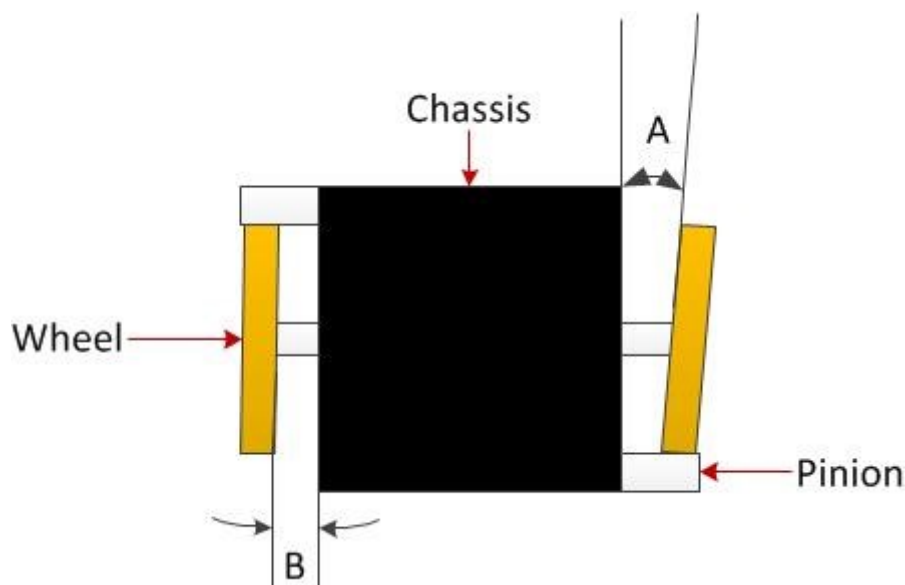
Before conducting detailed testing of the robot an initial assessment of the design was conducted. This involved driving the robot and observing to see if there were unusual emergent properties. For example, the grub screws being used to maintain a constant force between the motors and wheels was deemed unsuitable. It was observed that when the robot followed a motion command at random intervals one of the wheels would slip causing erratic motion. This was due to the eccentricities resulting from the wheels' manufacturing process. To improve upon this, tighter tolerance control during the manufacturing of the wheels was required. However, this may not completely eradicate the slippage. Therefore, to improve the design it was decided to replace the grub screw with springs. By using springs the flexure would alter in relation to the wheel maintaining a constant force between the motor and wheel, thus accommodating the slight variations within the wheel due to the manufacturing tolerances. The spring was chosen based on the outer diameter that could be accommodated by the chassis and by using a low enough spring rate so that the radial load on the Smoovy motor did not exceed the maximum allowable load provided in the datasheet [59]. An Ø2 mm spring was chosen with a 0.02 N/mm spring rate that provided a radial load of 0.062 N. These springs are passed through holes in the chassis and are retained by pins that sit in machined grooves (Figure 3-11).



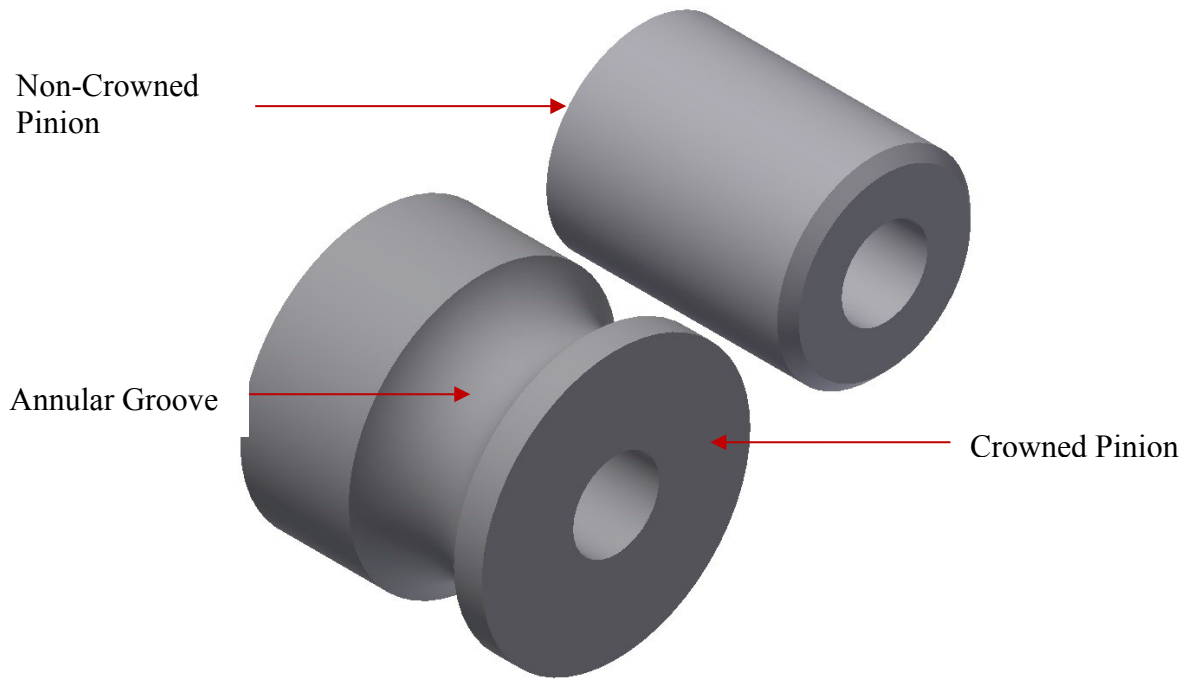
**Figure 3-11: Spring Holes**

Another alteration to the design was required based on this initial design assessment. Once the grub screws were replaced it was found that the robot, when sent a linear command, would travel in a circle. On inspection of the design it was observed that the pinions were the primary cause of this circular motion.

Originally the pinions, attached to the motor shafts, had an annular groove (crowned) to accommodate the O-ring of the wheel. It was hypothesised that the wheels would find a position on the annular groove that would misalign the wheels to one another as shown in Figure 3-12. Angle A is greater than Angle B resulting in the robot driving in a large circle. By replacing the pinions with non-crowned versions (Figure 3-13), that were grit blasted to increase the friction between the pinions and the O-rings, the issue was resolved suggesting that the hypothesis was correct.



**Figure 3-12: Illustration of wheel misalignment with motor pinion**



**Figure 3-13: Pinions Crowned and Non-Crowned**

Finally, during assembly and handling of the robot it became evident that the motor's gear head was fragile. The output shaft of the gear head is attached to a brass plate that is glued to a thin plastic casing housing the planetary gear stages as shown in Figure 3-14. The brass plate, which is the sintered bearing and output shaft in Figure 3-14, would break from the casing when overloaded with a force greater than 0.1 N (10 grams) and the tiny gears would fall out. Due to this it was necessary to develop detailed handling and assembly procedures:

- Attach pinions to the motor shaft.
- Once the motor is located in the chassis and the wheels are attached the motor housing must not to be handled or touched.
- When disassembling, the motors you first need to push the motors back into the housing to disengage the motors and wheels.
- The motors should be the last component to be added to the robot during assembly and the first components to be removed during disassembly.

## Precision Gearheads

### Planetary Gearheads

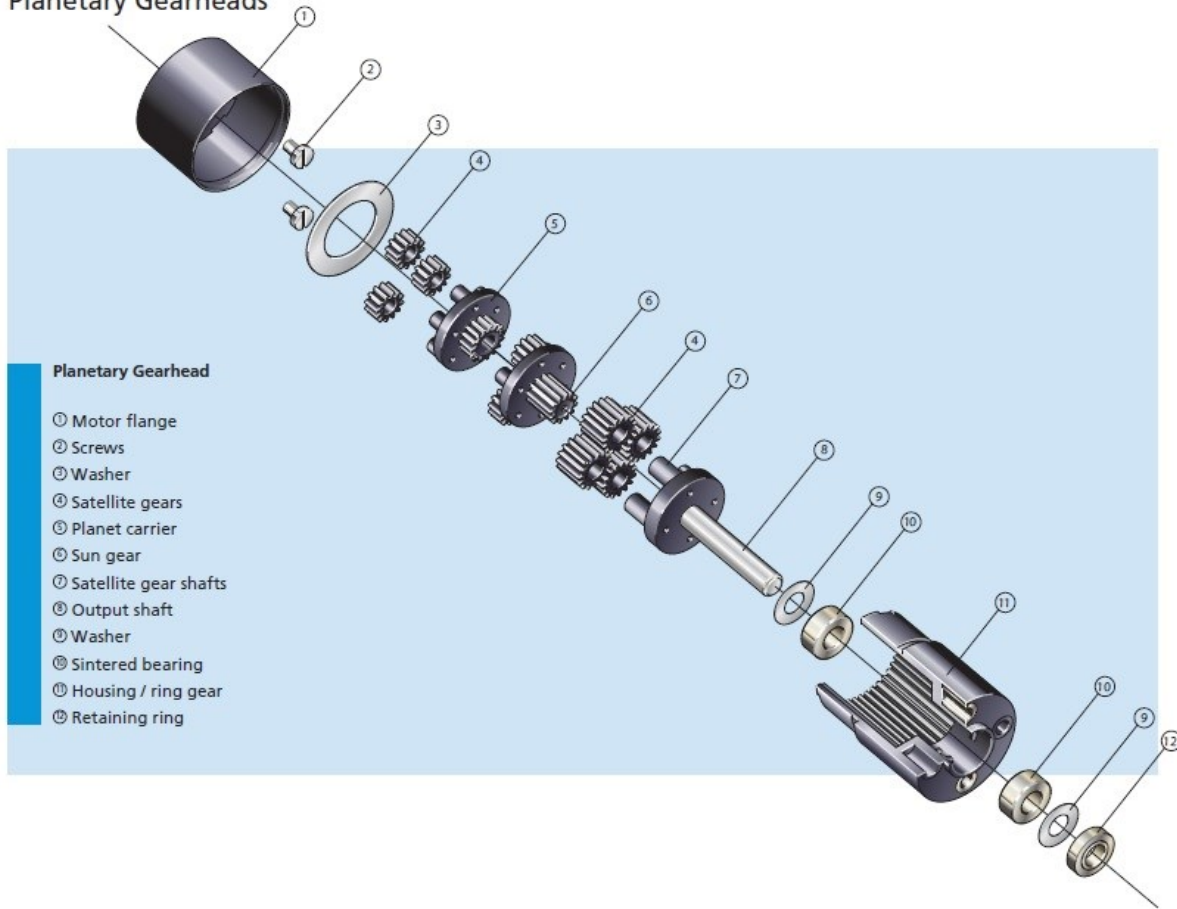
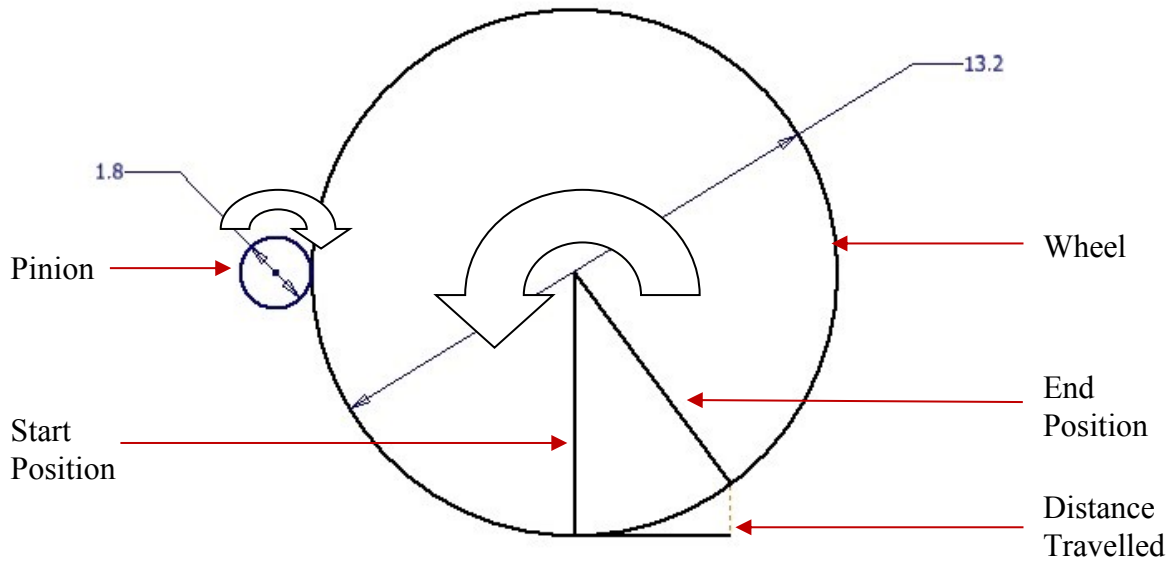


Figure 3-14: Gear head Assembly [61]

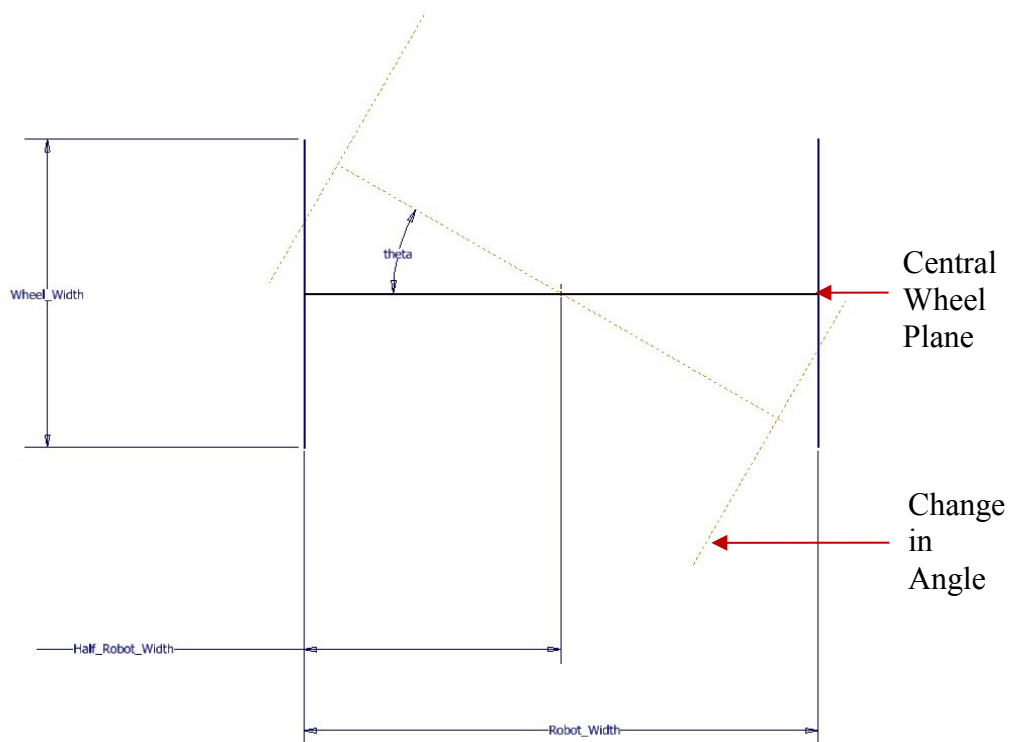
### 3.3 Theoretical Performance

The rotation of a Smoovy motor is controlled by issuing step commands; therefore it was essential to determine the relationship between the number of motor steps and the equivalent distance that the robot will travel from the manufacturer datasheets [59, 61] were consulted; the motor shaft rotates by 1.0472 mrad/step. Given the size of the wheels ( $\varnothing$  13.2 mm including O-ring tyre) and  $\varnothing$  1.8 mm motor pinion (Figure 3-15) the coupled ratio is 0.1. Applying the equation of an arc to the wheel it was calculated that for a single motor step command the robot would travel 1  $\mu$ m. This does not take backlash inherent to the gear head into account and is considered later on in this thesis.



**Figure 3-15: Schematic of wheel and pinion combination**

This linear equation is used to determine the relationship between the motor rotation and the rotational movement of the robot, which is based on the robot geometry, as illustrated in Figure 3-16. It is assumed that  $\sin\theta \approx \theta$  for single steps due to the short travel. The rotation angle is  $\theta = \tan^{-1}\left(\frac{\text{Single step distance}}{0.5w}\right)$  where  $w$  is width between the wheels. This means that the robot should rotate 85.7  $\mu\text{rad}$  when commanded a single step.



**Figure 3-16: Rotational Step Theory**



### 3.4 Actual Performance

Open-loop tests were conducted to determine the linearity of the robot and its potential to meet the positional requirements on its own without assistance from the metrology module. This test provided insights into the differentially steered friction drive design, highlighting the capabilities of the motors and chassis design.

Due to the robot's small size, non-contact measurement methods were preferred over other methods. Therefore, a Nikon inspection microscope (Figure 3-17) was used to measure the location of three identifiable features on the robot as depicted in Figure 3-18. The microscope has digitally encoded micrometres which were used to manipulate the x-y backlit glass surface. The test procedure is:

1. Align crosshair with a distinguishing feature of the robot, such as a corner of the PCB.
2. Zero the micrometres.
3. Command the robot to move x steps forward to position 2 and take reading.
4. Command robot to move x steps in the opposite direction and take reading.

The test was repeated 16 times to ensure a good statistical sample has been taken and to average out any operator errors.

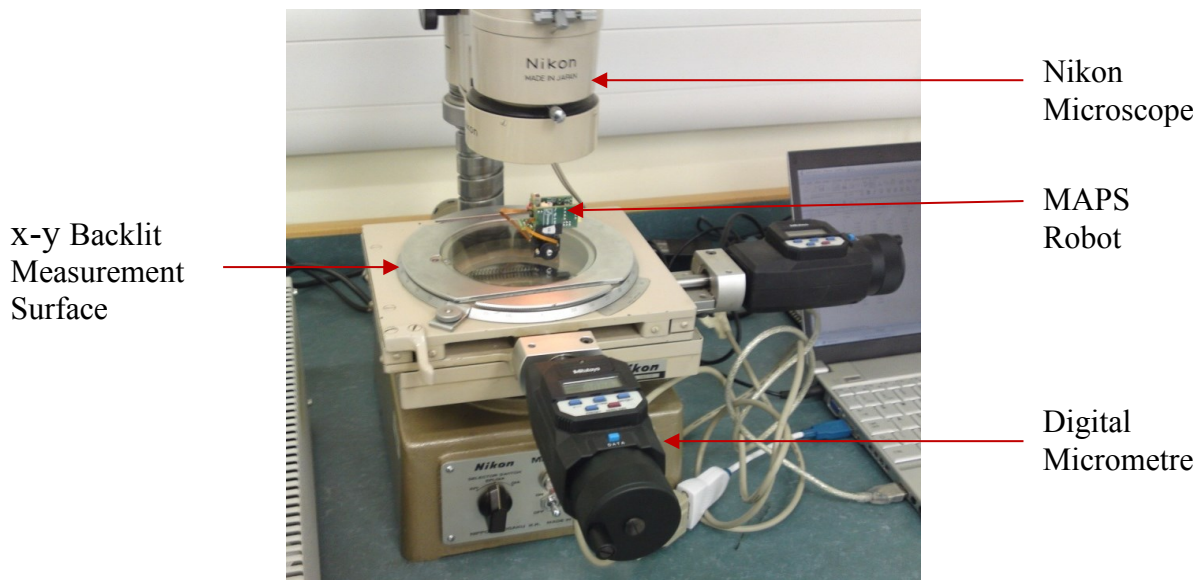
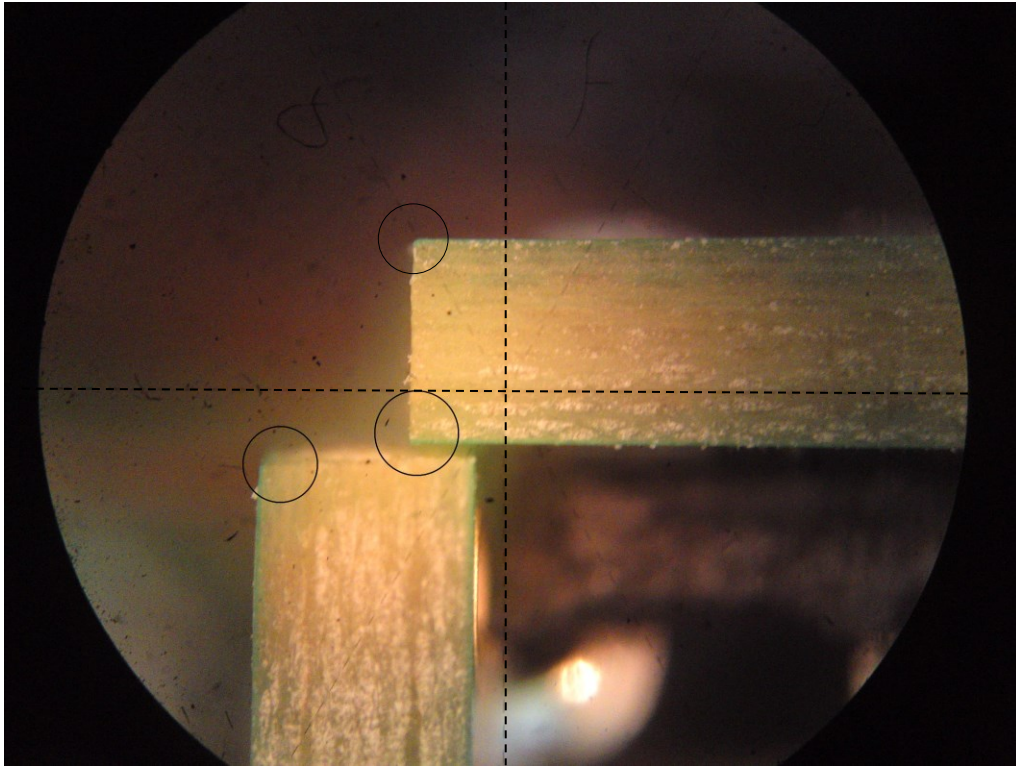


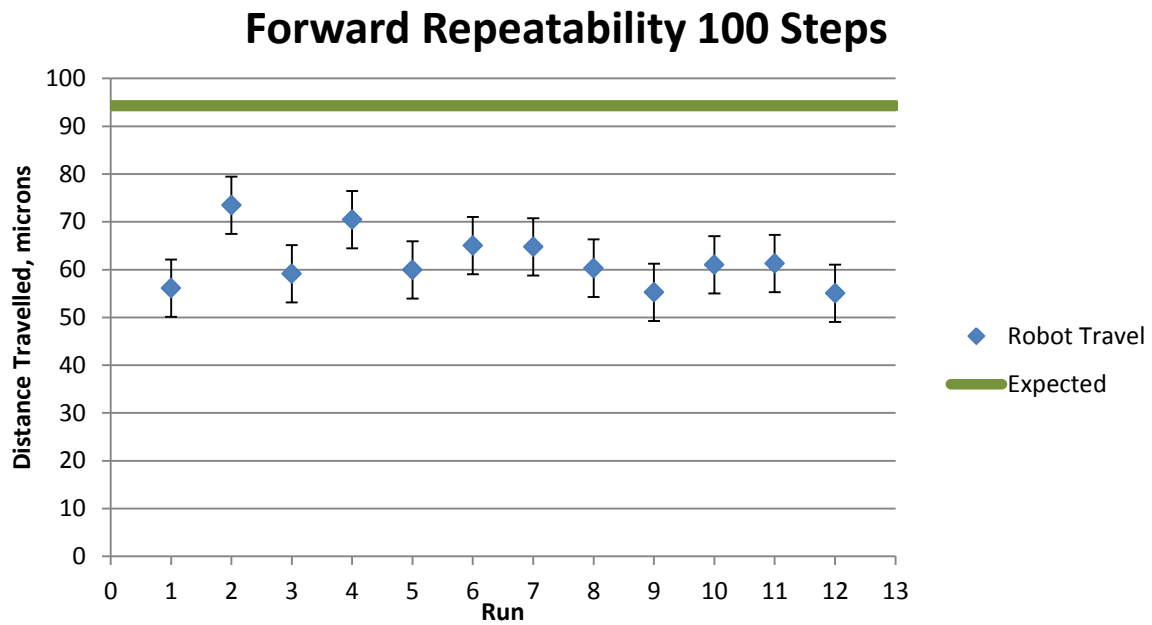
Figure 3-17: MA-BOT1 Straight Line Repeatability Test Setup



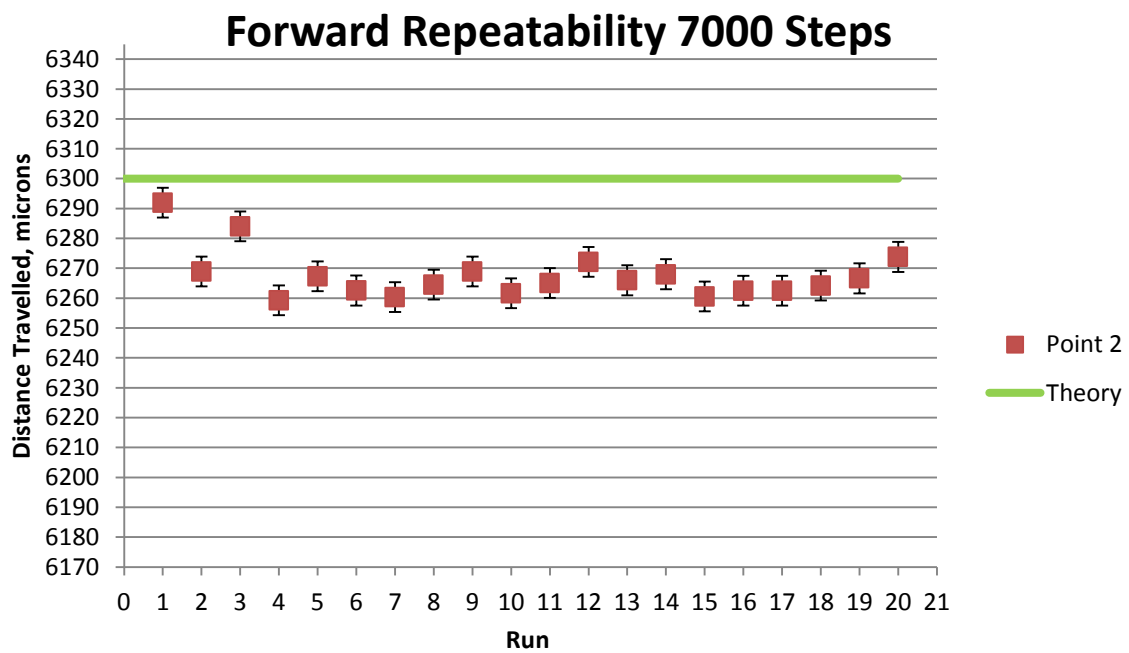
**Figure 3-18: Features measured using the Nikon microscope**

The maximum distance that the robot could be commanded to travel was limited by the x-y surface of the Nikon inspection microscope which is approximately 90 mm.

Figure 3-19 shows the results for the 100-motor step and 7000-motor step tests done. The measurement resolution for the Nikon microscope is less than 5  $\mu\text{m}$  and is represented as error bars on the y-axis of the graphs. The graphs show the distance travelled in the forward direction. It is clear for all the various step tests that the robot did not travel the expected distance. The offset between expected performance and actual performance also varied between the number of motor steps commanded (Figure 3-20). The graphs show that the robot stops short of its expected travel by  $33 \pm 5 \mu\text{m}$  for both 100 and 7000 motor steps. This was determined to be caused by the backlash inherent to the Smoovy motors gear heads and is characterised in detail later on in this thesis. Due to the test methodology applied the backlash was not being removed.

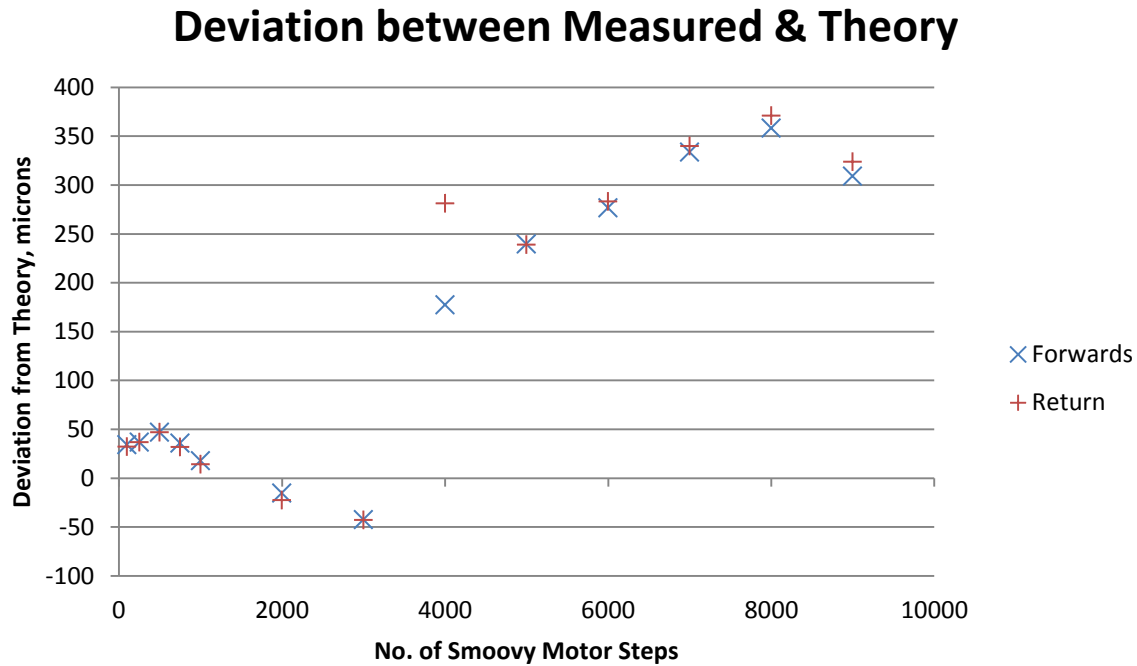


(a) Distance Travelled for 100 Step Commands



(b) Distance Travelled for 7000 Step Commands

**Figure 3-19: Sample of Repeatability Test Results**



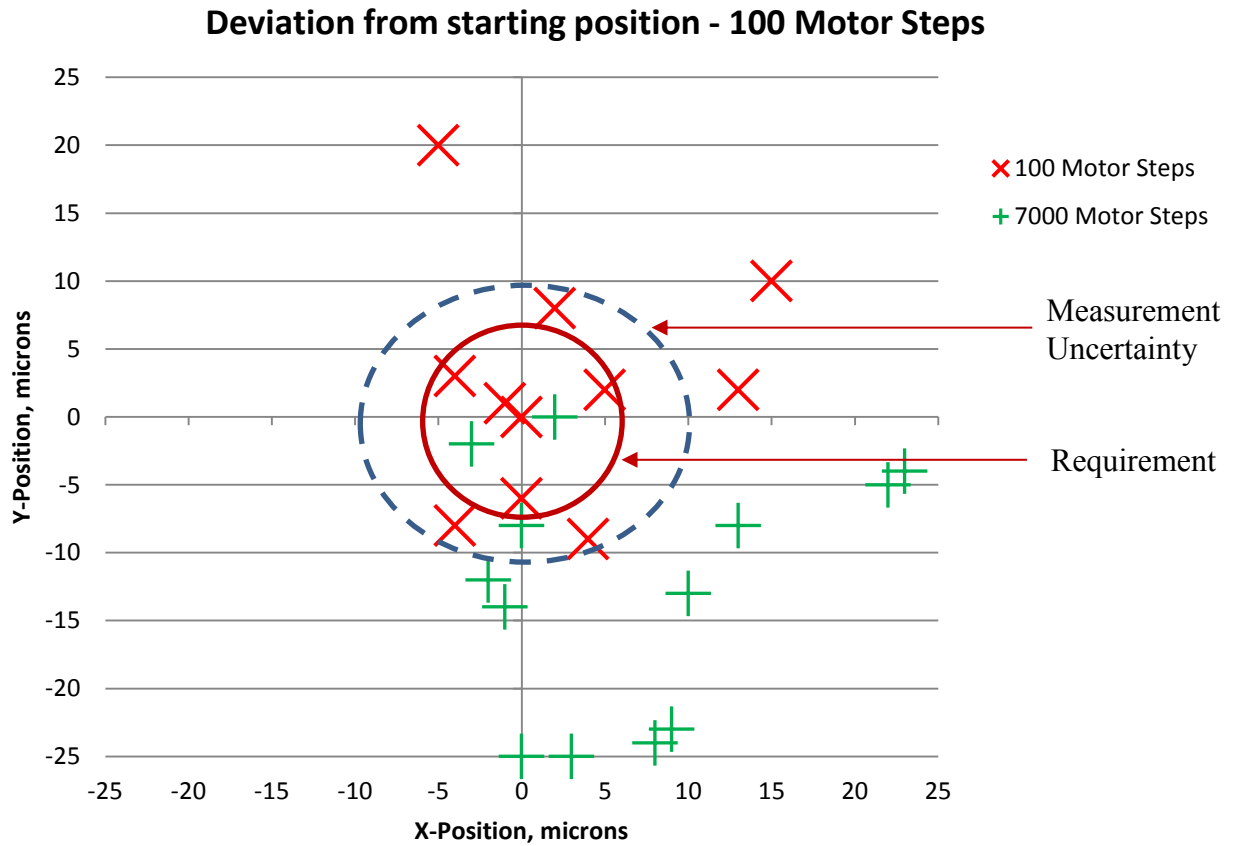
**Figure 3-20: Deviation of Measured Results from Theoretical Prediction**

Unfortunately, due to the limitations of the measuring surface, larger runs could not be achieved to see how this error might have continued to propagate.

Figure 3-20 shows the results from different number of Smoovy motor step tests. The reverse motion of the robot provided the same results as the forward motion shown in Figure 3-19 with an average variation of 2 microns between the direction commands. The results showed that the robot is repeatable in both directions with a standard deviation of 6  $\mu\text{m}$  showing that it can meet the requirements of the application. The deviation from the expected travel was due to backlash inherent to the motor's gear head, as the test does not account for this. According to the gear heads datasheet [64], there can be a maximum of  $4^\circ$  backlash present. The motor is being pulsed to act like a stepper motor and the shaft will rotate by  $7.5^\circ$  per step. This is being passed through a 125:1 planetary gearhead, therefore a single step at the output  $0.06^\circ$ . This means that a maximum of 67 motor steps can be lost through backlash. This has been tested and characterised further on.

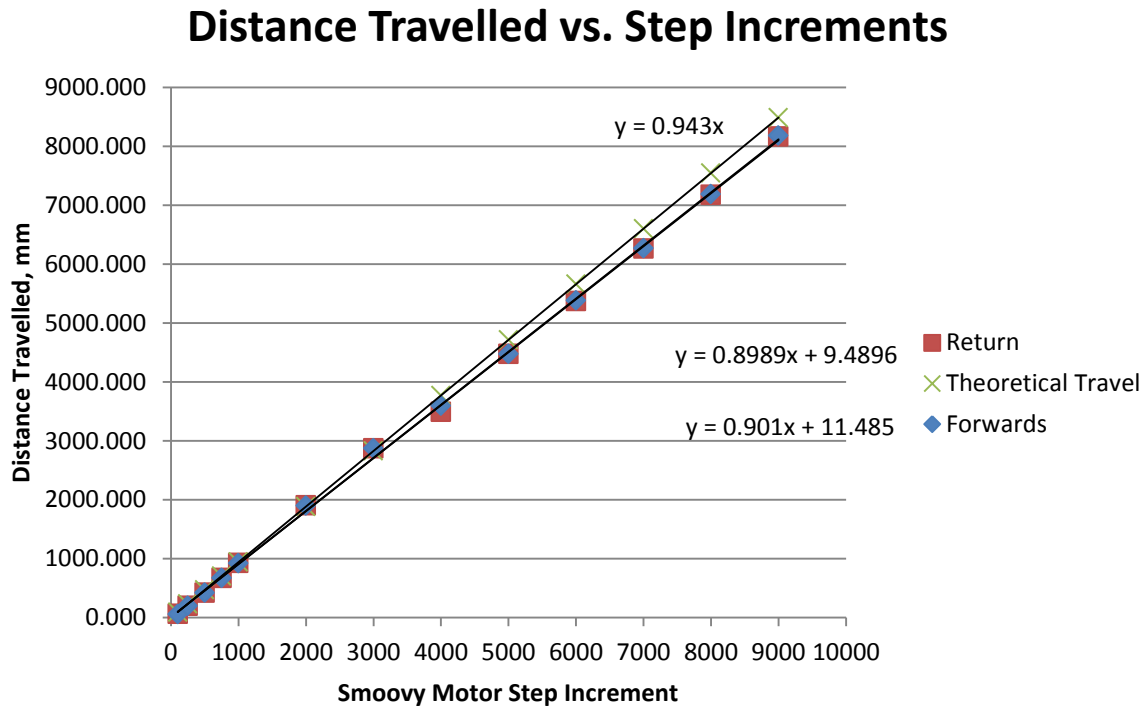
The repeatability of these results is highly encouraging as shown by Figure 3-21. This is an x-y position plot showing the deviation of the robots position from its original starting position on its return. Ideally, in a perfect system the robot would have always returned to (0, 0). The standard deviation of measured data sets is 6 microns which is less than what is required,

although the variation from the theoretical calculated distance is in the order of 32 microns for the 100-step test and 33 microns for the 7000-step test due to the backlash not being accounted for.



**Figure 3-21: Deviation plot of robot from starting position**

Figure 3-22 shows the measured results indicating the distance that the robot travelled for various numbers of steps. This shows that a single step command for the robot should result in  $0.9 \mu\text{m}$  of travel. The robot cannot move by a single step. This is because the motor has to overcome the initial friction, however once the friction has been overcome, every additional step will result in  $0.9 \mu\text{m}$  of travel. Therefore any command of less than 30 steps will result in no movement. If the robot is commanded to move by 30 steps, it will travel a distance of  $0.9 \times 30$  steps which is equivalent to  $27 \mu\text{m}$ . A 31 motor step command will move the robot  $27.9 \mu\text{m}$  and a 32 motor step command  $28.8 \mu\text{m}$ . Figure 3-22 also shows a small difference between the expected and measured results. It will be possible to compensate for this deviation once the system has been fully characterised.



**Figure 3-22: Distance Travelled for X Steps**

**Final note:** If a robot was handled incorrectly in between tests it was found that the results could alter when tests were repeated. The motor housing proved to be especially sensitive. A repeatability test was conducted where the robot was commanded to move 1000 motor steps (900  $\mu\text{m}$ ). The robot on average travelled 869  $\mu\text{m}$  with a standard deviation of 6  $\mu\text{m}$ , between measurements whereas on the next day, after handling the robot by touching the wheels, it travelled an average distance of 845  $\mu\text{m}$  with a standard deviation of 51  $\mu\text{m}$ . These variations are due to the sensitive relationship between the pinion and wheel. This emphasised the fragile nature of the robot indicating poor reliability and led to strict handling procedures being subsequently followed. After following the strict procedures the repeatability was improved and a cover was added to stop operators from incorrectly handling the robot, thus improving the reliability.

### 3.5 MA-BOT1.1

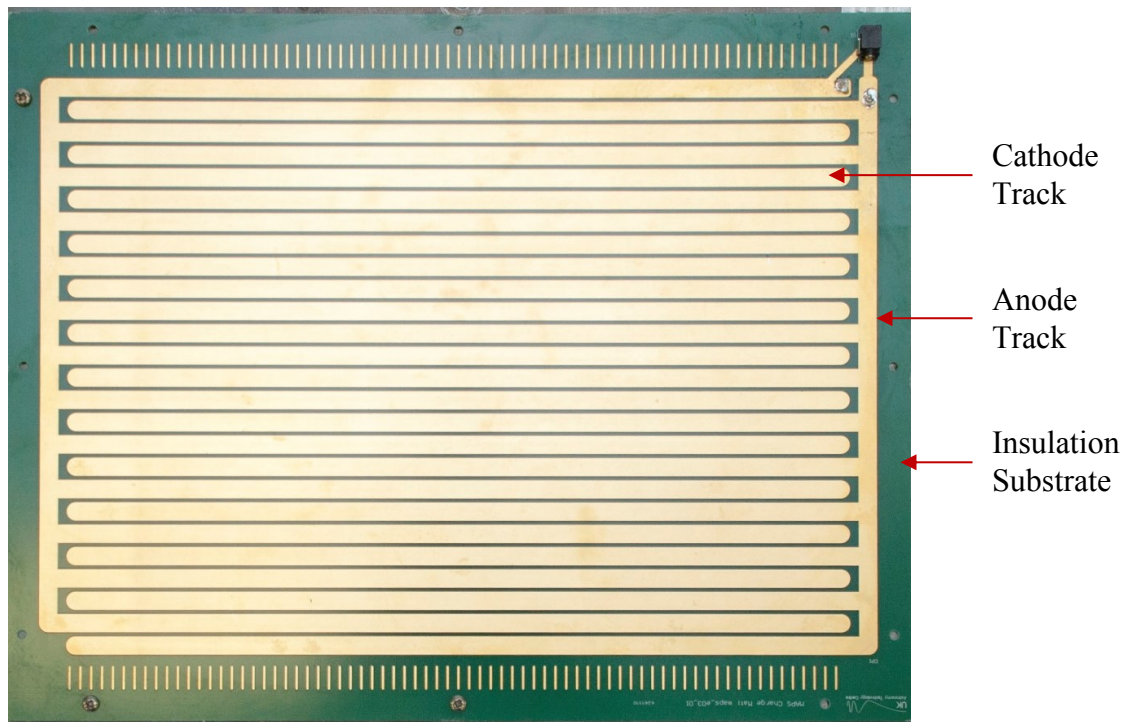
At the inception of the idea to use micro-autonomous robots to position pick-off mirrors to pick-off light from astronomical target the idea was to provide each robot with wireless power sufficient to operate for six to twelve months without the need for human intervention. Batteries, induction power and a direct PowerFloor as a means to provide power have been evaluated. The robots electronics are low voltage only requiring 3.7 V to operate. The largest

power consumption is when the motors are operating as they require approximately 340 mA each. During the linear tests, it was clear that it would not be possible to find a suitable battery that would last for the specified operational period. During the linear testing of the robot it was observed that the chosen battery provides approximately one hour of operation, while, the absolute minimum requirement is at least eight hours. For the final design a battery only system was not envisaged. As a result of the literature review (Chapter 2) it was clear that battery powered robots within this size domain will not be capable of delivering power to the robot and its electronics for longer than an hour.

Induction charging was first contemplated as a replacement to the battery. Due to the size of the focal plane ( $\varnothing$  2.5 m), having a single large coil going around the perimeter charging the smaller coils on the robot would have been inefficient: the efficiency of induction charging is greater for coils of similar size and in close proximity to one another. This could conceivably be achieved through a network of smaller coils that could be positioned underneath the focal plane. However, the system would still be inefficient as energy is often lost in induction charging through Eddy currents that are generated in surrounding materials. At the time, although the EAGLE instruments focal plane surface material was not finalised, it was highly probable that it would be a metal like steel due to its size and the stiffness required. The Eddy currents generated in the steel plate would cause the material to heat up and would dramatically interfere with the science observations, due to the introduction of thermal turbulence at the entrance of the instrument. As such for the time being induction charging was no longer considered.

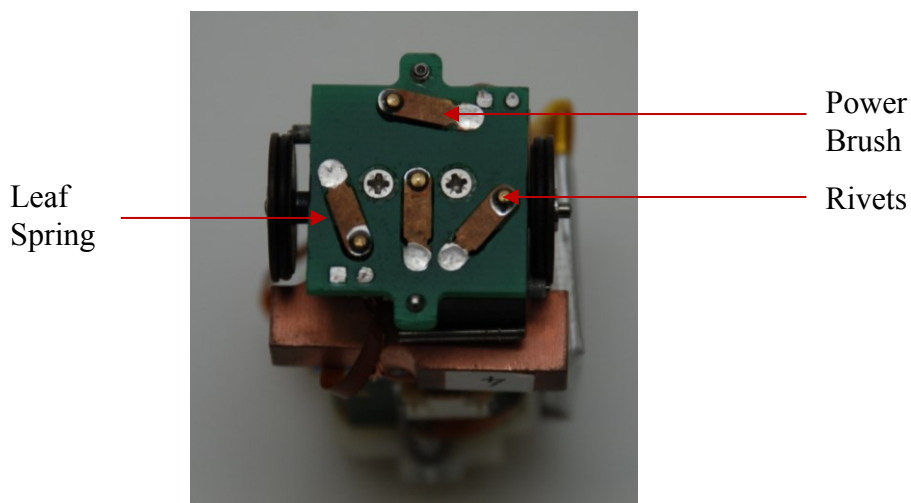
The PowerFloor concept was adapted from mobile phone technology (WildCharge [67]). The operating surface consists of two interlaced tracks that are positive and negative feeding 9.06 V constantly from a mains source, Figure 3-23. This has been produced using standard PCB manufacturing processes. The copper tracks were plated with a 100  $\mu$ m layer of gold to improve the current transfer between the tracks and the power pick-off points.





**Figure 3-23: PowerFloor**

The robot picks up power through four beryllium copper leaf spring contacts, as shown in Figure 3-24. Beryllium copper is used due to its electrical conductivity and as it is a common spring material. Rivets at the end of the springs make the physical contact with the floor; the rivet-head diameter was chosen to be less than the gap distance between tracks to avoid shorting the positive power and negative power tracks. The geometry of the contacts has been design such that regardless of the robot's position and orientation there is always at least one contact on each track. It does not matter which track a contact is on as the electronics have been designed to allow for switching.



**Figure 3-24: Power Brush PCB**



The PowerFloor concept has shown excellent potential but when the robot is moving it was observed that the traction and continuity of the power contacts is susceptible to multiple variables. This includes the robot's weight, weight distribution, stabilisers' height, stabilisers' location and spring stiffness. This is elaborated further in section 3.5.1 with the analysis of the PowerFloor's continuity.

Figure 3-25 shows the updated MA-BOT1, known as MA-BOT1.1. MA-BOT1.1 was used to test the PowerFloor for power losses and their duration. The power received from the PowerFloor was dissipated through a resistor and did not power the robot itself. MA-BOT1.1 was still powered by a battery so that it would continue moving across the PowerFloor. To monitor the power received by the PowerFloor, trailing leads were attached to the power pins that would go from the power delivery PCB to the control electronics in MA-BOT1.1.

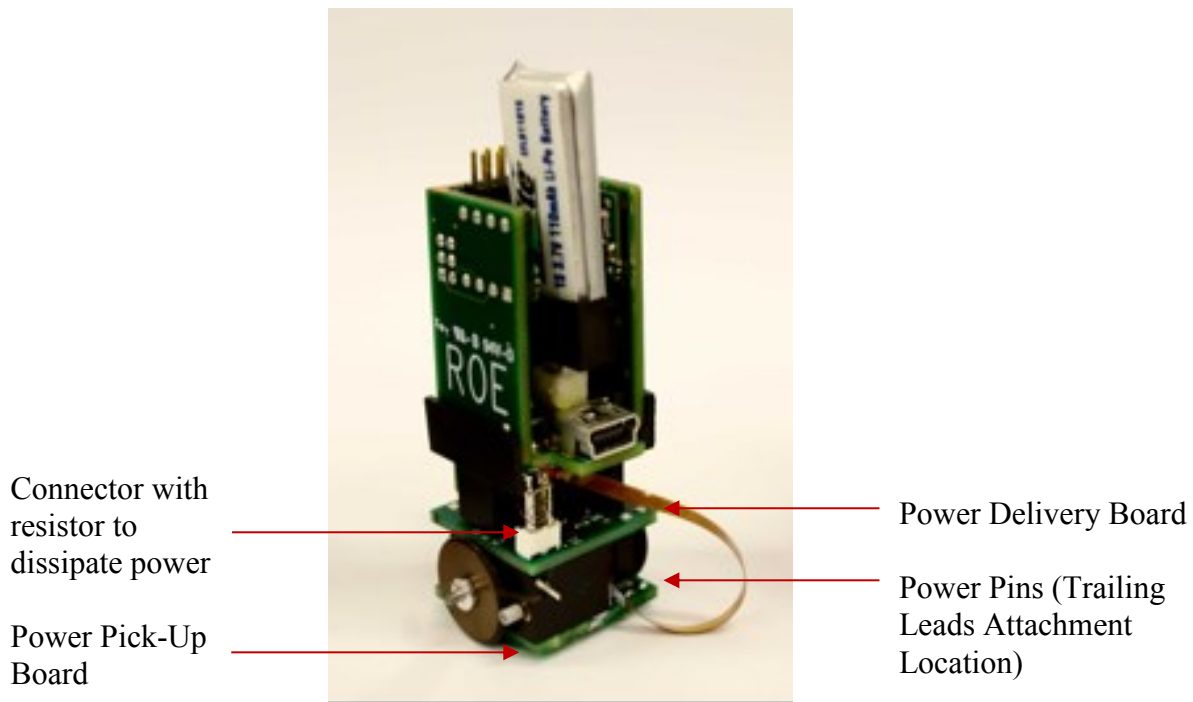


Figure 3-25: MA-BOT1.1

### 3.5.1 MA-BOT 1.1 PowerFloor Test

The robot was moved 10,000 motor steps, in both forwards and reverse, and the duration of power losses recorded (Figure 3-26). The robot was powered using the battery and used the power pick-ups to record if it could receive power from the PowerFloor. A bar plot of the power losses after 16 repetitions were produced to provide a statistical sample, Figure 3-27.

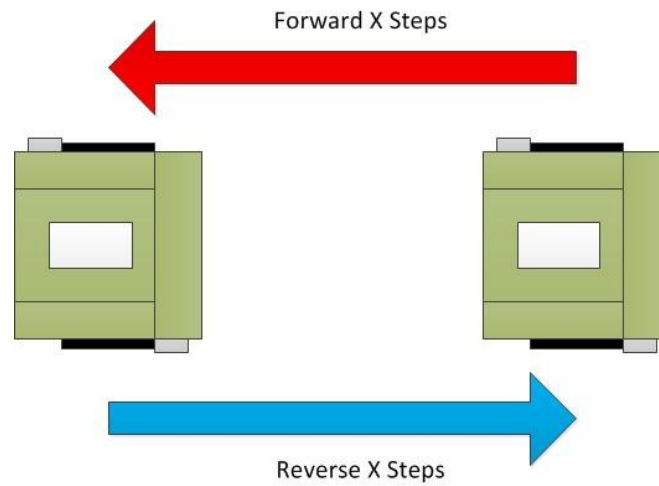
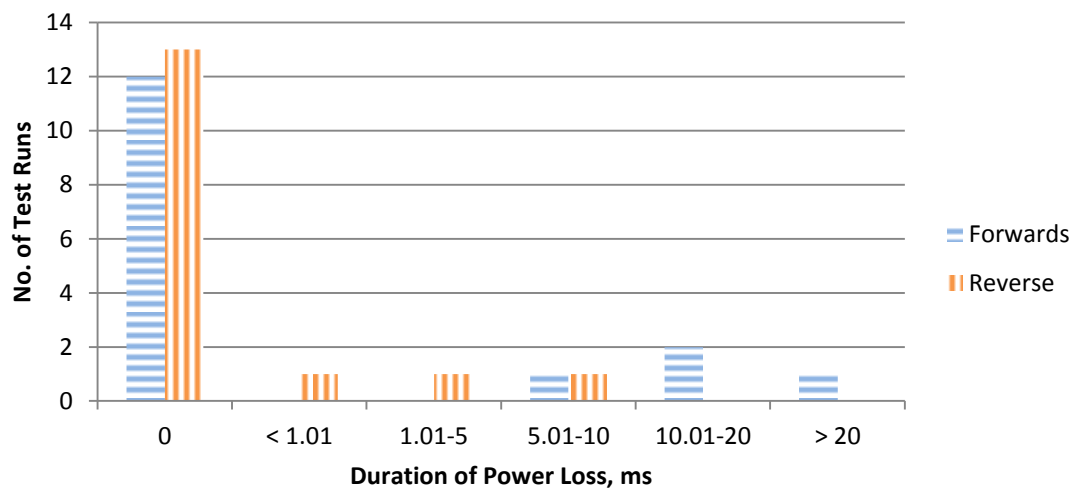


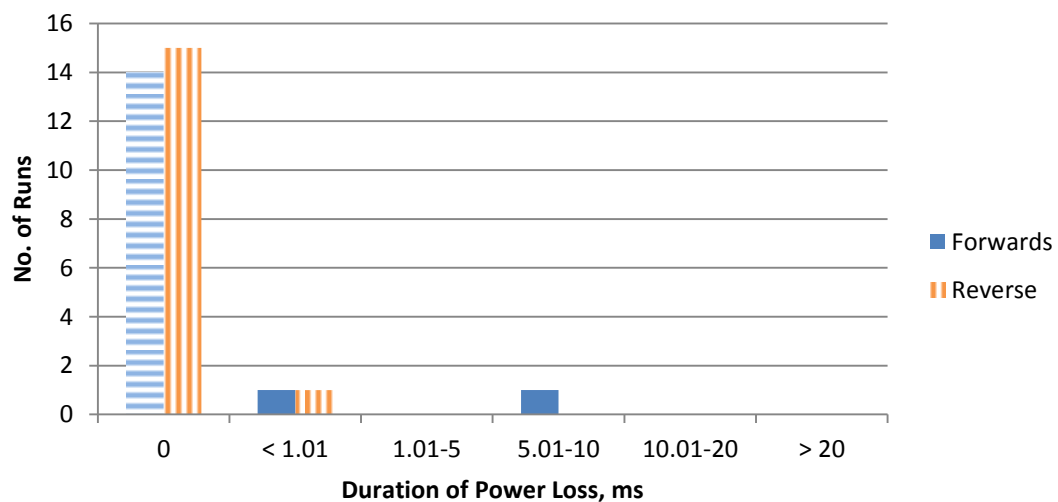
Figure 3-26: MA-BOT1.1 PowerFloor Test – A Single Run

### Straight Line Motion - 10,000 Motor Steps



(a) Straight Line Motion Power Loss Durations

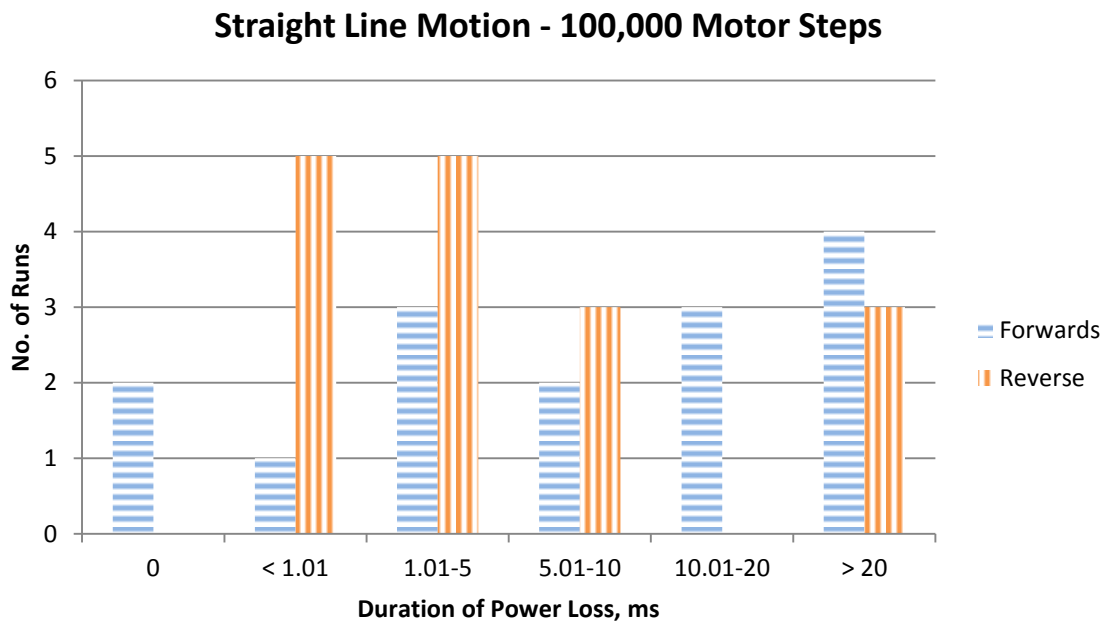
### Rotation Motion - 10,000 Motor Steps



(b) Rotation on the Spot Motion Power Loss Durations

Figure 3-27: Bar Plot of Power Loss Durations

The different hatch orientations represent different directions of motion. For short motions of 9 mm, the robot is able to move without power interruption on a regular basis. Based on Figure 3-27 the robot does not lose power often. The power continuity is more reliable when the robot rotates on the spot compared to a linear motion. However, it was found that for the same experiment for a longer straight-line motion (90 mm) power losses were more frequent, Figure 3-28. Power losses greater than 20 ms were detected for 25% of the runs in one direction and 50% of runs in the opposite direction. These power losses erase the robot's memory requiring the system to follow a restart procedure to reacquire the robot which is time consuming and unsuitable for the application.



**Figure 3-28: 90 mm Travel Power Loss Duration**

To mitigate the increased downtime various possibilities were investigated:

- Magnets integrated to the pick-ups – Increases contact force with PowerFloor.
- Software Control – The external metrology system corrects for power losses.
- Addition of Super Capacitors – Discharge during power losses to maintain robot's motion.

Small neodymium magnets were attached to the individual power pick-ups behind the rivet heads to attract the pick-ups towards the PowerFloor. This was not a viable solution as the magnetic field interfered with the Smoovy motors. Also due to the small footprint of the robot, the magnets were in close vicinity to one another resulting in them trying to attract to one another, which damaged the pick-ups.

The software was set to reacquire the robot when power losses were experienced that erased the robots memory. A request was sent to the robot to determine if it was active. If the robot did not respond then the robot had no power. If a response was received the metrology module was used to find the robot and continue with the previous positioning algorithm. However, occasionally the robot would not regain power, thus making a restart impossible.

A super capacitor was added to attempt to bridge over long power losses. A super capacitor was preferred over a battery because of its quick charge times and because it does not require additional circuitry. The capacitance requirement, 4 mF, was determined based on the results shown in the previous figures. There were no 9 V capacitors with this capacitance available that could be fitted inside the robot therefore two 5.5 V capacitors joined in series with an 8 mF capacitance were used. These capacitors produced by ‘Cellergy’ were 12.5 x 12 x 3.1 mm<sup>3</sup>. The addition of super capacitors was still unable to overcome the power loss durations.

The PowerFloor technology was fully incorporated into a newer version of the MAPS robot, which is presented in Chapter 4, after trialling the concept using a modified version 1 robot. This was used for the development of MA-BOT2, where a battery was added to compliment the PowerFloor as it provides greater autonomy to overcome the power loss issues. MA-BOT1 was powered with only a battery and this provided approximately 40 minutes of full autonomy. Hence a PowerFloor was added to the system. It was found with MA-BOT1.1 that as the robot moves over the PowerFloor the power pick-ups could lose contact with the PowerFloor resulting in power losses lasting longer than 20 seconds. The power losses would erase the robots memory resulting in commands needing to be sent once again to get it into the required position. This was why the additional battery was required to overcome the power losses.

Chapter 3 has shown that a differentially steered DC propelled miniature autonomous robot (MA-BOT1) can be built. From the research test data it is clear that the robot design has the potential of meeting the 10 micron positioning requirement. The robot had suffered from issues such as the pinions effect on the straight line performance. This highlights how the interaction between components at this scale can have a large effect on the robots performance. This chapter also shows that a battery powered robot is unable to last the 8 hour duration time required in MOS instruments. A PowerFloor was developed to provide the robot with continuous power. However, it was found that as the robot travels across the PowerFloor it would lose power and reset its instructions. This resulted in the need to combine the PowerFloor with a battery to power the robot continuously and be capable of overcoming power losses during motion that is detailed in chapter 4.

## Chapter 4 – The MAPS Robot (MA-BOT2)

A MA-BOT2 robot was developed based on the original design, however with the following enhancements:

- Smaller electronics packaging.
- Additional Smoovy motor to operate a turret for fine rotation process.
- Power provided by a PowerFloor with a battery on-board as a back-up power source.

The enhancements to the robot's design were needed to provide continuous power for longer than 8 hours as required by the multi object spectrograph instruments. The enhancements also provide a smaller form factor and fine rotation stage for higher accuracy orientations. This chapter focuses on the changes that were made and concludes with the robot's performance.

### 4.1 MA-BOT2 On-Board Electronics

The primary change from MA-BOT1 to MA-BOT2 was the electronics packaging and the development of a PowerFloor removing the robot's need to be powered with batteries. Dreamapact developed the new electronics packaging based on requests from the UK ATC that were determined from the documented tests discussed in chapter 3. This included the removal of surplus connectors, addition of a third motor and easier to assemble layout. The motivation to change the primary energy source was that it was unacceptable from an operational viewpoint to have to replace or charge batteries on a daily basis within an astronomical instrument. Figure 4-1 shows the evolution from the first iteration robot to the second iteration.

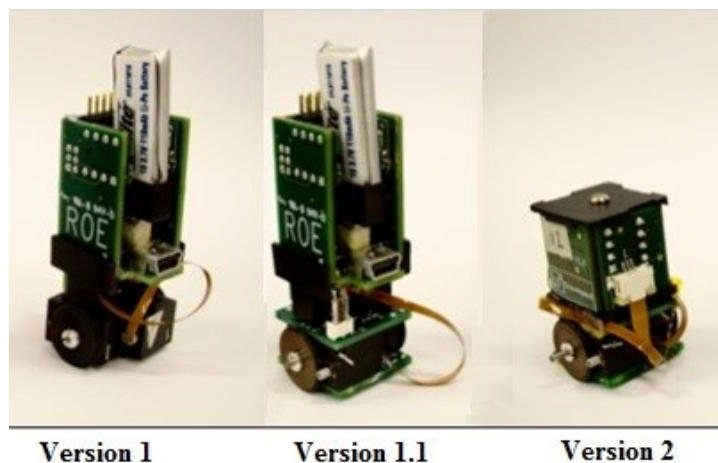
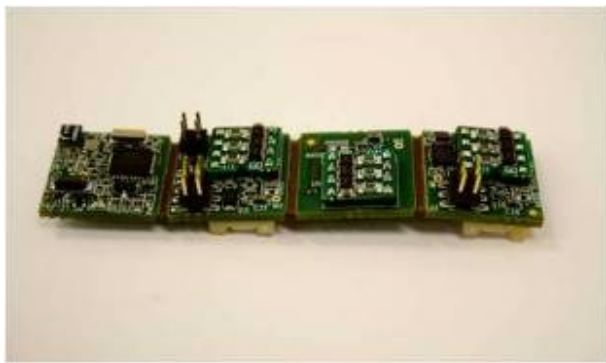
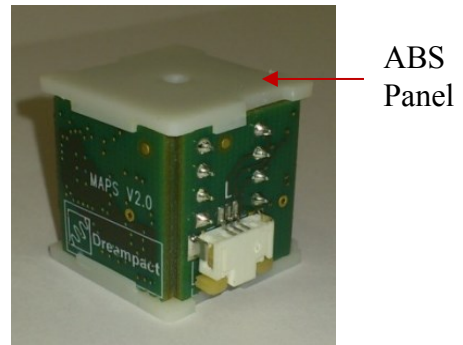


Figure 4-1: MAPS Robot Evolution

Since the first version of the electronics was a successful proof of concept, a second version (Figure 4-2) was developed to reduce the packaging size. This was achieved by removing the USB port and pin connector that was no longer required. To further aid with the size reduction the right-angle pin connectors that were originally used to connect the PCBs together were removed and flexible connectors were used between the boards so that the electronics could be folded into a cube. The cube was then held in place using two ABS panels with machined grooves that press onto the PCB edges. The resulting cube was 20 mm x 20 mm x 20 mm and was attached to the chassis through a central bolt that makes use of the existing threaded hole. Despite its smaller size, this second version of the electronics also provided the additional ability to control a third Smoovy motor for use with a fine alignment stage.



(a) MA-BOT2 electronics opened out

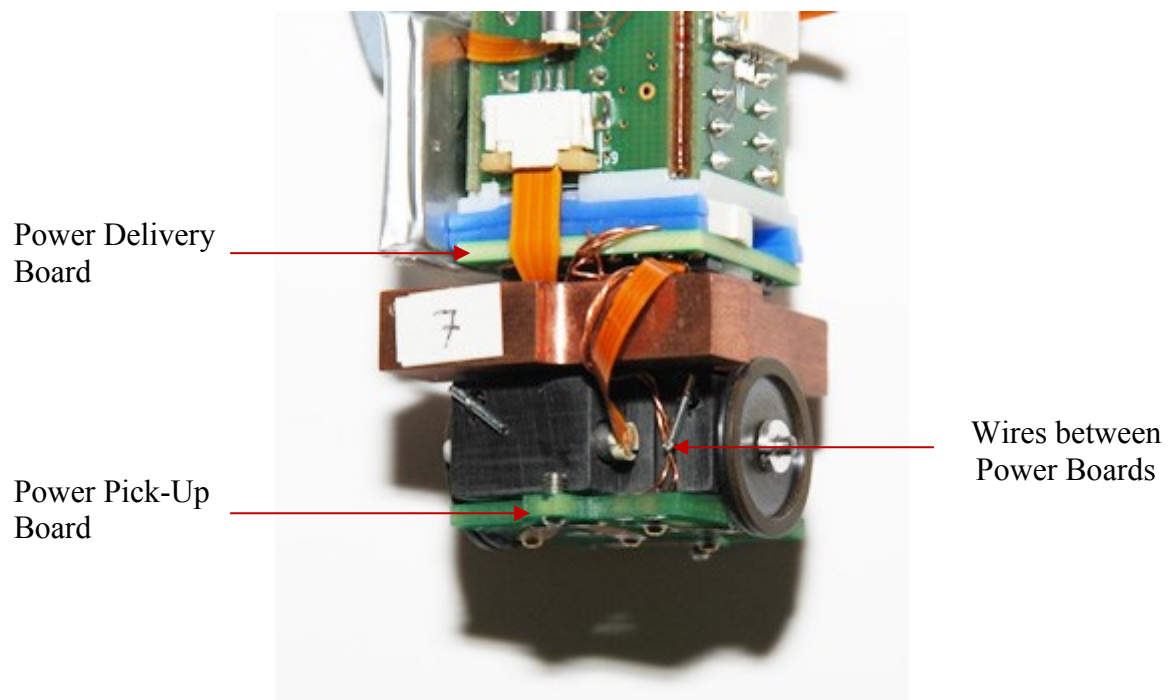


(b) MA-BOT2 electronics in cube arrangement

**Figure 4-2: MA-BOT2 Electronics**

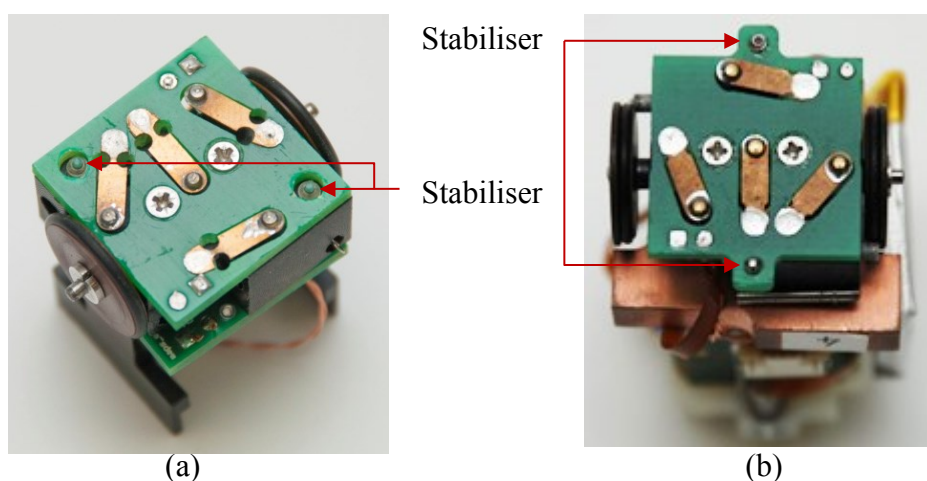
## 4.2 Modifications to the robot

To incorporate the power pick-up, power delivery PCB boards and MA-BOT2 electronics, minor changes to the chassis were required. The chassis was reduced from 10mm to 8mm in height to accommodate the power pick-up PCB. Two M1.6 threaded holes were added as attachment points for the power pick-up board. To avoid increasing friction on the chassis between the motor housings and power pick-up board, a spacer was inserted between the two components. The power pick-up board was joined to the power delivery PCB through wires that were soldered in place. Figure 4-3 shows how the wires were routed between the power pick-up board and power delivery board along the chassis.



**Figure 4-3: Wire routing between power boards**

It was observed that MA-BOT1.1 would rock from front to back while moving during the power characterisation tests (Section 3.5.1). Closer inspection revealed that this was due to the location of the stabilisers. The positioning of the two stabilisers and central pick-up limited the pick-ups contact with the PowerFloor. To remedy this, the power pick-off board was altered by moving the stabilisers back to a central axis between the wheels, as can be seen in Figure 4-4.



**Figure 4-4: Stabiliser Locations for PowerFloor Robot (a) First Location, (b) New Location**

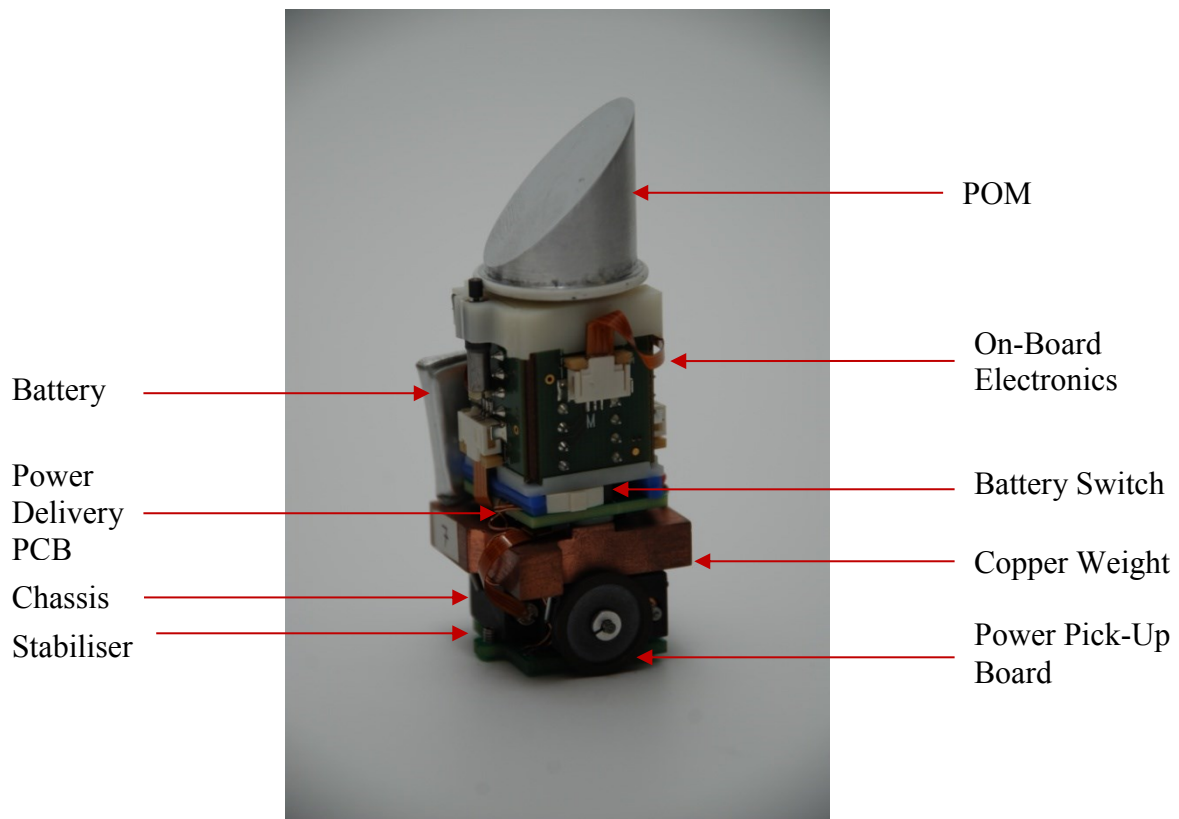
The power pick-ups were originally designed to each provide 5 grams of downward force based on a 0.325 mm deflection. This accumulates to a 20 gram upward reaction force. At the time the robot weighed less than 20 grams, therefore the reaction force from the power pick-ups raised the robot off its wheels causing a loss of traction. To compensate, the power pick-ups springs were reduced from 100 microns to 80 microns thick, making them less stiff resulting in a lower reaction force to 2.6 grams and a return of traction. Another method to reduce the reaction force would have been to reduce the deflection, for a 100 micron thick spring the force increases by 1.56 grams for every 0.1 mm increase to the deflection. This is now 0.8 grams for every 0.1 mm change in deflection.

To maintain power continuity additional weight was originally added to the robot in the form of 20 mm x 20 mm lead weights. A copper weight was subsequently machined to fit between the power boards as can be seen in Figure 4-5. Copper was chosen as it is relatively easier to machine compared to lead and is a highly dense material ( $8930 \text{ Kg/m}^3$ ). The copper weight lowered the centre of gravity, thus improving stability and increasing traction and power continuity. Changing the chassis to a dense material such as copper was also considered thus removing the need for an additional component. However, this would require a redesign of the chassis as the hinge was only suitable for a plastic material due to its better elasticity properties compared to a metal. Therefore, it was decided to continue with the plastic chassis and add an additional weight component.

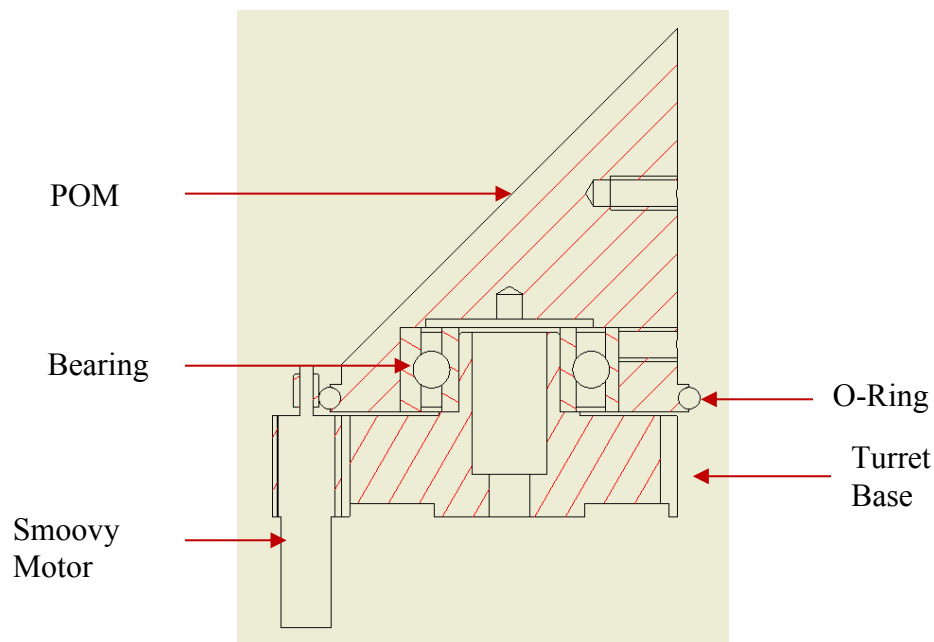
The additional Smoovy motor added to the MA-BOT2 electronics was for the addition of a turret stage to the robot enabling the mirror to rotate independently of the chassis. This was necessary as the robot has the potential to slip out of its x-y position as it rotates, which is not desirable. The turret with its independent motion therefore simplifies the final positioning of the robot.

The Fine Rotation Stage (FRS) is based on the same friction drive principle as the drive section of the chassis. A Smoovy motor is forced towards the POM by a tension spring. The pinion presses against an o-ring that is stretched over an annular groove on the POM. The POM sits on a bearing that is press fit onto a piece of ABS. The ABS also doubles as a panel that holds the electronics cube together. A fully built FRS with electronics cube is illustrated in Figure 4-5 and a schematic shown in Figure 4-6.



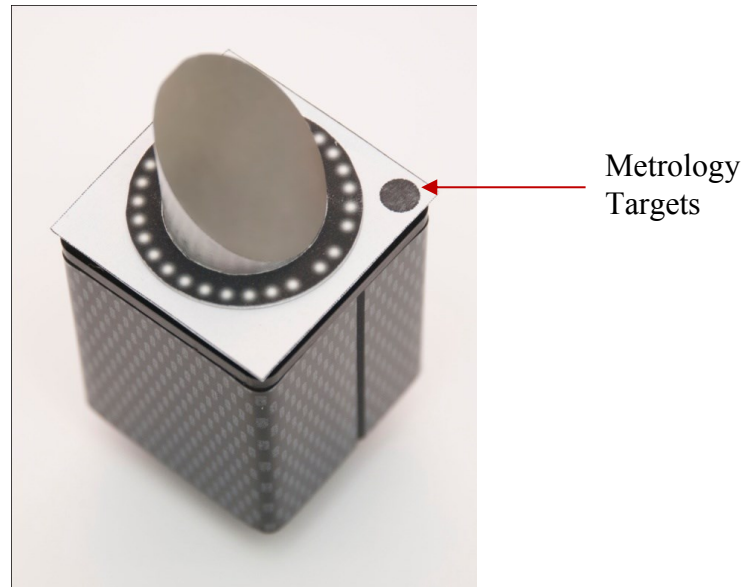


**Figure 4-5: Second Iteration Robot with Copper Weight**



**Figure 4-6: FRS with Electronics Cube Sub-Assembly**

A plastic cover was added to the robot to protect the electronics from shorting should the robot fall over due to an earthquake or come in contact with another robot. Figure 4-7 shows a fully built MA-BOT2 including the cover and metrology target. The small grey dots are the Gaussian profile spots that the metrology camera uses to precisely determine the robots location [32].



**Figure 4-7: MA-BOT2**

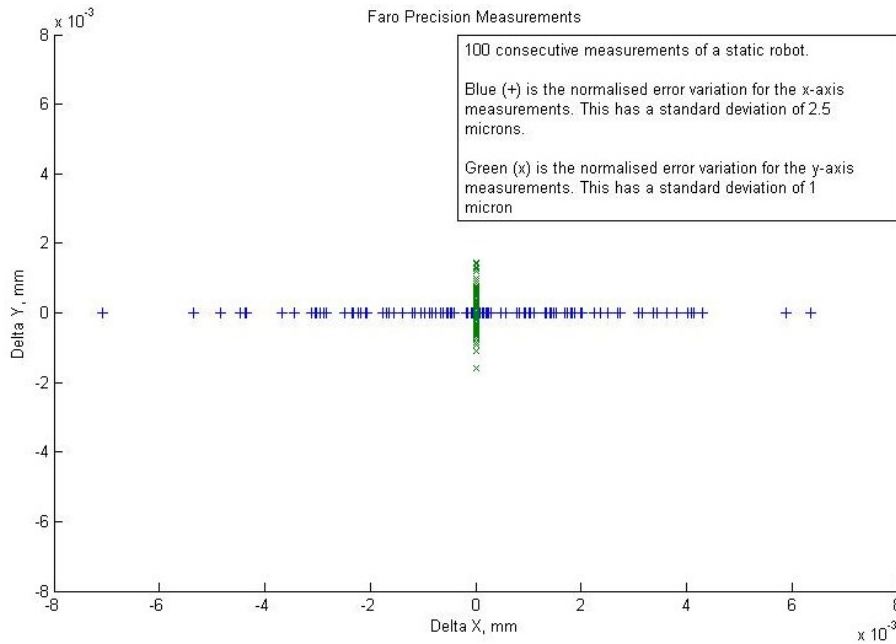
### **4.3 Expected Performance**

Testing showed that the relationship between the motor steps and distance travelled for MA-BOT2 was the same as MA-BOT1 (Section 3.3) as the concept has not been changed. Although the robot's drive concept was not changed the decision to repeat the tests was to ensure that the changes made to the robot did not affect the performance in an unforeseen manner. The turret will have its own relationship between motor steps to output angle. The pinion and mirror diameters are 1.8 mm and 22 mm respectively giving a ratio between the components of 0.08 meaning the POM rotates at  $0.0048^\circ$  per motor step ( $84 \mu\text{rads/step}$ ). The gear head has  $4^\circ$  of backlash inherent to it, which equates to  $0.192^\circ$  ( $3351 \mu\text{rads}$ ). This is the equivalent to 41 motor steps.

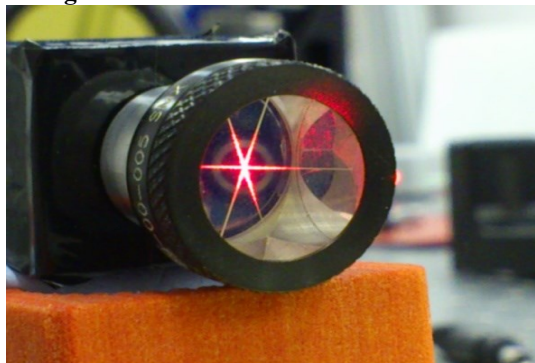
### **4.4 Actual Performance – Open-Loop Straight Line**

The open-loop performance of the robot was tested first by commanding it to move in a straight-line. The purpose was to confirm that the robot would maintain the same relationship between motor steps and distance travelled as seen with MA-BOT1 (section 3.3). The robot was commanded to travel a considerably longer distance compared with the MA-BOT1 tests. This was made possible by using the PowerFloor. To measure the robot's path travelled a Faro laser beam tracker was used. The laser beam tracker is capable of rotating around two perpendicular axes. Encoders on each axis allow the tracker to know which direction it faces. The laser beam tracker measures the time it takes for photons it emits to be reflected back to it

from the target object. By knowing this distance and both angles it is able to calculate x, y, z coordinates using itself as a reference point. Repeated measurements of the robot at a predefined fixed position indicated the tracker had a measurement repeatability of  $\sim 3 \mu\text{m}$ , Figure 4-8. However, the measurement error of the laser tracker according to the datasheet is  $10 \mu\text{m}$  [68]. For the measurements the POM was replaced with a target mirror that the tracker locked onto and followed Figure 4-9.



**Figure 4-8: Faro Precision Measurements**



**Figure 4-9: Target Mirror used to replace the POM**

The robot was located at a starting position at one end of the PowerFloor. The following procedure was applied:

1. Measure the starting position at one side of the PowerFloor
2. Move the robot by 21,100 motor steps (18.99 mm) and measure the position
3. Repeat Step 2 12 times as this takes the robot to the end of the PowerFloor
4. Repeat steps 2 and 3 in the opposite direction

The robot was expected to follow a straight path making equidistant movements and then follow this path in reverse. For each position the tracker took at least 16 measurements and the position was calculated by averaging the sixteen measurements. The 18.99 mm travel was chosen as it would provide 12 positions for measurements before the robot has travelled the entire length of the PowerFloor.

Figure 4-10 plots the robot's motion across the PowerFloor during the test. From the graph it is clear that the robot did not move in a straight line, instead it was curving to the left. A similar deviation, although less pronounced was observed in the reverse direction.

Table 4-1 is a summary of the results indicating that the robot deviates from an expected path by  $39.4 \pm 0.003$  mm. The results show that when the robot is moved without feedback control it has a relatively high error due to its non-linear motion. The angular error between the expected forward movement end position and actual end position from the forward movement was calculated to be 8 degrees. It was determined that the positional deviation after compensating for the angular error was 4.6 mm.

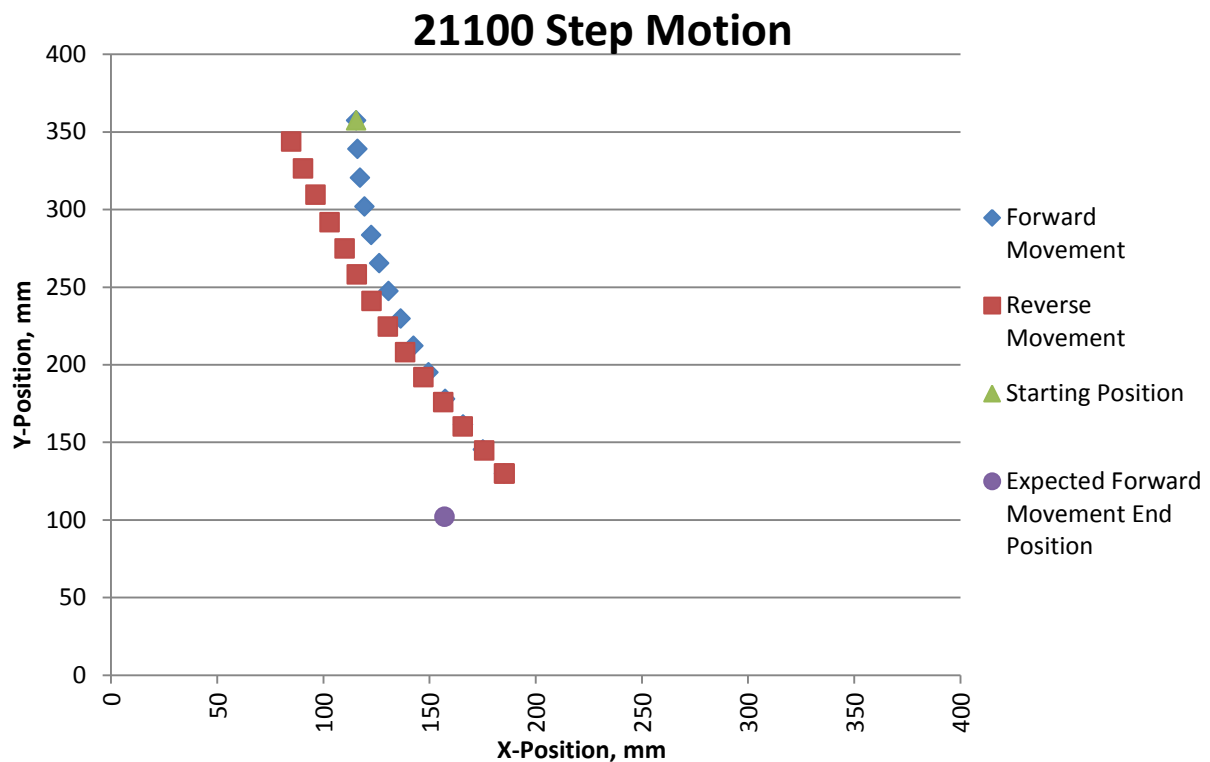


Figure 4-10: 21100 Step Results for 274300 Step overall travel

**Table 4-1: Straight Line Test Results**

<b>Direction</b>		<b>Forwards</b>	<b>Reverse</b>
<b>Theoretical displacement, mm</b>	<b>Between positions</b>	18.99	18.99
	<b>Total travel</b>	246.87	246.87
<b>Measured displacement, mm</b>	<b>Average between positions</b>	18.557	18.268
	<b>Total travel</b>	241.241	237.484
<b>Deviation, mm</b>	<b>Between expected and measured end positions</b>	39.461	33.444
	<b>Between positions</b>	1.34	1.629
<b>Deviation, %</b>	<b>Between expected and measured end positions</b>	15.98	13.55
	<b>Between positions</b>	7.22	8.92
	<b>From expected total travel</b>	2.28	3.8

The above test was repeated using a single 274,300 motor step command (Table 4-2) that would move the robot the same total distance as the sum of all the smaller motions. This was to compare the robot's performance between doing a single long run against shorter motions. Figure 4-11 indicates that the robot's motion for the longer run follows a similar trend as the short runs. The angular error was approximately 8 degrees and the positional error once compensated for was 3.294 mm.

**Table 4-2: 274300 Motor Step Straight Line Test Results**

<b>Direction</b>		<b>Forwards</b>	<b>Reverse</b>
<b>Displacement, mm</b>	<b>Theory</b>	246.87	
	<b>Tested</b>	243.576	243.229
<b>Deviation, mm</b>		3.294	3.641
<b>Deviation %</b>		1.3	1.5

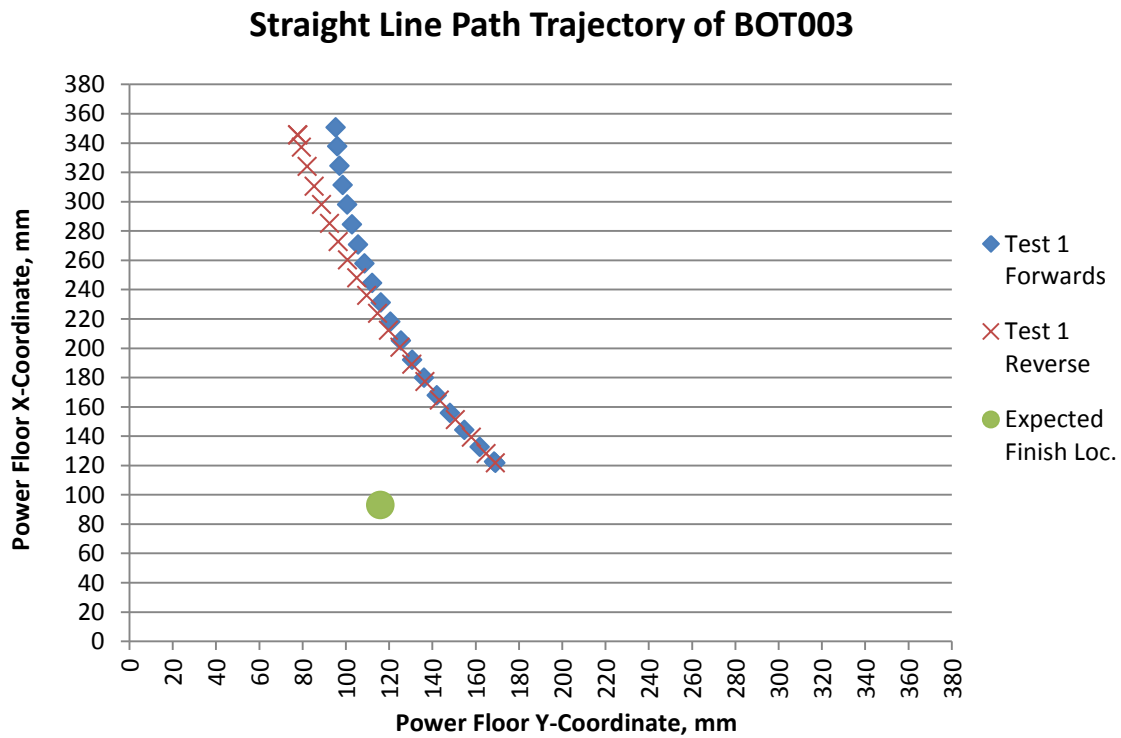
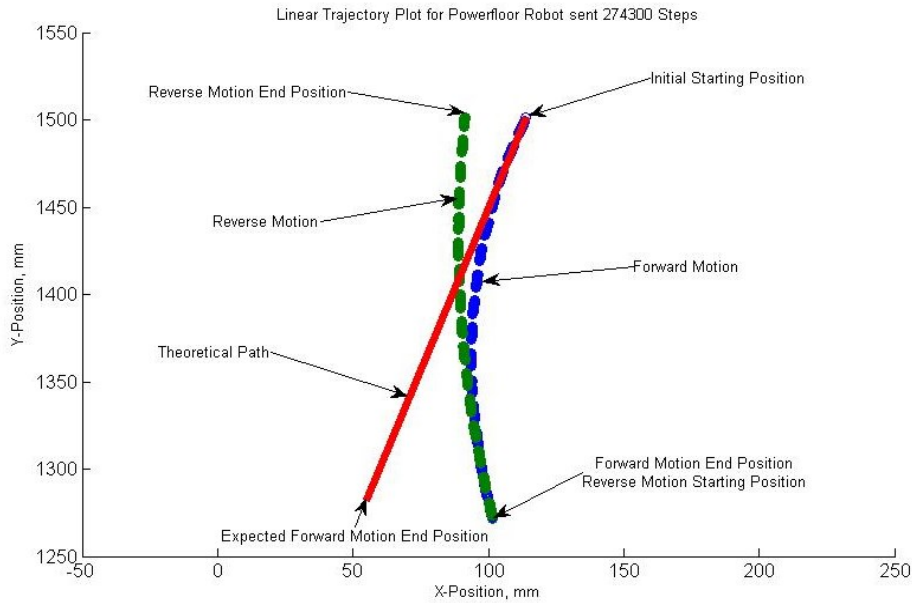


Figure 4-11: 274300 Step Motion

The 274,300 motor-step test was repeated applying different motor clock rates to observe the effect that the speed of the motor has on the robots trajectory. The expectation was that the robot would perform as it did previously which it did, Figure 4-12. Note that the scaling of the graph exaggerates the curving of the robots motion. Table 4-3 shows the averages from at least 10 runs for each motor clock rate that was tested with the standard deviation between the runs. The results indicate that for the distance travelled there is a deviation of 1.6 mm between the varying clock rates. This distance is comparable with the standard deviation on multiple runs at the same speed and given the large travel distance, this is not considered an appreciable difference, which suggests that altering the motor clock rate has little effect on the robot's performance.



**Figure 4-12: Robot's Motion along the PowerFloor at 10,000 Hz Clock Rate**

**Table 4-3: Linear Repetition from different clock rates**

Motor Clock Rate, Hz	Avg. Forward Distance Travelled, mm	Avg. Reverse Distance Travelled, mm	Avg. Deviation on Return, mm
2000	224.754 ± 0.843	225.682 ± 2.568	32.751 ± 2.568
4000	225.901 ± 1.898	227.622 ± 2.609	21.848 ± 2.609
6000	227.979 ± 0.998	229.818 ± 1.978	23.395 ± 1.978
8000	227.298 ± 0.869	227.959 ± 1.761	23.085 ± 1.761
10,000	228.888 ± 0.546	229.285 ± 1.573	23.839 ± 1.573
Standard Deviation, mm	1.648	1.616	4.405

#### 4.5 Actual Performance – Open-Loop Rotational Tests

The differentially steered design of the MAPS robot means that it can turn on the spot. A test was setup using a Lumenera camera that images the metrology targets on top of the robot. The following procedure was executed:

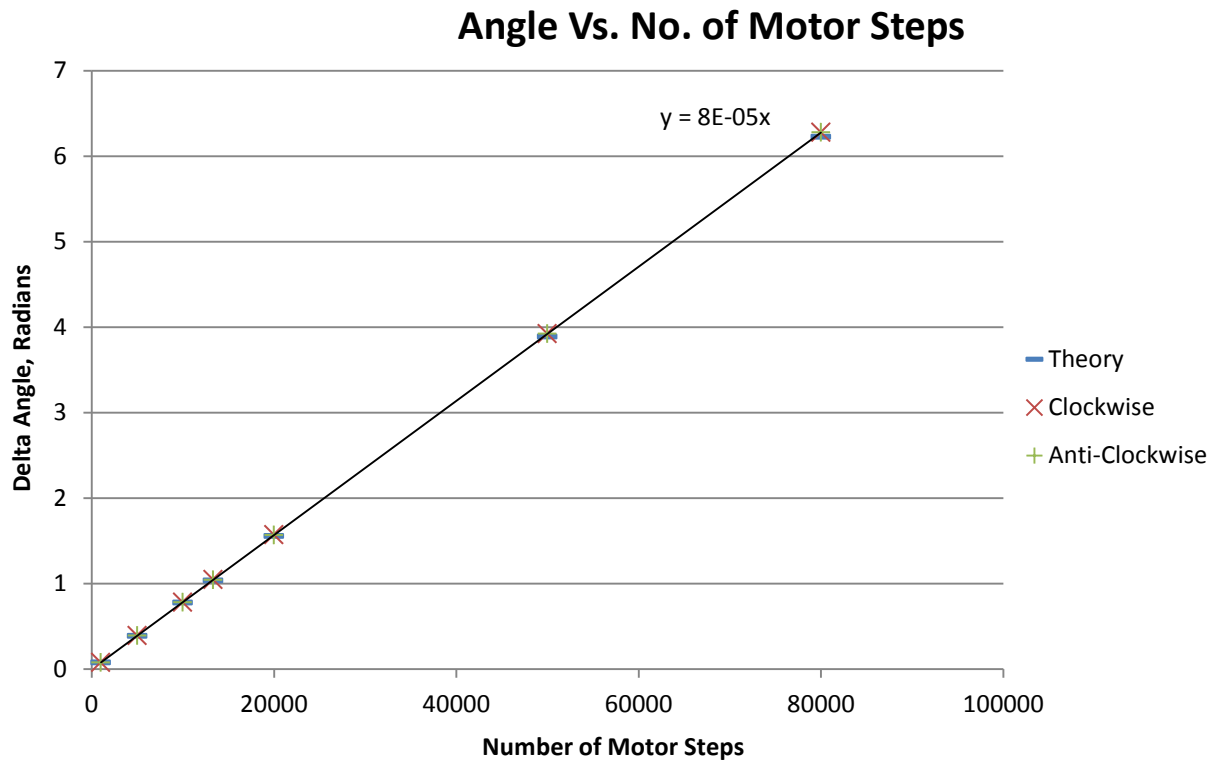
1. Measure the robot's position and orientation
2. Rotate the robot in one direction by x motor steps and measure the orientation
3. Step 2 was repeated 16 times for a statistical sampling

The test was completed using various motor step commands allowing a comparison between the expected output angles with the actual output. The test also monitored the x, y position of the robot to determine slippage. In an ideal system there would be no slippage however due to the tolerances with alignment of shafts, wheels and motors some slippage would be expected in practice. It was difficult to predict how much slippage would occur as it depended on interactions between individual components.

Table 4-4 is a summary of the results obtained compared with the expected outcome. There is negligible difference between the measured results and expected results as illustrated by Figure 4-13. The test shows that the robot will rotate by  $79 \pm 1 \mu\text{rad}/\text{motor step}$ .

**Table 4-4: Rotation Test Results**

Step Command	Theory Angle, radians	Clockwise Rotation Test Results, radians	Anti-Clockwise Rotation Test Results, radians
1000	0.078	0.078	0.078
5000	0.389	0.391	0.391
10000	0.778	0.782	0.783
13333	1.037	1.046	1.045
20000	1.556	1.57	1.569
50000	3.89	3.922	3.924
80000	6.224	6.277	6.276

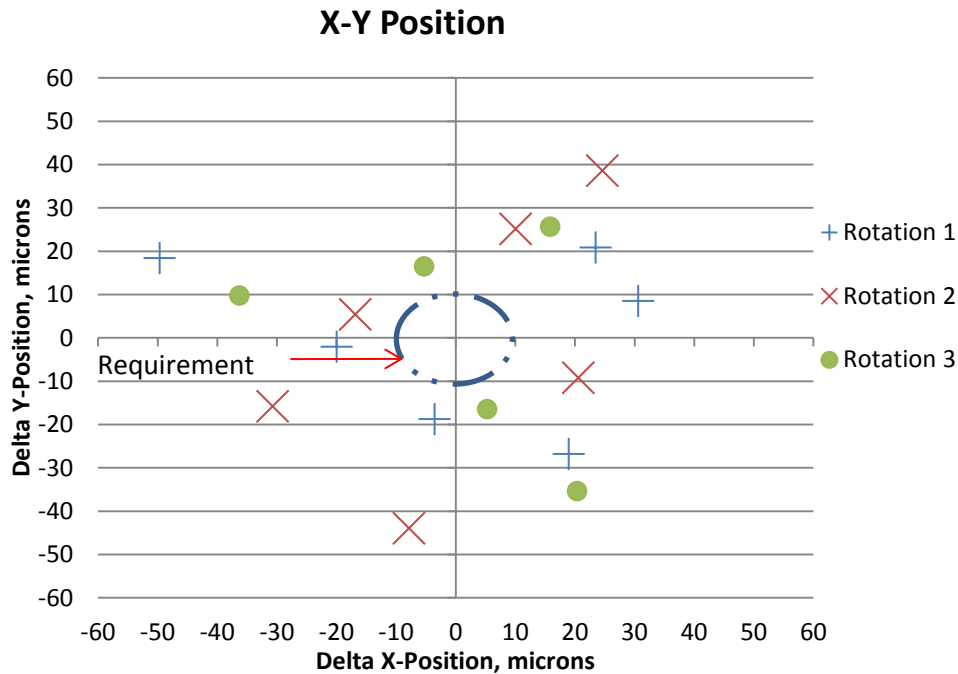


**Figure 4-13: Angle to Step Relationship based on tested results**

Figure 4-14 is an example of the typical slippage results collected from the rotational tests. The graph shows a change in the robot's x-y position from the initial starting position (0, 0) when conducting a rotation command, for this example it was 60 degree rotations. The different markers are to indicate a complete rotation. The results indicate a deviation within 40 microns, this is due to slippage. The measurement error of the camera is  $0.9 \mu\text{m}$  and is not visible due to the graph's scale. This indicates that the robot is unable to turn on the spot and



maintain the positional requirement. The x-y positional slippage is not systematic and cannot be calibrated out through software. It is unlikely to be improved upon through hardware refinement and has led to the decision that a turret stage should be investigated as an alternative to turning on the spot.

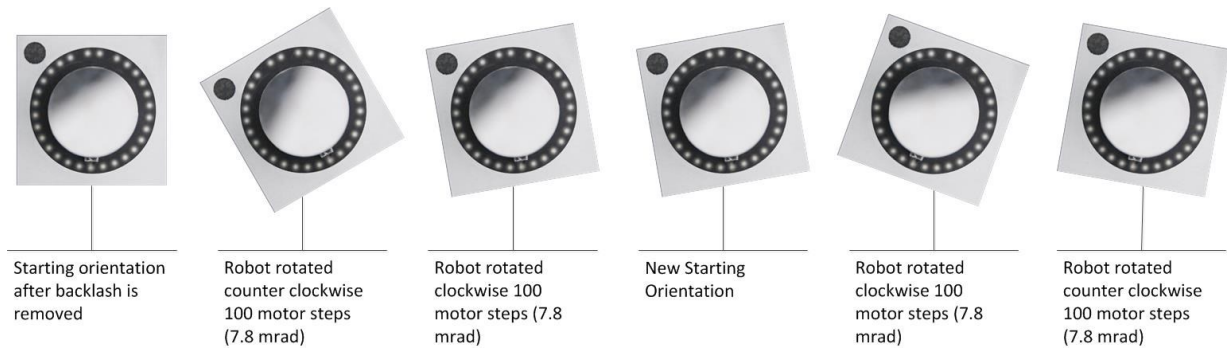


(a) Raw Data

**Figure 4-14: Rotational Slippage 60° Rotations**

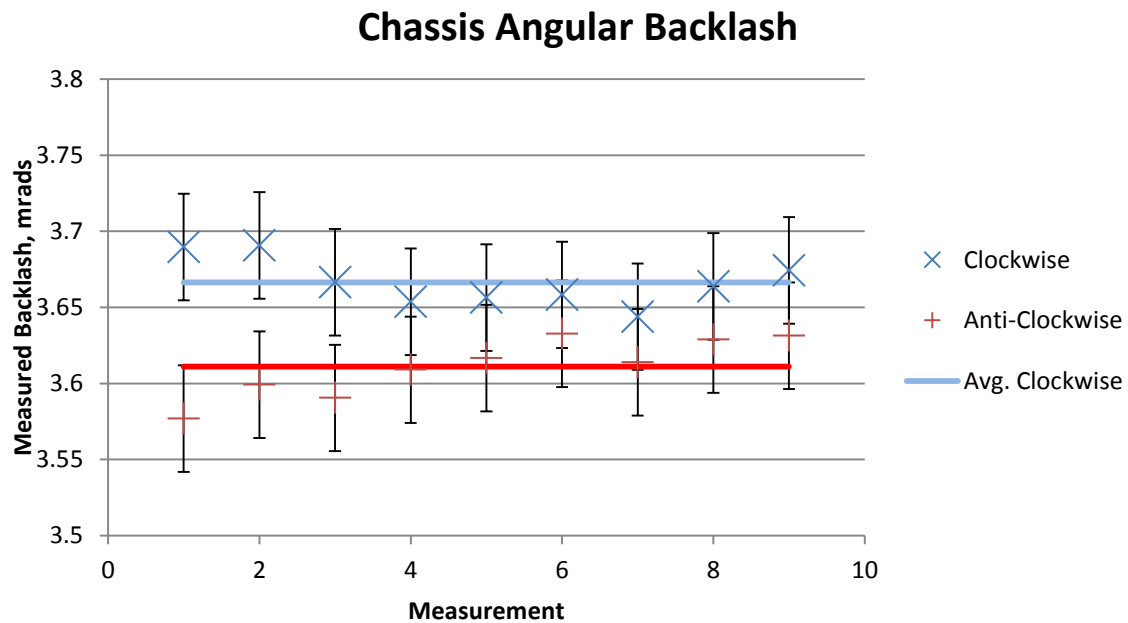
Rotational testing of the robot was also used to determine the backlash inherent to the drive mechanism. The test procedure was completed using 100 motor steps and the Lumenera camera following this process (Figure 4-15):

1. Remove the backlash and measure the robots orientation.
2. Command the robot to rotate 100 motor steps counter-clockwise and measure the new orientation.
3. Rotate the robot 100 motor steps clockwise and measure the robot's orientation. The difference in orientation between the initial and the final value is equivalent to the backlash. The last orientation will be the starting point for the next measurement.
4. The robot is rotated clockwise and the orientation measured. It is then rotated counter-clockwise and the orientation measured. This value with the new starting orientation is used to determine the backlash.
5. Repeat steps 3 and 4 at least 10 times to get a statistical sample.



**Figure 4-15: Chassis Backlash Test Procedure**

Figure 4-16 shows the results of ten measurements; the positive and negative sign convention on the y-axis denotes the robot's rotation direction. The camera's measurement error is in the order of  $35 \mu\text{rad}$ . The measured backlash is approximately  $3.7 \text{ mrad}$  equating to  $46 \pm 7$  motor steps. This needs to be compensated for as it is almost 4 times greater than the required  $1 \text{ mrad}$  resolution. This can be compensated for by analysing the previous command that the robot followed and adjusting the next command accordingly.



**Figure 4-16: Rotational Backlash**

A Heriot Watt student project [69] repeated the test using straight-line motion and determined that the backlash is in the order of  $44 \pm 9$  motor steps. It is clear that the results of both tests correlates well and that the inherent backlash of the robot is equal to that of the motors, which is equivalent to  $\sim 39$  motors steps.

#### 4.6 Actual Performance – Open-Loop Turret Tests

The turret that the POM sits upon was characterised to determine possible x-y position changes, the angle-to-step relationship and the inherent backlash.

The turret was tested using the same test procedure as described in section 4.5. Table 4-5 and Figure 4-17 indicates the expected change in angle for specific motor step commands and the recorded results. The turrets delta angle is almost the same as the robot's coarse rotation as shown in Figure 4-17 and Figure 4-13. This is due to the similar arrangement and ratios between the motors and O-rings. Unlike the robot's coarse rotation, the turret's delta angle deviates slightly between clockwise and anti-clockwise motions. This deviation between the rotation directions was measured to be  $\sim 40 \mu\text{rad}$ , which is insignificant in comparison to the angular accuracy specification of 1 mrad for the application.

Table 4-5: Turret Results

Motor Steps	Theoretical Delta Angle, Radians	Measured Delta Angle, Radians	Difference between Theoretical and Measured Angle, Radians
100	0.008	0.008	0.001
500	0.042	0.040	0.002
1000	0.084	0.082	0.002
5000	0.419	0.400	0.019
10000	0.838	0.807	0.031
25000	2.094	2.020	0.074
50000	4.189	3.976	0.213
75000	6.283	6.010	0.273
100000	8.378	8.033	0.344

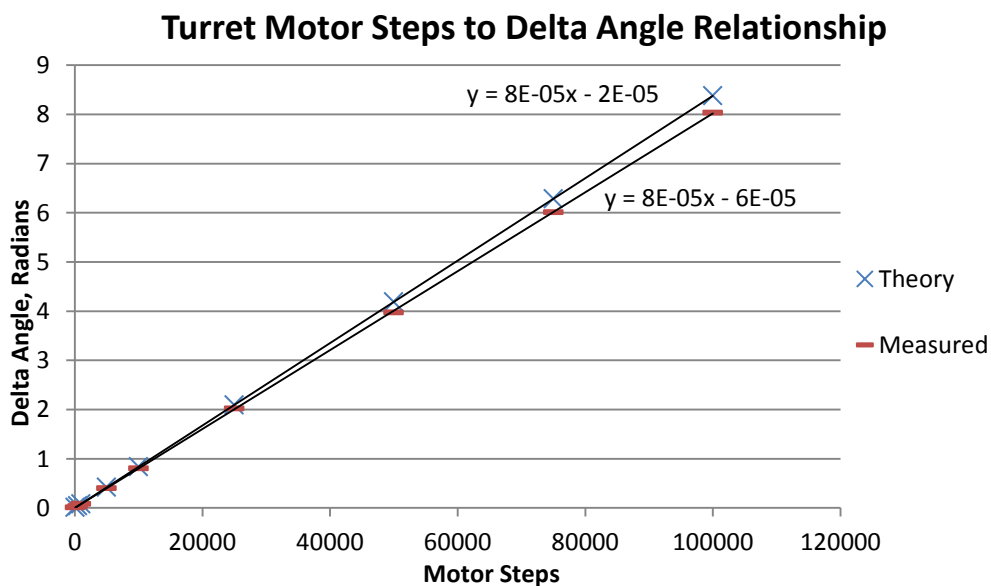
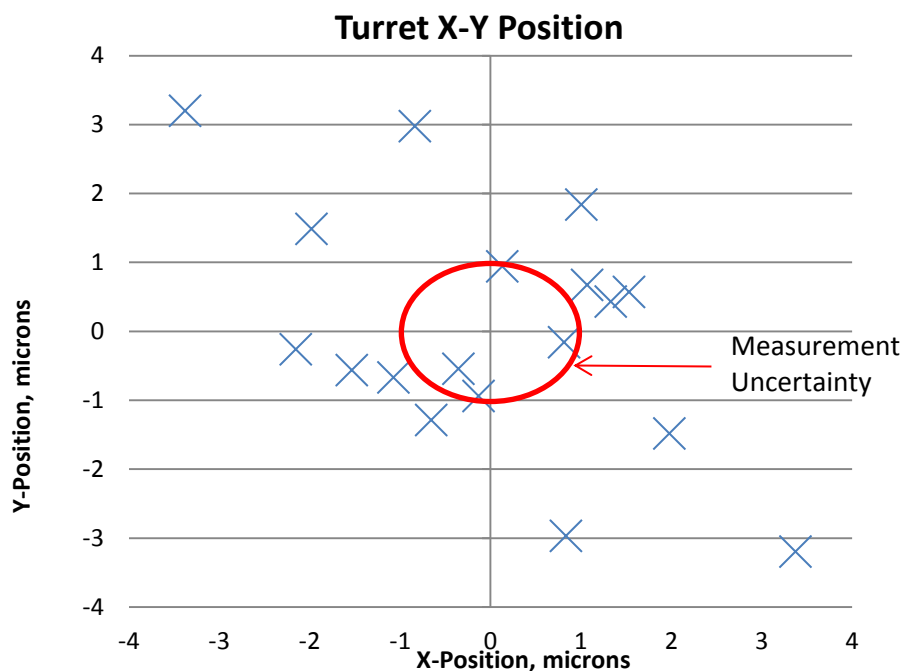


Figure 4-17: Turret Motor Steps to Delta Angle Relationship

Figure 4-18 shows the same test for the turret stage that was conducted on the chassis rotation. The graph shows the change in position relative to the starting point (0, 0) for 10,000 motor steps ( $48^\circ$ ). The rotations are repeated 15 times showing that the x-y position varies within 4 microns. This is due to the assembly tolerances between the POM, bearing and the ABS base. To improve this, higher manufacturing tolerances for the assembly between parts would be required, increasing costs. This is within the positioning repeatability requirement of 10 microns; however it would only be acceptable if the robot was in position to take measurements within 6 microns. This is because the turret would be altered after the robot has moved into the x, y position. This increases the difficulty to achieve requirement on the current robot's chassis design to meet a better than 6 micron positioning requirement. However, the turret has shown that its x, y slippage is better than trying to rotate the chassis.



**Figure 4-18: Turret x-y Position for changes in angle**

To measure the turret's backlash the same procedure was applied as that used to the chassis backlash using 100 motor steps ( $\sim 8.029$  mrad).

After repeat testing it was determined that the backlash was 3.491 mrad, which equates to  $44 \pm 7$  motor steps. This coincides with the backlash values determined from the chassis tests. This is sensible as the motor and the reduction gearing is the primary source of the backlash. The friction drive interaction should be relatively backlash free [70].

## **4.7 Closed Loop System Tests**

A full closed-loop system test concludes the MAPS characterisation. The closed-loop system differs from the open-loop test because it uses the command and control feedback that is a part of MAPS instead of a human operator to drive the robot into position. The objective was to determine if the MAPS system was capable of positioning the robot as required in a multi-object spectrograph instrument. The following subsections details two methods (the dual camera and Faro tracker) to gain a deeper insight of the overall MAPS performance. The difference between the two setups was the equipment used to record information, one utilised two cameras the other a Faro laser beam tracker. The second method utilised the Faro laser beam tracker to independently determine the positional repeatability of the robot and monitor how it moves into position.

### ***4.7.1 Dual Camera Configuration***

Figure 4-19 depicts the test configuration using two cameras allowing for the detection of misalignment that could be due to positional error or robot tipping. Two lasers are used to represent the light from two objects of interest. A fully built robot, as it would be used in a Multi-Object Spectrograph reflects the photons from one of the lasers towards two targets via a beam splitter that separates the light into two directions with an equal amount of flux in each beam. Both targets are set at different predefined distances from the beam splitter. By having one target further away from the beam splitter than the other, tip and rotation of the POM will be emphasised by the camera. The cameras are setup in the same manner as the targets at the second laser, as depicted in Figure 4-19. The resolution of the measurement is dependent on the camera sensors resolution and the distance that the laser has to travel after being reflected from the robot, the greater the distance the higher the resolution.

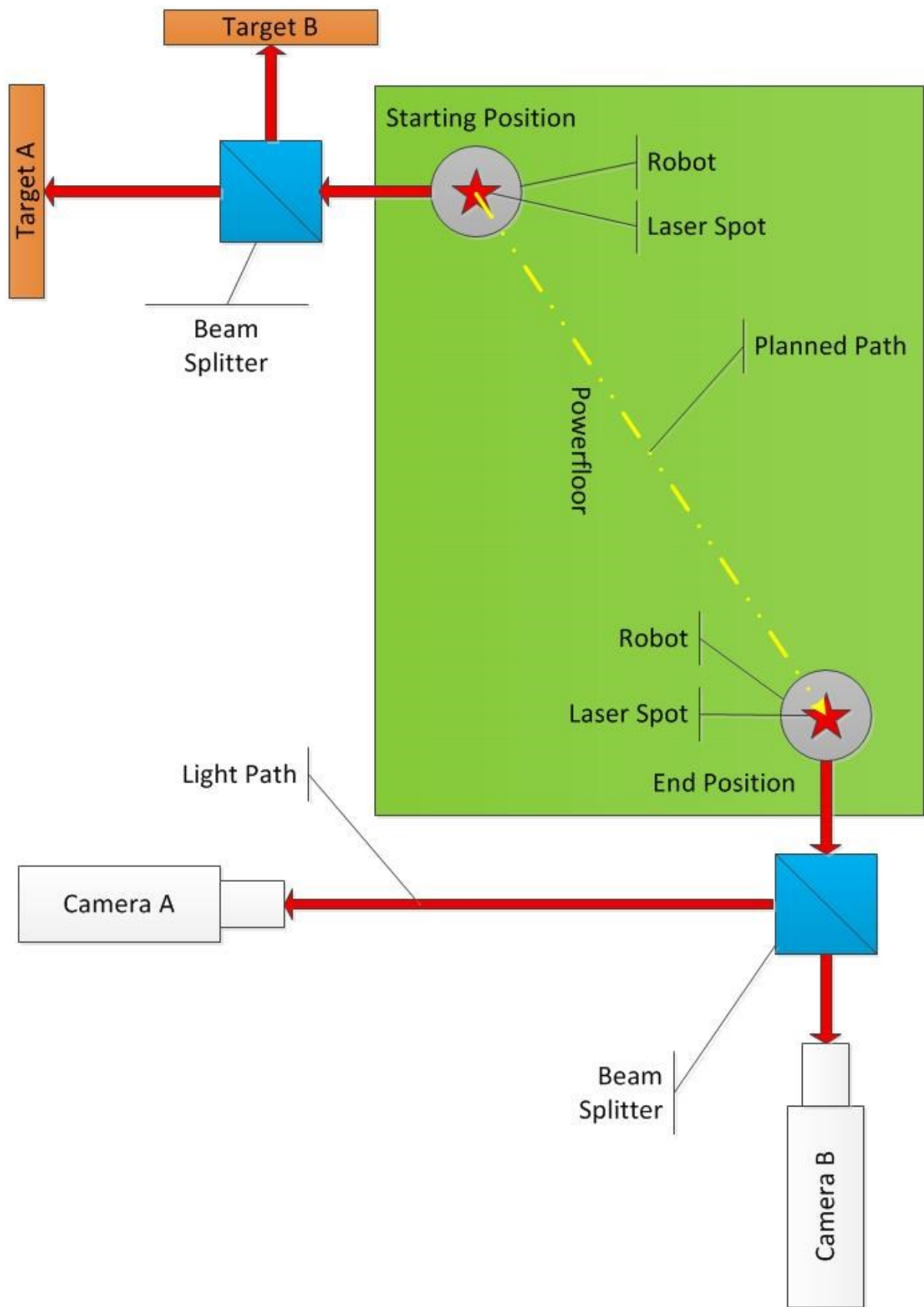


Figure 4-19: Closed Loop Test Setup

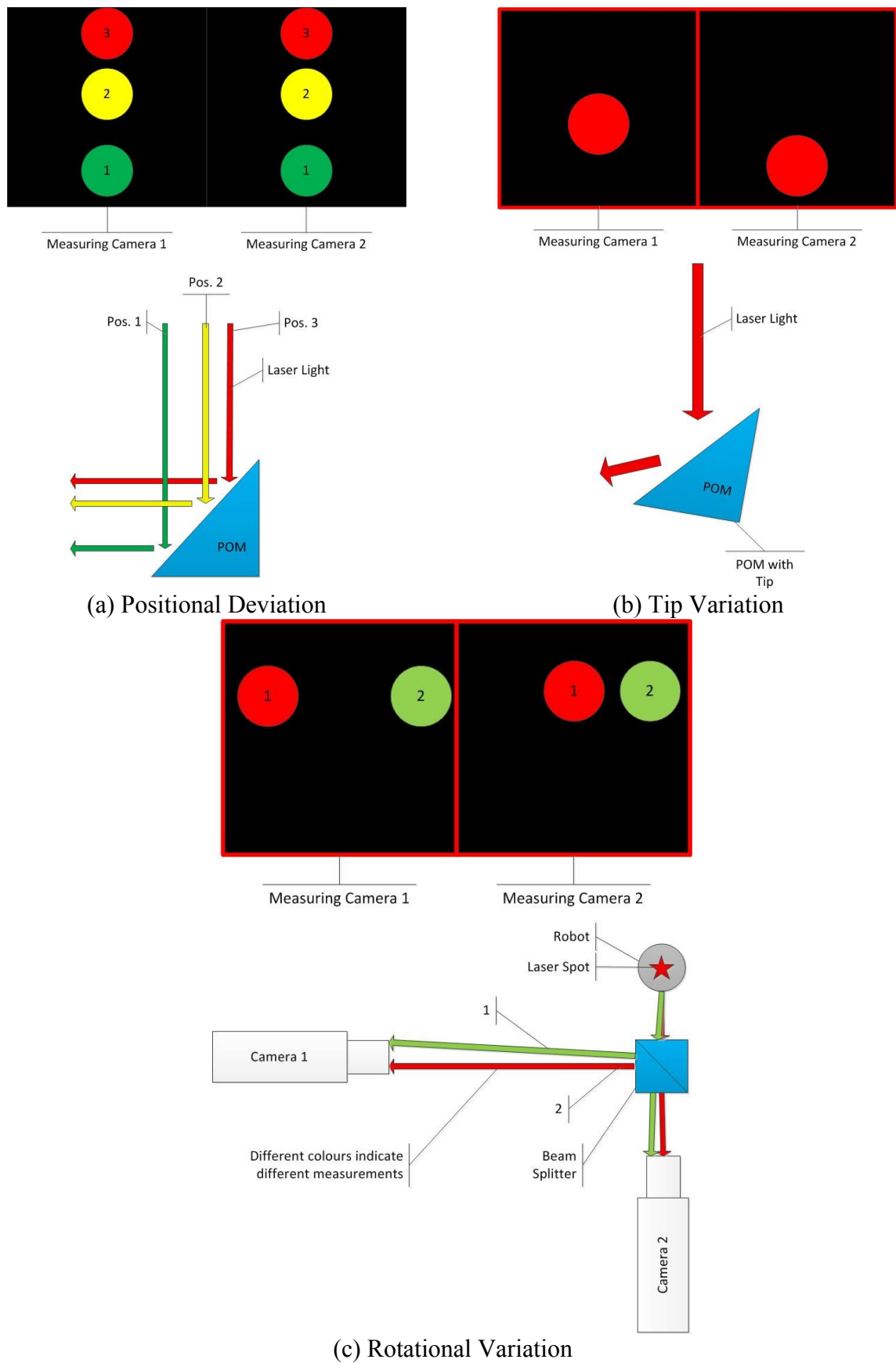
First, the robot is positioned under the laser associated with the cameras and then at the targets. A recording is taken on each measurement target/camera for a reference point. The metrology camera measures the position and orientation of the robot, which is the position that the robot will be commanded to move to. Starting from the targets, the robot drives to the other laser position guided only by the metrology module, i.e. closed loop. Once in position the location is recorded using the metrology module and targets/measurement cameras. The test procedure invoked was:

1. Align robot at the end position – measure the position with the measurement cameras and metrology camera
2. Align robot at the start position – record position with the targets a metrology camera
3. Send the robot to the average position determined from step 1 using the robot's close loop feedback system
4. Measure the final location using the metrology camera and measurement cameras
5. Send robot to the average position determined from step 2 using the robot's close loop feedback system
6. Record the position
7. Repeat steps 2 – 6 collecting a statistical sampling of results

Tests were conducted for both the PowerFloor and a blank PCB to ascertain the robots positioning capabilities on different working surfaces.

Figure 4-20 illustrates the type of results that will be viewed at the cameras and targets. It highlights the robot's errors in position, orientation and if there is tip when moving to a specific position:

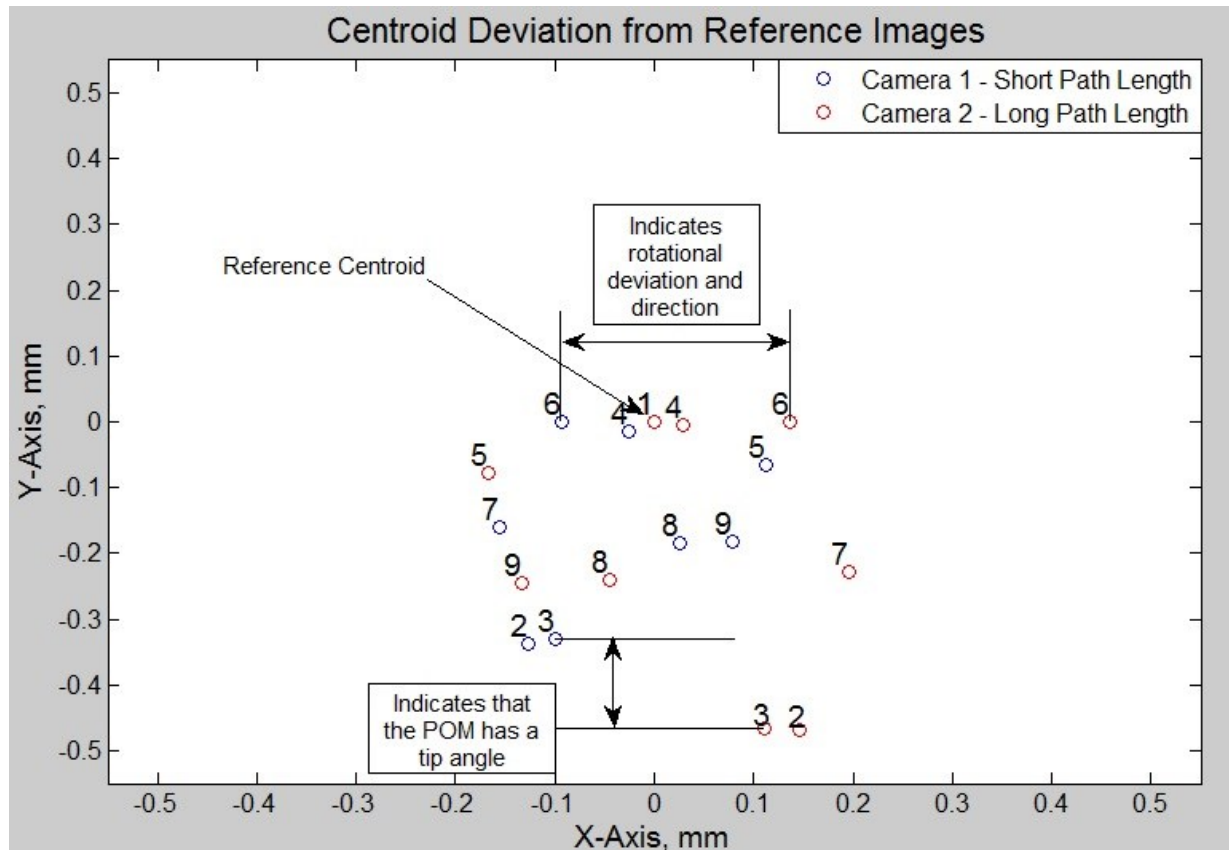
- Positional error can be seen only when the robot was misaligned in the direction towards the beam splitter. This appears as an equal magnitude misalignment on both cameras (Figure 4-20(a)).
- Orientation error is viewed on both cameras as a change on the x-axis. The magnitude is larger on the more distant camera (Figure 4-20(c)).
- Tip error is viewed as a change on the y-axis by varying amounts between both cameras with the camera that is further away showing a larger change in position (Figure 4-20(b)).



**Figure 4-20: Beam Spot Description**



Figure 4-21 shows the output from both of the sensors overlaid onto the same scale from a single test using the dual camera setup. This image is representative of where the laser influences the measurement cameras sensor and not the scale of misalignment. A centroiding program was used to determine where the laser spots were on the sensors giving a measurement error of  $\pm 12 \mu\text{rad}$ . Object '1' within Figure 4-21 indicates the reference centroid that ideally if MAPS were operating perfectly it would always return to. All other numbered objects are the offset of the measured centroids from both cameras.



**Figure 4-21: Normalised Image of Centroid Measurements on PowerFloor Surface**

Trigonometry determines the rotational misalignment of the robot to its target position with the delta x-axis from the reference image and the distance to the measurement camera. Table 4-6 shows an example of the results obtained. The table shows eight measurements from a single test, showing that the metrological cameras deviation for the robots angle to be greater than what was being measured by the measurement cameras. The results are within 1.7 mrad, which is within the precision setting applied for the tests. The angular results are promising with potential to meet the requirements.

**Table 4-6: Angular Robot Misalignment**

Run	Measured Angular Misalignment, Degrees	Metrology Camera Measured Angular Misalignment, Degrees	Deviation between Measured Misalignment and Metrology Camera, Degrees
1	0.01	0.09	0.08
2	0.01	0.06	0.05
3	0.00	-0.01	-0.01
4	0.02	-0.09	-0.07
5	0.01	0.03	0.02
6	0.02	0.07	0.05
7	0.00	-0.04	-0.04
8	0.01	-0.06	-0.05

The PowerFloor includes a 0.1 mm bump at each track due to the insulation layer. The other side of the PowerFloor is a smooth surface consisting entirely of an insulation layer. It was necessary to determine if the PowerFloor's bumps would affect the robot's positioning therefore decided to repeat the test using the smoother underside of the board. Table 4-7 summarises the average tip angle and the standard deviations from the measurements. The results show little variation between both sides of the PowerFloor. The high standard deviation on the majority of the results indicates a high variation around the mean for each test. The variation of position by the robot had negligible effect on the tip angle.

**Table 4-7: Measured Tip Angles**

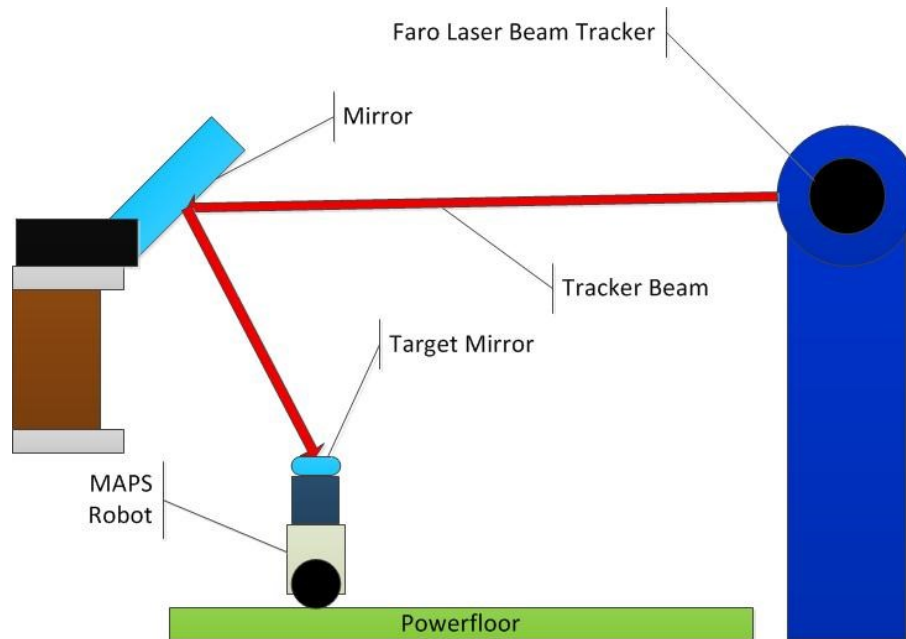
Test	Avg. Tip Angle for PowerFloor, Degrees	Standard Deviation for PowerFloor, Degrees	Avg. Tip Angle for Smooth Surface, Degrees	Standard Deviation for Smooth Surface, Degrees
1	-0.042	0.021	-0.015	0.019
2	0.003	0.003	-0.018	0.014
3	0.002	0.006	0.003	0.012

These results show that the PowerFloor does not affect the positional performance of MA-BOT2 any differently to that of it operating on a smooth floor. The variation in tip is the same regardless of the operating surface.

#### **4.7.2 Faro Laser Tracker Setup**

The Faro tracker test procedure and setup is the same as the dual camera experiment (section 4.7.1) excluding the measurement cameras and targets. This test was not done on the smooth surface as the dual camera test showed negligible difference between the PowerFloor and smooth surface. Positioning was monitored using the Faro tracker to independently determine the positional repeatability and gain a greater insight into the x-y positioning capabilities of the robot. To accommodate the target mirror a plastic mount was attached to the top of the robot

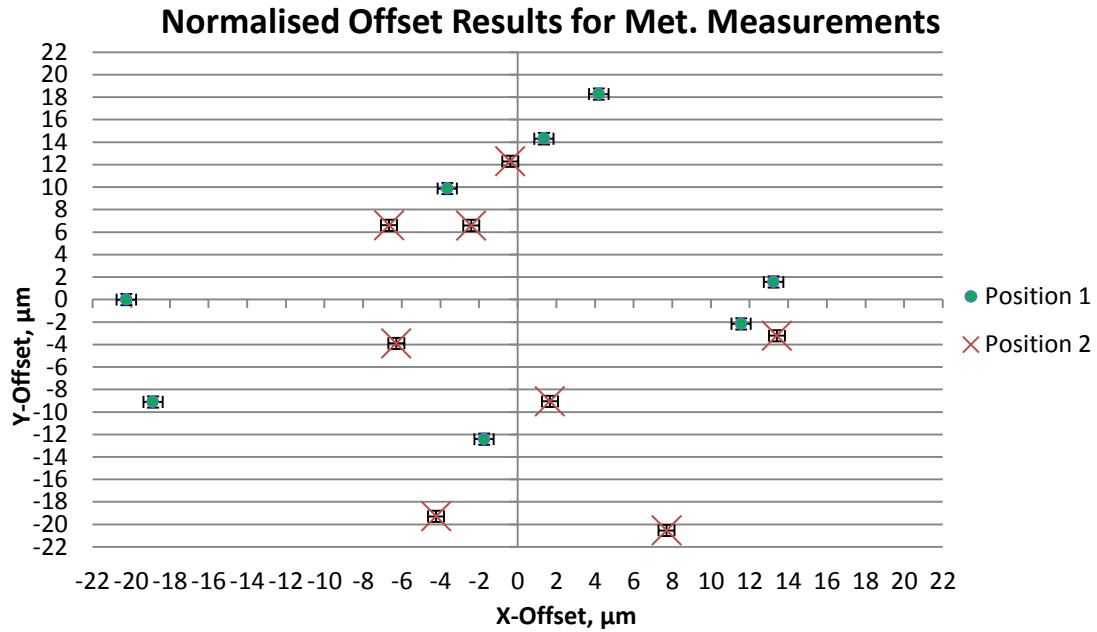
replacing the POM. Due to the 19.2 mm diameter of the target mirror it had to be attached facing vertically, otherwise some of the spots on the metrology target would be hidden from view. To maintain line of sight between the robot and the Faro, an optically flat ( $\lambda/10$ ) reference mirror reflected the Faro beam towards the robot to maintain line of sight, Figure 4-22. The Faro was set to take continuous measurements.



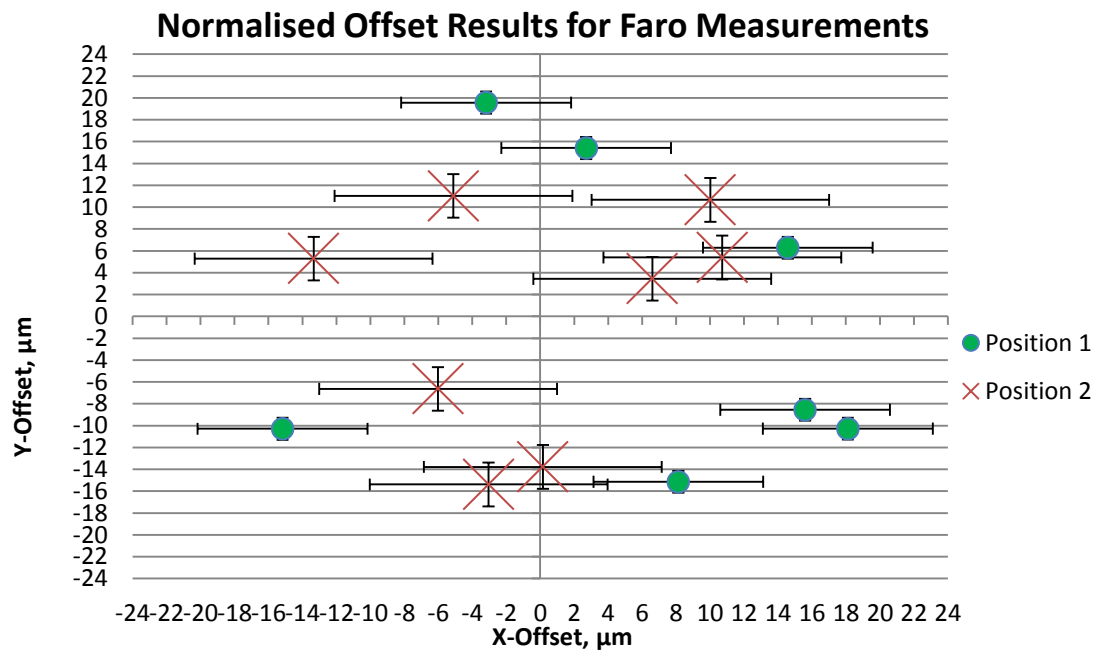
**Figure 4-22: Faro Tracker Alignment**

Figure 4-23(a) shows the normalised offset between the x-y reference position and the measured position of the robot on the PowerFloor. Each measured position is the average of ten measurements taken with the metrology camera. The markers are representative of the laser positions that the robot was commanded to reach. It is clear that for both positions at either end of the PowerFloor, within the camera's field of view, the robot would reach its position within a sphere of  $22 \pm 3 \mu\text{m}$ . As the metrology software was set to reach the position to an accuracy  $\leq 24 \mu\text{m}$  this was an expected outcome. However, it takes the metrology module between 10 to 20 attempts to position the robot within this accuracy. This could suggest that the robot is finding its position randomly.

The Faro laser tracker confirms this repeatability, Figure 4-23(b), as an external independent measuring source. This extrapolates 3D coordinates based on the time it takes its internal laser to reflect from a target back to itself and reading this against two rotational encoders. Note that the reference coordinates and measurement error of both devices are not the same because they are different measuring techniques.



(a) Metrology Camera Measurements



(b) Faro Laser Tracker Measurements

**Figure 4-23: Robot Offset from Commanded Position for red & green laser positions**

As a further confirmation that the results measured by both devices coincide, the resultant distance between the lasers for each test run was calculated and compared, Table 4-8. The repeatability is determined by taking the standard deviation for eight runs by the robot towards each laser. The deviation between the measurements of both systems was less than  $5 \mu\text{m}$  that is within the measurement error of the Faro ( $\leq 7 \mu\text{m}$ ). The results indicate that MAPS can potentially reach a position on the PowerFloor to within  $17 \mu\text{m}$ .

**Table 4-8: MAPS Robot Closed Loop Repeatability**

Test Post Reassembly		1	2	3	4	Average Standard Deviation
Red Laser Repeatability, $\mu\text{m}$	Metrology Camera	19.3	17.2	16.0	8.3	15.9
	Faro Tracker	16.5	22.0	18.5	5.0	15.1
Green Laser Repeatability, $\mu\text{m}$	Metrology Camera	21.3	20.7	17.0	4.5	15.2
	Faro Tracker	20.9	18.7	23.8	5.9	16.2
Combined Repeatability of both Positions, $\mu\text{m}$	Metrology Camera	20.6	18.3	16.0	7.1	15.5
	Faro Tracker	18.4	19.7	20.6	8.2	16.7
Difference between Metrology Camera & Faro Repeatability, $\mu\text{m}$		2.2	-1.4	-4.6	-1.1	-1.2

#### 4.8 Conclusions

MA-BOT2 does not fully meet the MOS instruments requirements for the x-y fine positioning of  $\leq 10 \mu\text{m}$ . The robot however was able to repeatedly move to a position to within 24 microns as dictated by the control interface. The overall optical error budget from the focal plane to the detector is  $\leq 35 \mu\text{m}$  which includes all the optical components in the optical train to the detector. Theoretically, if all components are perfectly aligned then the MAPS robot would have the  $35 \mu\text{m}$  to position itself. This suggests that if the other components can be positioned to within a higher tolerance for an acceptable cost then the positioning requirements of the robot can be relaxed. However it would still be preferable to further refine the robot and improve its positional performance. Table 4-9 is a summary of the actual, expected and required performance of MA-BOT2.

**Table 4-9: Summary of MABOT2**

<i>Parameter</i>	<i>Requirement</i>	<i>Performance</i>	
		<i>Expected</i>	<i>Actual</i>
X – Y Positioning Accuracy	$\leq 10 \mu\text{m}$	1 $\mu\text{m}$	$\leq 24 \mu\text{m}$
Z – Axis Angular Resolution	$\leq 1 \text{ mrad}$	84 $\mu\text{rad}$	79 $\mu\text{rad}$
Operation Time	$\geq 8$ hours per night	Continuous	Continuous
Footprint	$\leq 30 \text{ mm} \times 30 \text{ mm}$	30 mm x 30 mm	30 mm x 30 mm
Height	$\leq 60 \text{ mm}$	60 mm	50 mm
Communication Range	$\geq 4 \text{ m}$	$> 4 \text{ m}$	$> 4 \text{ m}$

The MAPS research clearly indicates that pick-off components can be positioned to a high precision using electromagnetically propelled miniature autonomous robots and has the

potential to be a viable alternative to current positioning systems. This also shows that electromagnetic autonomous robots can be a substitute for piezo driven robots for high precision applications that requires the robots to reach a location to within tens of microns. This provides the advantages of cheap low voltage electronics and no tether limiting the robots travel that is a common issue with piezo robots. Currently, MAPS technology readiness level can be categorised as level 4, “Technology Development”. Further research and technical development is required to bring the prototypes up to level 9 where they can then be deployed on MOS instruments. This will require improving the angular shift that has been seen with the linear motion tests. The assembly process needs to be automated to improve assembly tolerances such as wheel alignment on the dowels. A “rolling road” test could be developed to analyse the performance of each of the wheels independently to indicate if one motor is driving the robot further than the other or if one motor is beginning motion noticeably sooner than the other.

Table 4-10 compares the hardware cost for 25 MAPS robots against 25 KMOS arms. A cost analysis between 25 robots and arms was chosen because currently the Very Large Telescope is using 25 KMOS arms. To build 25 MAPS robots it will cost almost 2 percent of the cost to build 25 KMOS arms. This demonstrates that MAPS is cheaper than another POM positioning system. The KMOS arms cost more because they were designed to operate in cryogenic temperatures and include more optical components for the correction of the light’s path length. The MAPS robots are not required to operate at those temperatures or to correct the optical path length; this functionality is implemented by the MOS instrument further down the optical train.

**Table 4-10: Cost Comparison**

<b>Hardware</b>	<b>MAPS (£)</b>	<b>KMOS (£)</b>
Motors including drivers	5,000	254,000
Electronics	1,250	199,000
Mechanical Components	7750	215,000
Assembly	5,000	338,000
Total Cost	19,000	1,006,000

This use of miniature mechatronics has led to an investigation into expanding the pick-off mirror’s functionality with additional degrees of freedom and the capability to counter the tip of the POM. Chapters 5 and 6 presents the design, build and characterisation of a self-adjusting mirror that can be used for correcting optical misalignments associated with the non-telecentric and non-concentric optical properties of a typical large instruments focal plane.

## Chapter 5 - Self Adjusting Mirror

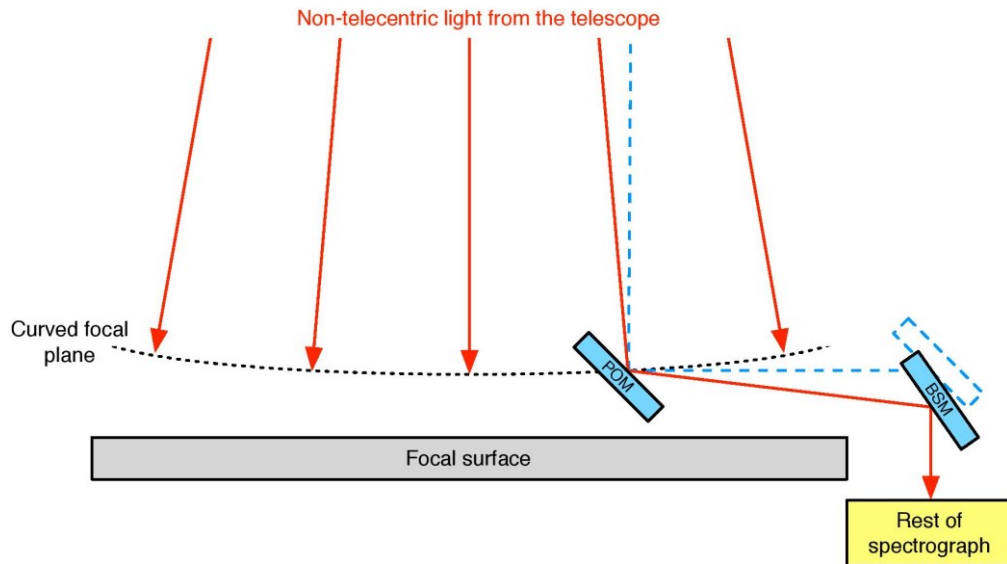
MAPS demonstrated the potential to use miniature robotics for the placement of POMs where these mirrors can be used to pick-off astronomical targets for spectral analysis. To further reduce the size of MOS instruments the possibility of adding extra functionality to that of the Pick-Off-Mirror was investigated. It is useful to reduce the overall size of the pick-off system especially at focal stations with limited back focal lengths, as there is limited room for compensation optics. The majority of telescopes deliver curved optical focal planes to the focal stations. Currently beam steering mirrors (BSMs) are used to align the light beam reflected from the pick-off mirror with the centre of the beam steering mirror. Due to the curved focal plane the BSM requires a third degree of freedom, in a direction perpendicular to the focal plate (which is flat) to compensate for changes in the beam's angle across the field, as reflected from the pick-off mirror. For the E-ELT MOS instrument the travel range required by the beam steering mirror is 33.5 mm, and it is more difficult to achieve the positional accuracy and stability. More importantly the space available for the complete pick-off system is also very limited. By incorporating this functionality in the pick-off mirror, the instrument can be optimised in terms of both the accuracy and stability. This investigation resulted in the development, build and characterisation of a self-adjusting mirror (SAM). The design work was carried out during a six-month placement at CSEM in Switzerland, while the build and characterisation work was completed at the UK ATC.

This chapter lists the application requirements for the self-adjusting mirror. These requirements drive the overall system design. A review on the current state-of-the-art tip/tilt mirrors shows that it will be possible to use current MAPS technology to build miniature SAMs for use in astronomy. Various implementations follow with a summary of the trade-off analysis discussing the SAM design chosen for further investigation. The chapter concludes with the initial design ideas for the self-adjusting mirror. The nomenclature for SAM are defined in the coordinate system definition unless otherwise stated.

### 5.1 The Reason for SAM

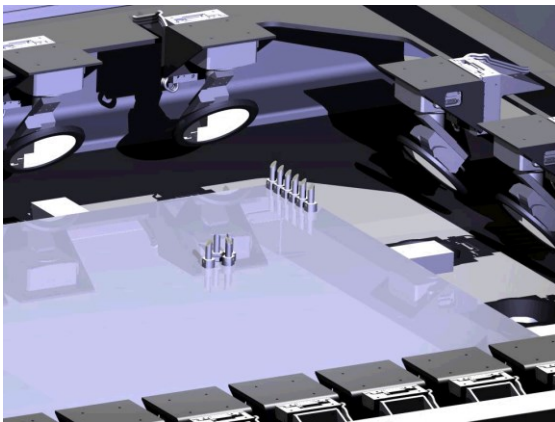
Most astronomical instruments gather light at the focal planes of telescopes – i.e. the region where light is brought to a focus and an image is formed. In an ideal system the focal plane should be completely flat. However for large instruments such as EAGLE this is not possible and the focal plane has a curvature equivalent to  $\sim 50$  m radius due to the telescope's optics. As

discussed previously, pick off components such as POMs collect the photons from objects of interest and guide this light towards the next set of corrective optics before entering a spectrograph. However, since the focal plane is curved when the light is collected at the POM, its reflection deviates away from the optical axis as shown in Figure 5-1.

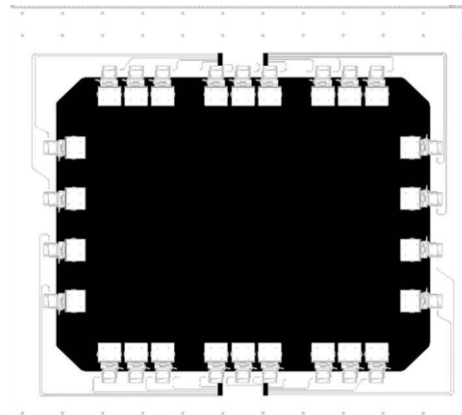


**Figure 5-1: Optical Misalignment Description [32]**

In the current EAGLE design beam steering mirrors (BSMs) ensure that the optical axis between the pick-off mirror and the rest of the optical train is aligned. BSMs are located around the perimeter of the focal plane (Figure 5-2(a)). Each BSM implements three degrees of freedom: a rotational, linear and tip stage as illustrated in Figure 5-2(b).



(a)





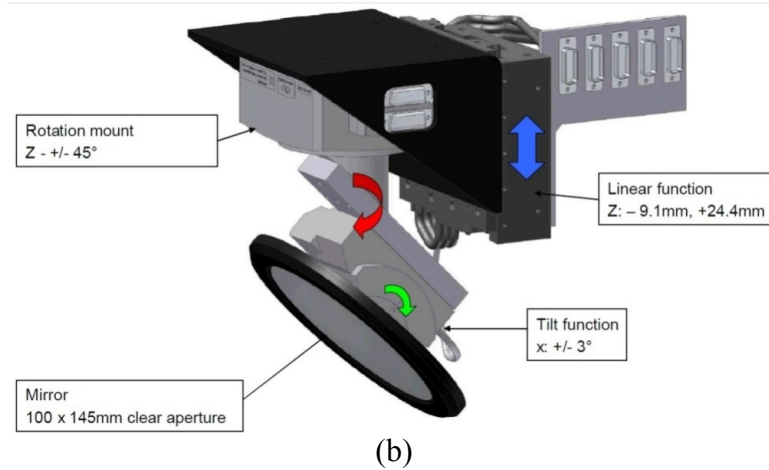


Figure 5-2: (a) BSM arrangement around the focal plane, (b) BSM Design [57]

Figure 5-2 shows that the BSM is quite large with a volume of  $\sim 2008156 \text{ mm}^3$  and weighting in the order of 5.9 kg [71]. As there are 26 beam steering mirrors bulky support structures are needed to hold them in place. It is proposed that by moving some BSM functionality to the POM will simplify the supporting structure as it can reduce the weight (each BSM would be 3.3 kg lighter), reducing the overall weight of the MOS instrument. This can be achieved by removing the tilt and linear function from the beam steering mirror and adding a rotation and tip function to the pick-off mirror. Tip and tilt is corrected by combining the tip and rotation functionality of the POM with the rotation functionality of the BSM. Figure 5-3 shows the simplified BSM.



Figure 5-3: Simplified BSM

## 5.2 Current Miniature Self Adjustable Mirrors

Listed in Table 5-1 are currently commercial-of-the-shelf available mirrors. Research findings concluded that multi degrees of freedom adjustable mirrors within a small footprint ( $\leq 50 \text{ mm}^2$ )

are currently not available. Mostly these mirrors only incorporate a single degree of freedom. Therefore implying that multiple stages will have to be integrated together to provide all the functions required. This will result in a unit that will be far too large. There are commercially available examples of single-axis adjustable mirrors (galvanometers) that are used within laser systems.

**Table 5-1: Summary of Adjustable Mirrors**

<b>Mirror</b>	<b>Application</b>	<b>Dimensions (mm)</b>	<b>Minimum Step Size (<math>\mu</math>rad)</b>	<b>Range (rad)</b>	<b>Drive Method</b>
PI S-334 [72] [73] [74]	Commercially available tip/tilt mirror	33 x 38 + 50 x 30 x 14	5 $\mu$ rad	0.1 rad	Piezoelectric
Single Axis GMS [75]	Laser imaging & etching; Confocal Microscopy – Commercially Available	86.4 x 47.1	69.8 $\mu$ rad	0.28 rad	Information not available
DynAXIS T [76]	Laser Deflection – Commercially Available	Ø16.5 x 45 (Without Mirror) 8.5 Mirror Aperture	Information not available	$\pm$ 0.21 rad	Magnetic Inertia Drive
8300K [77]	Commercial Scanning Technologies	Ø9.5 x 29.1 (Without Mirror) 7 Mirror Aperture	8 $\mu$ rad	0.7 rad	DC Motor
MEMS Micromirror [78]	Commercial Product	7.26 Packaging Ø4.2 mirror	8.73 $\mu$ rad	$\pm$ 0.1 rad	Electrostatic Actuator
(TTP)-DM	Commercial Product	9.3 Mirror Aperture (331 Hexagonal Segments)	Information not available	$\pm$ 0.006 rad	Electrostatic

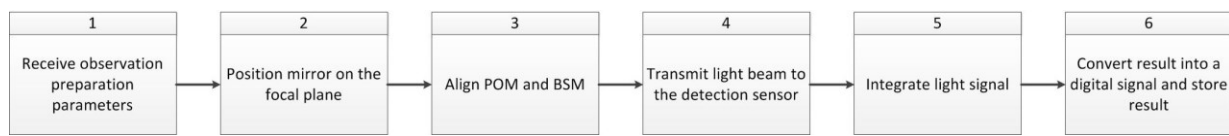
From the review, galvanometers were identified as being the most suitable product available. These products are capable of small enough step sizes and reasonably large travel ranges. However these devices are limited in the number of degrees of freedom provided, while the volume envelopes are also much larger than the desired mirror footprint.

There are small (with an aperture in the order of 10 mm) MEMS mirrors that can be controlled precisely. These MEMS mirrors use electrostatic actuation which requires high driving voltages and therefore the driving electronics would be larger than the volume of the POM. It would require the electronics to be off-board with a tether to the mirror. This is unsuitable for the same reason as it is unsuitable to tether the robots positioning the mirrors.

The findings clearly indicate a current lack of availability of small fully self-contained mirrors that support multiple adjustable degrees of freedom within the required footprint to perform the high precision tasks required. SAM will have the potential to fill this gap in the market.

### 5.3 System Design

Based on the overall system architecture design the requirements for the self-adjusting mirror were derived. To derive the requirements it is important to identify all the functions required to implement the observation strategy to perform the science.



**Figure 5-4: Top-Level Function Diagram**

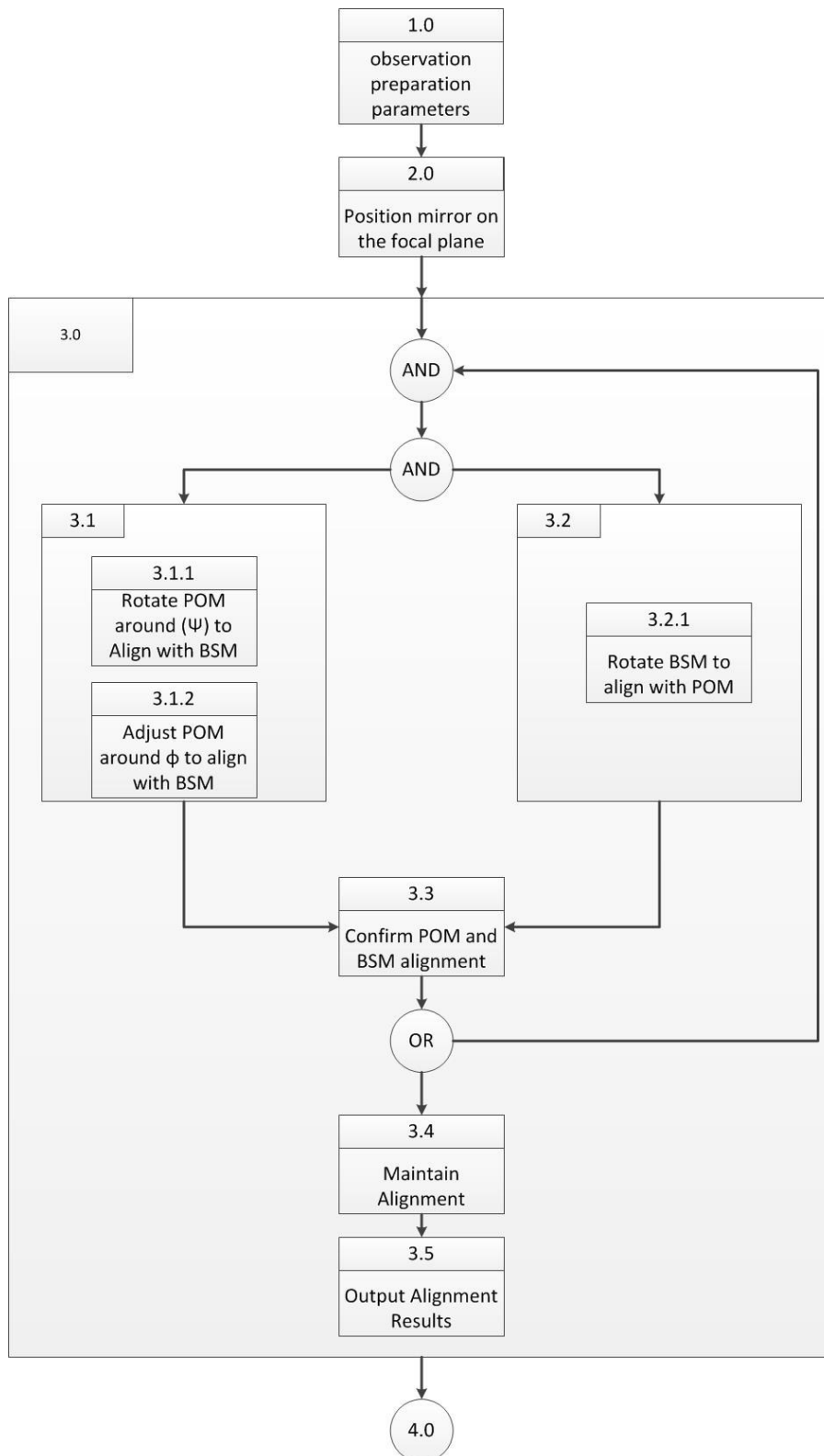
Defined in Figure 5-4 is an overview of the functions required to implement a typical observation strategy. This thesis focusses on functions 2 and 3. The method of positioning the POMs were described in the previous chapters, the rest of this thesis is dedicated to solving the problem of alignment between the POM and the BSM. The locations of objects on sky to be studied are used to calculate the position where the POMs have to be placed on the focal plane. Once in position the POMs are aligned with its associated BSMs (for each observation, the path analysis determines the pairings of POMs and BSMs). This alignment needs to be maintained for the duration of the observation. The alignment needs to be maintained so that the light from the source object is received at the same part of the detector throughout the exposure otherwise the signal would be lost to noise. The BSM directs the light received from the POM to the next component in the optical chain of the instrument (function 4). This determines the tolerable drift over an observation period.

The primary function of the self-adjusting mirror is to align the beam reflected from the POM with the centre of the BSM. This alignment must be maintained throughout an observation.

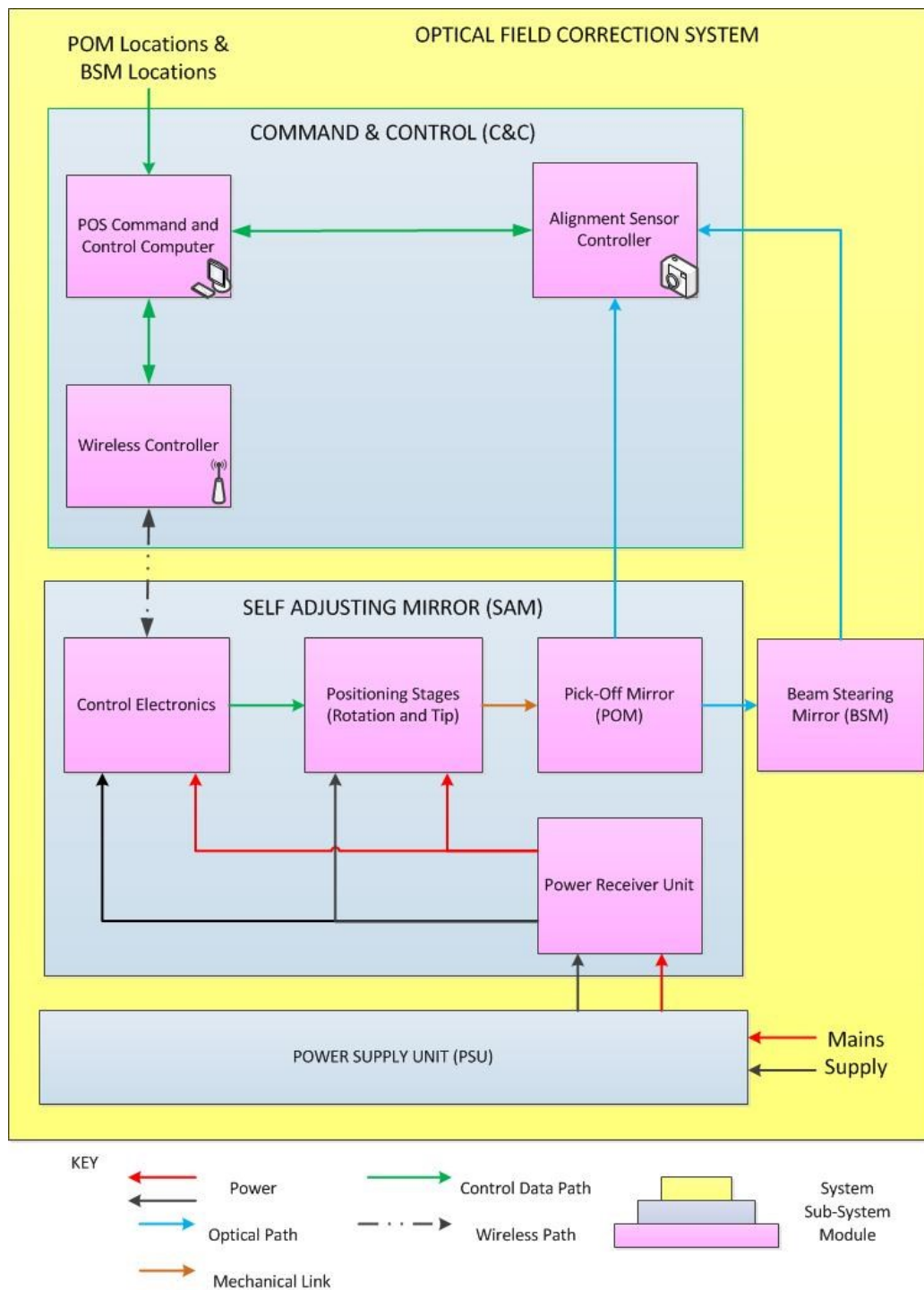
Alignment is achieved through the rotation of both the POM and BSM around the  $\psi$ -axis followed by the pick-off mirror adjusting its angle (around the x-axis) of incidence.

Function 3.0 is where the self-adjusting mirror technology would be used. Figure 5-5 breaks function 3.0 down further. Once the self-adjusting mirrors are put into place on the focal plane the POM will be rotated around the z- and x – axes to face the BSM. At the same time the BSM is rotated around the z-axis to the POM. Once the BSM and POM are adjusted the system confirms that both technologies are aligned. This is done externally to SAM and is out with the scope of this thesis work. If they are not aligned the process of adjusting both the BSM and POM is repeated until alignment has been achieved. Once achieved alignment is maintained and monitored throughout a telescope’s observation period. The light being collected by the POM is transmitted to the BSM and then towards the sensor where the light is integrated over a large exposure duration. The integration of multiple images is required because the objects being studied are extremely faint. Therefore, it is important that the photons from the object of interest align to the same part of the detector for the entirety of the observation. This is why the alignment of the POM with the BSM is extremely important and must be maintained throughout the observation. The results gathered are converted to a digital signal and stored for analysis by astronomers.

The POM and BSM will return to a “start” position when an observation ends. The shutdown procedure is the reverse of the observation procedures listed earlier. Based on the functions that the self-adjusting mirror has to execute a design was developed. The system architecture derived is depicted in Figure 5-6. The self-adjusting mirror design builds on the micro autonomous positioning system, utilising a number of the existing building blocks, namely the command and control module with the exception of the alignment sensor, mirror and power delivery concept. The resulting system architecture is very similar to that of MAPS as can be seen in Figure 5-6.



**Figure 5-5: POM/BSM Configuration Functional Flow Diagram**



**Figure 5-6: SAM System Design Overview**

Once SAM is in position the PowerFloor, will work well because the problems experienced with the MAPS power delivery were all related to the robot having to move across the tracks. Therefore it can be concluded that for the purpose of evaluating SAM the PowerFloor will be adequate.

By implementing the functions listed in Figure 5-4 and Figure 5-5, the SAM requirements were derived and these are summarised in Table 5-2. Both the goal and the desired requirements are captured in Table 5-2. The ‘goal’ specifications define the minimum requirements that must be met for the application.

**Table 5-2: SAM Requirements**

Requirement	Sub-Requirement		Specification		Comment
			Goal	Desired	
<b>Φ Tip Module</b>	Resolution		≤ 0.9 mrad	≤ 0.2 mrad	Step increments for the Φ rotation.
	Range		-17.5 mrad to 34.9 mrad	± 69.8 mrad	± denotes the max/min travel range. The mirror is expected to travel to angles within these values.
	Tolerable Drift		≤ 0.113 mrad/hr	≤ 25 μrad/hr	Based on an 8 hour observation
<b>Ψ Rotation Module</b>	Resolution		≤ 1 mrad	≤ 25 μrad	Defined by BSM and POM requirements
	Range		± 3.142 rad	≥ 6.283 rad	Bi-directional would be acceptable.
	Tolerable Drift		≤ 0.125 mrad/hr	≤ 3.125 μrad/hr	Based on an 8 hour observation
<b>General</b>	Dimensions		≤ 40 mm x 40 mm x 80 mm	≤ 20 mm x 20 mm x 50 mm	Footprint is based on the current POM
	Design Type		Modular		To allow interfacing with different POS
	Power		≥ 8 hours		PowerFloor used due to its ready development from MAPS
	Stability	Period	≥ 8 hours		Operation time is based on a single night’s operation. The drift is based on linear z allowances of the BSM
	Control		Wired	Wireless	Mirror is operating in an environment not desirable for interaction with people.
			≥ 2 m	≥ 10 m	
	Operating Plane		Horizontal & Vertical ± 90°		Operating plane will vary

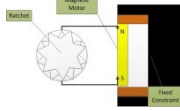
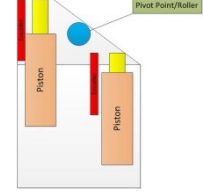
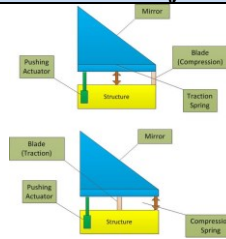
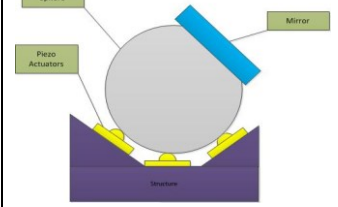
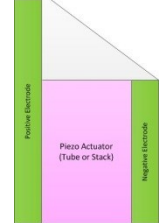
The tip and rotation range requirements were determined based on the geometry of a MOS instruments focal plane like EAGLE. It is assumed that the BSM is aligned with the optical axis of the focal plane when the MOS instrument is built. The tip module's travel range depends on the radius of the optical field curvature and Snell's law. The angle at which the light reflects from a 45 degree mirror will deviate from the optical axis dependent on where the POM is positioned on the focal plane. The tip module is altered around the x-axis to bring the optical path back into alignment with the optical axis. The resolution is based on the minimum change required as the objects being studied would move across the sky during an observation. The dimensions of SAM are based on the POMs footprint requirements. The POMs need to be able to be placed next to one another with a minimum separation distance of 40 mm from centre-centre. This means that SAM cannot have a footprint greater than 40 mm<sup>2</sup>. Power and stability need to last for longer than an observation period which is 8 hours per night. SAM can be controlled either through wires or wireless. It is more desirable to be wireless as this simplifies the placement of POMs as it removes trailing wires. The wireless communication needs to be capable of sending and receiving information from POMs that can be located anywhere on the focal plane which is 2 m long. Therefore, the communication range needs to be greater than at least 2 metres. Each module's tolerable drift has to be less than the resolution of the stage over the 8 hour observation period. This keeps the signal on the same part of the detector throughout an entire observation.

#### **5.4 Potential Concepts**

Various ideas were considered and are based on mechanism designs described in, Table 5-3. In Table 5-3 each possible solution together with the advantages and disadvantages are described. In addition a numerical trade-off method was used to select the most promising concept for evaluation. This involved defining the key criteria that would influence the design and application of the solution. Each criteria was proportioned a weight factor based on its importance. The concepts were judged against each criterion by calculating a rating.



**Table 5-3: Summary of Classical Mechanical Methods**

	<b>Ratchet Mechanism</b>	<b>Piston Actuated</b>	<b>Full POM Adjustment</b>	<b>NanoPositioner Int.</b>	<b>Piezo tube</b>
					
<b>Operating Principle</b>	Ratchet mechanism locks mirror at specific angles. Lever is released and the disc rotates freely, lever comes down locking the mirror at an angle [79]	Pistons push the back of the mirror causing rotation around a central point [79]	Actuator pushes base of POM so mirror rotates at the base. Blade and spring added to guide and control the POM [79]	Mirror is attached to a sphere that sits on three or six piezo legs. These actuators walk on the sphere causing it to change orientation [80]	A piezo tube with a 45° cut has a mirror adhered to it. Electrodes within the tube deform the material to meet required angles [81]
<b>Advantages</b>	<ul style="list-style-type: none"> <li>• Locks the mirror into an angle</li> <li>• Simple concept does not necessarily require an accurate motor</li> </ul>	<ul style="list-style-type: none"> <li>• Simple design</li> <li>• Can possibly be created using a single piston</li> </ul>	<ul style="list-style-type: none"> <li>• Provides more space for actuators</li> </ul>	<ul style="list-style-type: none"> <li>• Nanometre resolution possible</li> <li>• Compact</li> <li>• Mechanically simple</li> </ul>	<ul style="list-style-type: none"> <li>• Compact</li> <li>• Mechanically Simple</li> <li>• High precision</li> </ul>
<b>Disadvantages</b>	<ul style="list-style-type: none"> <li>• Resolution requirements dictate number of teeth required.</li> </ul>	<ul style="list-style-type: none"> <li>• Assembly difficulties for more than one motor due to the space available</li> </ul>	<ul style="list-style-type: none"> <li>• Increases the height of the overall POM</li> </ul>	<ul style="list-style-type: none"> <li>• Need to manufacture actuators, commercially available ones not readily available</li> <li>• Requires large control electronics and a tether</li> </ul>	<ul style="list-style-type: none"> <li>• Requires large control electronics</li> <li>• Requires a tether</li> </ul>

The trade-off parameters used in the numerical trade off study were divided into three broad categories:

- Project related items such as timescales, cost etc.
- Technical performance parameters and how these compare with the requirements specifications.
- Utilities such as ease of manufacturability, assembly, maintainability and reliability.

A Measure of Effectiveness (MOE) model was created for each of the solutions. The MOE model used the unit value functions defined in Table 5-4. Non-technical parameters were scored out of ten, where 1 was considered poor and a 10 was given to solutions which matches the requirements exactly. A weighting was applied and the scores totalled. Weights were proportioned between the parameters with the most critical parameters being awarded the higher weight. The concept with the highest total score determined the chosen solution.

**Table 5-4: Scoring Determination**

Form	Equation	Description
Positive Score	$Score = \left[ \frac{Value}{Maxvalue} \right]$	Used when more of something is better than less of something
Negative Score	$Score = \left[ \frac{Minvalue}{Value} \right]$	Used when less of something is better than more of something

Table 5-5 shows the numerical analysis template used and

Table 5-6 is the results of the numerical analysis. The MOE section of Table 5-5 is the columns capabilities, score and weighted score.

**Table 5-5: Numerical Analysis Template**

	Priority	Criteria	Requirement	Weight	Concept Design Title		
					Capabilities	Score	Weighted Score
PROJECT RELATED	1	Potential to meet deadlines (1-10)		2			0
	2	Cost (1-10)		1.4			0
TECHNICAL RELATED	3	Tilt Resolution	$\leq 0.9 \text{ mrad}$	1			0
	4	Tilt Range	$\pm 35 \text{ mrad}$	1			0
	5	Rotational Resolution	$\leq 1 \text{ mrad}$	1.5			0
	6	Rotational Range	$\geq 6.283 \text{ rad}$	0.5			0
	7	Tilt Accuracy	$\leq 0.9 \text{ mrad}$	0.6			0
	8	Rotational Accuracy	$\leq 1 \text{ mrad}$	0.6			0
	9	Dimensions	$\leq 30 \times 30 \times 60 \text{ mm}^3$	0.5			0
MISCELLANEOUS RELATED	10	Reliability (1-10)	$\geq 16100 \text{ rotations per stage}$	0.4			0
	11	Ease of manufacturability (1-10)		0.3			0
	12	Ease of assembly (1-10)		0.2			0
					Total Weighted Score		0

**Table 5-6: Results of Numerical Analysis**

<b>Conceptual Designs Ranking</b>	
<b>Concept</b>	<b>Weighed Score (Out of 10)</b>
Piston Actuated	9.5
Prismatic Joint/Motor	8.5
Flexure Actuated	8.1
Piezo Tube	7.6

The NanoPositioner Int. concept (Table 5-3) was not included in the trade-off analysis as it would not have been feasible to develop and evaluate the actuators within the available timescale. This was unfortunate as it is a very novel concept and appeared to be able to meet the requirements better compared with most of the other solutions. Based on the outcome of the trade study it was decided that the piston actuated solution will be the best solution for further analysis and evaluation. It was also clear that the research goals can be achieved within the time-scale of the study period. The piston actuated solution, outperformed the other concepts in terms of its tip module. It has the potential of a higher resolution than the other concepts. The prismatic joint/motor concept would have a greater travel range however its resolution was expected to be poorer. The travel range of the piston actuated design was greater than the requirement and the better resolution made it a more preferred option.

## **5.5 SAM Computer Aided Design Evaluation**

Numerous piston actuated designs were digitally prototyped and analysed. These CAD models are shown in Table 5-8 which also summarise the advantages and disadvantages of each design. Based on the results the best solution (MK6) was chosen for further evaluation.

Table 5-7: Summary of SAM designs part 1

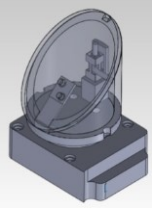
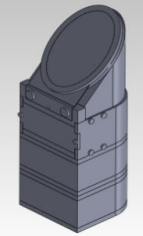
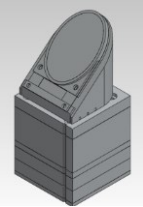
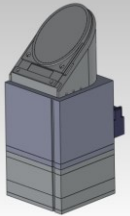
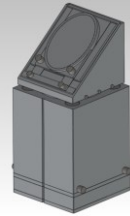
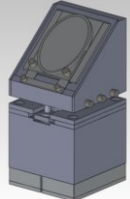
		Footprint, mm <sup>2</sup>	Tip Stage	Rotation Stage	Advantages	Disadvantages
<b>MK1</b>		~25.5 x 18	<ul style="list-style-type: none"> <li>• Pre-loaded Flexure</li> <li>• Actuation motor - Squiggle SQL 1.8 RV (Ultrasonic Piezo Motor) encoder available</li> </ul>	<ul style="list-style-type: none"> <li>• Actuation motor – SmarAct SR-2013-S (Stick/Slip Piezo Motor) with built-in encoder</li> <li>• Direct Drive Arrangement</li> </ul>	<ul style="list-style-type: none"> <li>• High resolution</li> <li>• Simple Design</li> <li>• Off-the-shelf Components, easily accessible</li> <li>• Expected tip travel range 0.1 radians</li> </ul>	<ul style="list-style-type: none"> <li>• Rotary motor requires large control electronics</li> <li>• Would require a tether for electronics</li> <li>• Tip resolution is non-linear due to proposed fitting angle</li> </ul>
<b>MK2</b>		27 x 25	<ul style="list-style-type: none"> <li>• Pre-loaded Flexure</li> <li>• Actuation motor - Squiggle SQL 1.8 RV encoder available</li> <li>• Squiggle motor angled at 45° to the mirror</li> <li>• Hemisphere added to Squiggle motor for coupling purposes</li> </ul>	<ul style="list-style-type: none"> <li>• Actuation motor – Faulhaber ADM 0620 Stepper motor</li> <li>• Software can micro-step the motor</li> <li>• Connects to mirror via a worm and spur gear train</li> </ul>	<ul style="list-style-type: none"> <li>• Relatively simple electronics</li> <li>• Self-contained electronics within POM</li> <li>• Linear response from tip stage</li> </ul>	<ul style="list-style-type: none"> <li>• Inherent backlash between at each gear</li> <li>• Precision concerns due to component interactions</li> <li>• Multiple components, increased complexity</li> <li>• Mirror holder shape can generate unwanted torsion within the flexure</li> </ul>
<b>MK3</b>		29.75 x 29.75	<ul style="list-style-type: none"> <li>• Pre-loaded Flexure</li> <li>• Actuation motor - Squiggle SQL 1.8 RV (Ultrasonic Piezo Motor) encoder available</li> <li>• Squiggle motor angled to the mirror at 45°</li> <li>• Hemisphere added to for coupling purposes</li> </ul>	<ul style="list-style-type: none"> <li>• Actuation motor – Brushless flat DC-micromotor</li> <li>• Direct Drive Arrangement</li> <li>• Posic Encoder chip with code wheel for feedback</li> </ul>	<ul style="list-style-type: none"> <li>• Potentially High resolution</li> <li>• Simple Design</li> <li>• Off-the-shelf Components</li> <li>• Self-contained electronics within POM</li> <li>• Linear response from tip stage</li> </ul>	<ul style="list-style-type: none"> <li>• Uncertainty about motors precision although the external feedback should compensate</li> </ul>

Table 5-8: Summary of SAM designs, part 2

		Footprint, mm <sup>2</sup>	Tip Stage	Rotation Stage	Advantages	Disadvantages
<b>MK4</b>		29.75 x 29.75	<ul style="list-style-type: none"> <li>• Pre-loaded Flexure</li> <li>• Actuation motor - Squiggle SQL 1.8 RV (Ultrasonic Piezo Motor) encoder available</li> </ul>	<ul style="list-style-type: none"> <li>• Actuation motor – DC Gear Motor 2619S006S R8:1 IE2-16</li> <li>• Built-in encoder</li> <li>• Direct Drive Arrangement</li> </ul>	<ul style="list-style-type: none"> <li>• High resolution</li> <li>• Simple Design</li> <li>• Off-the-shelf Components, easily accessible</li> <li>• Expected tip travel range 0.1 radians</li> <li>• Encoder feedback to maintain position</li> </ul>	<ul style="list-style-type: none"> <li>• Rotary motor increases overall height to ~ 83 mm</li> <li>• Potential resolution issues</li> <li>• Backlash in the rotary motor, built-in encoder should compensate</li> </ul>
<b>MK5</b>		30 x 30	<ul style="list-style-type: none"> <li>• Pre-loaded Flexure</li> <li>• Actuation motor - Squiggle SQL 1.8 RV (Ultrasonic Piezo Motor) in M3L Development kit</li> </ul>	<ul style="list-style-type: none"> <li>• Actuation motor - Zero backlash stepper motor</li> <li>• Direct Drive Arrangement</li> <li>• Limited to ± 200° due to cabling</li> </ul>	<ul style="list-style-type: none"> <li>• Self-contained electronics within POM</li> <li>• Linear response from tip stage</li> <li>• Compact design – electronics surround rotary motor</li> <li>• Development kit used for tip stage</li> </ul>	<ul style="list-style-type: none"> <li>• Rotation is not continuous due to wiring between stages</li> </ul>
<b>MK6</b>		30 x 30	<ul style="list-style-type: none"> <li>• Pre-loaded Flexure</li> <li>• Actuation motor - Squiggle SQL 1.8 RV (Modified M3L Development Kit)</li> </ul>	<ul style="list-style-type: none"> <li>• Actuation motor – Smoovy 0515B with 625:1 Planetary gear head</li> <li>• Friction Drive Arrangement</li> <li>• MicroE Systems optical encoder – 126 µrad resolution</li> </ul>	<ul style="list-style-type: none"> <li>• Potentially High resolution</li> <li>• Simple Design</li> <li>• Off-the-shelf Components</li> <li>• Self-contained electronics</li> <li>• Linear response from tip stage</li> <li>• Similarities to MAPS</li> </ul>	<ul style="list-style-type: none"> <li>• Rotation is not continuous due to wiring between stages</li> </ul>

From the early design investigation, it was decided to develop the MK6 further. The MK6 was chosen because it uses the same friction drive concept applied on the MAPS robot and was more compact compared to the other concepts. By using the same friction drive concept, it can be implemented using the same type of Smoovy motor, which is well characterised. The motor selected is the Smoovy 0515B with 03A planetary gearhead, which is a slightly larger motor (diameter of 5 mm opposed to 3 mm) with a five times higher gear ratio (625:1 instead of 125:1) providing a smaller single step size. The larger motor was chosen because of how fragile the smaller one was found to be during the development of the MAPS robot. This motor has a minimum step size of 0.2 mrad. With friction drive it is possible to achieve a very compact design in comparison with the other designs evaluated. The minimum step size is determined by the motor gear ratio and the size of the driven component responsible for the rotation of the mirror. The size of the driven component allows for a higher resolution to be obtained for the rotation stage compared to the directly driven concepts. If a slip ring is added between the tip module and rotation module continuous rotation will be possible. However, a slip ring was not included in the first prototype as it was deemed unnecessary at this stage to extend the requirements to provide an  $N \times 360^\circ$  rotational stage. For the tip module a Squiggle (piezo) motor was selected, because of the 1  $\mu\text{m}$  minimum step size that can be achieved in closed loop using low voltage driving electronics. A single step size of 1  $\mu\text{m}$  in the design equates to a rotation of 51  $\mu\text{rad}$  which is better than the 900  $\mu\text{rad}$  requirement. The Squiggle motor was also chosen because of its size (1.8 x 1.8 x 6 mm<sup>3</sup>). The small size was helpful for fitting the motor into the limited packaging space that was available. It was due to the motor choice that SAMs tip module exceeded the requirements detailed in Table 5-2. It was not chosen for the rotation module because it is a linear motor. It would have needed extra components and complexity to be made suitable for the rotation module. Since this work has been carried out, Newscale Technologies have developed a new Squiggle motor is a rotary version of this one.

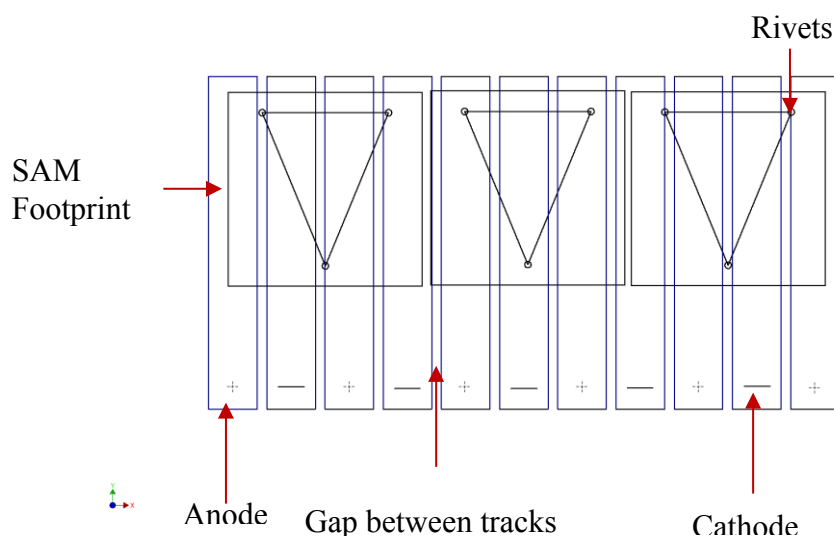
## 5.6 Description of evaluation model

The evaluation model consisted of four modules:

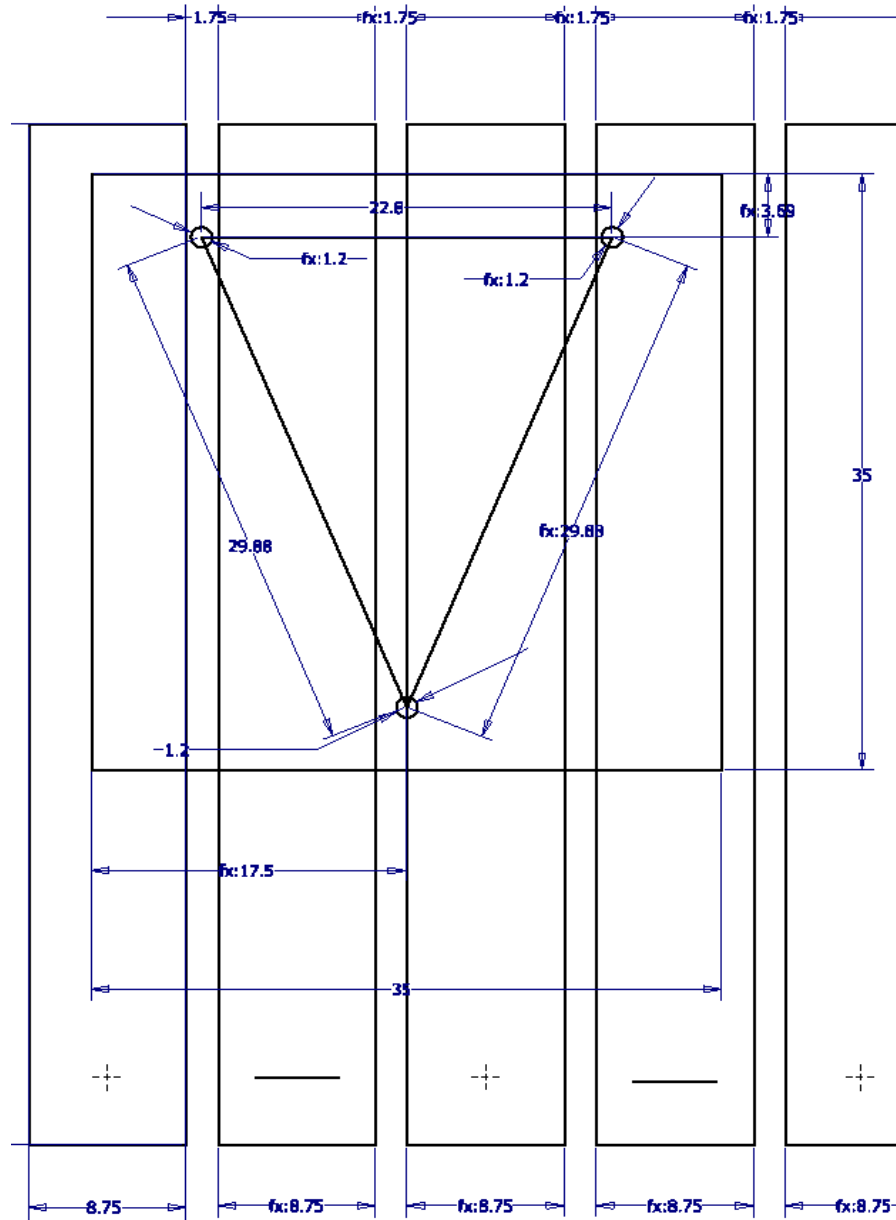
- Power
- Rotation
- Tip
- Mirror

The power module utilises the PowerFloor and as discussed previously is better suited to provide power to a static component such as SAM. The modularity of the design means that the power module could be replaced with any receiver that is designed to fit within a casing with a 35 mm<sup>2</sup> footprint.

Three rigid contacts (rivets) act as feet that sit on the PowerFloor. The head diameter of the rivet is less than the gap spacing between tracks to avoid shorts. Due to the geometry of the rivets, a contact will always be made with each track by at least one rivet as long as the front face of the power module is perpendicular to the direction of the tracks this allowed the SAM power module to use three pick-off pins rather than the four that is required by the MAPS robot. Figure 5-7 shows a 2D sketch of the rivet geometry and how it interacts with the PowerFloor. The rivets are used to conduct the power from the floor (9.2 V) to the on-board power conditioning module. These three rigid contacts provide greater stability of the device on the surface compared with the MAPS robot (combination of wheels, stabilisers and spring-loaded power contacts).



(a) Geometry of the rivets means one will also be on a required track

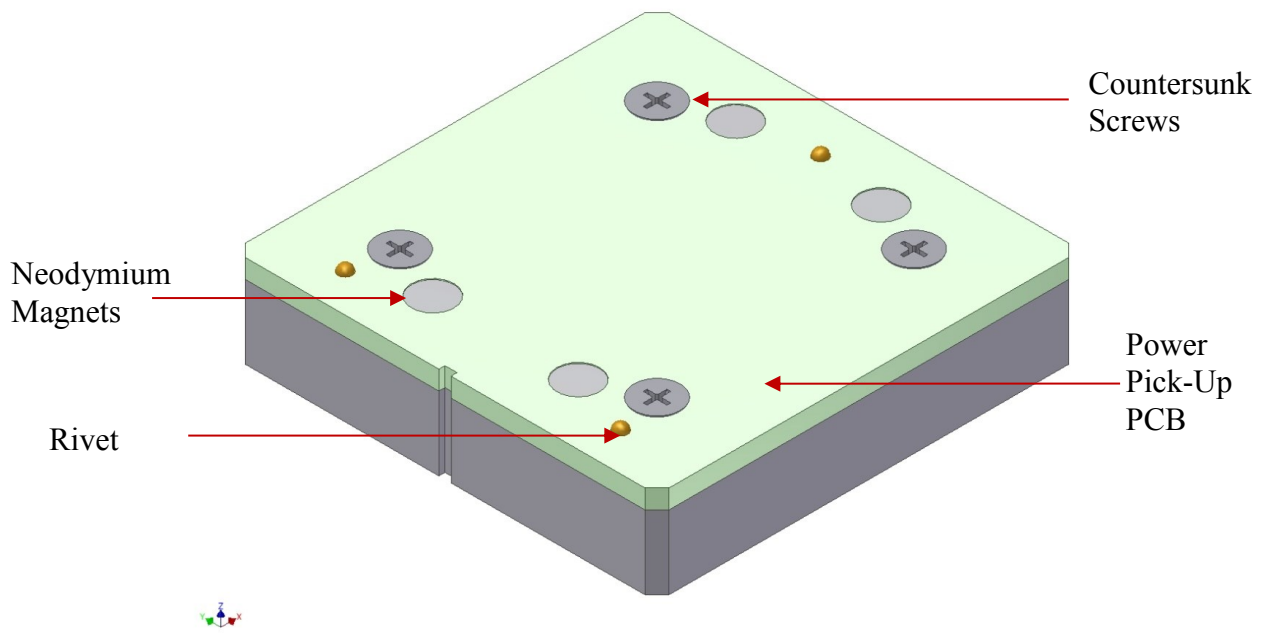


(b) Track and rivet dimensions

**Figure 5-7: SAM Rivet Geometry**

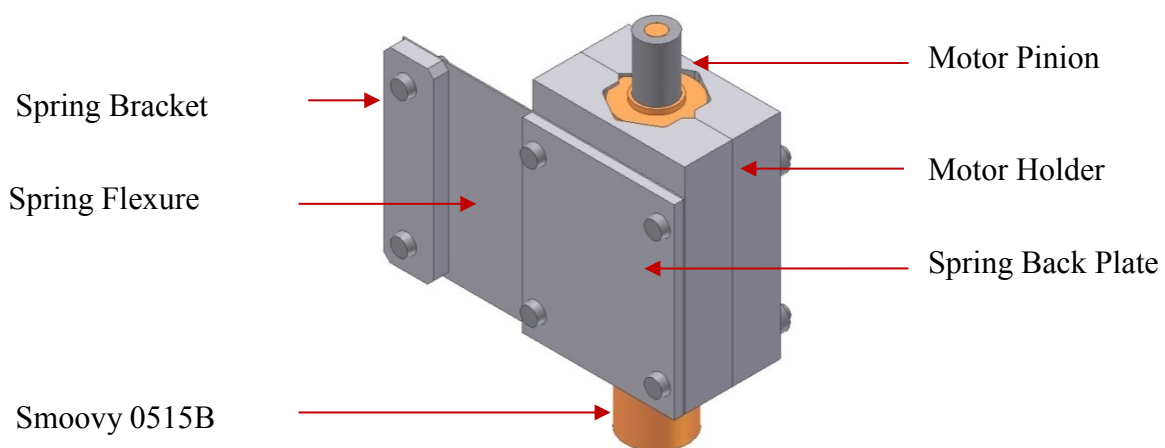
The underside of the power module (Figure 5-8) is a PCB. Counter bores on the PCB provide spaces for magnets to be press fitted. All the magnets poles must face the same direction; this is to add a force that will hold SAM on the instrument as a steel plate is located underneath the PowerFloor. Magnets are used to attach the rotation module on top of the power module. Magnets were used because it is easier and quicker to assemble and it can also be taken apart quickly if required. This also eases assembly between modules compared to using bolts and other standard macro assembly techniques.



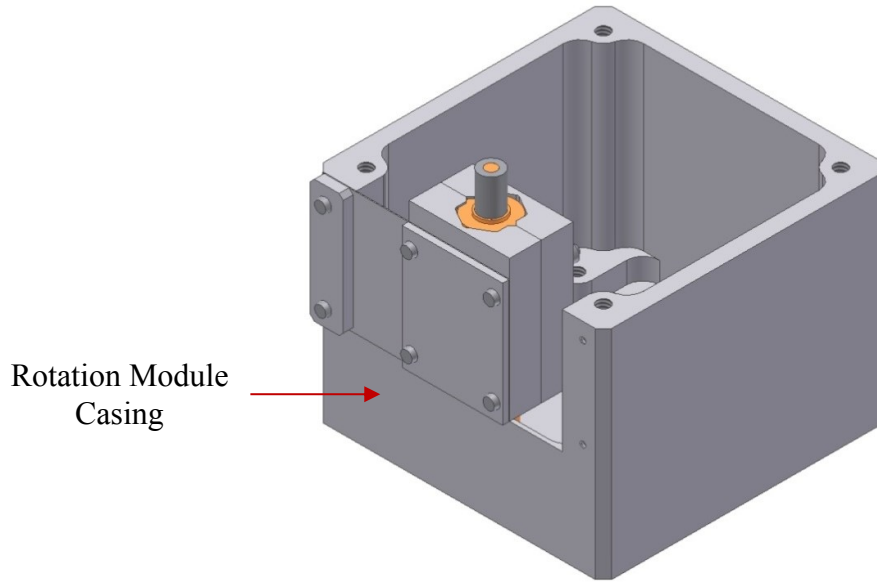


**Figure 5-8: Power Module Underside**

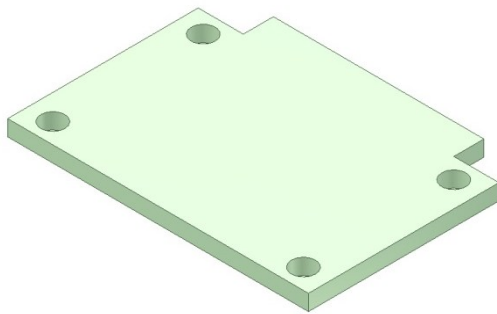
The rotation module uses the 0515B Smoovy motor with a 06A planetary 625:1 reduction gear head to provide a step size of 0.21 mrad. The friction drive arrangement is small and compact and allows enough space to accommodate the on-board electronics. A pre-loaded aluminium flexure maintains a constant force of 0.13 N between the motor's output shaft and the O-ring attached to the tip module as shown by Equation 6-1 that is explained further on in this section of the thesis. Figure 5-9 shows the various components of the rotation module.



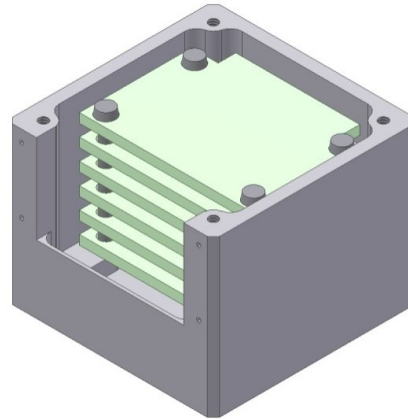
**(a) Spring Assembly**



(b) Rotation Module Casing with Spring Assembly



(a) Command & Control PCB

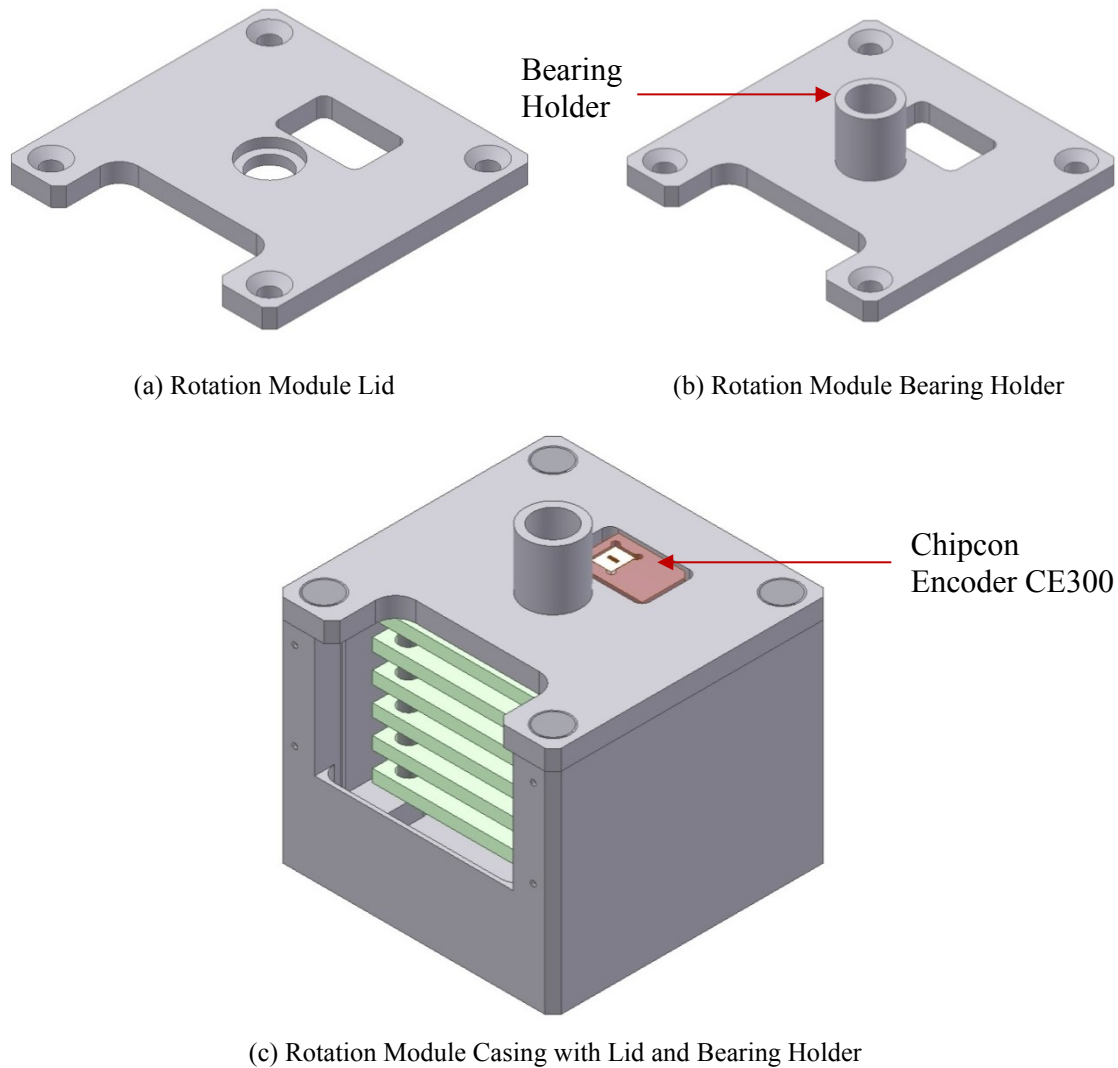


(b) Command & Control PCB stack within Rotation Module Casing

**Figure 5-9: Rotation Module**

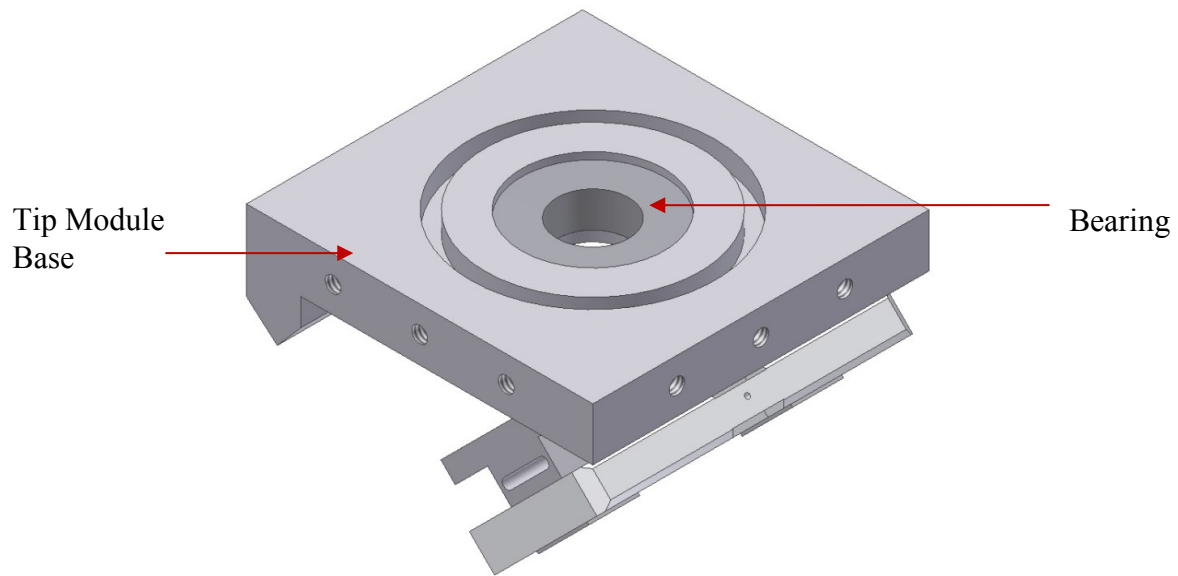
The tip module bearing is press fitted over a hollow aluminium cylinder, called the bearing holder, which is part of the Rotation Module (Figure 5-10). This component is hollow to allow wires between the Rotation Module and Tip Module. A bearing is used to facilitate rotation between a static part (The rotation module) and moving part (tip module). A bearing was chosen as it has low friction and they are very resilient.

The cut at the rear of the Rotation Module Lid is for the Chipcon optical encoder, [82]. The CE300-40 chip in combination with the R1910CE code wheel provides a measuring resolution of 126  $\mu$ rad, which is seven times better than the requirement (Table 5-2).

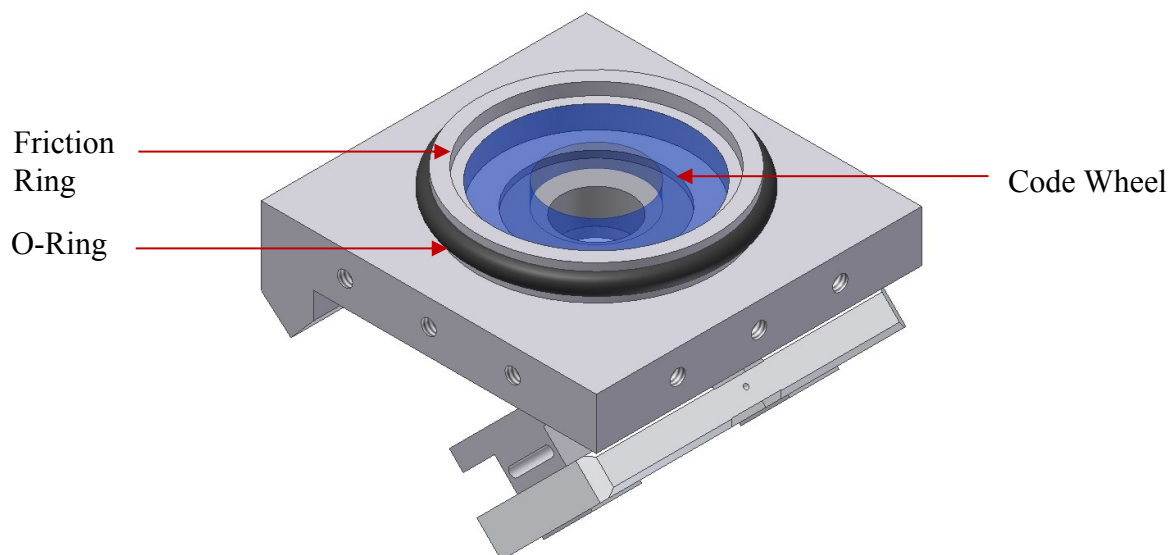


**Figure 5-10: Rotation Module Lid**

An aluminium ring is fitted to the bottom of the tip module base and the code wheel is glued to it, as shown in Figure 5-11. The code wheel is pressed into the aluminium ring and up against the base of the tip module. The tip module's base provides a flat surface that keeps the code wheel parallel to it. Once the code wheel is in place and the tip module is attached to the rotation module (explained later), the code wheel is measured using the accompanying encoder chip. However, it has not been successful to add the encoder as the alignment requirements are very tight. Components such as the bearing provides motion that alters the code wheels parallelism with respect to the rotation module, this in turn loses alignment between the two components. A stiffer design would be required to ensure alignment. The ring has an annular groove that an O-ring is stretched over.



(a) Underside of Tip Module with bearing

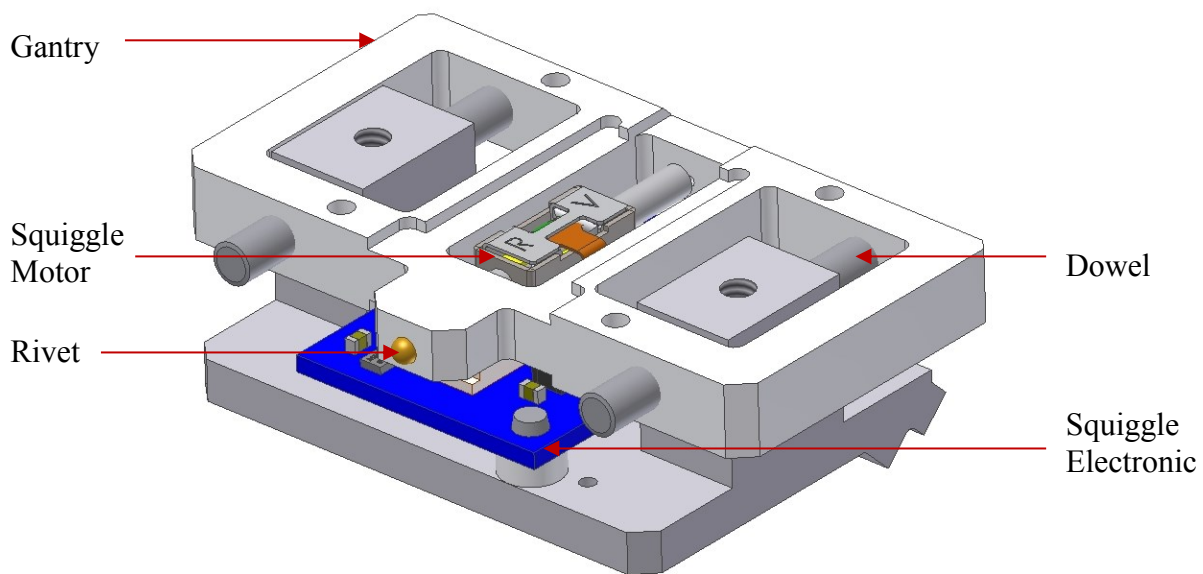


(b) Underside of Tip Module fitted with friction ring and code wheel

**Figure 5-11: Tip Module**

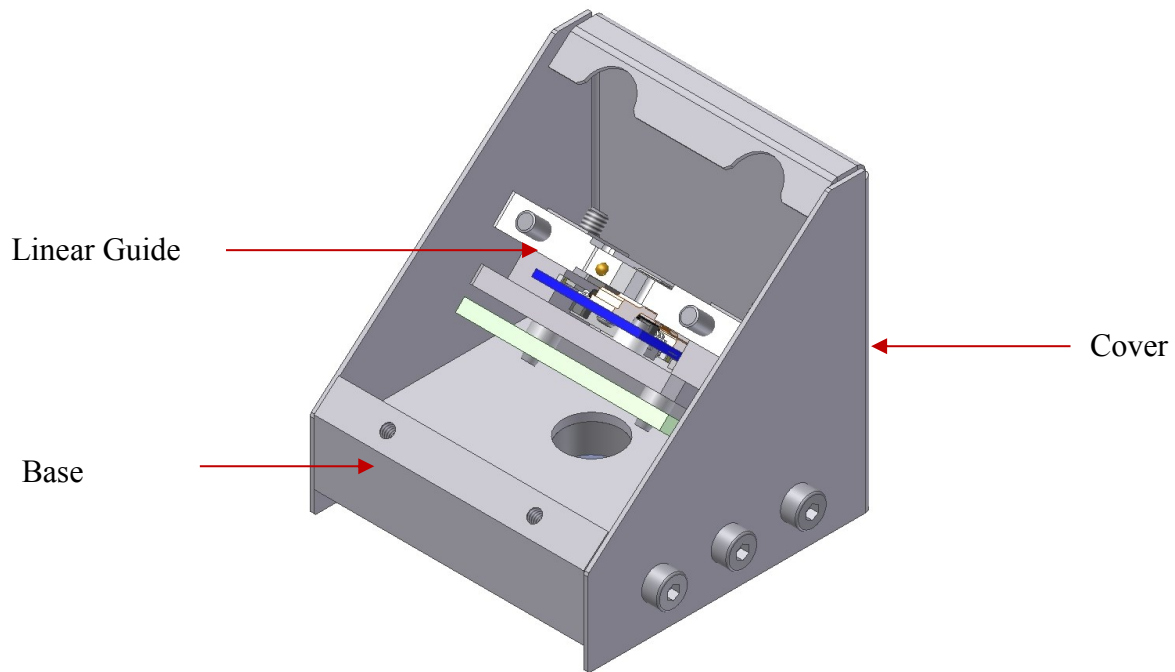
A linear guide angled at  $45^\circ$  from the tip module base is glued into a groove. The linear guide is angled at  $45^\circ$  to help maintain a smooth coupling between the linear guide and mirror module. Although this is not a precise assembly method it does not matter for this part as long as it mates with the mirror module in a smooth consistent fashion. The linear guide consists of two ground steel dowels that act as the slides for a gantry stage. The gantry is made from Polytetrafluoroethylene (PTFE) also known as Teflon, mainly chosen for its low friction properties. The linear guide consists of two dowels as depicted in Figure 5-12 to avoid torsion during movement. Torsion is not possible because the dowels pass through the gantry at both ends constraining the gantry to a single axis linear motion. Although this is technically over constrained, it was needed to provide stability during motion.

The squiggle motor pushes the gantry that in turn pushes the back of the Mirror Module. The linear motion of the Squiggle motor is transformed into a rotational motion by the flexure that attaches the mirror module to the tip module (described later). A Squiggle motor is a piezoelectric motor that's operation is based on the ultrasonic principle [83]. The Squiggle motor combines a hall sensor which is used to provide feedback regarding the relative movement of the stage and is used to control the stage closed-loop. A brass rivet attached to the gantry improves coupling between the linear guide and the Mirror Module as it is a curved surface pressing against a flat surface during motion. The linear motion of the Squiggle motor translates to an angular rotation for the mirror around the x-axis. Figure 5-12 shows a CAD model of the complete linear guide sub-assembly.



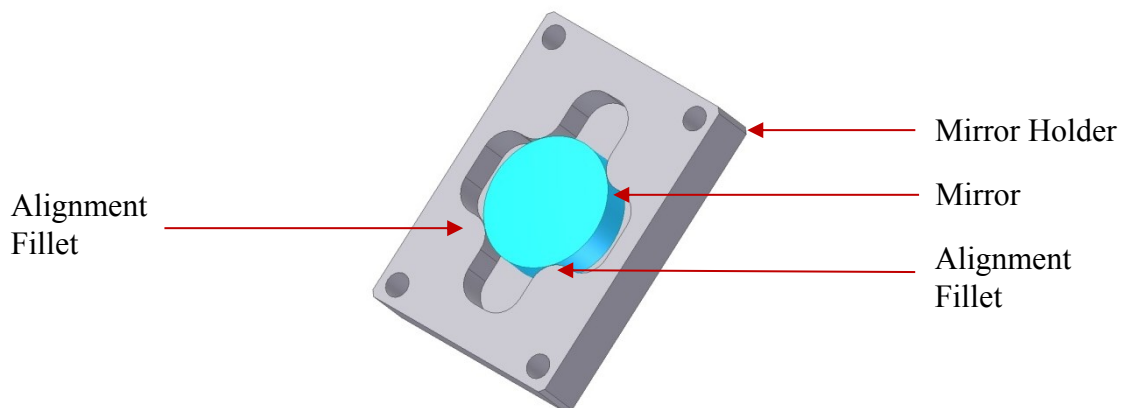
**Figure 5-12: Linear Guide Assembly**

The Tip Module Cover is a sheet metal part that is bolted around the perimeter of the base, Figure 5-13. The cover overhangs past the bottom of the Tip Module Base to cover the interface between the rotation module and tip module.



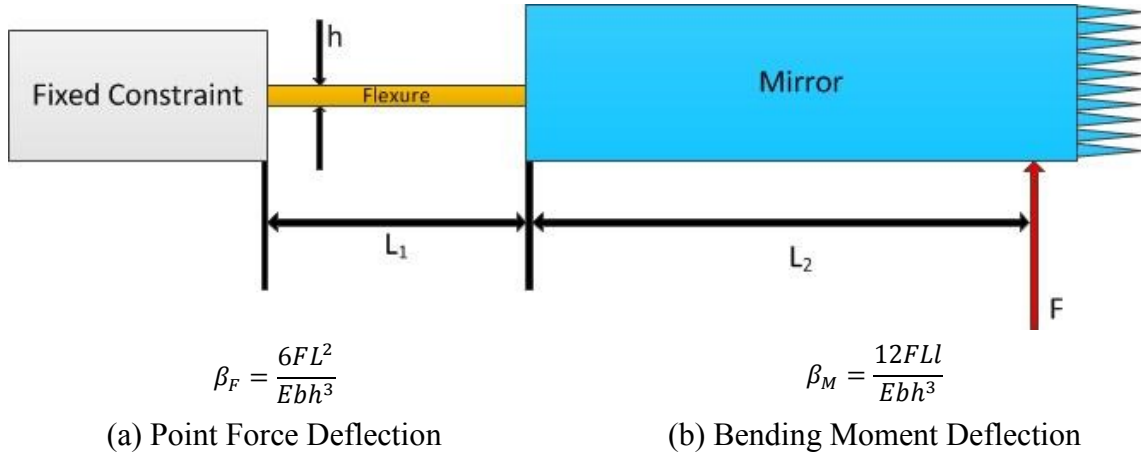
**Figure 5-13: Tip Module Cover**

The mirror holder was designed to hold an Edmund Optics  $\frac{1}{4}\lambda$  precision optical flat mirror. The mirror is glued in place. During the gluing process the mirror is forced towards two alignment fillets shown in Figure 5-14. These alignment fillets press against the curved surface of the mirror providing a precise location for the mirror within the mirror holder.



**Figure 5-14: Mirror Holder**

Figure 5-15 is a block representation of the mirror and flexure which is used to attach the mirror module to the base of the tip module. Figure 5-15 distinguishes the two interactions taking place with the flexure due to the tip and mirror module.



**Figure 5-15: Breakdown of Forces**

The equations provided in Figure 5-15 are combined to find the deflection of the flexure with respect to its geometry, material and the force being applied to it, (5-1).

$$\begin{aligned}
 \beta &= \beta_F + \beta_M \\
 \beta &= \frac{6FL^2}{Ebh^3} + \frac{12FLl}{Ebh^3} \\
 \beta &= \frac{F(6L^2 + 12Ll)}{Ebh^3}
 \end{aligned}
 \tag{5-1}$$

The minimum allowable thickness for the flexure in Aluminium and BeCu are 100  $\mu\text{m}$  and 80  $\mu\text{m}$  respectively. An initial set of dimensions was chosen based on the minimum footprint size of the POM. Flexure geometry values were evaluated to determine an acceptable force that the motor could move without being damaged. Due to the thickness having the highest impact it was first altered until limitations were reached.

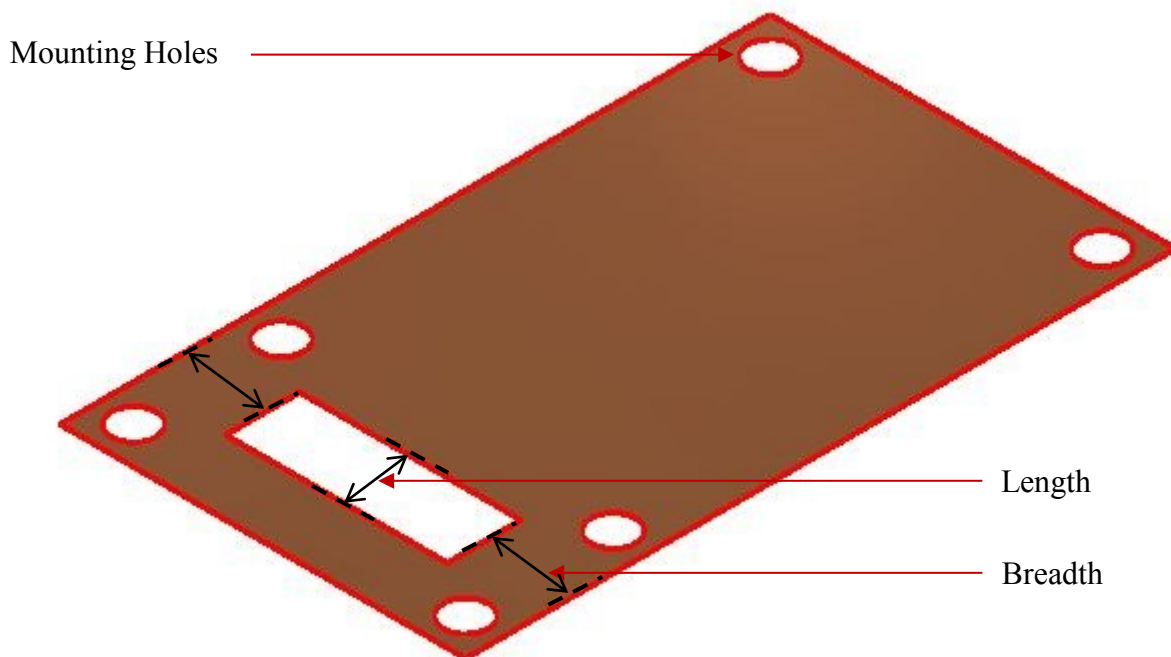
The minimum thickness was too stiff for the Squiggle motor. The next dimension altered was increasing the length to reduce the required force. Based on the room available within the footprint a maximum length of 4 mm was possible. This results in an acceptable force for the actuator, Table 5-9, however there is little margin for error. It is preferred that the actuator only be required to push  $\leq 0.2$  N to provide a safety margin. Therefore, the breadth was reduced to further lower the required force providing a safety margin of 1.5, Table 5-9.

**Table 5-9: Results from Varying Breadth**

	Travel Range (Rads)	Flexure Breadth, b (mm)	Force Location, L (mm)	Flexure Length, l (mm)	Flexure Thickness, h (μm)	Force Required, Al Flexure (N)	Force Required, BeCu Flexure (N)
<b>Various Breadths</b>	0.14	16	13.688	4	100	0.2	0.34
	0.14	15	13.688	4	100	0.19	0.32
	0.14	14	13.688	4	100	0.18	0.3
	0.14	13	13.688	4	100	0.17	0.28
	0.14	12	13.688	4	100	0.15	0.26
	0.14	11	13.688	4	100	0.14	0.23
	0.14	10	13.688	4	100	0.13	0.21

Aluminium meets the required force for any breadth  $\leq 16$  mm. BeCu does not meet the requirements for a 100 μm thick flexure and needs to be 80 μm thick for any breadth below 18 mm.

Based on the findings from Table 5-9 it was decided to manufacture the flexure at the minimal breadth of 10 mm to provide the actuator with the largest safety factor. The force required for Aluminium and BeCu with this breadth is 0.13 N and 0.11 N respectively. Figure 5-16 shows the flexure that was designed. The hole in the centre is used so that the breadth dimension can be split between the two ends of the flexure thus improving torsional rigidity.

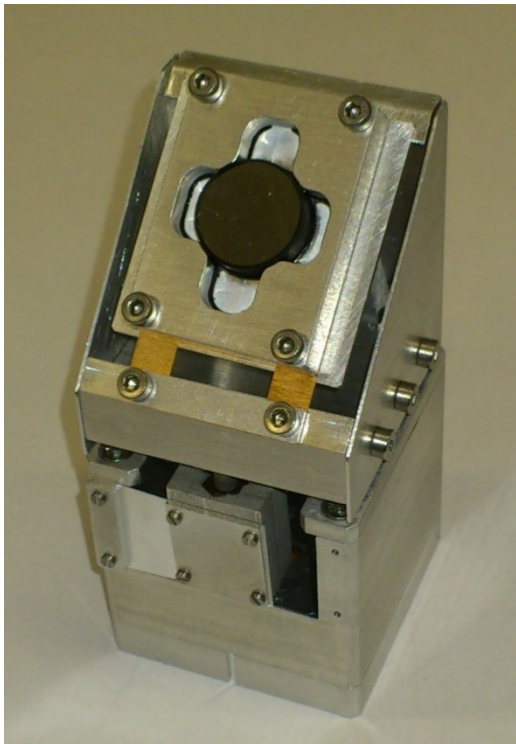


**Figure 5-16: Mirror Flexure**

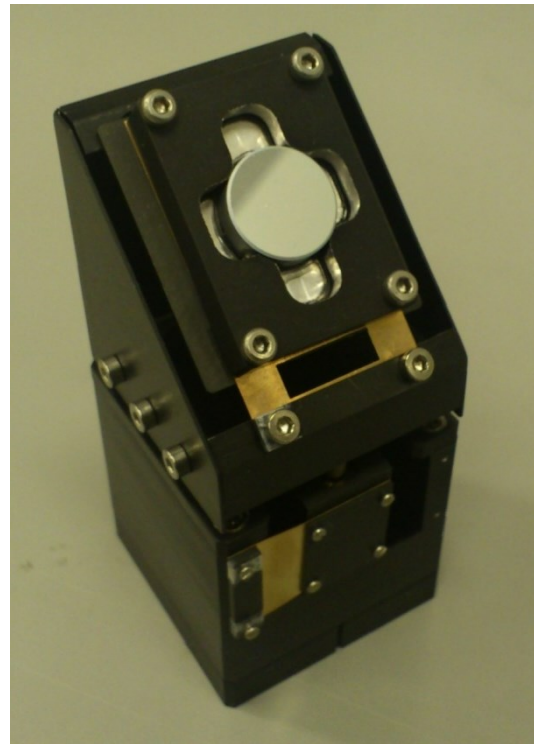


For the rotation module, the thickness was constrained to the requirements for the tip module for quick manufacturing. The width was not reduced below 15 mm because of torsion within the flexure. The flexure was produced with a 6.7 mm to provide a 0.05 N and 0.042 N, for Aluminium and BeCu, side load between the Smoovy motor and mirror module. The acceptable side load for the Smoovy motor is 0.3 N.

Figure 5-17 shows two SAM units, the silver one was the test prototype and the black one would be the finished anodised product. The anodise coating is to avoid unwanted stray light affecting the objects being studied within a MOS instrument. Appendix B provides the bill of materials for the construction of a SAM module has been added to.



(a) Silver SAM Prototype



(b) Anodised Black SAM, Finished Product

**Figure 5-17: SAM**

### 5.7 The Expected Performance

The performance of the SAM is separated into the tip and rotation modules. The primary objective for the testing of tip and rotation modules was to determine:

- Travel range
- Individual step capabilities, i.e. resolution
- Accuracy, repeatability and hysteresis

### 5.7.1 Tip Module

Position commands relative to the hard stop were sent to the Squiggle motor. The hard stop provides a maximum and minimum location that the Squiggle motor can reach and has a range between 0.001 mm to 4.28 mm. The mirror's angle is calculated based on the geometry of the actuator. Figure 5-18 presents the theoretical linear relationship for the Squiggle motor positional control. A trendline has been added that indicates that the positioning resolution is approximately 0.052 mrad (0.003°) which is within the 0.9 mrad requirements. The maximum range that the tip module is designed for is 216 mrad, which exceeds the 70 mrad requirement.

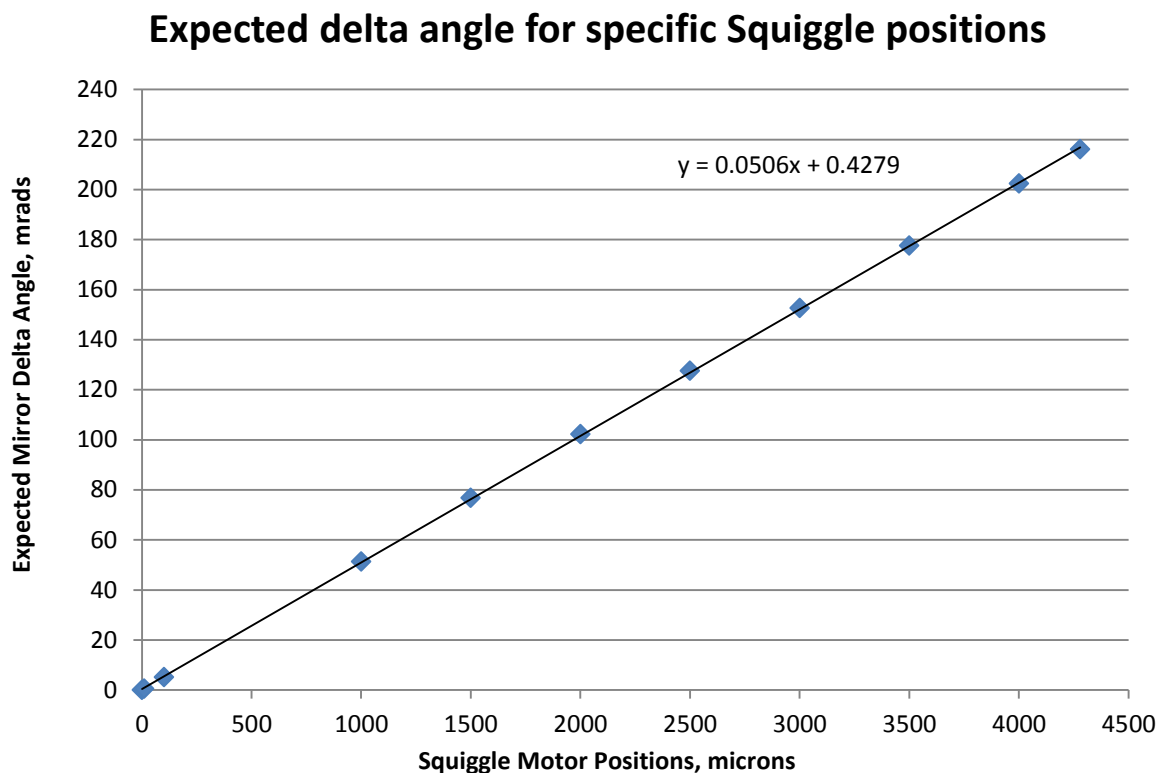


Figure 5-18: Tip Module Theoretical Results

### 5.7.2 Rotation Module

The test objectives for the rotation module are similar to that of the tip module, which was to characterise the stage in terms of the:

- Travel range
- Minimum step size and
- Backlash

To determine the step to angle relationship; the backlash and achievable resolution the rotational module was used in an open-loop control mode.

The relationship between the motor steps and delta angle is based on the ratio between the motor pinion ( $\varnothing$  2.85 mm) and tip module's friction ring ( $\varnothing$  26 mm), which is 0.11. The Smoovy 0515B motor with a 625:1 reduction gear head is designed to provide a minimum step size of 0.21 mrad/step rotation at the output shaft. In the friction drive arrangement, the expected relationship is 23.1  $\mu$ rad/step.

## **5.8 Actual Performance**

### **5.8.1 Tip Module**

An optical method was used to test SAM because it was a non-contact method that would provide a low measurement error. However its field-of-view was not large enough for the full range of motion. A contact method (described later in this section) was used to measure the entire travel range. For the optical method, a laser was set perpendicular to the ground surface and the beam was reflected from the mirror towards a Lumenera Lw11059M, which was used to record an image of the beam spot. A MatLab script was then used to find the centroid of the spot. This was repeated for various Squiggle motor positions and the change of centroid positions was used to determine the change in angle.

To start the laser is reflected off of SAM towards one edge of the camera sensor; the full spot needs to be imaged for the image processing to function properly. The test methodology used is outlined below:

1. Record initial position.
2. Command unit to move 1070  $\mu$ m (1<sup>st</sup> measuring position on the camera).
3. Record the first position.
4. Command unit to the 2<sup>nd</sup> measuring position on the camera (2140  $\mu$ m)
5. Record the second position.
6. Repeat steps 4 and 5 until the spot can no longer be imaged

The last measurement point in the forward direction will be used as the starting point, to measure the performance of the unit when commanded in the reverse direction. The final measured point should be equal to that of the starting position. This process was repeated a number of times, so that measurement errors can be averaged out.

The maximum travel distance that the Squiggle motor could be sent to during the test was 1050 microns. The range was limited by the cameras field-of-view (FOV) which is determined by the physical size of the cameras sensor. The range was segmented into four, thus providing five measurement positions. Figure 5-19 shows the average results of 16 measurements for

each Squiggle motor position. The standard deviation between the 16 measurements for each position was  $\leq 17.45 \mu\text{rad}$ .

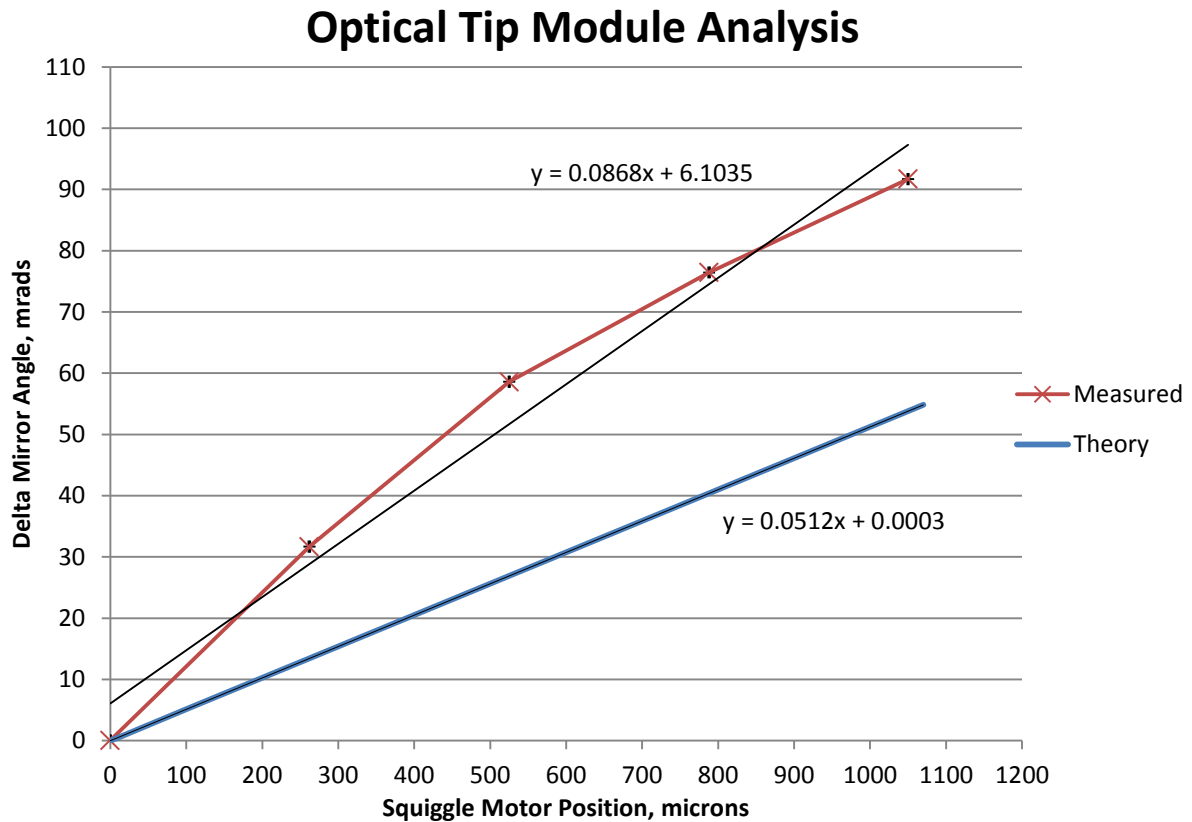
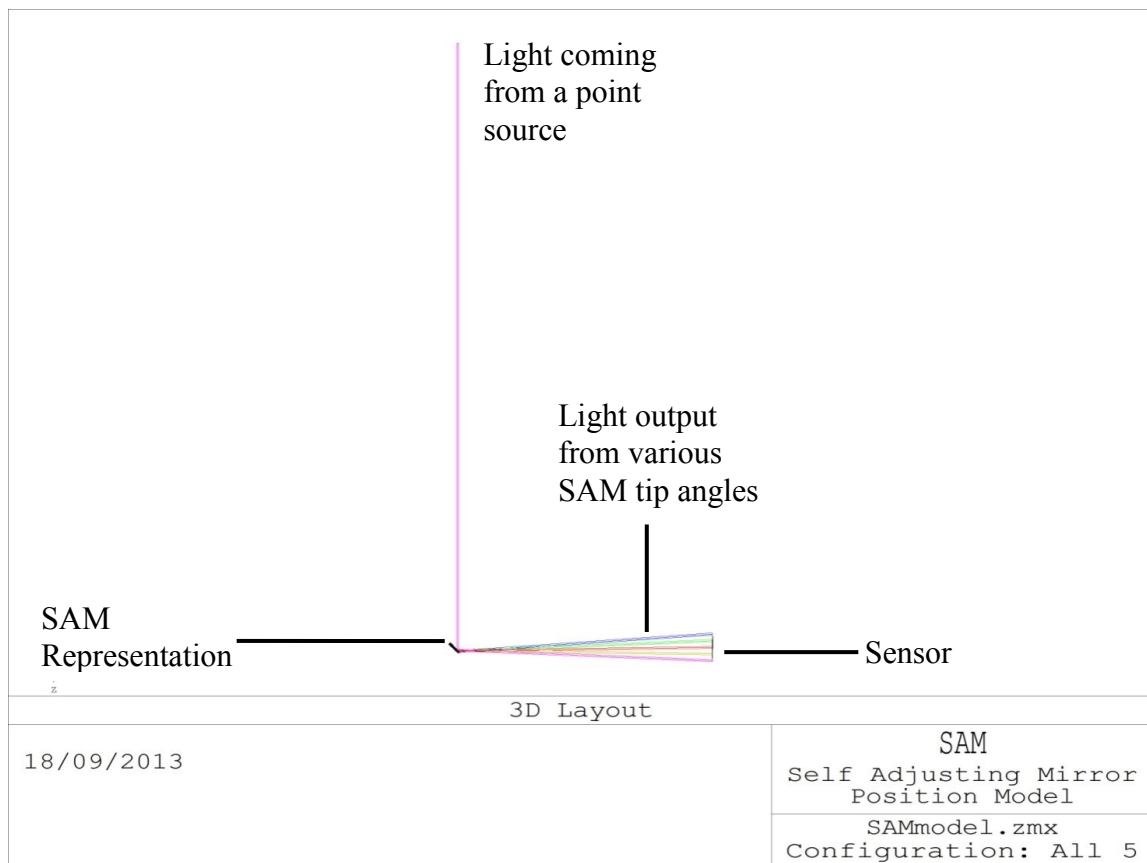


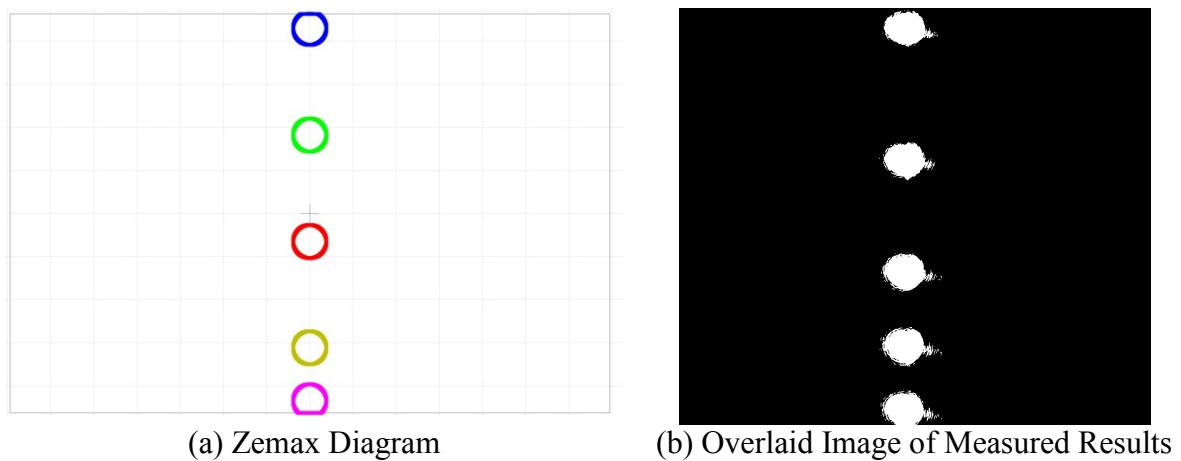
Figure 5-19: Optical Method Output

A linear response was expected; however, as can be seen in Figure 5-19, the recorded results were not. A further investigation was carried out and is explained later in this section. The deviation from the theory could be because the mirror's centre of rotation lies below the mirror rather than at the mirror's own centre. To confirm this hypothesis a Zemax ray-trace model was constructed, Figure 5-20, indicating the expected response of the light beam reflected from SAM to the sensor.

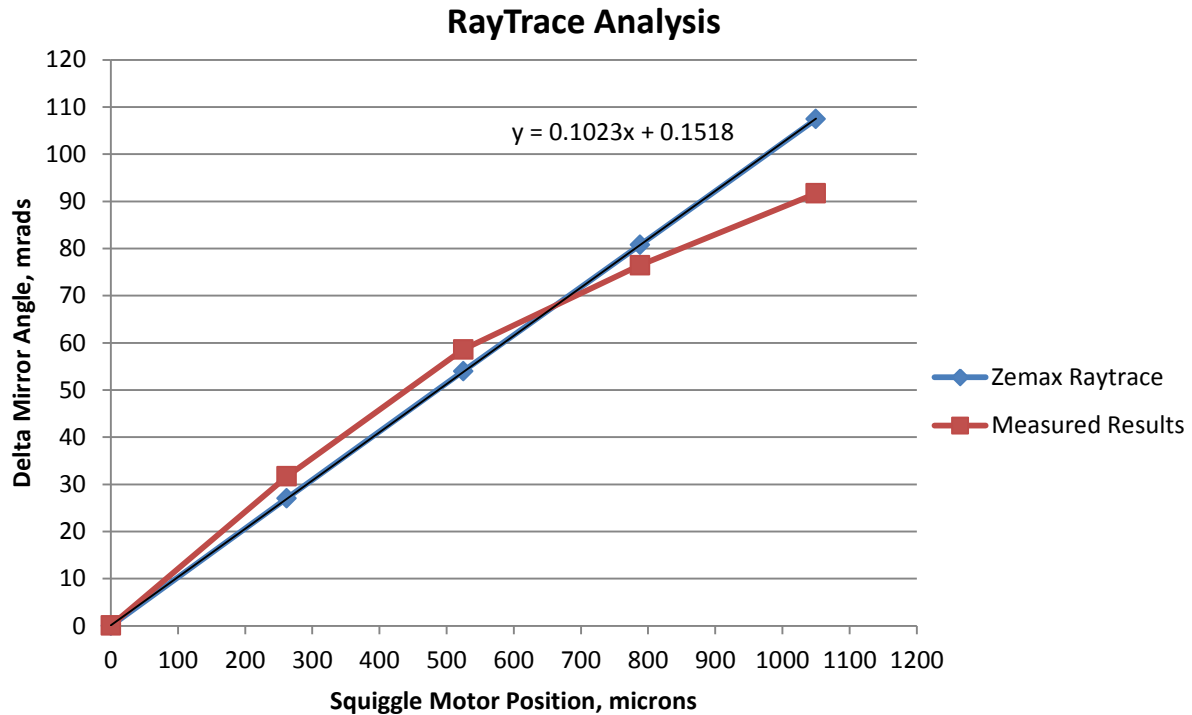


**Figure 5-20: Zemax model**

Figure 5-21 shows the actual image of where the laser intersects the sensor and that predicted by Zemax, as can be seen, there is good correlation between the two.



**Figure 5-21: Comparison of Zemax and Measured Output**



**Figure 5-22: Zemax and Experimental Results Comparison**

Figure 5-22 plots the Zemax output of the light beam on the sensor against the experimental results showing deviations as high as 17.5 mrad. These deviations are likely to be a mechanical issue within the tip module and are explained further on in this section. The measurement error was 0.05 mrads and has no bearing on the deviation that can be seen in the graph.

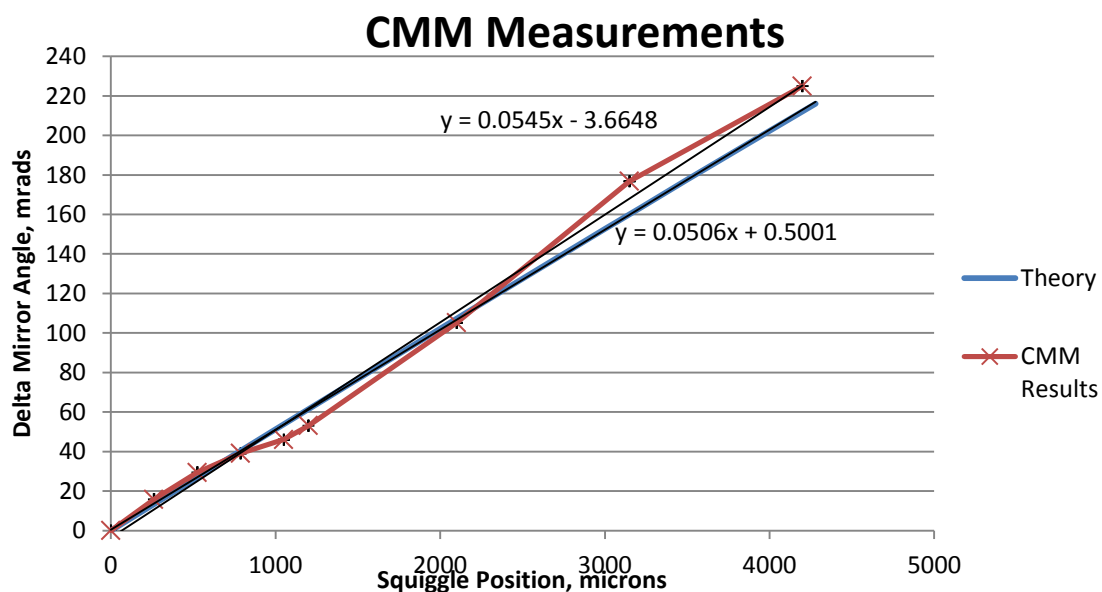
The optical method was capable of high resolution measurements, however was not capable of measuring the entire travel range thus a contact method involving the Coordinate Measuring Machine (CMM) was used. This would measure the mirrors angle in relation to the tip module's base and not the light path, which the optical method focuses on.

A Mitutoyo B706 CMM, capable of measuring a position to within 1.5  $\mu\text{m}$ , was used to measure the mirror module's angle in relation the horizontal plane. SAM's tip module was clamped to the CMM surface on an optical breadboard. Four points on the top surface of the optical breadboard were used to generate a reference plane. The mirror was set at its minimum position and four points measured on a single surface of the mirror holder creating a plane. The angle between this plane and the reference plane was recorded. The Squiggle motor was set to different positions and the mirror module's new planes measured to determine the angle. Figure 5-23 is the test setup for the contact method with the CMM.



**Figure 5-23: CMM Test Setup**

Figure 5-24 compares the experimental results with the theoretical mirror angles showing a deviation. The error for the change in mirror angle measured with the CMM varies for the different Squiggle motor positions. Generally, the greater the Squiggle motor position the greater the measurement error. This was because the mirror module is more susceptible to external forces such as the CMM's probe. On average across all the measurement positions the error was 0.87 mrad, with the highest measurement error did not exceeding 1.4 mrad.



**Figure 5-24: Comparison of CMM Measurements and Expected Results**

Figure 5-25 shows the mirror performance measured with both the CMM and camera. The camera measurements have been compensated to remove a deviation that was expected between the two data sets, as the optical set of results shows the change in the light path's angle and the CMM set shows the actual movement of the mirror's surface in relation to the base. This confirms that it is because the centre of rotation for the tip module is located below the mirror as described by Figure 5-21. It shows that the output from both the light path and the actual mirror position follow the same pattern for the set of positions measured, indicating a mechanical error within the tip module mechanism.

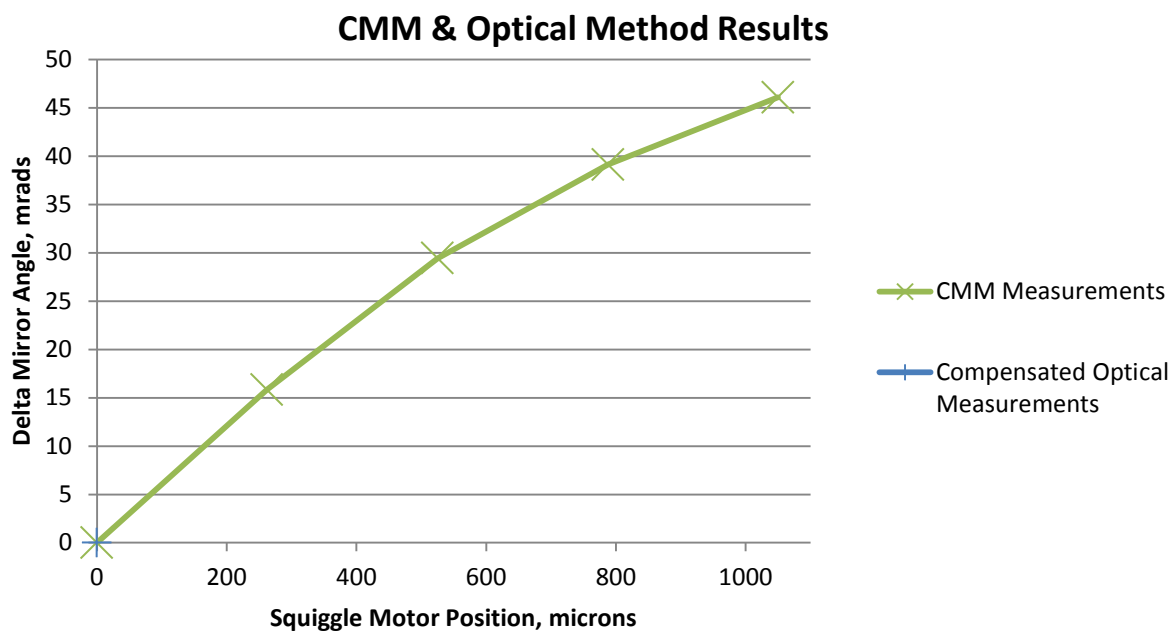


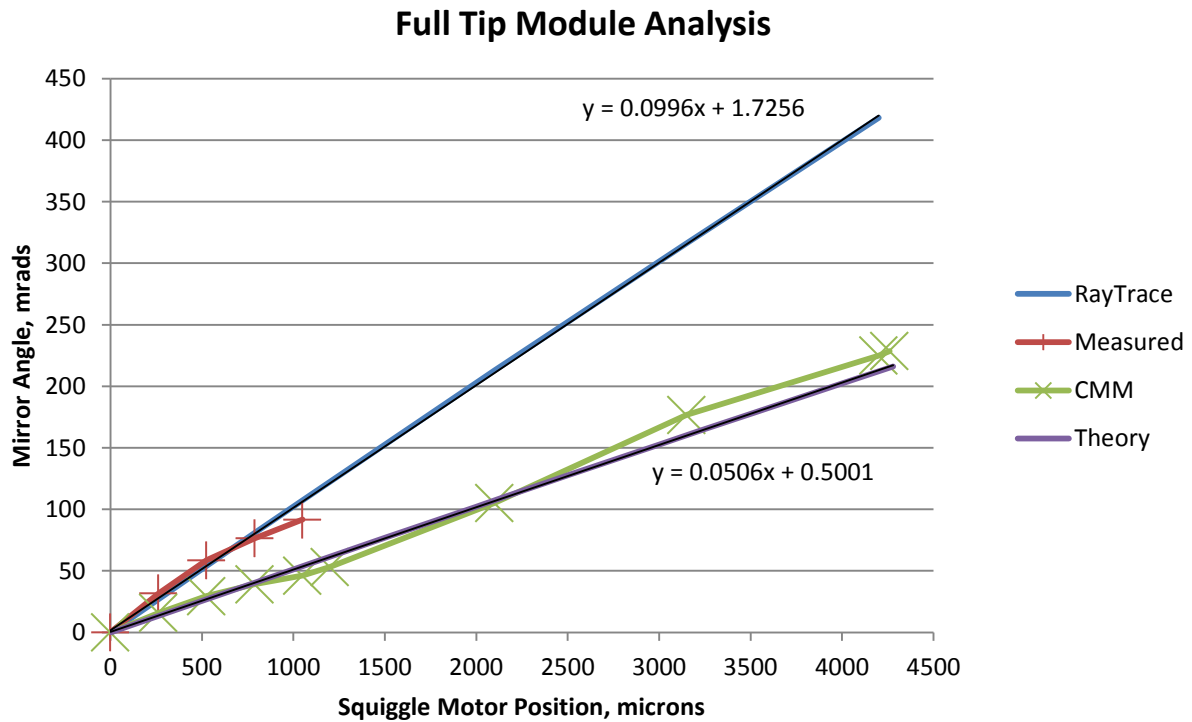
Figure 5-25: Comparison of Optical & CMM Results

It is likely that the cause of this non-perfect linear motion is due to a juddering motion at the linear guide. This is due to sticking caused by torsional motion as the PTFE gantry slides up the dowels. The magnet used for the encoder at this stage is attached to the PTFE gantry. If the gantry is juddering along the dowels (rails) of the linear guide it will shift the magnet over the hall sensor generating a higher error. The sensor will indicate that the guide is in the correct position even when it is slightly out of position as is being seen in Figure 5-24. The measured results follow the theory with an error of the angle that is within 1.75 mrad up to the 2100  $\mu\text{m}$  position. The error increases for larger positions and can be as high as 0.02 radians at the 3150  $\mu\text{m}$  position. Finer tolerances between the mating parts of the linear guide can be used to improve its performance and reduce the error. Removing the encoder from monitoring the Squiggle motor's position and putting this capability at the rotation point of the mirror



would allow an improvement in positioning accuracy. The motor can be driven open loop with step commands instead of position commands.

In its current form the error is within an acceptable level for the applications required travel range of up to the 0.122 radians. Figure 5-26 is the combination of the measured results from the optical and mechanical graphs. The graph also includes the Zemax raytrace and theory described in Figure 5-18.



**Figure 5-26: Combined Tip Module Graph**

The optical method has a higher measurement resolution and was used to measure the minimum incremental steps of the tip module. It measures an angle to within 1.4 mrad and the required resolution of the module is 0.9 mrad. The cameras in the optical method can be arranged to be more sensitive at detecting small angle changes within the SAM. The further the cameras are from the SAM, the greater the sensitivity. The same test procedure was applied as that used on the optical tests for the travel range with the step size command being altered to be 1  $\mu\text{m}$ .

To observe possible hysteresis a similar procedure to what was described was applied; SAM's mirror angle was altered in one direction with single micron Squiggle steps, an image was taken at each position until 10  $\mu\text{m}$  steps had been covered. The measurements were repeated

with the Squiggle motor moving in the opposite direction from this new position. This was repeated for 20 positions in this direction so that the original starting position was overshoot. From the new end position, the Squiggle motor was micron stepped in its original direction ten times. The result should be a return to the original output angle.

Figure 5-27 shows a set of measurements taken from the centre of the camera sensor. This is typical over the repeat sets of testing. It shows that for every individual micron step the Squiggle motor moved the change in angle was repeatedly  $78.54 \pm 5 \mu\text{rad}$ . When the motor's direction is reversed, it is clear that for the first step motion the delta angle is less than  $78.54 \mu\text{rad}$  but instead is  $\sim 17.45 \mu\text{rad}$ , a difference of  $61.09 \mu\text{rad}$ . This is due to the  $\pm 0.5 \mu\text{m}$  accuracy of the encoder at the Squiggle motor and friction within the linear guide. It is known that for every  $1 \mu\text{m}$  change of the Squiggle motor, the change in angle is  $50.6 \mu\text{rad}$  (Figure 5-26). This is acceptable as the application requires the angle resolution to be  $\leq 0.9 \text{ mrad}$ , therefore the Squiggle motor can meet this requirement by being stepped in  $2 \mu\text{m}$  increments.

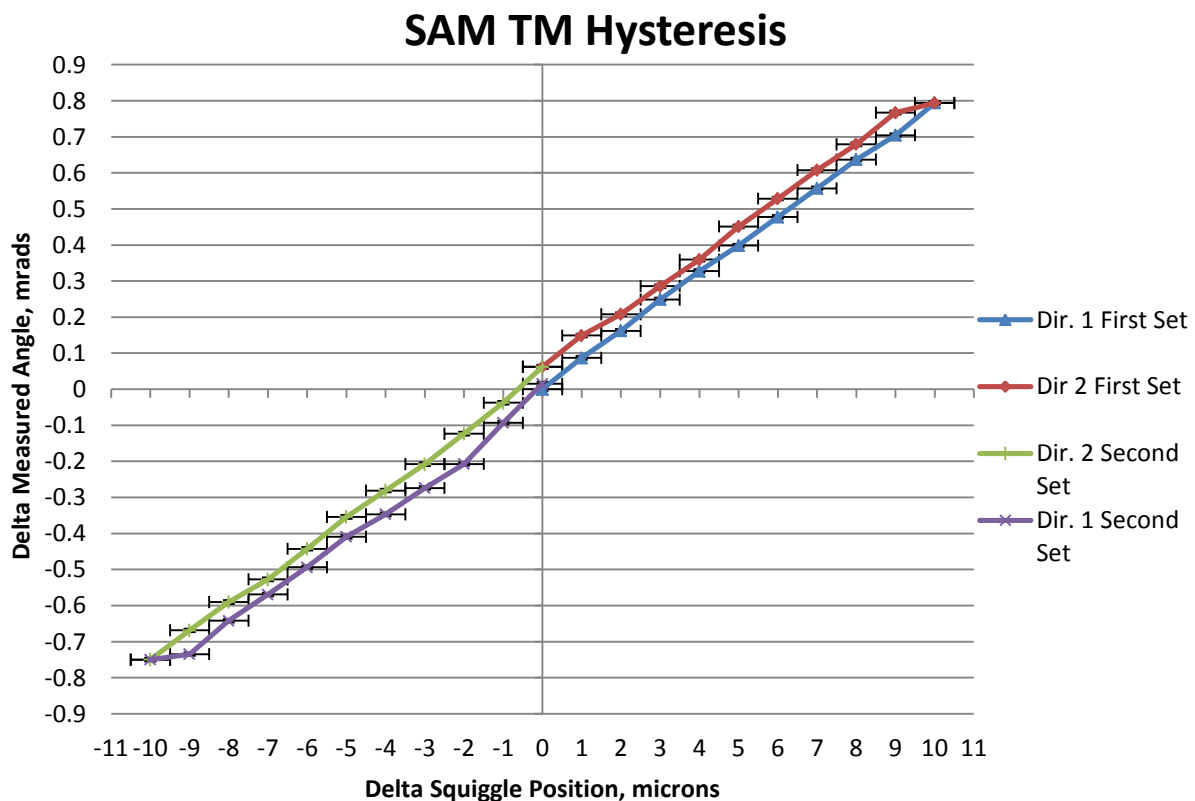
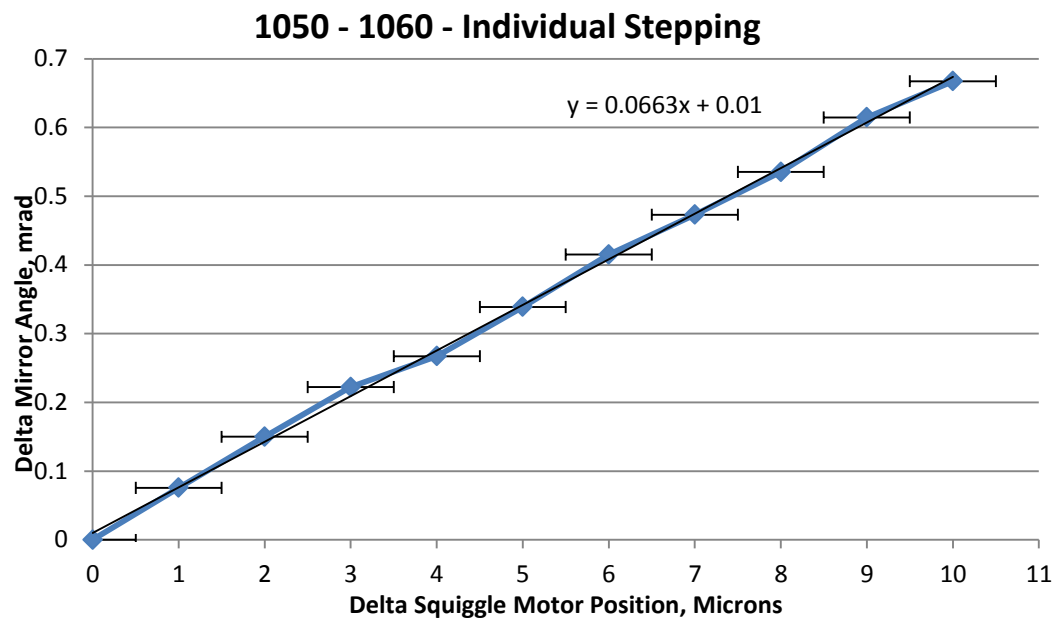


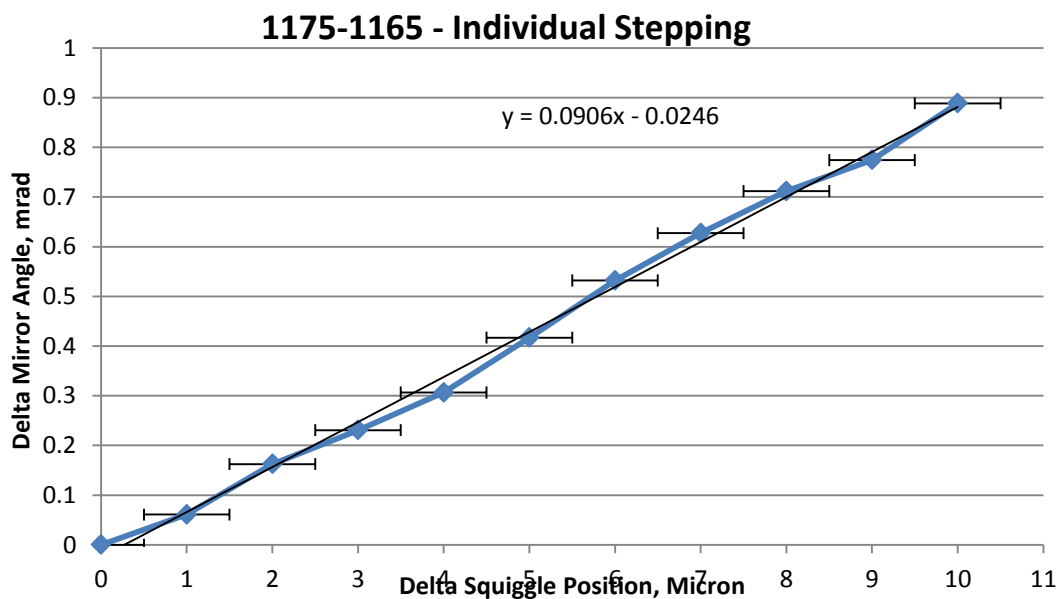
Figure 5-27: Single Squiggle Motor Step Motions

Figure 5-28 shows the change in angle for single Squiggle step motions at either end of the camera sensor, indicating its repeatability. The point of interest with the results is the

resolution value. At the bottom of the camera sensor, the value was 66.32  $\mu\text{rad}$  and at the top of the sensor, this was 90.76  $\mu\text{rad}$ , a difference of 24.43  $\mu\text{rad}$ . It was determined that the resolution from the centre of the sensor was 78.54  $\mu\text{rad}$ . This highlighted that the current SAM design resolution alters as the mirror angle varies. This is caused by the light being received at SAM shifting in x, y position as the mirror alters its tip angle. This variation has had little effect with the SAM tip module reaching commanded angles because of the much greater than required resolution, meaning that SAM meets the requirements. The resolution is also still well within the applications required  $\leq 0.9 \text{ mrad}$ .



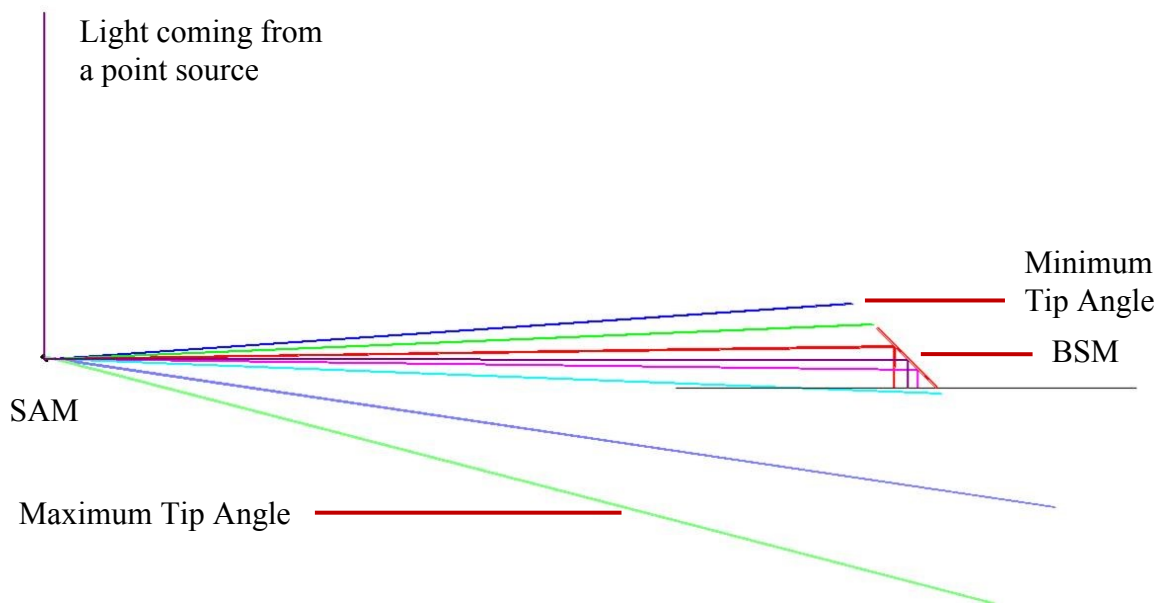
(a) Individual Stepping at the Bottom of the Sensor



(b) Individual Stepping at the Top of the Sensor

Figure 5-28: Individual Stepping Results

The tip stage has shown that it meets its expected performance mechanically but due to the centre of rotation it is not ideal optically. A Zemax model was produced to re-evaluate and confirm that SAM meets the travel range requirement, which it does. Figure 5-29 shows SAM receiving the light at the focal plane of a MOS instrument and reflecting to towards a BSM. Various angles including the two extremes of SAM's travel range, the dark blue beam and light green beam are illustrated. The beams overshoot the BSM's location showing that SAM can reflect the light to reach the BSM.



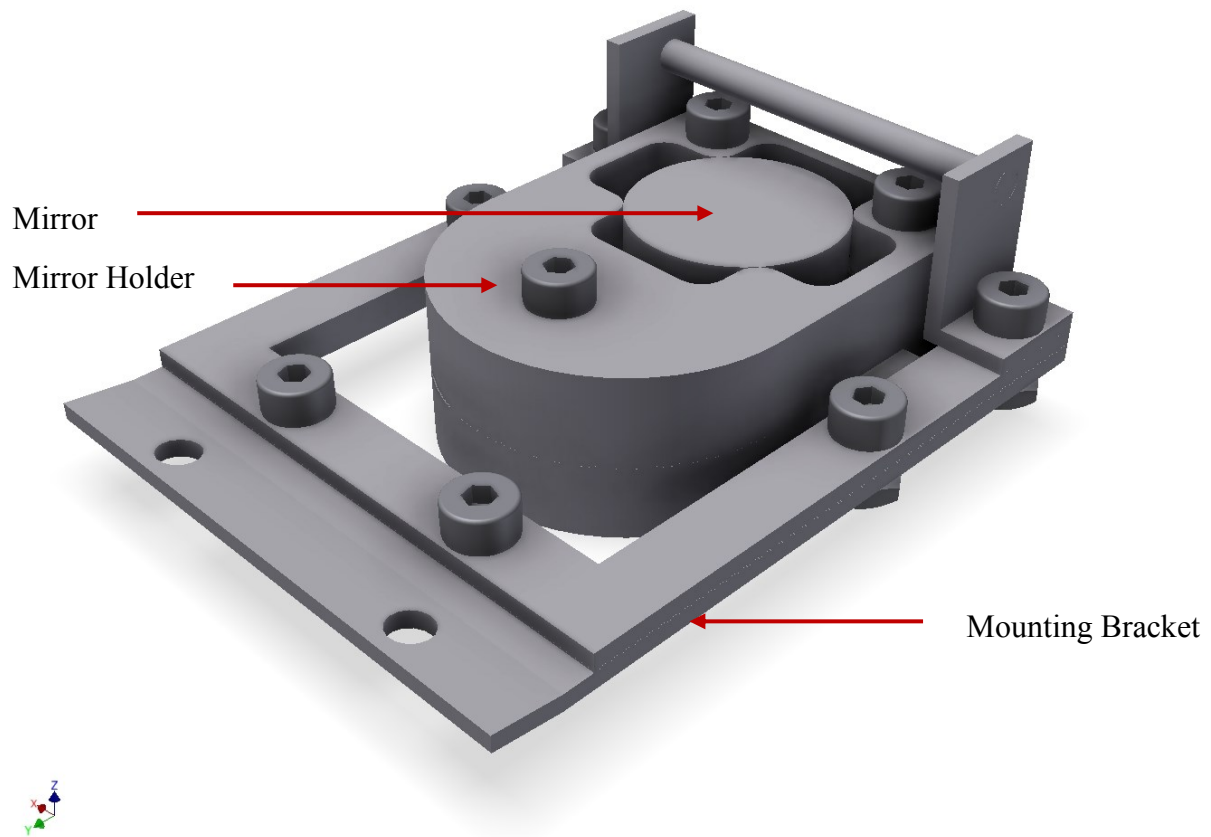
**Figure 5-29: Zemax Ray-trace of SAM in EAGLE**

Although the current SAM design has sufficient travel, there is concern with the varying resolution at different motor positions. Therefore, two techniques were devised that could improve the SAM tip module from an optical point of view.

- x-y Linear Stage Addition
- Mirror Module Re-design

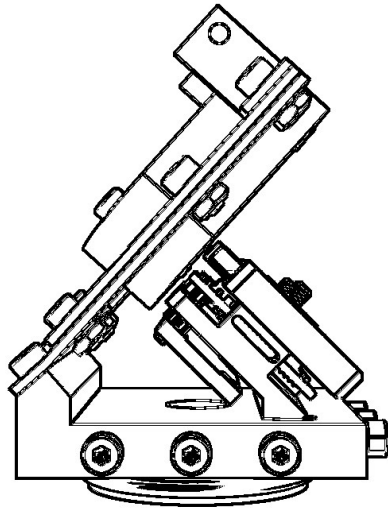
Two linear stages can be stacked underneath the rotation module to operate perpendicular to one another. The linear stages would correct for the light's offset in position as the mirror changes angle. This would increase the SAM unit height and complexity.

Another solution is to adapt the mirror module by moving the centre of rotation to be in line with the central axis of the mirror. An investigation into redesigning the mirror module without affecting the other modules resulted in Figure 5-30.

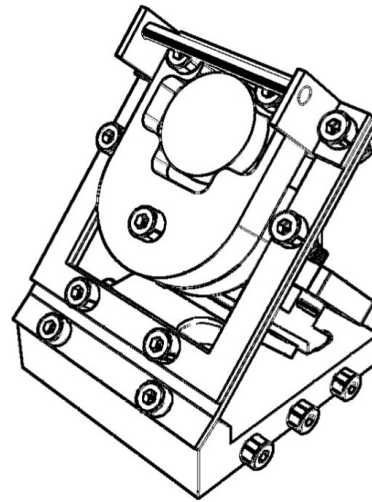


**Figure 5-30: Mirror Module Re-Design**

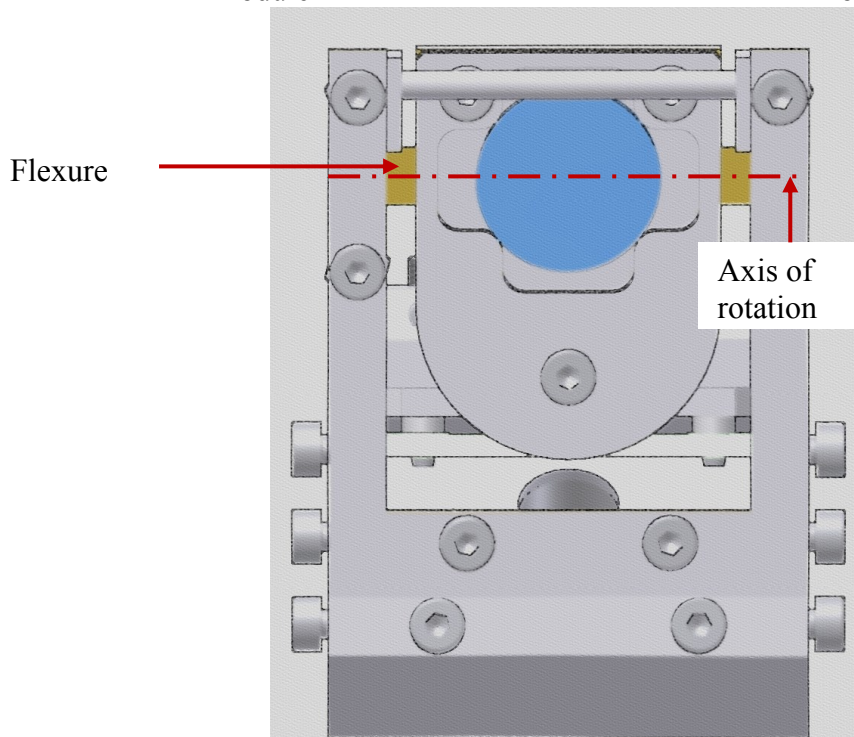
To move the rotation to the mirror axis it was required to alter the flexure so that it was going across the mirror. The Squiggle motor pushes against the holder producing a torsional force across the flexure. To highlight the motor's position in relation to the mirror a sketch has been provided in Figure 5-31(a) & (b). Figure 5-31(c) highlights the new location of the flexure and the axis of rotation. Instead of bending like a cantilever beam, like the current tip design, the flexures are twisted around this axis and is characterised by Equation 5-2 below. By rotating the mirror around this axis the receiving light at this mirror will have linear changes as the Squiggle motor is used.



(a) Side illustration of redesigned tip module



(b) Isometric illustration of redesigned tip module



(c) New flexure location

**Figure 5-31: Illustration of SAM Torsion Rotation**

Equation (5-2) determines the maximum angle achievable based on a set force applied solely by the motor, 0.2 N. The modulus of rigidity,  $G$ , is 26.95 GPa for aluminium [84] and  $K$  is the torsional stiffness constant. For a rectangular cross section  $K$  cannot be assumed to be the polar moment of inertia like it is with a circular beam. This is because sections of the beam warps when a torsional force is applied [85]. The torsional stiffness constant, equation (5-3, for a rectangular cross-section adjusts for the warping [85]. Table 5-10 details the symbol definitions used.

$$\theta = \frac{TL}{KG} \quad (5-2)$$

$$K = ab^3 \left[ \frac{16}{3} - 3.36 \frac{b}{a} \left( 1 - \frac{b^4}{12a^4} \right) \right] \quad (5-3)$$

Where the variables are:

**Table 5-10: Torsion Equation Variables**

Variable	Definition	Units
$\theta$	Deflection Angle	Radians
T	Torque	N.mm
L	Length	mm
K	Torsional Stiffness Constant	m <sup>4</sup>
G	Modulus of Rigidity	GPa
a	Half of the breadth of the flexure	mm
b	Half of the height of the flexure	mm

From the above equations, it was determined that a flexure with the following properties would provide a travel range of 0.107 rad:

- Length = 2 mm
- Breadth = 4 mm
- Height/Thickness = 100  $\mu$ m

This expected angle was confirmed through Finite Element Analysis (FEA) using Inventor 2014. It showed, based on the same material properties applied in Mathcad, that the rotation at the mirror centre is 98 mrad. It also showed that the mirror undergoes a displacement along the mirror plane towards the tip module's base. At the centre of the mirror, this has been determined to be 7.8  $\mu$ m and would have negligible effect on the output.

The analysis has indicated a difference between expected rotations of 9.041 mrad. On closer inspection at the flexure, it shows that it displaces in a parallel direction to the applied force of the Squiggle motor. This displacement is 0.54 mm at the centre of the mirror. This accounts for the difference between rotations from the expected Mathcad calculations. The rotation of 0.098 rad still encompasses the entire BSM.

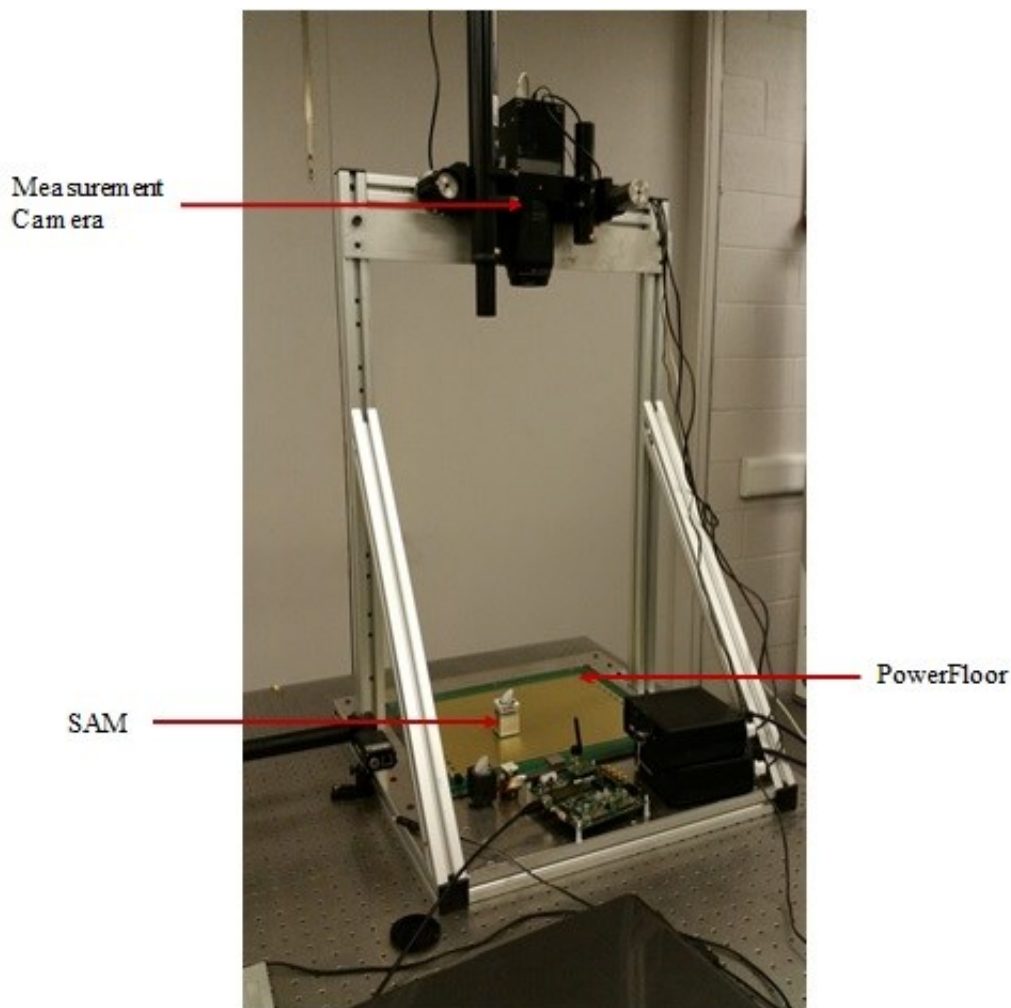
This change in mirror design would provide a constant linear resolution throughout the travel. Expected travel range is 0.098 rad and resolution of 0.105 mrad for micron steps.



### 5.8.2 Rotation Module Tests

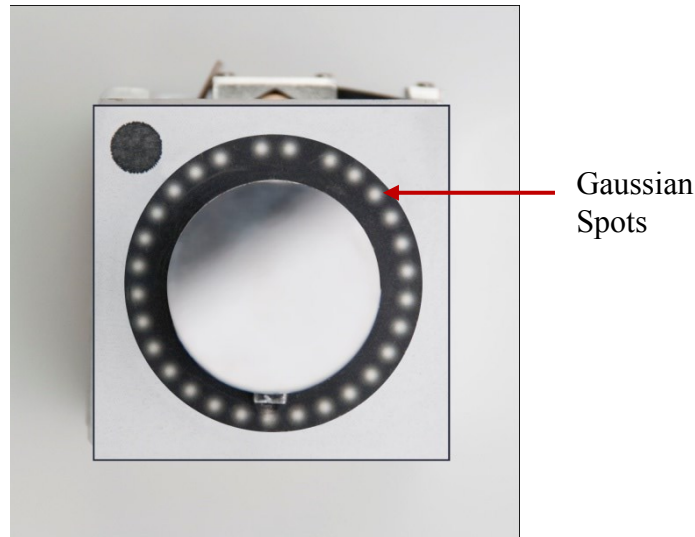
The rotation module is bi-directional and is limited through software to avoid damage between the wire links that go between the tip and rotation modules. To cover the entirety of the focal plane SAM would need to be able to rotate in either direction by  $> 3.142$  rad, making  $\leq 3.491$  rad an acceptable goal.

Due to the small size of the mechanism, an optical method was chosen to evaluate the rotation module to lower errors. A high-resolution black and white Lumenera camera was setup to image SAM from above, Figure 5-32(a). A pattern of spots is adhered to the centre of the tip module base. Images taken by the camera are processed to determine the orientation of the spot pattern, Figure 5-32(b). Each spot has a Gaussian profile that the software uses to determine the centre of the spots. A best-fit circle passing through the centre of each of the spots and it is the centre of this larger circle that determines the x, y centre of the target. The spot pattern has two spots grouped away from the rest to indicate a ‘front’.



(a) Rotation Module Test Setup



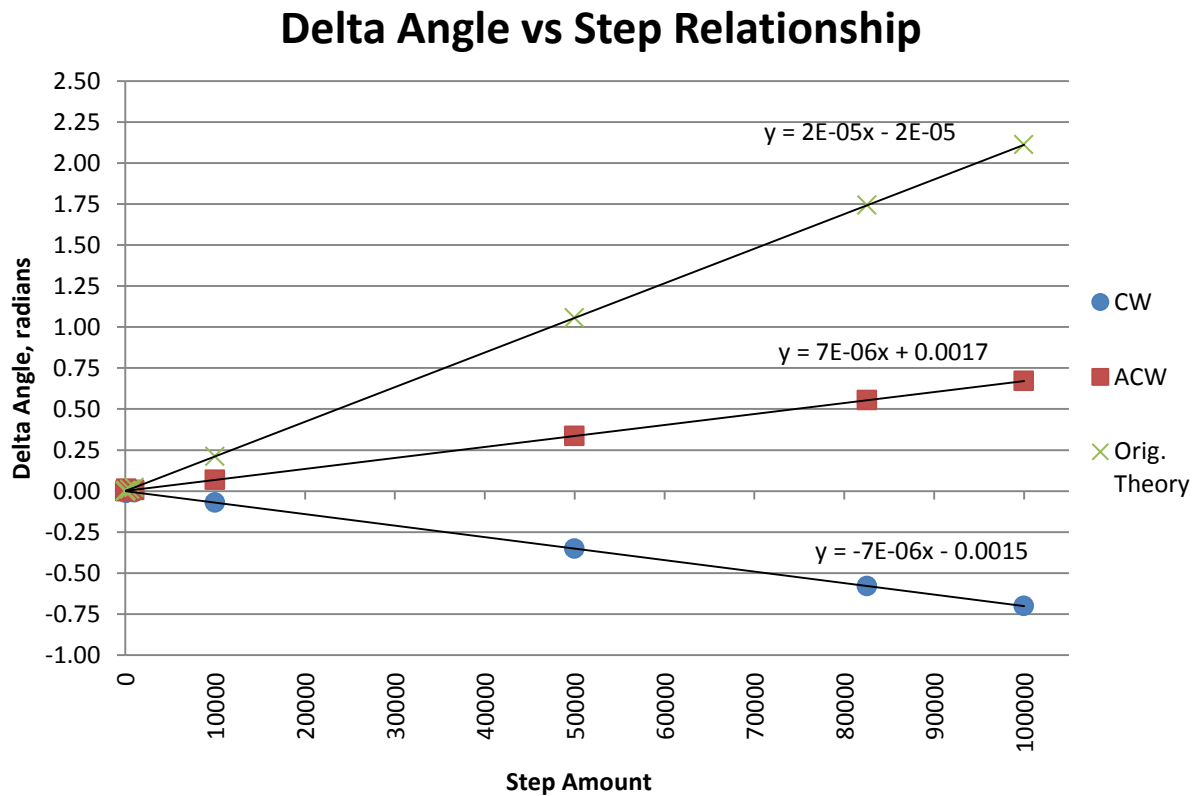


(b) Measurement Targets  
**Figure 5-32: Optical Measuring System**

This setup has an angular measurement resolution of  $17.5 \mu\text{rad}$ . This is acceptable as the required resolution is 1 mrad and the expected resolution is 0.2 mrad. The following was the test procedure:

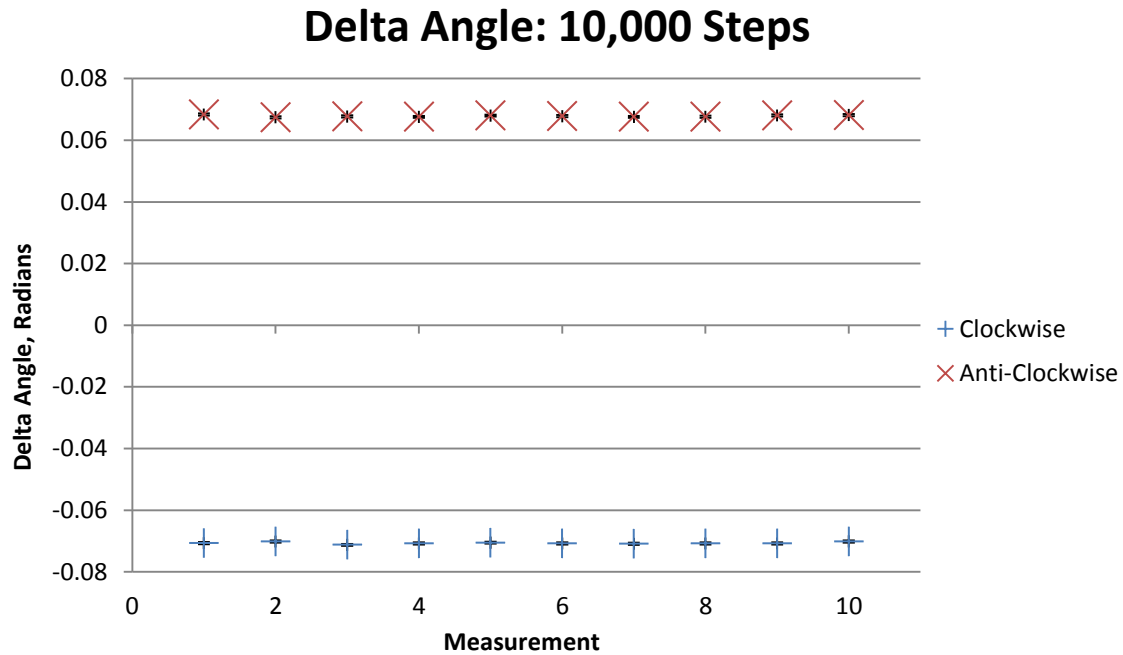
1. The SAM was set to its home position
2. The orientation recorded
3. The mirror was rotated by  $n$  steps and its position recorded
4. The mirror was rotated by a further  $n$  steps and the position recorded
5. Step four was repeated until five new orientations are achieved
6. The module was then rotated by  $n$  steps in the opposite direction and the position recorded
7. Step 6 was repeated 10 times
8. The module was then reversed once again by  $x$  steps and the position recorded
9. Step 8 was repeated 5 times

The compiled results from the various step tests provide an indication of the expected change in angle for a specific step command. Figure 5-33 shows the results of both clockwise and anti-clockwise rotations.



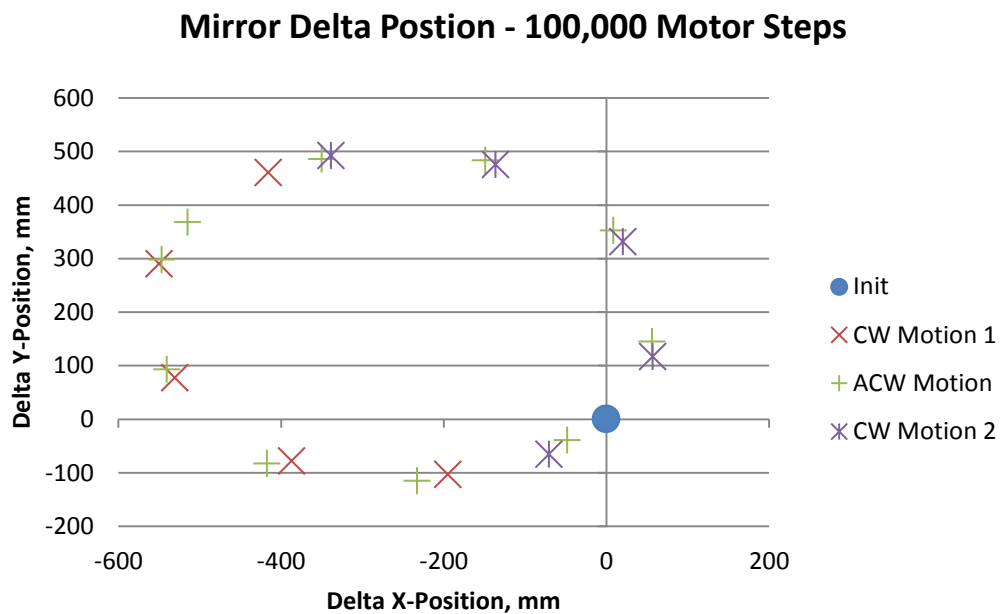
**Figure 5-33: RM Smoovy Motor Step to Angle Relationship**

Both directions indicate the same relationship that each step is equal to 7  $\mu$ rad. The results are encouraging as it repeatedly follows this relationship. However, the results differ from the theoretical by approximately a factor of 3, indicating a higher resolution compared to what would have been expected. It was determined that this was being caused by the electronics software on the drive chip. The chip receives the commands through the wireless communications and translates it to a form that can be processed and turned into pulse commands for the motor. The commands were being translated incorrectly and sending one third fewer pulses to the motor. Figure 5-34 reinforces this showing multiple measurements taken in both directions after a 10,000 motor step command. The standard deviation between the measurements was determined to be less than 0.35 mrad. It shows that the rotation module's change in angle for a 10,000 step command was equal to 70 mrad in either direction. It also shows that this is highly repeatable and is typical of results collected for different step amounts that were also measured.



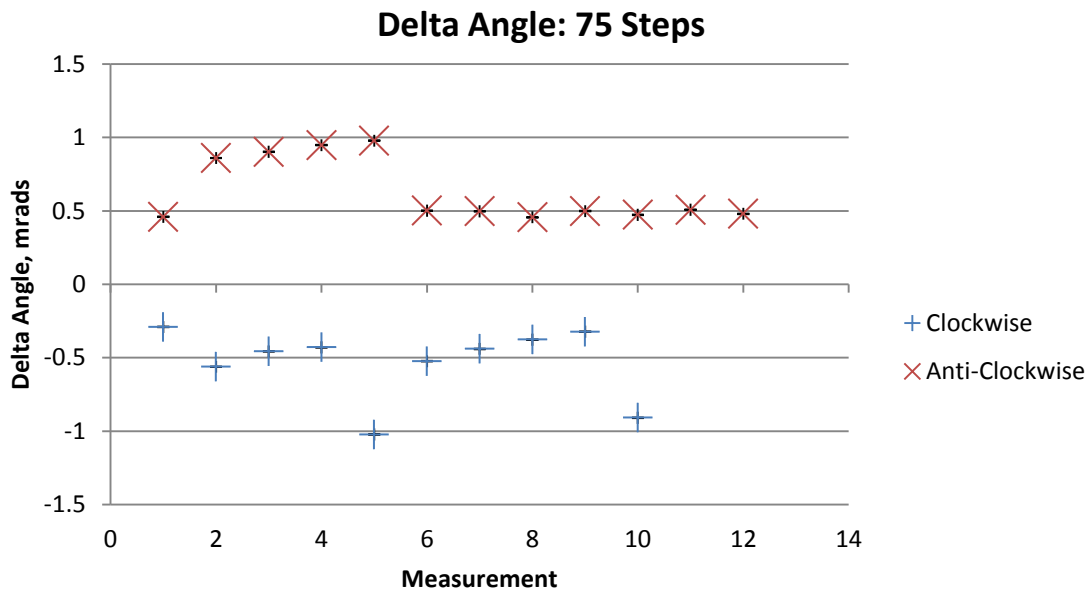
**Figure 5-34: Repeatability of 10,000 Step Command**

The mirror's x-y position would change during a rotation. Figure 5-35 illustrates that this shift is within a radius of 300  $\mu\text{m}$  and was due to the misalignment of the measurement target with the centre of rotation. Once this was compensated for it was found that when SAM rotates it would shift its x, y position by 6.7  $\mu\text{m}$ . It depends on the capabilities of a MOS instruments POM positioning system whether or not this is acceptable. If used in combination with MAPS for EAGLE, this would be acceptable assuming MAPS can get into position to within 3.4 microns.

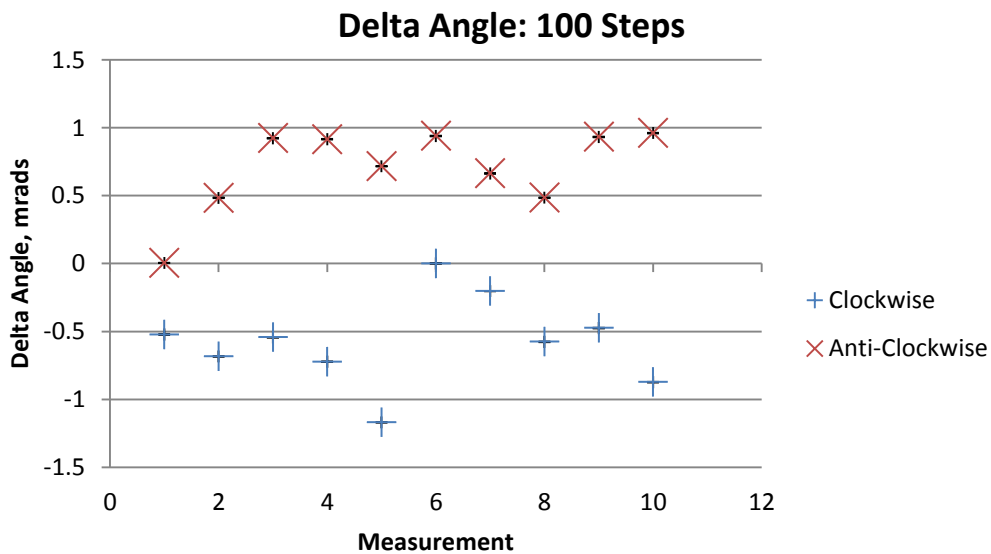


**Figure 5-35: Mirror's X-Y Shift during rotation**

The rotation module has a resolution requirement of  $\leq 1$  mrad with no reliable rotations below 75 motor steps. This was due to the required build-up of inertia within the motor to overcome the friction within the overall rotation module. At 75 motor steps and above the module rotated after each command as illustrated by Figure 5-36. The results show that the resolution is within 1 mrad. However, the repeatability is not consistent. During testing it was observed that the module upon executing a command would sometimes rotate again. By monitoring the electronics with an oscilloscope it was determined that the electronics is engaging an interrupt program and repeating an initial start-up command.



(a)



(b)

**Figure 5-36: Resolution Test Results**

## 5.9 Conclusions

The current SAM design is capable of guiding the light from a science object towards a BSM through the use of a rotation and tip module. Table 5-11 compares the requirements, expected performance and tested results, both optical and mechanical where applicable.

**Table 5-11: SAM Capabilities**

Module	Parameter	Requirement	Theoretical	Tested – Mech.	Tested – Optic.
Tip	Travel Range	$\geq 0.07$ rad	0.216 rad	0.225 rad	N/A
	Resolution	$\leq 0.175$ mrad	52.36 $\mu$ rad	52.36 $\mu$ rad	0.105 mrad
Rotation	Travel Range	$\pm 3.142$ rad	$\leq 3.491$ rad	$\pm 3.491$ rad	N/A
	Resolution	$\leq 1$ mrad	0.17 mrad	$\leq 1$ mrad	N/A

Although the current design meets the application requirements, the resolution of the tip module does change at different Squiggle motor positions. This is within acceptable limits and is due to where the centre of rotation for the mirror is located. Ideally, it should be in line with the centre of the mirror surface, so that as the mirror angle changes the light being reflected does not alter in x-y position on the mirror surface. This is considered more ideal as the resolution would be the same regardless of the Squiggle motors position. Solutions have been presented that can take this into account:

- x-y Linear Stage
- Mirror Module Redesign

The x-y linear stage is a solution requiring additional hardware to be added to the SAM. Ideally, an off-the-shelf linear mechanism that can be applied directly would be best as the development of a precise linear guide is costly. Another solution explored was redesigning the mirror module, which does not require additional hardware. A design was proposed using a torsional flexure with the current tip module. However, it does not have the same travel range as the current design (0.225 rad) it is capable of 0.098 rad, which still exceeds the application requirement of  $\geq 0.07$  rad. The current design has 3 times more travel available to it because of the travel range provided by the Squiggle motor in this configuration.

This study shows that a self-adjusting mirror can be developed to accurately correct for optical misalignment within multi-object instruments. Chapter 6 takes the information collected from this chapter and expands with the possibility of combining MAPS and SAM into a single integrated solution for the positioning of POMs and correcting of optical misalignment.

## Chapter 6 – Conclusion and Future Work

This research set out to determine if miniature mechatronic mechanisms could be used to position pick-off mirrors within multi-object instruments for astronomy, resulting in the development of such a robot and designing the framework for the characterisation of it and similar robots. The research also set out to determine if the functionality of the pick-off mirror could be enhanced to lessen the demands of beam steering mirrors. This led to the following goals:

- Characterise the MAPS robot, critically analysing the design to determine whether miniature robots are suitable for high precision positioning within multi-object instruments for astronomy
- Design a Self-Adjusting Mirror by adding functionality to the POM to correct for optical misalignments within MOS instruments
- Characterise SAM to determine whether a miniature self-adjusting mirror can replace some of the BSM functionality resulting in a smaller and more cost effective solution
- Prove that the use of micro robotics can be used in astronomy instrumentation

This work has shown that optical components such as pick-off mirrors can be positioned with a high precision (within tens of microns) using electromagnetically propelled miniature robots instead of piezoelectric ones. It has also shown that dead reckoning is not suitable for this type of application and closed-loop feedback is required. This thesis also showed that light path misalignments can be corrected using miniature adjustable mirrors as the pick-off mirrors, thus lessening the complexity of the beam steering mirrors in multi object spectrographs. Finally, this work has provided techniques for characterising miniature mechatronic mechanisms such as miniature robots for astronomy applications.

MAPS is a POM positioning system that incorporated an autonomous robot to meet the demanding requirements of the next-generation extremely-large telescopes. Multiple concepts were investigated for a MAPS and a specific design was developed and characterised. The research concluded that there are two possible categories of miniature robots that will be suitable for use in astronomical instruments namely: piezoelectric or electromagnetic driven robots. An electromagnetic propelled robot was developed as part of this study as it did not require hard lines to external electronics as described in Chapter 1. Miniature electromagnetic

robots had not previously been developed for high precision positioning tasks. The differentially steered robot that was developed is capable of high precision positioning, however the robot does not meet the high demands of MOS instruments although it shows potential. Table 6-1 shows the key requirements and compares this with the measured performance of the current design. A differentially steered robot design was chosen as it would be easier to assemble with fewer complex components.

**Table 6-1: EAGLE/MAPS Requirement/Capabilities Comparison**

	<b>EAGLE Requirement</b>	<b>MAPS Capability</b>
X – Y Fine Positioning	$\leq 10 \mu\text{m}$	$\leq 20 \mu\text{m}$
Z – Axis Angular Precision	$\leq 1 \text{ mrad}$	$\leq 1.4 \text{ mrad}$
Required Operation Time	$\geq 8 \text{ hours}$	Continuous
Footprint	$\leq 30 \text{ mm} \times 30 \text{ mm}$	$30 \text{ mm} \times 30 \text{ mm}$
Height	$\leq 60 \text{ mm}$	50 mm (without POM)

The research determined that the robot can be positioned to within 20 microns, a capability that has only been reported with piezoelectric robots. This showed that electromagnetic propelled miniature robots are capable of high precision positioning tasks within tens of microns. However, this did not meet the needs of the proposed MOS instrument. It was reported in Chapter 4 that the baseline requirement controlling the precision of the positioning of the POM could potentially be relaxed if the receiving optics could be assembled to a higher tolerance. Although this may be a possibility it is not ideal and the current design should be refined to find methods to improve the overall performance.

The PowerFloor technology that was adapted from a mobile phone charger design has proven to be an interesting power delivery method. This technology provides continuous power without constraining the robot's position or orientation. This was due to the need for the robot to operate for longer than 8 hours which is unusual for robots this size. The untethered miniature robots normally utilise a battery and only operate for less than an hour. The PowerFloor technology demonstrated within this study shows that miniature robot's that cannot have trailing wires can be powered continuously and still maintain full mobility. However, this technology still requires a small battery within the robot to overcome power losses during motion. This is due to the dynamic nature of the robot and it is perhaps possible for future robots to be designed that utilise the PowerFloor without a battery. This would require improving the interaction of the pick-ups with the PowerFloor. This may be achieved through redundancy by having more pick-ups than necessary to ensure that at any one time two or more points should be in contact with each track. It was also suggested within the research

that this can be improved by adjusting the parallelism of the power pick-up PCB with the PowerFloor.

MAPS has benefited the UK ATC with increased expertise and a knowledge base for miniature mechanisms that includes using a PowerFloor to provide continuous power over a large operating area, and an optical metrology system that can be used on various other projects. The expertise gained from MAPS and in particular with the miniature Smoovy motors is being applied to a Fibre-Fed Spectrograph currently under development. Astronomical targets will be picked-off by positioning fibres in exact positions on the focal plane using individual miniature 2-DOF robotic arms.

Based on the MAPS experience it was also possible to develop SAM. As SAM does not require the same amount of autonomy as MAPS, it lessens the complexity, however it was decided that encoders should be included within SAM, so it was certainly not a trivial task to design such a miniature precision mechanism. One challenge was finding suitable motors that have the balance of force, size, power and supporting control electronics. The Smoovy motor chosen was the size larger than that used in the MAPS robot this was due to the resolution requirement. Based on the experience gained with the MAPS Smoovy motor it was possible to adapt this to the SAM's rotation module with relative ease.

The tip module utilises a Squiggle motor that has proven very capable, although care is required with the linear guide. A summary of the results obtained in comparison to the expected results is provided in Table 6-2. The table shows that SAM meets the requirements for this application.

**Table 6-2: SAM Capabilities**

Stage	Capability	Requirement	Expected Results	Achieved Results
Tip	Travel Range	$\geq 45.4$ mrad	$\leq 0.216$ rad	$\leq 0.225$ rad
	Resolution	$\leq 0.9$ mrad	$\geq 0.175$ mrad	$\geq 0.11$ mrad (optically) $\geq 52.4$ $\mu$ rad
Rotation	Travel Range	$\geq 6.283$ rad	$\pm 3.491$ rad	$\pm 3.491$ rad
	Resolution	$\leq 1$ mrad	$\geq 0.19$ mrad	$\leq 1$ mrad with indications of 0.4 mrad

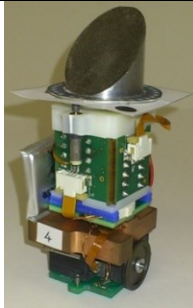
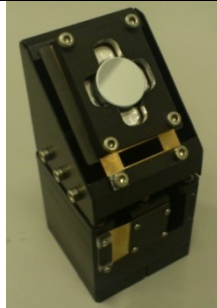
Through testing, it was showed that the reflected light had a varying resolution for different tip angles due to the location of the centre of rotation. Techniques were outlined that can mitigate the impact of this although the current design was still able to meet the application requirements.



## 6.1 MAPS & SAM Compared

Table 6-3 provides a comparison between the two projects highlighting their similarities and differences.

**Table 6-3: Miniature Astronomical Pick-Off Technologies**

		MAPS	SAM
			
<b>How are they interconnected?</b>	<b>Purpose</b>	Self-Positioning POMs	Self-adjust POM for optical field curvature corrections
	<b>Similarities</b>	Friction Drive Concept	Friction Drive Rotation Stage
		Smoovy Motor	Smoovy Motor (Rotation Stage – Larger Model)
		Self Sufficient POM	
		Potential to operate on various optical MOS instruments	
	<b>Evolution of Technology</b>	Positions the POM for desired science case	Alters the reflection angle at the POM to ensure reception of photons by detector
<b>How do they improve current MOS instruments?</b>	<b>Science</b>	Increase the amount of objects surveyed	Ensures objects are surveyed
	<b>Instrumentation</b>	Lessen the size & weight of the overall MOS instrument	
		Lower overall cost	
<b>What has this technology proved?</b>		Miniature autonomous robots can be used to deploy POMs	Miniature mechanisms can be used to correct for optical misalignment
<b>What has been developed?</b>		Robots that carry POMs, however require improved precision & reliability	Mirrors capable of correcting OFC but require a single rotation stage within a BSM
<b>What is the next step?</b>		Improve/re-design the robot	Incorporation of another DoF for new application possibilities

## 6.2 Precision Autonomous Mirror

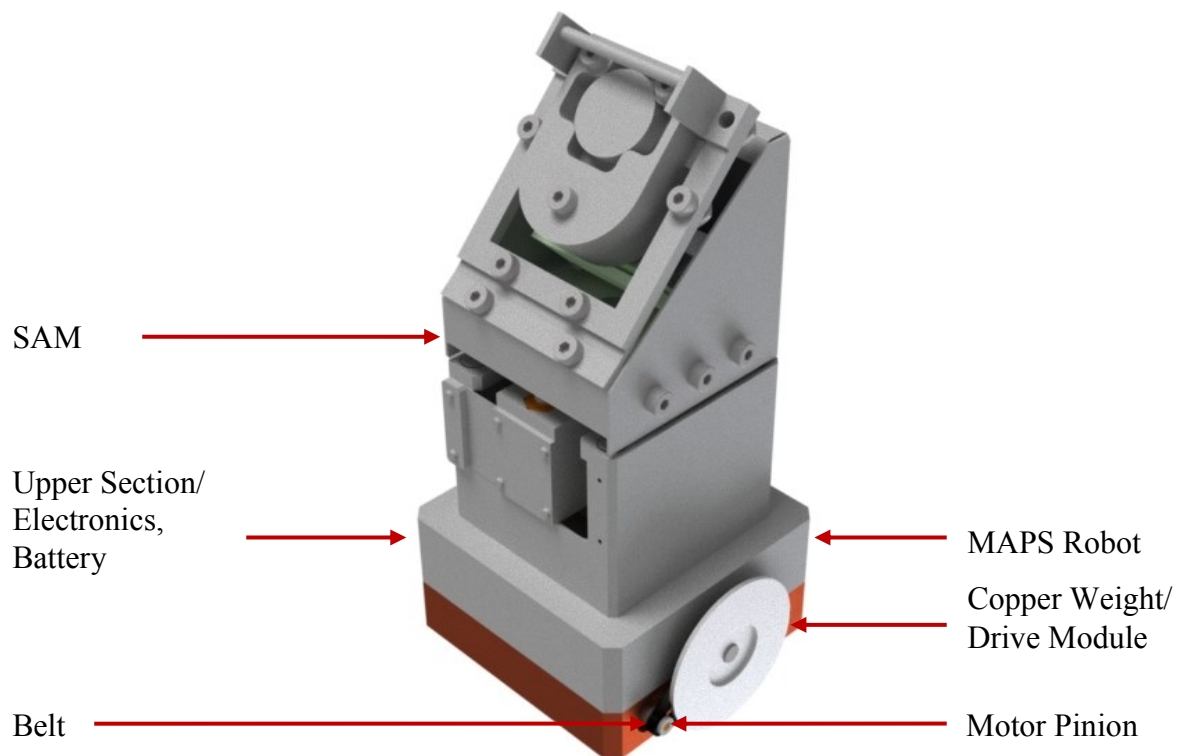
Finally, it is an interesting exercise to consider how SAM and MAPS could be combined to form PAM the Precision Autonomous Mirror.

Due to the size of the SAM, the MAPS robot footprint would need to be increased to incorporate the self-adjusting mirror. The increased size would provide space for the larger Smoovy 0515B motor to be used instead of the 0308B. The larger motor has a higher reduction gear head; higher torque output and is more robust allowing for greater radial loading compared to the current MAPS Smoovy motor. It utilises the same drive electronics as the smaller motor meaning that the current MAPS electronics would not need to be altered. The larger motor would also suffer from the problem of needing a minimum number of motor steps before motion will begin has shown by its use in the SAM rotation module. If the minimum motor steps are the same as the previous motor, which is possible as they are both of the same construction, then the higher reduction gear head means that the resolution will be better, potentially meeting the MOS requirements for positional accuracy.

To ease with assembly and manufacturing a belt driven configuration for the friction drive setup was analysed. A belt driven design could possibly ease assembly by removing the challenges associated with assembling the current designs springs and the fragility of the motors. The biggest concern for a belt driven design is possible slippage. Belt slippage would affect the linear performance of the robot. Slippage means missing steps during motion resulting in the robot undershooting its target position, directly affecting the positional accuracy. Although, metrology can compensate for this, it is not desirable to have slipping within the robot. The primary cause of slippage within belt driven systems is environmental factors such as dust and water lubricating the belt lowering the friction with the pulley. As the robot operates on an environmentally controlled instrument the likelihood of contaminates affecting the belt is low. A toothed belt can also be used reducing chances of slippage occurring.

Figure 6-1 shows the PAM concept, the MAPS section of the robot is the two bottom boxes. The drive module is copper so that the chassis incorporates the weight from the current MAPS robot. The robot's footprint has increased to 45 mm x 45 mm to accommodate the 35 mm<sup>2</sup> SAM footprint. The robot replaces the power module on the SAM and they are joined together through the existing magnets. This increase in footprint means extra internal space that can

accommodate the battery and electronics (upper section). The power pick-up PCB is located towards the front of the chassis. It is altered so that only three of the pick-ups are spring loaded, and the one at the front of the robot is fixed. This fixed pick-up doubles as the stabiliser that the robot's weight will favour. The CoG is set so that the weight distribution favours the front stabiliser. A spring plunger acts as a rear stabiliser forcing the balance back towards the front of the robot if there is any rocking. Magnets added to the bottom of the chassis generate a downward pulling force.

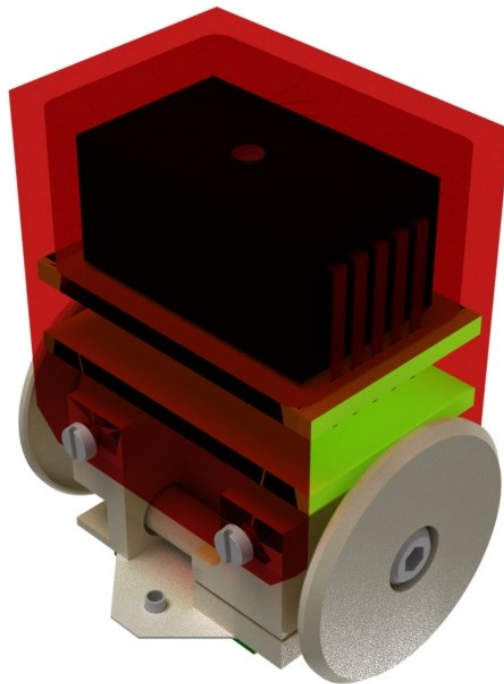


**Figure 6-1: Belt Driven Robot Concept**

SAM's control remains separate to PAM allowing both to operate as standalone devices. The MAPS metrology targets would need to be added to the top of the SAM for the current MAPS metrology module. This could potentially be etched into the SAM cover.

### 6.2.1 *Going One Step Further*

Miniature spectrometers are seeing a surge in development [86]. If these spectrometers continue development focussing on making them more sensitive with a higher spectral resolution, there could be a time when they operate within telescopes. MAPS-like robots could carry the miniature spectrometers into position instead of POMs, which merely reflect light into a spectrograph. Such a breakthrough in this technology could simplify telescopes but it is not at that stage yet. However, this would require advances from the robot as well. Current spectrometers are cryogenically cooled to reduce detector noise and limit the thermal background noise within the science channels. This would require the hypothesised miniature spectrograph robot to be capable of operating at temperatures around 100 K for the near-IR (lower temperatures for longer wavelengths). Figure 6-2 is a concept of the miniature robot spectrograph designed at the UK ATC. This model utilises the Ø5 mm Smoovy motor and a Hamamatsu mini spectrograph [86]

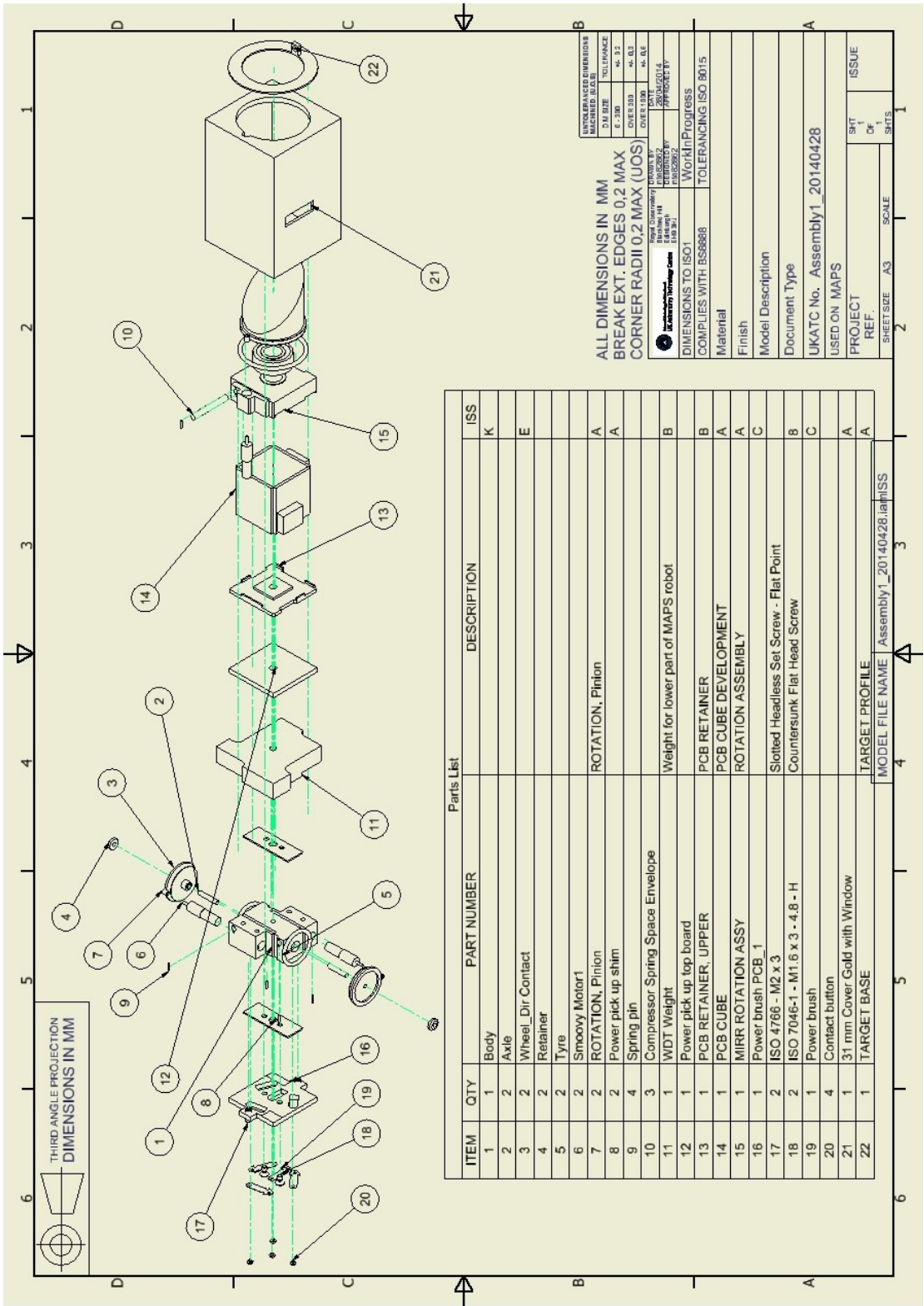


**Figure 6-2: Mini Robot Spectrograph Concept**

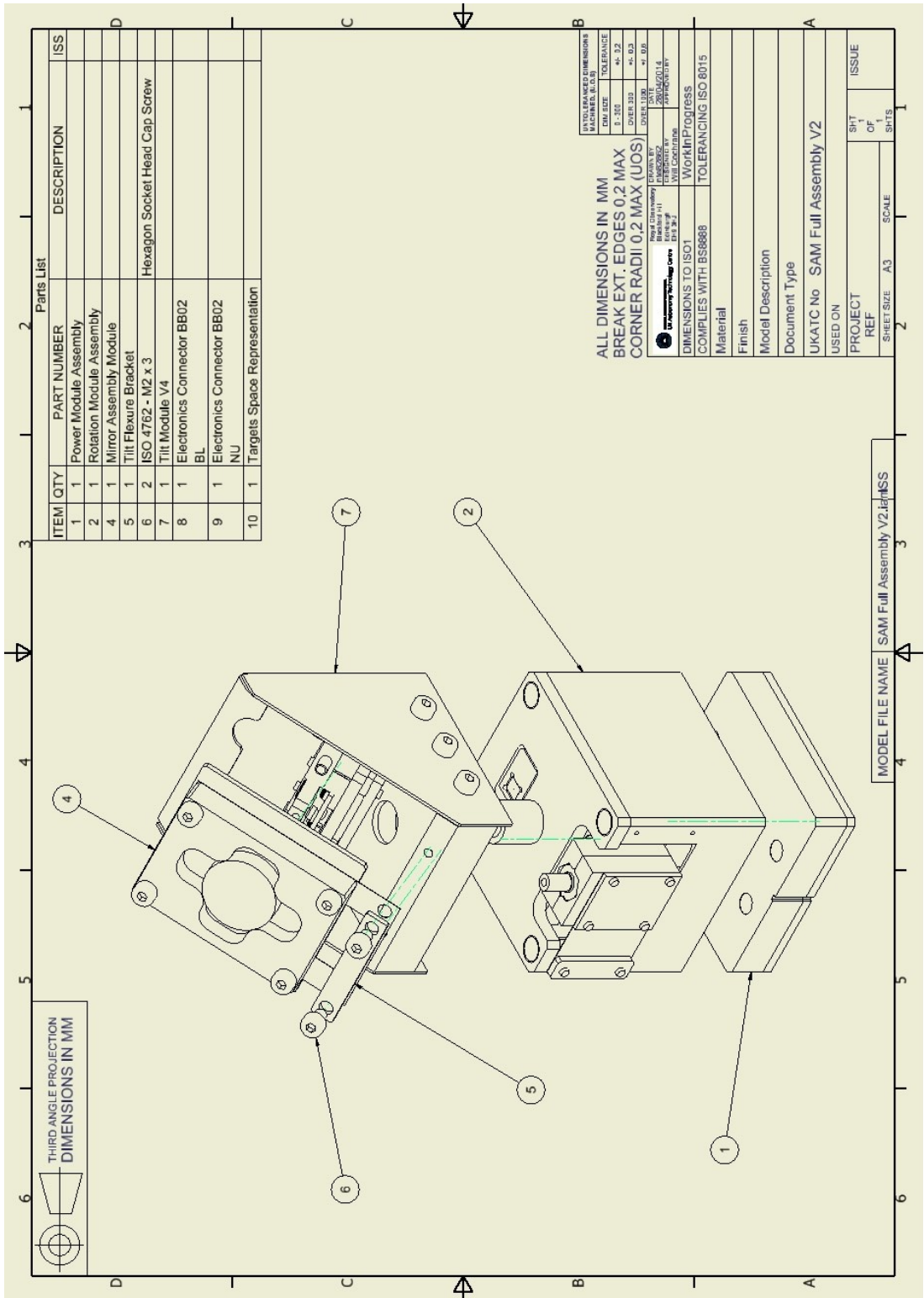
### **6.2.2 *Closing Remarks***

The technologies developed over the course of this research have shown that there is great potential for the use of miniature mechanisms for high-precision work in the field of astronomy. It has also shown that electromagnetically propelled robots are capable of high precision tasks to within tens of microns, an alternative to piezo driven robots. This provides the benefits of simpler low voltage electronics that thereby removes the need for a tether to an external electronics rack. This presents a path that could allow future instruments to be made smaller. By reducing the size of instruments it might be possible for instruments to share a focal plane allowing simultaneous observations. It is remarkable to think that something so small could potentially have a huge impact on the design of future astronomical instruments.

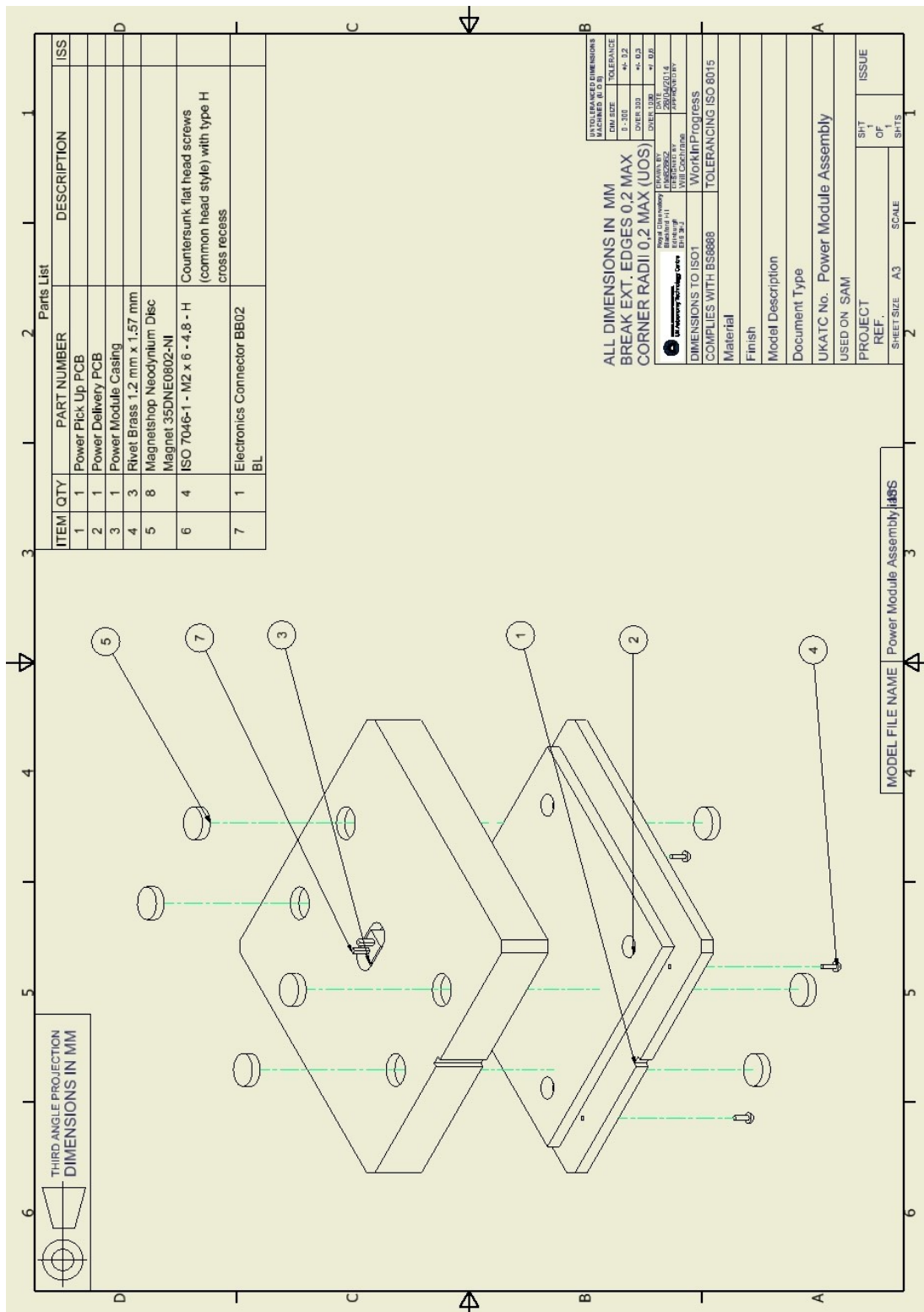
Appendix A– MAPS Assembly and BOM



Appendix B- SAM BOM



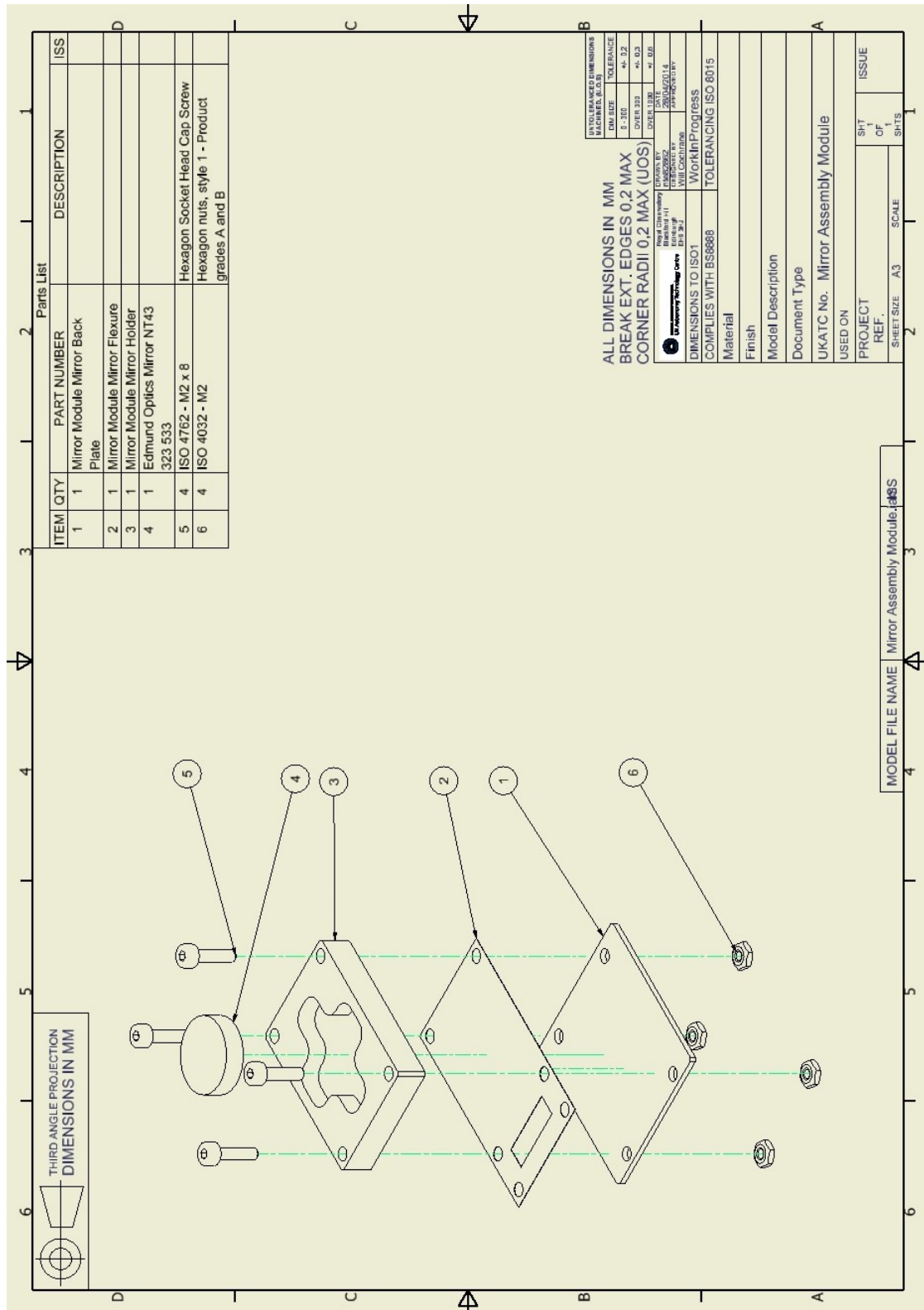












## References

- [1] European Southern Observatory, "Technology for Telescopes," ESO, 05 2014. [Online]. Available: <http://www.eso.org/public/teles-instr/technology/>. [Accessed 26 05 2014].
- [2] N. N. Weinberg, M. Milosavljevic and A. M. Ghez, "Stellar dynamics at the galactic center with an extremely large telescope," *The Astrophysical Journal*, vol. 622, pp. 878-891, 2005.
- [3] J. E. Nelson, "Design concepts for the California Extremely Large Telescope (CELT)," in *Proc. SPIE 4004, Telescope Structures, Enclosures, Controls, Assemblies/Integration/Validation, and Commissioning*, Munich, 2000.
- [4] A. H. a. F. S. J. M. Rodriguez, *Instrumentation for Large Telescopes*, Cambridge: Cambridge University Press, 1997.
- [5] European Southern Observatory, "The European Extremely Large Telescope," ESO, [Online]. Available: <https://www.eso.org/public/teles-instr/e-elt/>. [Accessed 06 03 2014].
- [6] J. Amos, "European Extremely Large Telescope given go-ahead," BBC News, 11 06 2012. [Online]. Available: <http://www.bbc.co.uk/news/science-environment-18396853>. [Accessed 06 03 2014].
- [7] European Southern Observatory, "E-ELT Optical Design," ESO, 16 06 2011. [Online]. Available: <http://www.eso.org/sci/facilities/eelt/telescope/design/>. [Accessed 06 03 2014].
- [8] J. Heanshaw, *Astronomical Spectrographs and their History*, Cambridge: Cambridge, 2009.
- [9] P. Massey and M. M. Hanson, *Astronomical Spectroscopy*, Cornell University Library, 2010.
- [10] P. Spanoudakis, L. Girienis, S. Henein, L. Lisowski, A. O'Hare, E. Onillon, P. Schwab and P. Theurillat, "Configurable slit-mask unit of the multi-object spectrometer for infra-red exploration for the Keck telescope: integration and tests," in *Proc. SPIE 7018, Advanced Optical and Mechanical Technologies in Telescopes and Instrumentation*, Marseille, France, 2008.
- [11] B. e. a. Buzzoni, "The ESO Faint Object Spectrograph and Camera (EFOSC)," *ESO Messenger*, vol. 38, pp. 9-13.
- [12] C. e. a. Snodgrass, "EFOSC2 Episode IV: A New Hope," *ESO Messenger*, vol. 132, pp. 18-19, 2008.
- [13] H. e. a. Dekker, "Multi Object Spectroscopy with the ESO Multi Mode Instrument at the NTT," *The Messenger*, vol. 63, pp. 73-76, 1991.
- [14] I. e. a. Appenzeller, "Successful commissioning of FORS1 - the first optical instrument on the VLT," *ESO Messenger*, vol. 94, 1998.
- [15] I. e. a. Appenzeller, "FORS - The focal reducer for the VLT," *ESO Messenger*, vol. 67, 1992.
- [16] I. Saviane, A. Smette and C. Dumas, "FORS User Manual," Very Large Telescope, 2010.
- [17] L. Schmidtbreick and e. al, "IOT Overview: Optical Multi-Object Spectrographs," in *The 2007 ESO Instrument Calibration Workshop*, Springer, 2008.
- [18] O. Le Fevre and e. al, "Commissioning and performances of the VLT-VIMOS," *SPIE*, vol. 4841, no. 1670, 2003.
- [19] O. Le Fevre, "Vimos User's Manual," 2002.
- [20] S. Nicholas Raines, S. S. Eikenberry and R. M. Bandyopadhyay, "FLAMINGOS-2: A near-IR Multi Object Spectrometer Ideal for Surveying the Galactic Centre," Cornell University Library, 2008.
- [21] L. Pasquini and e. al, "Installation and commissioning of FLAMES, the VLT multifibre facility," *ESO Messenger*, vol. 110, 2002.
- [22] L. Pasquini and e. al, "Performance of FLAMES at the VLT: one year of operation," *SPIE*, vol. 5492, no. 136, 2004.
- [23] P. Gillingham and e. al, "Mechanical features of the OzPoz fiber positioner for the VLT," *SPIE Optical and IR Instrumentation and Detectors*, vol. 4008, pp. 914-921, 2000.
- [24] G. Smith and e. al, "A survey of fiber-positioning technologies," *SPIE*, vol. 5495, pp. 348-359, 2004.
- [25] Q. A. Parker, "6dF: The new automated multi-object fibre-optic spectroscopy system on the UKST," Royal Observatory Edinburgh, [Online]. Available: <http://www.roe.ac.uk/ifa/wfau/6df/6df.html#SEC1>. [Accessed 09 04 2011].
- [26] I. R. Parry and e. al, "Autofib-2: an automated fiber positioned for the prime focus of the William Herschel Telescope," *SPIE*, vol. 2198, p. 125, 1994.

- [27] I. J. Lewis and e. al, "Autofib-2: commissioning results of a robotic multiobject fiber system for the William Herschel Telescope," *SPIE*, vol. 2871, p. 1318, 1997.
- [28] J. M. Hill and P. Hall, "MX Spectrometer Information," [Online]. Available: <http://abell.as.arizona.edu/~hill/mxspec/>. [Accessed 09 04 2011].
- [29] J. M. Hill, "The History of Multiobject Fiber Spectroscopy," *ASP Conference Fiber Optics in Astronomy II*, vol. 3, p. 77, 1988.
- [30] F. G. Watson, A. P. Oates and P. M. Gray, "FLAIR wide-field multiobject spectroscopy system," *SPIE*, vol. 1235, p. 736, 1990.
- [31] European Southern Observatory (ESO), "K-band Multi-Object Spectrograph - KMOS," European Southern Observatory, 09 11 2013. [Online]. Available: <http://www.eso.org/sci/facilities/develop/instruments/kmos.html>. [Accessed 11 03 2014].
- [32] W. D. Taylor, *Massive Stars and Miniature Robots: Today's Research and Tomorrow's Technologies*, Edinburgh: University of Edinburgh, 2013.
- [33] G. Weigelt and G. Baier, "R136a in the 30 Doradus nebula resolved by holographic speckle interferometry," *Astronomy and Astrophysics*, vol. 150, no. 1, pp. L18 - L20, 1985.
- [34] P. Barmby and J. P. Huchra, "M31 Globul Clusters in the Hubble Space Telescope Archive. I. Cluster Detection and Completeness," *The Astronomical Journal*, vol. 122, no. 5, pp. 2458 - 2468, 2001.
- [35] C. Cunningham, *Opticon JRA5: Smart Focal Planes*, Edinburgh: UK Astronomy Technology Centre, 2008.
- [36] G. Caprari, "Autonomous Micro-Robots: Applications and Limitations," *EPFL Doctorate Thesis*, 2003.
- [37] F. Haideri, *CAD/CAM and Automation 5th Edition*, Nirali Prakashan, 2008.
- [38] G. Caprari and e. al, "The Autonomous Micro Robot "Alice": a platform for scientific and commercial applications," *IEEE Micromechanics and Human Science*, pp. 231-235, 1998.
- [39] S. Kesner, J. Plante, P. Boston and S. Dubowsky, "A hopping mobility concept for a rough terrain search and rescue robot," in *Int. Conf. Clim. Walk. Robots Support. Technol. Mobile Mach.*, 2007.
- [40] C. Anthierens, A. Ciftci and M. Betemps, "Design of an electro pneumatic micro robot for in-pipe inspection," in *ISIE '99. IEEE International Symposium on Industrial Electronics*, 1999.
- [41] A. Brunete, M. Hernando and E. Gambao, "Modular Multiconfigurable Architecture for Low Diameter Pipe Inspection Microrobots," in *ICRA 2005. IEEE International Conference on Robotics and Automation*, 2005.
- [42] H. Schnetler, C. Evans and P. Jagourel, "EAGLE Instrument Requirements Specification," UK ATC, Edinburgh, 2009.
- [43] T. Deyle, "Pico," Hizook, 05 01 2009. [Online]. Available: <http://www.hizook.com/projects/pico>. [Accessed 12 03 2014].
- [44] Sandia National Laboratories, "News Releases," Sandia National Laboratories, 31 01 2001. [Online]. Available: <http://www.sandia.gov/media/NewsRel/NR2001/minirobot.htm>. [Accessed 12 03 2014].
- [45] Poor Robot, "Pico," 08 10 2007. [Online]. Available: [http://www.hizook.com/files/publications/Pico\\_The\\_Micro\\_Robot.pdf](http://www.hizook.com/files/publications/Pico_The_Micro_Robot.pdf). [Accessed 12 03 2014].
- [46] J. McLurkin, "The Ants: A Community of Microrobots," MIT, [Online]. Available: <http://ai.mit.edu/projects/ants>. [Accessed 09 04 2011].
- [47] Epson, "Monsieur," [Online]. Available: [http://global.epson.com/company/corporate\\_history/milestone\\_products/pdf/23\\_monsieur.pdf](http://global.epson.com/company/corporate_history/milestone_products/pdf/23_monsieur.pdf). [Accessed 17 03 2014].
- [48] G. Caprari, K. O. Arras and R. Siegwart, "The Autonomous Miniature Robot Alice: from Prototypes to Applications," *IEEE Intelligent Robots and Systems*, pp. 793-798, 2000.
- [49] A. T. Nguyen and S. Martel, "A New Actuation Mechanism Based on a Synchronized Vibrating Platform for Micro- and Nanofactories," *5th IEEE International Workshop on Microfactories*, 2006.
- [50] Iminia Technologies, "miBot BT-11," 2013. [Online]. Available: [http://www.imina.ch/sites/default/files/product\\_pdf/iminatechnologies\\_mibot\\_technicalspecifications\\_en\\_web.pdf](http://www.imina.ch/sites/default/files/product_pdf/iminatechnologies_mibot_technicalspecifications_en_web.pdf). [Accessed 28 05 2014].
- [51] J. Gilbert, M. Goodwin, J. Heijmans, R. Muller, S. Miziarski, J. Brzeski, L. Waller, W. Saunders, A. Bennet and J. Tims, "Starbugs: all-singing, all-dancing fibre positioning robots," in *SPIE 8450, Modern Technologies in Space- and Ground-based Telescopes and Instrumentation II*, Amsterdam, 2012.

- [52] M. Goodwin, J. Heijmans, I. Saunders, J. Brzeski, W. Saunders, R. Muller, R. Haynes and J. Gilbert, "Starbugs: focal plane fiber positioning technology," in *Proc. SPIE 7739, Modern Technologies in Space- and Ground-based Telescopes and Instrumentation*, San Diego, 2010.
- [53] S. Fahlbusch, S. Fatikow, J. Seyfried and A. Buerkle, "Flexible Microrobotic System MINIMAN: Design, Actuation Principle and Control," in *IEEE/ASME International Conference on Advanced Intelligent Mechatronics*, 1999.
- [54] J. Lopez-Sanchez, U. Simu, M. Puig-Vidal, S. Johansson, P. L. Miribel, E. Montane, S. Bota and J. Santier, "A Miniature Robot driven by Smart Power Integrated Circuits," in *IEEE/RSJ International Conference on Intelligent Robots and Systems*, Lausanne, 2002.
- [55] H. Schnetler, "CFI Micro-Autonomous Positioning System Final Analysis and Design Report," UK ATC, Edinburgh, 2010.
- [56] H. M. & H. Schnetler, "E-TRE-ATC-567-0030: EAGLE POS Analysis and Design," UK ATC, Edinburgh, 2009.
- [57] H. S. P. J. Helen McGregor, "Livelihood ROE - EAGLE Project - EAGLE POS Analysis and Design Document (E-TRE-ATC-567-0030)," 29 09 2009. [Online]. Available: [https://livelihood.roe.ac.uk/Livelihood/livelihood.exe/E-TRE-ATC-567-0030\\_POS\\_Analysis\\_and\\_Design\\_Document.pdf?func=doc.Fetch&nodeid=5386300&docTitle=E-TRE-ATC-567-0030%20POS%20Analysis%20and%20Design%20Document&vernum=17&verType=pdf](https://livelihood.roe.ac.uk/Livelihood/livelihood.exe/E-TRE-ATC-567-0030_POS_Analysis_and_Design_Document.pdf?func=doc.Fetch&nodeid=5386300&docTitle=E-TRE-ATC-567-0030%20POS%20Analysis%20and%20Design%20Document&vernum=17&verType=pdf). [Accessed 08 08 2012].
- [58] Faulhaber, "Brushless DC-Micromotors, Series 0308...B," 2012. [Online]. Available: [http://www.faulhaber.com/uploadpk/EN\\_0308\\_B\\_DFF.pdf](http://www.faulhaber.com/uploadpk/EN_0308_B_DFF.pdf). [Accessed 27 4 2012].
- [59] Faulhaber, "Planetary Gearheads Series 03A - Datasheet," 2014. [Online]. Available: <https://fmcc.faulhaber.com/productdetails.xhtml#jump>. [Accessed 15 01 2014].
- [60] Faulhaber, "BLD 05002 S Operating Instructions," Faulhaber, 2012.
- [61] Faulhaber, "Technical Information," Dr. Fritz Faulhaber GmbH & Co. KG, Schönaich, 2012.
- [62] W. A. Cochrane, "Conceptual Design of an Autonomous Micro-Robot for Astronomical Instrumentation," Heriot Watt University, Edinburgh, 2009.
- [63] S. T. Smith, *Foundations of Ultra-Precision Mechanism Design*, 2005.
- [64] Faulhaber, "Micro Planetary Gearheads, Series 03A," 2012. [Online]. Available: [http://www.faulhaber-group.com/uploadpk/EN\\_03A\\_DFF.pdf](http://www.faulhaber-group.com/uploadpk/EN_03A_DFF.pdf). [Accessed 27 04 2012].
- [65] DuPont, "DuPont Vespel SP-3 Polyimide Isostatic Shapes," DuPont, 2010.
- [66] S. P. & P. Thompson, "MAPS Dreamact User Guide," Dreamact, Edinburgh, 2010.
- [67] PureEnergy Solutions, "Wire-Free Power - Technology," PureEnergy, 2014. [Online]. Available: <http://pureenergy.com/our-technologies/wire-free-solutions/technology/>. [Accessed 15 01 2014].
- [68] Faro Europe GmbH & Co. KG, "Faro Laser Tracker X and Xi: Measuring at the speed of light - Operation, Technical Data & Applications," Faro, Stuttgart-Wellmndorf, 2005.
- [69] R. J. Ramakrishna, *The Characterization of a Micro-Autonomous Robot for Use in Astronomical Instrumentation*, Edinburgh: Heriot Watt University, 2014.
- [70] C. W. de Silvia, *Mechatronics: An Integrated Approach*, CRC Press, 2005.
- [71] P. Jagourel, "Target Acquisition System Analysis and Design Document," GEPI, 2009.
- [72] Physik Instrumente, "Fast Steering Mirrors/Active Optics," [Online]. Available: [http://www.physikinstrumente.com/en/pdf\\_extra/2009\\_PI\\_Fast\\_Steering\\_Mirror\\_Scanner\\_Catalog.pdf](http://www.physikinstrumente.com/en/pdf_extra/2009_PI_Fast_Steering_Mirror_Scanner_Catalog.pdf). [Accessed 19 03 2014].
- [73] Physik Instrumente, "P-882, P-883, P-885, P-887, P-888 PICMA Stack Multilayer Piezo Actuators," Physik Instrumente, 2013. [Online]. Available: <http://www.physikinstrumente.com/en/products/prdetail.php?sortnr=100810>. [Accessed 19 03 2014].
- [74] Physik Instrumente, "E-831 OEM Piezo Driver," Physik Instrumente, 2013. [Online]. Available: <http://www.physikinstrumente.com/en/products/prdetail.php?sortnr=601950>. [Accessed 19 03 2014].
- [75] Thorlabs, "Small Beam Diameter Scanning Galvo Mirror Systems," 2014. [Online]. Available: <http://www.thorlabs.de/thorcat/20300/GVS012-Manual.pdf>. [Accessed 19 03 2014].
- [76] Laser 2000, "System Components for Integrators," 05 2010. [Online]. Available: [http://www.laser2000.co.uk/ds/DS\\_00771.pdf](http://www.laser2000.co.uk/ds/DS_00771.pdf). [Accessed 19 03 2014].
- [77] Cambridge Technology, "High-Stability Galvanometers," 2013. [Online]. Available:

- [http://www.camtech.com/index.php?option=com\\_content&view=article&id=104&Itemid=78](http://www.camtech.com/index.php?option=com_content&view=article&id=104&Itemid=78). [Accessed 19 03 2014].
- [78] Mirrorcle Technologies Inc., "MEMS Mirrors," Mirrorcle Technologies Inc., 2014. [Online]. Available: <http://www.mirrorcletech.com/devices.html>. [Accessed 19 03 2014].
  - [79] Mahalik, Mechatronics: Principles, Concepts and Applications, Tata McGraw-Hill Publishing Company Limited, 2003.
  - [80] J. Samitier, M. Puig-Vidal, J. Lopez, P. Miribel, J. M. Lopez-Villegas, R. Casanella, C. Madrid and A. Juarez, "Manipulation tools for biological applications using microrobots with nano-range accuracy," in *SPIE - The International Society for Optical Engineering*, 2003.
  - [81] M. Goodwin, J. Heijmans, I. Saunders, J. Brzeski, W. Saunders, R. Muller, R. Haynes and J. Gilbert, "Starbugs: focal plane fiber positioning technology," in *SPIE 7739, Modern Technologies in Space- and Ground-based Telescopes and Instrumentation*, 2010.
  - [82] MicroE Systems, "Chipcon Encoder Datasheet," MicroE Systems, Bedford, 2011.
  - [83] N. S. Technologies, "New Scale Technologies - About New Scale Technologies," 2006 - 2012. [Online]. Available: [http://www.newscaletech.com/nst\\_background.html](http://www.newscaletech.com/nst_background.html). [Accessed 10 08 2012].
  - [84] Budynas-Nisbett, Shigley's Mechanical Engineering Design 8th Edition, McGraw-Hill, 2006.
  - [85] W. C. Young and R. G. Budynas, Roark's Formulas for Stress and Strain - 7th Edition, McGraw-Hill, 2002.
  - [86] Hamamatsu, "Mini-Spectrometer MS Series C10988MA-01," Hamamatsu, [Online]. Available: <http://www.hamamatsu.com/us/en/product/category/5001/4016/C10988MA-01/index.html>. [Accessed 31 03 2014].
  - [87] A. T. T. a. R. Jedicke, "New Generation Ground-Based Optical/Infrared Telescopes," in *Encyclopedia of the Solar System*, University of Hawaii, Academic Press, 2006.
  - [88] E. S. Observatory, "The European Extremely Large Telescope ("E-ELT") Project," European Southern Observatory (ESO), 13 April 2012. [Online]. Available: <http://www.eso.org/sci/facilities/eelt/>. [Accessed 13 April 2012].
  - [89] S. Daily, "Ground-Based Telescopes have an Extremely Large Future," Space Daily, 11 April 2005. [Online]. Available: <http://www.spacedaily.com/news/telescopes-05p.html>. [Accessed 13 April 2012].
  - [90] E. S. O. (ESO), An Expanded View of the Universe: Science with the European Extremely Large Telescope, ESO.
  - [91] P. M. a. M. M. Hanson, Astronomical Spectroscopy, Cornell Uni. Lib, 2010.
  - [92] J. Allington-Smith, "Integral Field Spectroscopy," 30 June 1998. [Online]. Available: [http://star-www.dur.ac.uk/~jra/integral\\_field.html](http://star-www.dur.ac.uk/~jra/integral_field.html). [Accessed 13 April 2012].
  - [93] C. Vanderriest, "A fiber-optics dissector for spectroscopy of nebulosities around quasars and similar objects," *Publications of Astronomical Society*, vol. 92, p. 858, 1980.
  - [94] B. B. e. al, "The ESO Faint Object Spectrograph and Camera (EFOSC)," *ESO Messenger*, pp. 9 - 13.
  - [95] C. Snodgrass, "EFOSC2 Episode IV: A New Hope," *ESO Messenger*, pp. 18 - 19, 2008.
  - [96] H. D. e. al, "Multi Object Spectroscopy with the ESO Multi Mode Instrument at the NTT," *The Messenger*, pp. 73 - 76, 1991.
  - [97] Aerospace Online, "Smoovy Series 0308...B: 3mm Brushless DC Motor," 1996 - 2012. [Online]. Available: <http://www.aerospaceonline.com/doc.mvc/Smoovy-Series-0308B-3mm-Brushless-DC-Motor-0001?VNETCOOKIE=NO>. [Accessed 27 04 2012].
  - [98] W. Taylor, "His Thesis".
  - [99] R. Fu, *V. Piezoelectric Actuation*, Edinburgh: Heriot Watt University, 2011.
  - [100] L. muRata Manufacturing Co., "Micromechatronics," muRata Manufacturing Co. Ltd, [Online]. Available: <http://www.google.ch/imgres?q=piezoelectric+principle&um=1&hl=en&client=firefox-a&sa=N&rls=org.mozilla:en-GB:official&biw=786&bih=766&tbm=isch&tbnid=r0P5JLgsvS5SZM:&imgrefurl=http://www.murata.com/products/micromechatronics/feature/actuator/index.html&doc>. [Accessed 08 08 2012].
  - [101] H. M. a. P. Hastings, "Livelihood ROE - EAGLE Project," 24 11 2008. [Online]. Available: [https://livelihood.roe.ac.uk/Livelihood/livelihood.exe/POS\\_Architecture\\_%28Discussion%29.pdf?func=doc.Fetch&nodeid=2390194&docTitle=POS%20Architecture%20%28Discussion%29&vernum=20&verType=pdf](https://livelihood.roe.ac.uk/Livelihood/livelihood.exe/POS_Architecture_%28Discussion%29.pdf?func=doc.Fetch&nodeid=2390194&docTitle=POS%20Architecture%20%28Discussion%29&vernum=20&verType=pdf). [Accessed 08 08 2012].



- [102] A. S. AG, "Attocube - Nanopositioners - Working Principle," 2001 - 2012. [Online]. Available: [http://www.attocube.com/nanoPOSITIONING/working\\_principal.html](http://www.attocube.com/nanoPOSITIONING/working_principal.html). [Accessed 09 08 2012].
- [103] Attocube, "Attocube - Nanopositioning - rotators - ANR51," 03 2012. [Online]. Available: [http://www.attocube.com/nanoPOSITIONING/ANR51/Specifications\\_ANR51.pdf](http://www.attocube.com/nanoPOSITIONING/ANR51/Specifications_ANR51.pdf). [Accessed 09 08 2012].
- [104] Attocube, "attocube - nanopositioners - rotators - ANR31," 03 2012. [Online]. Available: [http://www.attocube.com/nanoPOSITIONING/ANR31/Specifications\\_ANR31.pdf](http://www.attocube.com/nanoPOSITIONING/ANR31/Specifications_ANR31.pdf). [Accessed 09 08 2012].
- [105] Attocube, "Attocube - Nanopositioners - Goniometers - ANGt50," 03 2012. [Online]. Available: [http://www.attocube.com/nanoPOSITIONING/ANGt50/Specifications\\_ANGt50.pdf](http://www.attocube.com/nanoPOSITIONING/ANGt50/Specifications_ANGt50.pdf). [Accessed 09 03 2012].
- [106] Attocube, "Attocube - nanopositioners - goniometers - ANGp50," 03 2012. [Online]. Available: [http://www.attocube.com/nanoPOSITIONING/ANGp50/Specifications\\_ANGp50.pdf](http://www.attocube.com/nanoPOSITIONING/ANGp50/Specifications_ANGp50.pdf). [Accessed 09 08 2012].
- [107] S. GmbH, "SmarAct - Driving Principle," 2011. [Online]. Available: <http://www.smaract.de/index.php/technology>. [Accessed 09 08 2012].
- [108] SmarAct, "SmarAct - Linear Actuators - SL-0610," 2011. [Online]. Available: <http://www.smaract.de/index.php/products/positioniers/linearpositioniers/sl-06-positioner>. [Accessed 09 08 2012].
- [109] SmarAct, "SmarAct - Positioners - Rotary Positioners - SR-1908," 2011. [Online]. Available: <http://www.smaract.de/index.php/products/positioniers/rotarypositioniers/sr-1908>. [Accessed 09 08 2012].
- [110] SmarAct, "SmarAct - Positioners - Rotarty Positoners - SR-2008," 2011. [Online]. Available: <http://www.smaract.de/index.php/products/positioniers/rotarypositioniers/sr-2008>. [Accessed 09 08 2012].
- [111] SmarAct, "SmarAct - Positioners - Rotary Positioners - SR2013S," 2011. [Online]. Available: <http://www.smaract.de/index.php/products/positioniers/rotarypositioniers/sr-2013-s>. [Accessed 09 08 2012].
- [112] A. International, "APC International - About Us," 2012. [Online]. Available: <http://www.americanpiezo.com/about-us.html>. [Accessed 10 08 2012].
- [113] A. I. Ltd, "APC International - Standard Products - Stripe Actuators - Background Information," 2012. [Online]. Available: <http://www.americanpiezo.com/standard-products/stripe-actuators/background.html>. [Accessed 10 08 2012].
- [114] A. I. Ltd, "Piezo-Mechanics: An Introduction," 2011. [Online]. Available: [http://www.americanpiezo.com/images/stories/content\\_images/pdf/APC\\_Stack\\_Principles.pdf](http://www.americanpiezo.com/images/stories/content_images/pdf/APC_Stack_Principles.pdf). [Accessed 10 08 2012].
- [115] P. Systems, "Nano Metrology of Magnetic Recording Industry using Equioment from Park Systems," 17 04 2008. [Online]. Available: <http://www.azonano.com/article.aspx?ArticleID=2114>. [Accessed 10 08 2012].
- [116] PiezoMotor, "PiezoMotor - Company - History," 2012. [Online]. Available: <http://www.piezomotor.se/company/history/>. [Accessed 13 08 2012].
- [117] PizoMotor, "PiezoMotor - Technology - Pizo LEGS," 2012. [Online]. Available: <http://www.piezomotor.se/technology/piezo-legs/>. [Accessed 13 08 2012].
- [118] PiezoMotor, "PiezoMotor - Technology - PiezoWave," 2012. [Online]. Available: <http://www.piezomotor.se/technology/piezowave/>. [Accessed 13 08 2012].
- [119] PiezoMotor, "150075\_WL0104A," PiezoMotor, Uppsala, 2012.
- [120] PiezoMotor, "Piezo LEGS Rotary 50 mNm," PiezoMotors, Uppsala, 2012.
- [121] PiezoMotors, "Piezo LEGS Rotary 80 mNm," PiezoMotors, Uppsala, 2012.
- [122] PiezoMotion, "PiezoMotion - Products - Rotary Motors - Piezo LEGS WavePlate," 2012. [Online]. Available: <http://www.piezomotor.se/products/rotary/piezo-legs-waveplate/>. [Accessed 13 08 2012].
- [123] MICROMO, "MICROMO - Corporate Overview - The FAULHABER-Group," 2012. [Online]. Available: <http://www.micromo.com/the-faulhaber-group.aspx>. [Accessed 13 08 2012].
- [124] MICROMO, "MICROMO - Corporate Overview - Minimotor SA," 2012. [Online]. Available: <http://www.micromo.com/minimotor-sa.aspx>. [Accessed 13 08 2012].



- [125] MICROMO, "MICROMO - Corporate Overview - Dr. Fritz Faulhaber," 2012. [Online]. Available: <http://www.micromo.com/dr-fritz-faulhaber.aspx>. [Accessed 13 08 2012].
- [126] G. Lazaridis, "PCBheaven - How Stepper Motors Work," 07 05 2010. [Online]. Available: [http://pcbheaven.com/wikipages/How\\_Stepper\\_Motors\\_Work/](http://pcbheaven.com/wikipages/How_Stepper_Motors_Work/). [Accessed 13 08 2012].
- [127] MICROMO, "Faulhaber - Technical Library - Stepper Motor Tutorials - Microstepping: Mythes and Realities," Faulhaber, 2008 - 2012. [Online]. Available: <http://www.micromo.com/microstepping-myths-and-realities.aspx>. [Accessed 13 08 2012].
- [128] G. Lazaridis, "PCBheaven - How Brushless DC Motors Work (BLDC)," PCBheaven, 27 03 2010. [Online]. Available: [http://pcbheaven.com/wikipages/How\\_Brushless\\_Motors\\_Work/](http://pcbheaven.com/wikipages/How_Brushless_Motors_Work/). [Accessed 14 08 2012].
- [129] T. C. LLC, "WikiPLC Industrial Electrical and Maintenance," TW Controls LLC, 2012. [Online]. Available: [http://www.patchn.com/index.php?option=com\\_content&view=article&id=48:encoder-basics&catid=18:motors-and-drives&Itemid=116](http://www.patchn.com/index.php?option=com_content&view=article&id=48:encoder-basics&catid=18:motors-and-drives&Itemid=116). [Accessed 16 08 2012].
- [130] A. H. Slocum, "4.3 Optical Encoders," in *Precision Machine Design*, Michigan, Society of Manufacturing Engineers, 1992, pp. 164 - 167.
- [131] N. Instruments, "Magnetic Encoder Fundamentals," National Instruments, 06 09 2006. [Online]. Available: <http://www.ni.com/white-paper/4500/en>. [Accessed 16 08 2012].
- [132] L. Precision, "Capacitive Sensor Operation and Optimization," Lion Precision, 2007. [Online]. Available: <http://www.capacitive-sensing.com/capacitive-sensor-theory.html>. [Accessed 16 08 2012].
- [133] L. Precision, "Eddy Current Sensors Overview," Lion Precision, 2012. [Online]. Available: <http://www.lionprecision.com/inductive-sensors/index.html>. [Accessed 16 08 2012].
- [134] N. Jena, "Company," Numerik Jena, 2002 - 2012. [Online]. Available: [http://numerik.cycro-project.de/frontend/pre\\_cat\\_2-id\\_180\\_\\_stat\\_back\\_id=175.html](http://numerik.cycro-project.de/frontend/pre_cat_2-id_180__stat_back_id=175.html). [Accessed 16 08 2012].
- [135] Renishaw, "Corporate Information - About Renishaw," Renishaw, 2001 - 2012. [Online]. Available: <http://www.renishaw.com/en/Our+company--6432>. [Accessed 17 08 2012].
- [136] M. Systems, "ChipEncoder CE300," MicroE Systems, 2012. [Online]. Available: <http://www.microesys.com/specifications/compact-encoders/chip-encoder-CE300>. [Accessed 17 08 2012].
- [137] M. Systems, "Company Overview," MicroE Systems, 2012. [Online]. Available: <http://www.microesys.com/about-us>. [Accessed 17 08 2012].
- [138] S. Nasiri, "A Critical Review of MEMS Gyroscopes Technology and Commercialization Status," InvenSense, California.
- [139] ADI, "Company Profile," Analog Devices Inc, 1995 - 2007. [Online]. Available: <http://investor.analog.com/overview.cfm>. [Accessed 20 08 2012].
- [140] Qioptiq, "Winlens Homepage," Qioptiq, 2012. [Online]. Available: <http://www.winlens.de/>. [Accessed 21 08 2012].
- [141] H. Zumbahlen, "Chapter 3: Sensors," in *Linear Circuit Design Handbook*, Newnes - Analog Dialogue, 2008, pp. 3.1 - 3.99.
- [142] R. Longoria, "Note on LVDTs," University of Texas at Austin - Department of Mechanical Engineering, 30 03 2000. [Online]. Available: <http://www.me.utexas.edu/~me244L/labs/forcemotion/lvdt.html>. [Accessed 22 08 2012].
- [143] D. Engineering, "A beginner's guide to accelerometers," Dimension Engineering, 2012. [Online]. Available: <http://www.dimensionengineering.com/info/accelerometers>. [Accessed 22 08 2012].
- [144] Posic, "About Posic," Posic, 2008. [Online]. Available: [http://www.posic.ch/default\\_en.asp/2-0-86-12-6-1/](http://www.posic.ch/default_en.asp/2-0-86-12-6-1/). [Accessed 27 08 2012].
- [145] Posic, "Technology," Posic SA, 2008. [Online]. Available: [http://www.posic.ch/default\\_en.asp/2-0-87-12-6-1/](http://www.posic.ch/default_en.asp/2-0-87-12-6-1/). [Accessed 27 08 2012].
- [146] Ladyada, "Overview," Adafruit Learning Systems, [Online]. Available: <http://learn.adafruit.com/tilt-sensor/overview>. [Accessed 27 08 2012].
- [147] T. F. Company, "Tilt Sensors," The Fredericks Company, 2008. [Online]. Available: [http://www.frederickscom.com/sens\\_tilt\\_0717\\_4313.tpl](http://www.frederickscom.com/sens_tilt_0717_4313.tpl). [Accessed 27 08 2012].
- [148] T. F. Company, "Technical Info Overview," The Fredericks Company, 2008. [Online]. Available: [http://www.frederickscom.com/sens\\_tech\\_00.tpl](http://www.frederickscom.com/sens_tech_00.tpl). [Accessed 27 08 2012].
- [149] T. F. Company, "Corporate Overview," The Fredericks Company, 2008. [Online]. Available:

- <http://www.frederickscom.com/about.tpl>. [Accessed 27 08 2012].
- [150] J. K. Ilju Moon, "Using EWOD (electrowetting-on-dielectric) actuation in a micro conveyor system," *Sensors and Actuators A*, vol. A, no. 130-131, pp. 537-544, 2006.
  - [151] P. Systems, "Nano Metrology of Magnetic Recording Industry Using Equipment from Parks Systems," *The A to Z of Nanotechnology*, 2012. [Online]. Available: <http://www.azonano.com/article.aspx?ArticleID=2114>. [Accessed 31 08 2012].
  - [152] D. C. France, "Electromagnetism - Generator," GCSE Science, 2011. [Online]. Available: <http://www.gcse-science.com/pme18.htm>. [Accessed 05 09 2012].
  - [153] E. S. Ferguson, *Kinematics of Mechanisms from the Time of Watt*, Gutenberg.org, 2008.
  - [154] J. Hearnshaw, *Astronomical Spectrographs and their History*, Cambridge: Cambridge, 2009.
  - [155] KEOPSY, "Spectroscopy - The interaction between matter and radiated energy," KEOPSY, 06 03 2014. [Online]. Available: <http://www.keopsys.com/index.php/en/applications/scientific/spectroscopy.html>. [Accessed 10 03 2014].
  - [156] Astronomy 162, "Atomic Absorption and Emission Spectra," [Online]. Available: <http://csep10.phys.utk.edu/astr162/lect/light/absorption.html>. [Accessed 11 03 2014].
  - [157] J. Hearnshaw, *Astronomical Spectrographs and their History*, Cambridge: Cambridge University Press, 2009.
  - [158] Q. A. Parker, F. G. Watson and S. Miziarski, "6dF: An Automated Multi-Object Fiber-Spectroscopy System for the UKST," *Fiber Optics in Astronomy III*, vol. 152, 1998.
  - [159] J. Guerin and e. al, "Multi-Object Spectroscopy with Optical Fibres at the ESO 3.60m Prime focus in a One Degree field: The MEFOS Instrument," *ASP Conference Fiber Optics in Astronomy II*, vol. 37, 1991.
  - [160] Robot Matrix, "SCARA Robot," Robotmatrix, 12 04 2011. [Online]. Available: <http://www.robotmatrix.org/SCARARobotic.htm>. [Accessed 11 03 2014].
  - [161] Macron Dynamics Inc, "Gantry Systems: Working Outside the Envelope," Macron Dynamics Inc, [Online]. Available: <http://www.macrondynamics.com/job-stories/gantry-systems-overview>. [Accessed 11 03 2014].
  - [162] T. Deyle, "Inchy," Hizook, 05 01 2009. [Online]. Available: <http://www.hizook.com/projects/inchy>. [Accessed 12 03 2014].
  - [163] H. Ishihara and T. Fukuda, "Miniaturized Autonomous Robot," *SPIE*, vol. 3202, pp. 191 - 196.
  - [164] H. Ishihara and T. Fukuda, "Micro Autonomous Robotic System," *SPIE*, vol. 2593, pp. 32 - 37.
  - [165] S. Ramsay, S. D'Odorico, M. Casali, J. C. Gonzalez, N. Hubin, M. Kasper, H. U. Kaufl, M. Kissler-Patig, E. Marchetti, J. Paufique, L. Pasquini, R. Siebenmorgen, A. Richichi, J. Vernet and F. M. Zerbi, "An overview of the E-ELT instrumentation programme," in *Proc. SPIE 7735, Ground-based and Airborne Instrumentation for Astronomy III*, San Diego, 2010.
  - [166] C. Billard, "Design of a micro-robot for MOS system," *Heriot Watt University Dissertation*, vol. School of Mechanical Engineering and Physical Sciences, 2008.
  - [167] J. Gilbert, M. Goodwin, J. Heijmans, R. Muller, S. Miziarski, J. Brzeski, L. Waller, W. Saunders, A. Bennet and J. Tims, "Starbugs: all-singing, all-dancing fibre positioning robots," in *SPIE 8450, Modern Technologies in Space- and Ground-based Telescopes and Instrumentation II*, Amsterdam, 2012.
  - [168] C. D. Near, "Piezoelectric actuator technology," in *SPIE 2717, Smart Structures and Materials 1996: Smart Structures and Integrated Systems*, San Diego, CA, 1996.
  - [169] ephotozine, "ephotozine," ephotozine, 31 10 2012. [Online]. Available: <http://www.ephotozine.com/article/stfc-photo-walk-2012-20570>. [Accessed 22 04 2014].
  - [170] J. Seyfried, M. Szymanski, N. Bender, R. Estana, M. Thiel and H. Worn, *The I-SWARM Project: Intelligent Small World Autonomous Robots for Micro-manipulation*, Santa Monica, CA, USA: Springer Berlin Heidelberg, 2005.
  - [171] I. Appenzeller, *Introduction to Astronomical Spectroscopy*, Cambridge: Cambridge University Press, 2012.